Study and Modeling of Fluctuating Fluid Forces Exerted on Fuel Rods in Pressurized Water Reactors

(Etude et Modélisation des Forces Fluides Fluctuantes s'Exerçant sur les Crayons Combustibles en Réacteur à Eau Pressurisée)

Thèse présentée devant

L'AIX-MARSEILLE UNIVERSITÉ

École Doctorale 353: Sciences pour l'Ingénieur: Mécanique, Physique, Micro et Nanoélectronique
Spécialité: Mécanique et Physique des Fluides

pour obtenir le grade de

DOCTEUR (Ph.D.)

par

Saptarshi BHATTACHARJEE

soutenue publiquement *le 06 avril 2016* devant le jury:

Olivier VAUQUELIN	Professeur, Université Aix-Marseille	Président
Mohammed El GANAOUI	Professeur, Université de Lorraine	Rapporteur
Jean-Pierre FONTAINE	Professeur, Université de Clermont-Ferrand	Rapporteur
Stéphane ETIENNE	Professeur Agrégé, Ecole Polytechnique de Montréal	Examinateur
Stéphane VIAZZO	Maître de Conférences, Université Aix-Marseille	Directeur de Thèse
Guillaume RICCIARDI	Ingénieur-Chercheur, CEA Cadarache	Co-encadrant

Thèse préparée au Laboratoire d'Hydromécanique du Coeur et des Circuits (DTN/STCP/LHC),
Commissariat à l'Énergie Atomique et aux Énergies Alternatives (CEA), Cadarache,
13108 Saint Paul lez Durance, France

(Cover page in English)

Study and Modeling of Fluctuating Fluid Forces Exerted on Fuel Rods in Pressurized Water Reactors

---

Dissertation submitted to

AIX-MARSEILLE UNIVERSITY

Doctoral School 353: Engineering Sciences: Mechanics, Physics, Micro and Nanoelectronics
Specialization: Mechanics and Physics of Fluids

for the degree of

DOCTOR OF PHILOSOPHY (Ph.D.)

by

Saptarshi BHATTACHARJEE

and defended in public on the 6^{th} *of April 2016* in front of the jury:

Olivier VAUQUELIN	Professor, Aix-Marseille University	President
Mohammed El GANAOUI	Professor, Université de Lorraine	Reviewer
Jean-Pierre FONTAINE	Professor, Université de Clermont-Ferrand	Reviewer
Stéphane ETIENNE	Associate Professor, Ecole Polytechnique de Montréal	Examiner
Stéphane VIAZZO	Associate Professor, Aix-Marseille University	Director of Thesis
Guillaume RICCIARDI	Research Engineer, CEA Cadarache	Co-supervisor

---

The dissertation work was carried out at
Laboratory of Hydromechanics of Cores and Circuits (DTN/STCP/LHC),
Alternative Energies and Atomic Energy Commission (CEA), Cadarache,
13108 Saint Paul lez Durance, France

Dedicated to my parents

Subrata Bhattacharyya
& Sunanda Bhattacharjee

Acknowledgments

It gives me immense pleasure to write this note of acknowledgement for everyone who has been involved with this project in one way or the other. First of all, I would like to thank my supervisor, Guillaume, for accepting me as a PhD student. I wholeheartedly thank you for the constant support and encouragement during the entire duration of my PhD. I take this opportunity to thank Stéphane for agreeing to be the director of my thesis and his constant guidance throughout. Your insight on the intricacies of turbulence modeling is highly appreciated. Thank you Guillaume for your valuable inputs while writing the manuscript. Your time and effort in helping me analyze the results have been invaluable. My sincere thanks to both Guillaume and Stéphane for correcting and improving the manuscript time and again. This work would not have been possible without your dynamic and efficient guidance during the past three years.

I would like to thank all the jury members. Thank you Prof. Fontaine and Prof. El Ganaoui for your thorough reports which has helped me to improve the present manuscript. Thanks to Prof. Vauquelin, the President of the jury and Prof. Etienne for your pertinent questions and comments on the day of my defense. I take this opportunity to thank my lab chief in CEA, Isabelle Tkatschenko, for allowing me to present my work in international conferences. Thank you Isabelle for personally taking initiative to solve administrative issues to facilitate my participation in these conferences. Many thanks to my ex-chiefs François Boussard and Etienne Tevissen for welcoming me as a PhD student initially. Thank you for allowing me to attend the French language course at Cadarache. I also acknowledge the financial support from CEA for this entire PhD project. Thanks to the Department of Nuclear Technology (DTN) for access to the Curie, Airain and Mezel supercomputers. Many thanks to Francis Moreno for sharing the results of CALIFS experiment.

My sincere thanks to Ulrich Bieder for organizing numerous video conference sessions and sharing his wealth of experience in TrioCFD code. I appreciate the prompt assistance from the TrioCFD

technical support team of Pierre Ledac, Marthe Roux and Celine Capitaine. Thanks to Pierre Ledac for hosting me at CEA Grenoble for two introductory TrioCFD user sessions. Special thanks to my friend and colleague Aakanksha for sharing valuable user experience with TrioCFD!

Thank you Guillaume and Stéphane once again for sharing your expertise during numerous discussions from time to time. Thanks Guillaume for making my stay comfortable during the initial months and helping me with administrative formalities and in addition, acting as a translator! Thank you Stéphane for your help in dealing with the university from time to time.

Thanks to everyone in my lab LHC for making my stay pleasurable and memorable! I would like to make a special mention of Isabelle Mounet who helped me to improve my French vocabulary immensely. Our lunch-time discussions helped me discover a lot about France. My heartfelt thanks to you for encouraging me to speak French and patiently correcting me every time I made mistakes! Thanks to Petra and Claudia for our lovely coffee-time interactions; to Jean-François (Ivars) and Phillipe (Latil) for sharing your traveling experiences throughout the world; and to my fellow PhD lab-mates Simon, Antoine, Guangze, Roberto for the wonderful time spent in the lab. Thank you all for the hospitality!

Heartfelt thanks to all my friends in Aix-en-Provence (our "Kübler-Ross fan club") for the amazing time spent together. Without you, my life in Provence would never have been the same! It has been a wonderful learning curve for me. Thank you Gregoire for correcting the French version of the thesis at a short notice! Thanks to my family and friends back home in India and elsewhere for your blessings. Most importantly, I would like to thank my parents for your support at every stage of my life. Thank you all for being present, physically or virtually, during the day of my defense and sharing this important occasion with me.

This PhD thesis has been the combined effort of so many people, my supervisors Guillaume and Stéphane, my friends and family...

Thank you all!

Saptarshi Bhattacharjee

Abstract

Flow-induced vibrations in a pressurized water reactor (PWR) core can cause fretting wear in the fuel rods. Due to friction, wear occurs at the contact locations between the spacer grid and the fuel rod. This could compromise the first safety barrier of the nuclear reactor by damaging the fuel rod cladding. In order to ensure the integrity of the cladding, it is necessary to know the random fluctuating forces acting on the rods. However, the spectra for these fluid forces are not well known.

The goal of this PhD thesis was to use simple geometrical elements to check the reproducibility of realistic pressurized water reactor spacer grids. As a first step, large eddy simulations were performed on a concentric annular pipe for different mesh refinements using the CFD code TrioCFD (previously Trio_U) developed by CEA. A mesh sensitivity study was performed to obtain an acceptable mesh for reproducing standard literature results. This information on mesh resolution was used when carrying out simulations using various geometric obstacles inside the pipe, namely, mixing vanes, circular spacer grid and a combination of square spacer grid with mixing vanes. The last of the three configurations is the closest to a realistic PWR fuel assembly. Structured mesh was generated for the annular pipe case and circular grid case. An innovative hybrid mesh was used for the two remaining cases of the mixing vanes and the square grid: keeping unstructured mesh around the obstacles and structured mesh in the rest of the domain. The inner wall of the domain was representative of the fuel rod cladding. Both hydraulic and wall pressure characteristics were analyzed for each case. The results for the square grid case were found to be an approximate combination of the mixing vane case and circular grid case. Simulation results were compared with experiments performed at CEA Cadarache. Some preliminary comparisons were also made with classical semi-empirical models.

Keywords: large eddy simulation, LES, wall pressure fluctuations, spacer grid, mixing vanes, CFD, Trio_U, TrioCFD.

List of Abbreviations

Note 1: The words 'spacer grid', 'circular grid', 'square grid', 'grid' all refer to the spacer grid structure present in the fuel assemblies of pressurized water reactors. The word 'grid' does not refer to computational mesh. The word 'mesh' has been exclusively used for that purpose.

Note 2: Since late 2015, the code 'Trio_U' has been renamed as 'TrioCFD'. So, throughout the present thesis, it has been referred to as TrioCFD. However, in the bibliography references section, the name has been retained as it is in the original paper.

axi	Axial
azi	Azimuthal
C1 *or* PC	Simulation case of an annular pipe with a coarse mesh
C2	Simulation case of an annular pipe with a second coarse mesh
CAD	Computer-Aided Design
CALIFS	Single rod test section at CEA Cadarache
CASL	Consortium for Advanced Simulation of Light water reactors
CCRT	Computing Center for Research and Technology
CEA	French Alternative Energies and Atomic Energy Commission
CFD	Computational Fluid Dynamics
CG	Simulation case of an annular pipe with circular spacer grid
DES	Detached Eddy Simulation
DFT	Discrete Fourier Transform
DIVA	Two-phase (DIphasique) Vibration Analysis loop
DNS	Direct Numerical Simulation
EF_stab	Finite Element Stabilized

EX	Experiment
F1	Simulation case of an annular pipe with a fine mesh
F2 *or* PF	Simulation case of an annular pipe with a second fine mesh
FA	Fuel assembly
FFT	Fast Fourier Transform
FIV	Flow-induced Vibration
FSI	Fluid Structure Interaction
FW	Fretting wear
GENCI	Grand Équipement National de Calcul Intensif
GFR	Gas-cooled Fast Reactor
GTRF	Grid-to-Rod Fretting
HD	Hydraulic Diameter
HPC	High Performance Computing
HP RGS	HP Remote Graphics Software
HTR	High Temperature Reactor
ID	Inner Diameter
KAERI	Korea Atomic Energy Research Institute
LDA	Laser Doppler Anemometry
LDV	Laser Doppler Velocimetry
LES	Large Eddy Simulation
LHC	Laboratory of Hydromechanics of Cores and Circuits
LSVF	Large Scale Vortex Flow mixing vane
MATiS-H	Measurements & Analysis of Turbulence in Subchannels - Horizontal
MPI	Message Passing Interface
MV	Simulation case of an annular pipe with mixing vanes
OD	Outer Diameter
OECD/NEA	Organization for Economic Co-operation and Development / Nuclear Energy Agency
PCG	Preconditioned Conjugated Gradient
PDF	Probability Density Function
PIV	Particle Image Velocimetry

POC	Proper Orthogonal Component
POD	Proper Orthogonal Decomposition
POM	Proper Orthogonal Mode
POV	Proper Orthogonal Value
PSD	Power Spectral Density
PWR	Pressurized Water nuclear Reactor
RANS	Reynolds Averaged Navier Stokes method
RMS	Root Mean Square fluctuation *OR* standard deviation
SFR	Sodium-cooled Fast Reactor
SGS	Sub-Grid Scale
SQ	Simulation case of an annular pipe with square spacer grid with mixing vanes
SSOR	Symmetric Successive Over-Relaxation
SSVF	Small Scale Vortex Flow mixing vane
TBL	Turbulent Boundary Layer
TKE	Turbulent Kinetic Energy
UF	Simulation case of an annular pipe with an ultra-fine mesh
URANS	Unsteady Reynolds Averaged Navier Stokes method
VEF	Finite Volume based Finite Element Method
VIPER	Westinghouse Vibration Investigation and Pressure-drop Experimental Research loop
VITRAN	Vibration Transient Analysis Non-linear
VVER-1000	Russian PWR. It stands for 'Vodo-Vodyanoi Energetichesky Reaktor' (in Russian) which literally means Water-Water Power Reactor
WALE	Wall-Adaptive Local Eddy viscosity

List of Symbols

English Symbols

A_{flow}	Surface area of duct cross-section
A_i	Surface area of inner wall of the annular pipe
A_o	Surface area of outer wall of the annular pipe
D_i	Inner diameter of annular pipe
D_o	Outer diameter of annular pipe
f	Frequency in Hz
f_{red}	Reduced frequency (non-dimensionalized)
$\vec{k} = (k_x, k_z)$	Wave vector in Cartesian co-ordinates
k_x	Longitudinal wavenumber
k_z	Transverse wavenumber
K	Norm of $\vec{k}$
L	Element size in unstructured sub-domain
N_r	Number of grid points in radial direction
N_θ	Number of grid points in azimuthal direction
N_z	Number of grid points in axial direction
$P(k_x, k_z, \omega)$	Wavenumber-frequency spectrum of wall pressure
p	Pressure
PSD_{red}	Reduced power spectral density (non-dimensionalized)
P_{wet}	Wetted perimeter
Re_D	Reynolds number based on hydraulic diameter
Re_θ	Reynolds number based on momentum boundary layer thickness
S_{ij}	Strain rate

St	Strouhal number
U_b	Bulk or free-stream velocity
U_c	Convection velocity
u_τ	Friction velocity
y^+	Distance of first grid point in wall units

Greek Symbols

$\Gamma(x, z, \omega)$	Cross spectral density
δ	Boundary layer thickness
δ/a	Ratio of boundary layer thickness to cylinder radius in axisymmetric cylindrical flow
μ	Dynamic viscosity ($Pa.s$)
μ_t	Turbulent or eddy viscosity
ν	Kinematic viscosity (m^2/s)
ω	Angular frequency
$\phi(\omega)$	Spectral density in frequency
ρ	Fluid density (kg/m^3)

Contents

Chapter 1

General Introduction

Fuel rods in the core of a pressurized water reactor (PWR) are subject to high axial fluid velocities of the order of 5 m/s to ensure proper heat transfer. This high coolant velocity induces vibrations in the fuel rods known as flow-induced vibrations (FIV). In such a situation, the flow is turbulent with Reynolds number $Re_D \approx 500000$. These vibrations may cause fretting wear. In the US, 80 % of the failures in PWRs, where thousands of hot irradiated fuel rods are cooled by fast-flowing water, are caused by grid-to-rod fretting (GTRF): a flow-induced vibration problem that leads to wear and failure of the rods [ADTSC Science Highlights, 2013]. For example, in a 17 $\times$ 17 PWR core, there are 193 fuel assemblies each containing 289 rods (264 fuel rods and 25 control rods). So, in total, there are approximately 55000 rods in a PWR core. Contact points between the spring and the fuel rod cladding (Fig. 1.1) cause wear, leading to fuel leakage. Failure of more than a few rods in a fuel assembly forces a full power plant shutdown and increases maintenance costs. Most importantly, it breaches the first safety barrier of nuclear power plants which may lead to radioactive leakage. Typical reactor fuel cycles range from 18 to 24 months, and increasing the life span of reactor fuel significantly improves the economic viability of electricity generated from nuclear power.

Figure 1.1: PWR fuel assembly with fuel rods (taken from ADTSC Science Highlights [2013])

In PWRs, grid-to-rod fretting (GTRF) is a flow-induced vibration problem resulting in wear and failure of the rods in fuel assemblies. It has not been possible to completely characterize the flow-induced fluid-structure interaction (FSI) problem. Given the incompressible nature of the coolant, the relatively high Reynolds number, and the flexible character of the fuel rods and spacers, the FSI problem at the reactor core scale is very challenging. PWR fuel assemblies are vertical rod bundles where water flows from the bottom to the top. Spacer grids are placed along the bundles at regular axial distances. Mixing vanes are fitted to the top of the grids to generate swirl flow structures. The mixing vanes are responsible for the increase in turbulence and heat transfer in the rod bundles. The swirl structures are very strong immediately downstream of the mixing vanes and it decays as the flow travels further downstream. The hydrodynamic forces loading the fuel rods are believed to be responsible for rod vibration and GTRF wear. The wear phenomenon is a major concern for nuclear safety and lifetime of fuel rods. To understand the root causes of fretting wear, one must investigate the turbulent coolant flow in the core of nuclear reactors. One can do away with neither the turbulent flow nor the spacer grid structures which enhance turbulence and heat transfer [King et al., 2002]. As discussed by Pettigrew [1993], Rubiolo [2006], Rubiolo and Young [2009], fretting wear damage in nuclear reactors could be analyzed with respect to multiple phenomenon which occur during reactor operation like the hydrodynamic forces on fuel rods, changes in the mechanical properties of fuel rods, effects of neutron irradiation, geometrical factors etc.

The hydrodynamic fluid forces induced by the grid are not well-known although some empirical models exist. This thesis consists of a numerical study of the hydrodynamics of turbulent flow developed inside a PWR fuel assembly. The goal of the thesis is to understand these hydrodynamic forces exerted on fuel rods by the fluid. Since the Reynolds-averaged Navier Stokes (RANS) method of turbulence modeling simulates information on averaged quantities only, large eddy simulation (LES) modeling is necessary to study the fluctuating quantities. However, a transient CFD simulation of a complete fuel assembly would require huge computational resource which is not feasible. Hence, characterization has often been done using simplified smaller geometrical configurations [Chang et al., 2008, Caraghiaur et al., 2009, Conner et al., 2010, Christon et al., 2011, Elmahdi et al., 2011, Bieder, 2012, Delafontaine and Ricciardi, 2012, Frank et al., 2012, Bakosi et al., 2013, Nourgaliev et al., 2013, Smith et al., 2013]. In this PhD thesis, it is proposed to investigate what could be a satisfactory geometrical element which reproduces the behavior closest to that of a realistic spacer grid. The goal was to understand the physics behind the problem and a simple geometrical element gave faster

computational results.

LES modeling was used to simulate incompressible turbulent flow in four 'simple' 3D geometries, namely,

- an annular pipe,
- an annular pipe with two symmetrically opposite mixing vanes (MV),
- an annular pipe with a circular spacer grid (CG), and
- an annular pipe with a square spacer grid with two symmetrically opposite mixing vanes (SQ).

Instead of reactor-scale Reynolds number 500000, numerical simulations were done at 8900. At this Reynolds number, it was possible to obtain stable solutions for the above-mentioned geometries within a limited amount of time. Thereafter, comparative studies between these configurations could be performed without wasting computational resource because a simulation at a higher Reynolds number requires a more refined mesh and longer time for computation. Such studies would let one know if it is feasible to use such simplified models. The 3D geometries were designed according to the CALIFS experimental setup at CEA Cadarache, France (Section 2.5.3) with certain simplifications which have been explained in later chapters. The simulation results were compared to these experimental results. The Reynolds number 8900 was specifically chosen due to the availability of numerous simulation and experimental data [Nouri et al., 1993, Nouri and Whitelaw, 1994, Azouz and Shirazi, 1998, Chung et al., 2002, Kaneda et al., 2003, Liu and Lu, 2004, Chung and Sung, 2005, Ould-Rouiss et al., 2009, Hadžiabdić et al., 2013].

Following this introduction, in Chapter 2, a bibliography report on the subject is presented. It includes descriptions on various physical phenomena, mathematical tools and the codes and machines used for simulation. In Chapter 3, simulations on the annular pipe are discussed. Simulations were performed on five meshes with increasing levels of mesh refinement. A mesh sensitivity study on these meshes is presented. In Chapter 4, three different geometrical obstacles are introduced into the pipe (enumerated above and denoted as MV, CG and SQ) and their effect on the flow field is studied. All these three cases have a downstream section of length 4 times the hydraulic diameter (HD) which allows comparison between the different geometries. In Chapter 5, a detailed characterization of the wall pressure field is presented for five cases (MV, CG, SQ and two cases for the annular pipe). The comparison with CALIFS experiment is also presented in this chapter. The fluid forces on the wall obtained from these simulations could be further used as input data in structural mechanics codes to

study vibration and damage in the fuel rods. Finally, Chapter 6 presents the general conclusion of the thesis and some future perspective work on the subject.

All simulations presented in this thesis were carried out using the CFD code TrioCFD (previously Trio_U) on the Curie and Airain supercomputers [Computing Center for Research and Technology (CCRT)]. Few small-scale test simulations were also performed on the Mezel supercomputer at CEA Cadarache.

Chapter 2

Bibliography Study

2.1 General background

A typical pressurized water reactor (PWR) core consists of 17×17 fuel assemblies arranged in a square array (Fig. 2.1). Each fuel assembly contains 264 fuel rods containing uranium pellets and 25 guide tubes for reactor control. Fuel rods in PWRs consist of cylindrical pellets stacked one on top of the other, inserted in a tube-like structure made of zirconium alloy. In the axial direction, 8 spacer grids are placed at equal intervals, plus 2 end grids attached to the top and the bottom of the fuel assembly. Mixing vanes are attached to the 8 spacer grids.

- **Spacer grid** (Fig. 2.2) provides support to the rods. It also helps to maintain a certain gap between adjacent rods, thereby preventing the formation of hotspots at the contact locations of two adjacent rods.
- Fuel rods are held by the **spring-dimple** configuration (Fig. 2.3) placed at the inner surface of the spacer grids. This configuration facilitates the insertion and extraction of the fuel rods.
- **Mixing vanes** generate strong swirls in the sub channels, thereby improving the heat transfer between the cladding and coolant. This leads to high fuel burn-up. But the flow is highly turbulent and induces vibrations in the fuel rods.

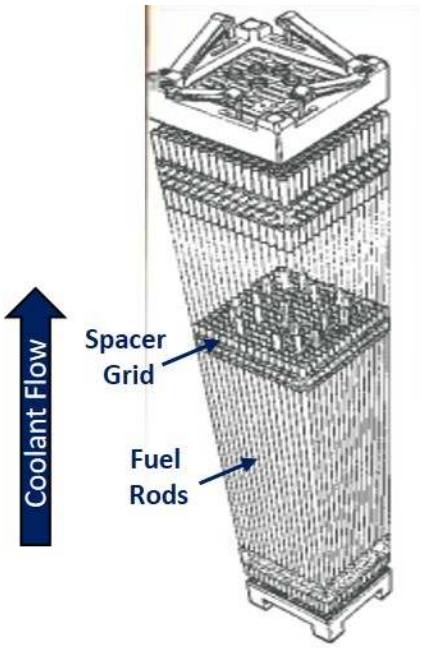

Figure 2.1: PWR Fuel Assembly

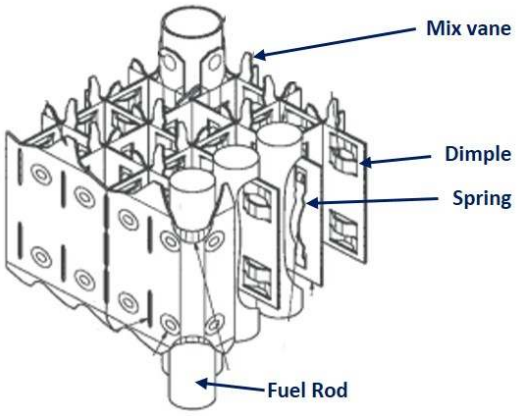

Figure 2.2: Spacer Grid

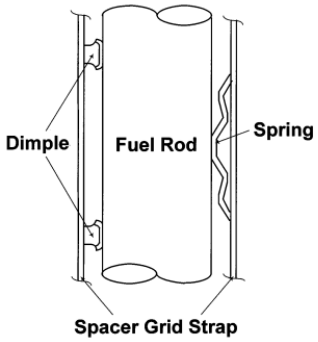

Figure 2.3: Spring-dimple configuration

2.2 Turbulence modeling

At low velocities, fluids have a regular orderly motion. But as the velocity increases, the motion becomes more random and disordered. This phenomenon is known as turbulence. In turbulent flows, any perturbation gets amplified due to the dominance of inertial effects over viscous effects. Inertial effects tend to amplify the perturbations, hence ensuring better mixing of fluid elements. The **Reynolds number** is defined as the ratio between inertial and viscous forces and it gives an idea about the flow regime. In any turbulent flow, the transport variables like pressure and velocity fluctuate randomly with respect to space and time. Due to this velocity fluctuation, there is a significant momentum transfer between fluid elements. This momentum transfer leads to strong mixing. However,

modeling turbulence is very complex due to the wide range of length and time scales.

Visualization of turbulent flows reveal rotational flow structures called **eddies**. These are basically lumps of rotating fluid elements. The largest eddies are of the order of system length scale and the smallest ones of molecular length scale. The largest eddies extract kinetic energy from the mean flow by vortex stretching. The larger ones being unstable, breakup in to smaller eddies to which the energy is subsequently transferred by inviscid processes. At the smallest scales, the energy is dissipated by viscous action. This entire phenomenon is known as **energy cascading** and it was proposed by Richardson [1922]. Detailed discussion on turbulence modeling and its related mathematical treatment can be found in Hinze [1959], Lesieur [1995], Pope [2000], Versteeg and Malalasekara [2007], Anderson Jr. [2009].

In 1941, Kolmogorov [1941a,b] hypothesized that:

- Directional property is lost as we go down to smaller scales. At lengths much smaller than the largest eddy length scale, turbulent motion is statistically isotropic.
- Information about geometry of large eddies is lost. So statistics of small scale eddies are universal.

At the system scale, the length scale of the eddies is of the order of the system scale, and so the Reynolds number (being proportional to the system scale) is large. Hence inertial effects are dominant over viscous effects. As we go down to smaller eddies, the length scale decreases. Thus the inertial force being proportional to length scale also decreases. At the smallest eddy, inertial force is just equal to viscous force. Smallest eddy is characterized by Reynolds number of 1. It is interesting to note that the smallest eddy length scale (called **Kolmogorov scale**) does not depend on the system scale, but on the rate of dissipation of turbulent kinetic energy. Comparing the system scale (l) and Kolmogorov scale (η), one can obtain an approximate expression as follows:

$$\frac{\eta}{l} \approx Re_l^{-3/4} \tag{2.1}$$

where Reynolds number at the system scale is

$$Re_l = \frac{\rho v l}{\mu} \tag{2.2}$$

For example, if $Re_l = 10000$, the difference in length scales is 1000. Greater the Reynolds number, greater is the difference in length scales. Thus one has to deal with a wide range of length and time scales and this makes the problem very complex.

The fluid dynamics, both in laminar and turbulent flow regimes, is governed by the three fundamental physical principles of conservation of mass, momentum and energy. These form the basis of the Navier-Stokes equations. Detailed mathematical formulation can be found in Anderson Jr. [2009], Pope [2000], Versteeg and Malalasekara [2007]. For the sake of completeness, the three components of the momentum conservation equations are written below.

$$\textbf{x-component} : \frac{\partial(\rho u)}{\partial t} + \nabla.(\rho u\vec{V}) = -\frac{\partial p}{\partial x} + \mu\frac{\partial^2 u}{\partial x^2} + \mu\frac{\partial^2 u}{\partial y^2} + \mu\frac{\partial^2 u}{\partial z^2} + \rho f_x \tag{2.3}$$

$$\textbf{y-component} : \frac{\partial(\rho v)}{\partial t} + \nabla.(\rho v\vec{V}) = -\frac{\partial p}{\partial y} + \mu\frac{\partial^2 v}{\partial x^2} + \mu\frac{\partial^2 v}{\partial y^2} + \mu\frac{\partial^2 v}{\partial z^2} + \rho f_y \tag{2.4}$$

$$\textbf{z-component} : \frac{\partial(\rho w)}{\partial t} + \nabla.(\rho w\vec{V}) = -\frac{\partial p}{\partial z} + \mu\frac{\partial^2 w}{\partial x^2} + \mu\frac{\partial^2 w}{\partial y^2} + \mu\frac{\partial^2 w}{\partial z^2} + \rho f_z \tag{2.5}$$

where p denotes pressure, μ denotes absolute viscosity, f_x, f_y, f_z denote the body forces in x, y, z directions respectively, ρ denotes density and $\vec{V} = u\hat{i} + v\hat{j} + w\hat{k}$ denotes the velocity vector field in Cartesian coordinates.

Various techniques have been developed to model turbulence. Below are listed three commonly used techniques in increasing order of computational difficulty.

- **Reynolds averaged Navier Stokes simulation (RANS)**: It involves maximum number of approximations but is computationally the fastest. Any instantaneous turbulent quantity at a point is assumed to be composed of a temporal mean value plus fluctuations (**Reynolds decomposition**). As a result, the Navier-Stokes equation yields an additional term called the Reynolds stress tensor. The various common approaches to model it are $k-\epsilon$ model (two additional equations), mixing length model (one equation), Reynolds stress transport model (seven additional equations).

- **Large eddy simulation (LES)**: LES is an unsteady simulation approach. RANS involves only one length and time scale. But in fact, there exists a wide range of scales. The smaller

eddies are nearly isotropic and show universal behavior. The larger eddies are anisotropic and their behavior is dictated by geometry, boundary conditions etc. LES uses spatial filtering to filter out small eddies and model them separately without explicitly solving them. We chose to perform LES because it is computationally feasible and is more closer to reality than RANS. This technique is further discussed in the following sub-section.

- **Direct numerical simulation (DNS)**: It involves solving the Navier Stokes equation without any approximation. However in order to do so, the grid size should be of the order of Kolmogorov scale. For high Reynolds numbers, obtaining this grid size is computationally very intensive. So, DNS is only useful for simple geometries and moderate Reynolds numbers.

2.2.1 Large eddy simulation (LES)

A brief overview of large eddy simulation is presented here. One should refer to Sagaut [2005] for a detailed study. The basic idea of LES is that large turbulent structures efficiently transport the conserved properties whereas the smaller ones have a more general character and primarily dissipate the kinetic energy. In order to separate the large and small scale motions, a spatial filtering operation is applied to the conservation equations. A filter function is used as

$$\overline{\phi}(x,t) = \int\int\int_{-\infty}^{\infty} G(x,x^{'},\Delta).\phi(x^{'},t).dx_1^{'}.dx_2^{'}.dx_3^{'} \tag{2.6}$$

where $\phi(x^{'},t)$ is the original unfiltered function and $G(x,x^{'},\Delta)$ is the filter function. The top hat filter is widely used in finite volume implementation. It is defined as

$$G(x,x^{'},\Delta) = \begin{cases} \frac{1}{\Delta^3} & \text{for} \quad |x-x^{'}| \leq \frac{\Delta}{2} \\ 0 & \text{for} \quad |x-x^{'}| > \frac{\Delta}{2} \end{cases}$$

In finite volume implementation, a single value represents a flow variable in each grid cell. So cut off width Δ is of the order of grid cell size. In 3D grids with different Δx,Δy,Δz, the cut off width is defined as

$$\Delta = \sqrt[3]{\Delta x.\Delta y.\Delta z} \tag{2.7}$$

A flow variable $\phi(x,t)$ is split up as

$$\phi(x,t) = \overline{\phi}(x,t) + \phi^{'}(x,t) \tag{2.8}$$

where $\overline{\phi}(x,t)$ is the filtered function with spatial variation greater than Δ and hence resolved by LES calculation. $\phi^{'}(x,t)$ represents the unresolved spatial variation at length scales less than cut off width.

After applying the filtering operation, the momentum equations 2.3 to 2.5 have additional terms which are dimensionally stresses and so these terms are called sub grid scale (SGS) stresses. Substituting equation (2.8) in equation (2.9), the SGS stresses take the form:

$$\tau_{ij} = \rho\overline{u_i u_j} - \rho\overline{u_i}.\overline{u_j} \tag{2.9}$$

$$\tau_{ij} = \underbrace{\left(\rho\overline{\overline{u_i}.\overline{u_j}} - \rho\overline{u_i}.\overline{u_j}\right)}_{L_{ij}} + \underbrace{\left(\rho\overline{\overline{u_i}.u_j^{'}} + (\rho\overline{u_i^{'}.\overline{u_j}})\right)}_{C_{ij}} + \underbrace{\left(\rho\overline{u_i^{'}.u_j^{'}}\right)}_{R_{ij}} \tag{2.10}$$

As observed here, SGS stress has 3 types of contribution.

- Leonard stresses L_{ij} : it arises due to effects at resolved scale.
- Cross stresses C_{ij} : it arises due to interaction between SGS eddies and resolved flow.
- LES Reynolds stresses R_{ij} : it arises due to convective momentum transfer due to interaction of SGS eddies.

Two commonly used SGS turbulence models are discussed below.

Classical Smagorinsky model

The Smagorinsky model [Smagorinsky, 1963] is based on the Boussinesq approximation, i.e., turbulent Reynolds stress is proportional to the mean rate of strain or deformation

$$-\rho\overline{u_i^{'}.u_j^{'}} = \mu_t\left(\frac{\partial\overline{u_i}}{\partial x_j} + \frac{\partial\overline{u_j}}{\partial x_i}\right) \tag{2.11}$$

where μ_t is the turbulent or eddy viscosity. Isotropy of the small eddies is assumed. In this model, all 3 components of stresses are clubbed together and turbulent stress is modeled as single entity. The turbulent viscosity is

$$\mu_{SGS} = \rho.(C_{SGS}.\Delta)^2.\sqrt{2.\overline{S_{ij}}.\overline{S_{ij}}} \tag{2.12}$$

where

$$\overline{S_{ij}} = \frac{1}{2}\left(\frac{\partial \overline{u_i}}{\partial x_j} + \frac{\partial \overline{u_j}}{\partial x_i}\right) \tag{2.13}$$

Estimation of the constant C_{SGS} has shown certain disparities; 0.17 - 0.21 [Lilly, 1966, 1967], 0.19 - 0.24 [Rogallo and Moin, 1984], 0.1 [Deardorff, 1970]. This inconsistency in the values points to the fact that small eddies are not exactly isotropic which is the assumption in Boussinesq hypothesis. Improvements on the classical Smagorinsky model have been done by Germano et al. [1991] (dynamic Smagorinsky model), Lilly [1992], Leveque et al. [2007].

Wall adaptive local eddy viscosity (WALE) model

The WALE sub-grid scale model was developed by Nicoud and Ducros [1999]. It has the following major properties:

- it goes naturally to zero at the wall; hence neither a damping function nor dynamic procedure is necessary to reproduce the effect of the no-slip condition unlike the Smagorinsky model
- it has proper near wall scaling $O(y^3)$ for eddy viscosity
- it reproduces the laminar to turbulent transition correctly
- it has a unique parameter - a constant C_w
- it is a function of both the strain and rotational rates

The eddy viscosity is written as

$$\mu_{SGS} = \rho \times (C_w \Delta)^2 \times \frac{OP_1}{OP_2} \tag{2.14}$$

where

$$\begin{aligned}
OP_1 &= \left(s_{ij}^d . s_{ij}^d\right)^{3/2} \\
OP_2 &= (S_{ij} . S_{ij})^{5/2} + \left(s_{ij}^d . s_{ij}^d\right)^{5/4} \\
s_{ij}^d &= \frac{1}{2} . \left(g_{ij}^2 + g_{ji}^2\right) - \frac{1}{3} . \delta_{ij} . g_{kk}^2 \\
S_{ij} &= \frac{1}{2} . \left(\frac{\partial \overline{u_i}}{\partial x_j} + \frac{\partial \overline{u_j}}{\partial x_i}\right) \\
g_{ij} &= \frac{\partial \overline{u_i}}{\partial x_j} \\
g_{ij}^2 &= g_{ik} . g_{kj}
\end{aligned}$$

OP_1 and OP_2 are two operators representative of the turbulent activity. S_{ij} is the velocity gradient tensor. s^d_{ij} is the traceless symmetric part of the square of the velocity gradient tensor. δ_{ij} is the Kronecker delta symbol and the constant $C_w = 0.5$.

2.2.2 Law of the wall

There are two approaches for studying the near-wall behavior [Sagaut, 2005].

- Either direct resolution of wall layer is done by placing the first grid point such that $y^+ \sim O(1)$.
- Or the wall layer is modeled by placing the first point in the logarithmic layer (in practice, $20 \leq y^+ \leq 200$). The main advantage of this approach is that the number of degrees of freedom in the simulation can be reduced greatly; but since a part of the dynamics is modeled, it constitutes an additional source of error.

Many model equations have been developed for describing the law of the wall. Temmerman et al. [2003] used some of these equations to investigate the effect of these various wall functions in a channel flow. The **Reichardt wall law** [Reichardt, 1951] is a linear equation combining the viscous sublayer, buffer layer and logarithmic layer. In the following equations, velocity u denotes either mean value (RANS framework) or filtered value (LES framework). Based on the standard normalized wall quantities

$$u_+ = \frac{u}{u_\tau} \quad , \quad y^+ = \frac{\rho y u_\tau}{\mu} \tag{2.15}$$

where y is the distance to the wall, friction velocity u_τ is defined in terms of shear stress tensor τ_w at the wall,

$$u_\tau = \sqrt{\frac{\tau_w}{\rho}} \tag{2.16}$$

The Reichardt wall law is written as follows and illustrated in Fig. 2.4. Further details can be found in Hinze [1959], Reichardt [1951].

$$u_+ = \frac{1}{\kappa} \ln\left(1 + \kappa.y^+\right) + 7.8 \left[1 - \exp\left(-\frac{y^+}{11}\right) - \frac{y^+}{11} \exp\left(-0.33 y^+\right)\right] \tag{2.17}$$

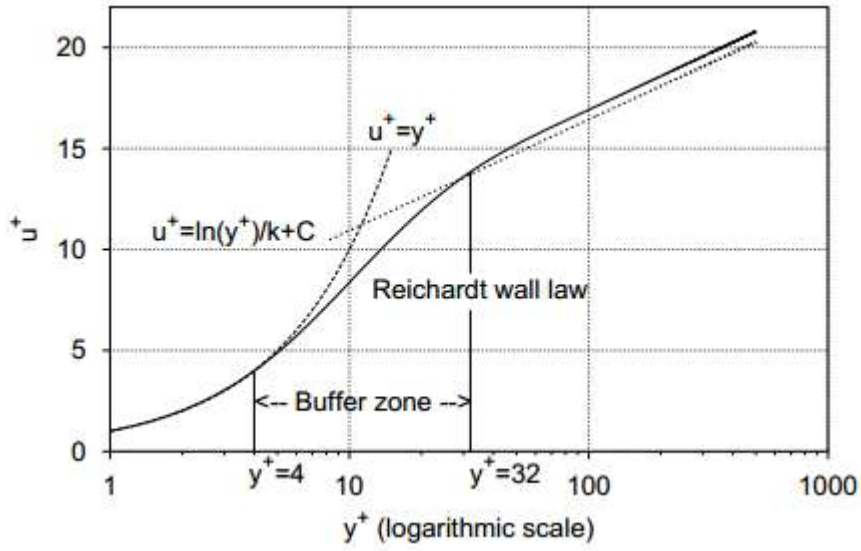

Figure 2.4: Comparison of Reichardt wall-law predictions with the laminar sub-layer and outer layer approximated flows (from Abalakin and Koobus [2000])

2.2.3 Available hydraulic benchmark data

Chung et al. [2002] performed DNS of turbulent flow in a concentric annular pipe. The concentric cylinders were non-rotating with a radius ratio 0.5. The Reynolds number based on the bulk velocity and hydraulic diameter was 8900. The simulation was performed on 1.6 million grid points (65, 128, 192 points in the radial, azimuthal and axial direction respectively). They validated their results with Laser Doppler Velocimetry measurements by Nouri et al. [1993] in a concentric annulus. All three components of mean velocity were measured in a fully developed concentric flow for a Newtonian fluid at bulk flow Reynolds numbers 8900 and 26600. The radius ratio of the annulus was 0.5. 5 mW He-Ne laser was used to measure velocity at four different quadrants. Also static pressure was measured with manometer at holes distributed longitudinally and circumferentially around outer diameter. 3000 samples were collected for each measurement.

DNS and LES data on concentric annular pipes of radius ratio 0.5 have also been reported by Nouri and Whitelaw [1994], Azouz and Shirazi [1998], Kaneda et al. [2003], Liu and Lu [2004], Chung and Sung [2005], Ould-Rouiss et al. [2009], Hadžiabdić et al. [2013].

2.3 The TrioCFD code

TrioCFD (previously Trio_U) is a CFD code developed at CEA, France [TrioCFD (previously Trio_U) webpage] for unsteady, incompressible and compressible monophasic and diphasic flows. It has been employed to perform analyses of turbulent flow and heat transfer in nuclear facilities. Since late 2015, it has changed from an in-house code 'Trio_U' to an open source code 'TrioCFD'. Angeli et al. [2015] recently presented a general overview of the code. It is designed for CFD calculations on structured (parallelepipeds) and non-structured (tetrahedrons) meshes of several millions of control volumes. The code runs on Linux machines. It is based on an object oriented, intrinsically parallel approach and is coded in C++ [Calvin et al., 2002]. The code structure is flexible: it allows the user to choose a suitable discretization method. Several convection schemes, time schemes and turbulence models are available. Châtelain et al. [2004] discussed the use of several numerical convection schemes in TrioCFD for heat transfer calculations using LES. Details of discretization methods can be found in Ducros et al. [2010], Bieder et al. [2007]. TrioCFD uses a hybrid finite volume based finite element (VEF) approach [Bieder et al., 2000a,b, Ducros et al., 2010]. This method involves determining a discrete solution, for a continuous problem, in the space of the finite element by maintaining the equilibrium between flux entering and leaving the finite volume [Bieder and Graffard, 2008]. The space discretization is performed with triangles in 2D and tetrahedrons in 3D. Velocity and temperature are located in the face center of the tetrahedral elements leading to a P1 non-conforming discretization (P1NC). The pressure is discretized at both the center (P0) and the vertices (P1) of an element. Friction velocity is calculated at the face center of an element. y^+ is calculated at the body center of an element. If the position of a pre-defined probe is not the same as the calculation position, TrioCFD makes an interpolation. To avoid obtaining such interpolated values, the code has an option to move the probe to any calculation position depending on the field under study. TrioCFD uses a domain decomposition method for parallelization: the initial domain is decomposed into smaller overlapping sub-domains which are distributed among the available processors. The 'programming model' is single program multiple data (SPMD). All the processors execute the same code by using different data. The processors communicate explicitly using MPI (message passing interface) libraries. For better performance, it is recommended to have 20000 - 30000 elements per processor [Vandroux and Barthel, 2013]. A full list of all keywords in provided in the TrioCFD User's Manual [2015].

OECD/NEA reports by Mahaffy et al. [2007], Smith et al. [2014] have mentioned the use of TrioCFD for nuclear reactor safety studies. Bieder et al. [2014a, 2015] used TrioCFD to perform LES on 4600 processors in parallel to simulate a 5×5 rod bundle. Bieder and Graffard [2008] presented the use of TrioCFD for full scale reactor applications. TrioCFD has also been used to study accident scenarios in nuclear reactors, namely, coolant mixing in the lower plenum of a VVER-1000 reactor due to a steam line break [Bieder et al., 2007], coolant mixing in a PWR due to a steam line break [Höhne et al., 2006], natural gas circulation in the primary coolant circuit during a high pressure severe accident scenario [Bieder et al., 2003], blocking of a few coolant channels in a helium cooled High Temperature Reactor (HTR) core [Cioni et al., 2006]. TrioCFD has been successfully run on massively parallel computers up to 10000 processors. Bieder et al. [2014b] performed LES for transverse flow along two typical PWR spacer grids on 10000 processors. More recently, Bieder [2015] studied non-axial flow in PWR fuel assemblies using LES on 10000 processors. TrioCFD has also been used to study heat transfer in sodium cooled fast reactors (SFR). Saxena [2014] performed LES to study heat transfer in sodium flow in a wire wrapped sub-assembly in a SFR. Also, Saxena et al. [2013] repeated the same for 'bare' rod bundles (i.e, without any spacer wire). Angeli [2015] used TrioCFD to study thermal striping behavior in SFR. Chandesris et al. [2013] used TrioCFD to perform DNS of turbulent flow in a porous medium. TrioCFD has also been coupled to system codes to study transient behavior at a global system scale by Chenaud et al. [2015] (in SFR) and Bavière et al. [2014] (in GFR).

2.4 Methods of statistical analysis

2.4.1 Time-series analysis

A signal x_i, e.g, pressure, velocity etc., is measured at i data points where $i = 1, 2, 3..., N$ at equidistant time intervals Δt. The sampling frequency is $f_s = 1/\Delta t$. The length of the signal is N. The standard deviation σ (or RMS fluctuation or simply RMS) and the mean $\overline{x}$ are respectively defined by

$$\sigma = \sqrt{\frac{1}{N-1}\sum_{i=1}^{N}(x_i - \overline{x})^2} \tag{2.18}$$

$$\overline{x} = \frac{1}{N}\sum_{i=1}^{N} x_i \tag{2.19}$$

2.4.2 Frequency domain analysis

Let $(x, 0, z)$ be the spatial separation vector and t be the temporal separation. Then the space-time correlation of the fluctuating field $p(X, Z, T)$ at (X, Z) at time T is given by

$$R(x, z, t) = E[p(X, Z, T).p(X + x, Z + z, T + t)] \tag{2.20}$$

The correlation of the field p between two spatial points (X, Z) and $(X + x, Z + z)$ is given by

$$R(x, z) = E[p(X, Z).p(X + x, Z + z)] \tag{2.21}$$

The goal of spectral analysis is to describe the frequency distribution of power contained in a signal. Power spectral density represents the frequency domain characteristic of a time series. The wavenumber-frequency spectral density of the field fluctuations, e.g., wall pressure, $P(k_x, k_z, \omega)$ and the space-time correlation $R(x, z, t)$ are related by the Fourier transform pair

$$P(k_x, k_z, \omega) = \frac{1}{(2\pi)^3} \int_{-\infty}^{-\infty} \int_{-\infty}^{-\infty} \int_{-\infty}^{-\infty} R(x, z, t) e^{[-i(k_x x + k_z z + \omega t)]} dx dz dt \tag{2.22}$$

$$R(x, z, t) = \int_{-\infty}^{-\infty} \int_{-\infty}^{-\infty} \int_{-\infty}^{-\infty} P(k_x, k_z, \omega) e^{[i(k_x x + k_z z + \omega t)]} dk_x dk_z d\omega \tag{2.23}$$

where $(k_x, 0, k_z)$ is the 2D wave-vector and ω is radian frequency. The single point spectrum $\phi(\omega)$ in the frequency domain is related to the space-time correlation function and wavenumber-frequency spectrum by

$$\phi(\omega) = \int_{-\infty}^{-\infty} \int_{-\infty}^{-\infty} P(k_x, k_z, \omega) dk_x dk_z \tag{2.24}$$

The cross-spectrum $\Gamma(x, z, \omega)$ in the space frequency domain is given by

$$\Gamma(x, z, \omega) = \frac{1}{2\pi} \int_{-\infty}^{-\infty} R(x, z, t) e^{[-i\omega t]} dt = \int_{-\infty}^{-\infty} \int_{-\infty}^{-\infty} P(k_x, k_z, \omega) dk_x dk_z \tag{2.25}$$

and the mean square pressure fluctuation $\overline{P^2}$ is given by

$$\overline{P^2} = R(0, 0, 0) = \int_{-\infty}^{-\infty} \phi(\omega) d\omega = \int_{-\infty}^{-\infty} \int_{-\infty}^{-\infty} \int_{-\infty}^{-\infty} P(k_x, k_z, \omega) dk_x dk_z d\omega \tag{2.26}$$

For a discrete signal $P_k(j)$ divided into K segments (either overlapping or not) of length L, the discrete Fourier transform (DFT) is given by

$$F(f_n) = \sum_{j=0}^{L-1} P_k(j) e^{(-2\pi i j k f_n)} \tag{2.27}$$

where

$$\text{Sampling frequency} = \frac{1}{L},$$

$$f_n = \frac{n}{L}, 0 \leq n \leq \frac{L}{2}.$$

While computing power spectral density (PSD), the signal is generally multiplied by a window function $W(j)$, e.g. Hanning window, before applying Fourier transform. This is done to provide a better spectral representation of the signal. For a window length *(N+1)*, Hanning window is defined by

$$W(j) = \frac{1}{2}\left(1 - \cos\left(2\pi \frac{j}{N}\right)\right), 0 \leq j \leq N$$

2.5 Wall pressure fluctuations

Turbulent velocity fluctuations in the boundary layer adjacent to a wall give rise to both shear and normal stresses (pressure) at the wall. The pressure and shear stress at the wall are related to the boundary layer flow: the wall shear stress τ_w is locally determined by the velocity gradient adjacent to the wall whereas the wall pressure is the result of an integrated effect of velocity fluctuations over the wall [Blake, 1986]. Wall pressure fluctuations arise from large-scale disturbances originating in the outer region of the boundary layer and small-scale disturbances in the inner region [Bradshaw, 1967]. Wall pressure fluctuations are important to study the flow-induced vibrations of structures. Blake [1986] provides an exhaustive treatment on this subject. Bull [1996] summarizes the research in this field from the 1950s to 1990s.

To describe the wall pressure field, one can study elementary properties like the frequency spectrum and mean square pressure as well as statistical functions like a correlation function in the space-time domain or a spectral function in the wavenumber-frequency domain. To analyze the vibrational response of a structure to turbulent excitation, a statistical space-time or wavenumber-frequency description of the wall pressure field is required as input [Bull, 1996]. Though, theoretically, the space-

time correlation function and the wavenumber-frequency spectrum represent the same information in different forms, the wavenumber-frequency spectrum has been used more often because it helps us appreciate the relevant wavelengths and frequencies in a problem.

For incompressible flow, the equation for pressure fluctuations is derived by taking the divergence of the Navier-Stokes momentum equation, using the continuity equation to drop terms, performing a Reynolds decomposition into mean and unsteady terms, and then subtracting the time-averaged equation, to obtain

$$\nabla^2 p = -2\rho \frac{\partial U_i}{\partial x_j} \frac{\partial u_j}{\partial x_i} - \rho \frac{\partial^2}{\partial x_i \partial x_j} \left(u_i u_j - \overline{u_i u_j} \right) \tag{2.28}$$

This is the Poisson equation for fluctuating pressure, p, in turbulent flow. Of the source terms on the right-hand side, the first term and the second terms respectively represent

$$\text{mean shear-turbulence interaction, } T_M(x, y, t) = 2\rho \frac{\partial U_i}{\partial x_j} \frac{\partial u_j}{\partial x_i}$$

$$\text{and turbulence-turbulence interaction, } T_T(x, y, t) = \rho \frac{\partial^2}{\partial x_i \partial x_j} \left(u_i u_j - \overline{u_i u_j} \right)$$

2.5.1 Characterization of wall forces

Due to turbulent flow of coolant, the fuel rods experience flow induced vibrations (FIV). When rods vibrate, friction between grid and rod lead to shear stresses at the contact locations. The arrangement of the fuel rod and the spacer grid can be equivalently described by a mounted beam clamped at 8 locations at regular intervals (Fig. 2.5).

FIV causes shear stress in both perpendicular and axial directions (with respect to fuel rod). Fuel rods are held by spring-dimple configuration. In the perpendicular direction (Fig. 2.6), the rod can have translatory motion (by impacting the grid structure), rotatory or whirling motion. Translatory motion leads to pressure force while rotatory and whirling motion leads to viscous force on the wall. It should be noted that the viscous force is relatively smaller (approximately 10%) compared to pressure force. In the axial direction (Fig. 2.7), the fuel rods can buckle under the coolant flow. Friction can occur at the contact locations due to the up and down movement of the rods and also the tilting of the rods. The net shear force is the addition of the axial and perpendicular components.

Figure 2.5: Mounted beam clamped at 8 locations (taken from Rubiolo [2006])

Figure 2.6: Shear forces in perpendicular direction (taken from Kim [1999])

Figure 2.7: Shear forces in axial direction (taken from Kim [1999])

2.5.2 Available experimental and numerical data for rod bundles

The net fluid force on the wall is given by the space integration of pressure and viscous (shear) stress respectively:

$$F_i(t) = -\int p(t) n_i dA + 2\int \mu S_{ij}(t) n_j dA \tag{2.29}$$

where F, p, n, A and $S_{ij} = (v_{i,j} + v_{j,i})/2$ denote the total force, pressure, outward surface normal, surface area and the strain rate of instantaneous velocity v respectively. The first term on right-hand side denotes pressure force and the second term denotes viscous force. This force time history is used to compute power spectral distributions and fed into structural dynamics codes to compute wear. The lateral components x and y are responsible for the pressure force while the z-component is responsible for the viscous force.

The flow pattern in rod bundles of PWR with spacer grids (fitted with mixing vanes) has been analyzed with CFD codes by numerous authors. Elmahdi et al. [2011] performed LES on 3×3 rod bundle geometry using STAR-CCM+ for $Re_D = 250000$ (which is half of reactor scale Reynolds number). y^+ value for the first grid point was 40 - 60. Using a synthetic turbulence method did not make any appreciable difference to the flow pattern downstream, hence they used uniform inlet velocity. The mesh was made up of uniform cubic hexagonal cells with refinement close to the walls. The CFD results were compared with PIV experimental data (conducted at half of the Reynolds number). However it has been shown by Conner et al. [2010] that flow structures in such a configuration are independent of temperature and Reynolds number. The domain length downstream was 304.8 mm. The entire rod surface was divided into equal segments. Looking at the integrated lateral forces on these segments along the surface, it was observed that the mixing vanes were the main source behind the excitation forces on the rod which decay as one goes further downstream. A comparative study between the excitation force generated by a spacer grid and mixing vanes and that by a spacer grid showed that the former generates much higher turbulence forces. In addition, spectral analysis showed that the spectral components of the excitation forces were below 200 Hz. These transient forces on the rod were later used as input to the VITRAN code (Vibration Transient Analysis Non-linear), which was developed by Westinghouse, to simulate non-linear vibration of fuel rod and dynamic interaction between the fuel rods and supports. It includes a fretting wear analysis method to predict wear (details in Rubiolo and Young [2008]). The reported preliminary calculations for the amplitude of vibration and rod acceleration showed good comparison with experimental data.

To understand the fluid dynamics of GTRF, Bakosi et al. [2013] performed LES on 3×3 and 5×5 rod bundles with a single spacer for $Re_D = 400000$. The 3×3 geometry was the same as in Elmahdi et al. [2011]. This work was based on previous studies by Christon et al. [2011] and Nourgaliev et al. [2013]. Christon et al. [2011] performed calculations using LES, detached-eddy (DES) and Spalart-Allmaras (URANS) models and concluded that out of the three, LES provides the most accurate realization of GTRF forces. Simulations were performed using the thermal-hydraulics code Hydra-TH [Nourgaliev et al., 2013] developed at Los Alamos National Laboratory, USA for the Consortium for Advanced Simulation of Light water reactors (CASL). Five different meshes of increasing resolution were used. The hybrid meshes generated by Cubit (hex-tet around the spacer and hex in the remaining region) in Christon et al. [2011] led to some spurious results due to the abrupt variation in mesh size during transition from hex-tet to hex. So the meshes in Bakosi et al. [2013] were generated by Numeca's Hexpress/Hybrid mesh generator 'Spider' which ensured smooth transition from more refined areas to the less refined areas. The y^+ values ranged from 20 to 60, except in some localized regions of the spacer where it was ≈ 1, thereby resulting in a poor LES mesh. Lateral forces on the central fuel rod and spacer were calculated. Shear forces on the rod and spacer were negligible compared to the pressure force, whereas the streamwise pressure force on the rod was zero. Also the streamwise pressure force on the spacer was an order of magnitude higher than the lateral pressure force on the rod, which illustrates that the spacer induces all the pressure drop. The RMS pressure force decreased downstream of the vanes indicating a decrease in turbulent intensity. Comparison of the RMS total force showed good agreement with the STAR-CCM+ results of Elmahdi et al. [2011]. Similarly, simulations on the 5×5 rod bundle were carried out and compared with the PIV measurements by Conner et al. [2013] at Texas A&M University. The hydraulic test loop at Texas A&M has vertical test section with flow moving from bottom to top. It has a 5×5 rod bundle with dimensions identical to a 17×17 PWR fuel assembly with multiple spacer grids. Detailed PIV data from this facility have been reported by Dominguez-Ontiveros et al. [2010] for $Re_D = 2000$ to 16300 and later by Conner et al. [2013] for $Re_D = 28000$.

Recently, OECD/NEA started an international CFD benchmark exercise associated to the MATiS-H experiment. As a part of it, [Smith et al., 2013], Frank et al. [2012] performed CFD simulations and validated it with experimental data from the KAERI MATiS-H 5×5 rod bundle facility. For all the MATiS-H experiments, $Re_D = 50250$. For CFD investigation, the full 5×5 rod bundle was reduced to a single sub-channel and then periodic boundary conditions were applied. Simulations

were performed for both split-type and swirl-type spacer grid. They implemented a hybrid meshing strategy: unstructured tetrahedral meshes around the grid and structured hexahedral meshes upstream and downstream.

Bieder [2012] meshed the MATiS-H test facility and performed LES and RANS to analyze the flow upstream and downstream of split-type vanes using TrioCFD. LES was used to treat anisotropic turbulence in a rod bundle with mixing vanes. The first calculation point being at y+≈30, Reichardt's wall law was used to model the near-wall behavior.

Bieder [2013], Bieder et al. [2014a, 2015] used the k-ϵ linear eddy viscosity turbulence model and LES approach in TrioCFD to simulate flow for $Re_D = 250000$ in the AGATE 5×5 rod bundle previously located at CEA Grenoble, France. The grid was fitted with split type mixing vanes inclined at an angle of 29°. The behavior downstream of a grid up to 50 HD in between two successive grids was observed whereas most other studies have focused up to 10-20 HD. A decrease in turbulent intensity was observed.

Caraghiaur et al. [2009] reported experimental data for pressure, velocity and turbulent intensity in a 24-rod fuel bundle fitted with spacer grids. This was also elaborated in Caraghiaur [2009]. The measurements were done in a vertical test section for single-phase water flow at $Re_D = 25000$, 32000 and 42000. Pressure measurements were obtained using a sliding pressure sensing rod where a single rod was drilled with 5 pressure taps in a vertical straight line. The pressure-sensing rod was rotated about its axis and traversed axially to collect data on the entire rod surface (though at different instants of time). The pressure taps were connected to piezoresistive differential pressure transducers. Laser Doppler Velocimetry (LDV) technique was used to measure the axial velocity and turbulence intensity across one of the spacer grids. Pressure drop across the spacer was compared to empirical models. They observed that the velocity fluctuations and turbulent intensity decrease downstream of vanes.

Delafontaine and Ricciardi [2012] performed LES at $Re_D = 75000$ with STAR-CCM+ to calculate the fluctuating fluid forces acting on one grid cell (one central rod surrounded by 4 sub-channels) for an axial length of 30 HD downstream of the grid. They showed that the contribution of viscous force is negligible compared to the pressure force. They observed that the RMS amplitude of pressure force decreases downstream of the grid implying a decrease in turbulent intensity. This conforms to previous observations by Yang and Chung [1998], Ikeno and Kajishima [2006], Caraghiaur et al. [2009], Conner et al. [2010]. Upon comparing their result with the PSD force spectrum for a tube bundle under

axial flow without mixing grids proposed by Axisa [2001], it was observed that the grid introduces additional turbulent excitation causing the greater spectral amplitude. Benhamadouche and Laurence [2003] performed LES on a 3×3 rod bundle for coarse and fine meshes using Code_Saturne.

Conner et al. [2010] used steady-state $k-\epsilon$ simulations to observe swirl structures downstream of mixing vanes in a square 5×5 rod bundle. Chang et al. [2008] experimentally observed similar swirl structures on a 5×5 square rod bundle at the MATiS-H facility horizontal test loop at Korea Atomic Energy Research Institute (KAERI) using Laser Doppler Anemometry (LDA) at $Re_D = 48000$ (axial bulk velocity 1.48 m/s). The bundle was 2.6 times larger than a real bundle size to have a closer look at the lateral flow structure at 5 different altitude locations. Two types of vane configurations were studied: split type and swirl type. The vanes were at an angle of 30° to the axial flow direction. Split type vanes, typically used in PWRs, resulted in a couple of symmetric small vortices in a sub-channel and showed a significant cross-flow between sub-channels. On the other hand, swirl type vanes, resulted in a single large vortex in a sub-channel and the cross-flow between sub-channels was relatively weak. A decrease in turbulent intensity downstream of the vanes was reported in all cases.

Ikeno and Kajishima [2006] used LES to simulate the decay of swirl structures in a 2×3 rod bundle for $Re_D = 4100$. Comparison of the LES result with the experimental results in a rod-bundle [McClusky et al., 2002] and in a pipe [Kreith and Sonju, 1965] illustrated that the decay of the swirl in a rod-bundle is faster than that in a pipe. They observed a decrease in turbulent intensity downstream of the grid.

Yang and Chung [1998] performed experiments on a 5×5 rod bundle fitted with spacer grid and mixing vanes at an angle of 22°. Using LDV, detailed hydraulic characterization (velocity and turbulent intensity measurements etc.) were done at $Re_D = 62500$. It was generally observed that turbulence intensity decays downstream of the grid. The flow immediately downstream was intensively fluctuating with a higher turbulence energy and more isotropic than just before the grid.

Lee and Choi [2007] simulated the effect of different types of mixing vanes on the thermal hydraulic performance for a 17×17 full scale square rod bundle (hexagonal being the other typical arrangement). The whole domain comprised of 13 million mesh points and it was solved using Reynolds Stress turbulence model (RSM-RANS) with the code FLUENT. The first grid point was at a y^+ of about 200. The mixing vanes were inclined at an angle 30°. Conventional mixing vanes are split-type and creates small scale vortices confined in a sub-channel; hence these are called small scale vortex flow mixing vane (SSVF). This creates a lesser amount of cross-flow and the turbulence decays rapidly

due to the small length scale. Bend-type mixing vanes create large vortices and are called large scale vortex flow mixing vane (LSVF). For this type, the cross-sectional turbulence intensities were higher than that of SSVF leading to turbulence sustenance for a longer distance. Further studies on SSVF and LSVF mixing vanes have been reported by An and Choi [2006a,b].

Dynamic particle tracking velocimetry (DPTV) results was reported by Dominguez-Ontiveros and Hassan [2014] for $Re_D = 23000$ on a 3×3 square rod array fitted with equidistant spacer grids (without any vanes).

LDV and PIV have been the conventional techniques for measuring the flow field inside rod bundles [McClusky et al., 2002, Yang and Chung, 1998]. However, due to the small gap of 3 mm in typical PWR fuel bundles and the presence of a number of rods, LDV and PIV techniques are restricted by the existence of invisible region in fuel rod bundles. Ikeda and Hoshi [2006] developed rod-embedded fiber LDV technique in which optical fibers were inserted inside a fuel cladding so that the flow field wasn't disturbed. A window on the cladding surface, through which laser beams could pass, ensured that there was no invisible region in the sub-channel. This rod could be inserted in an arbitrary grid location and adjusted to measure velocity at any rod position.

2.5.3 CALIFS single-rod experiment at CEA Cadarache

'CALIFS' single-rod experiment at the Laboratory of Hydromechanics of Cores and Circuits (LHC), CEA Cadarache was an attempt to characterize the excitation forces exerted by the coolant (water) on the fuel rod. The test section is shown in Fig. 2.8. This single rod test section was in fact a preliminary test for the 5×5 rod configuration which intends to develop instrumentation techniques and experimental tests to characterize hydraulics in the framework of GTRF. The excitation forces are derived mainly from the stresses associated with pressure forces; the stresses associated with viscous forces being relatively weak. Hence we characterized these forces from pressure fluctuation measurements at different points on the wall of the fuel rods upstream and downstream of the mixing grid. The magnitude of pressure fluctuations was expected to be low, around few hundred Pa in terms of RMS fluctuation.

In order to measure the fluctuating pressure on the wall of the rods in water, a system was designed by *LHC* and *Arts et Metiers ParisTech* in 2011-12. It was integrated with the rod and consisted of a dynamic pressure sensor, a measuring cavity, a pressure tap on the wall and a air purging system. It could measure pressure of the order of few Pa to around 1200 Pa. In the frequency domain, the power

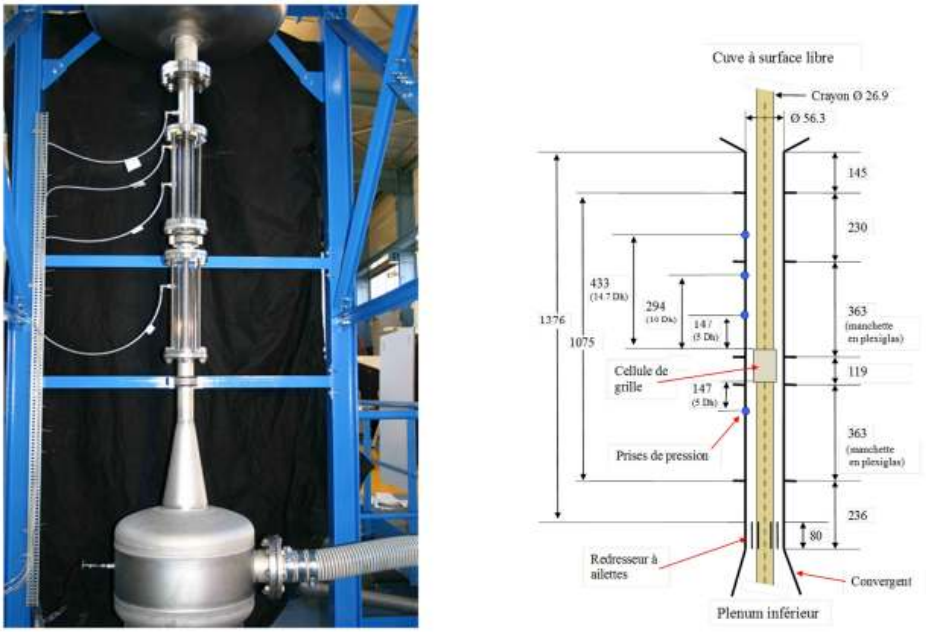

Figure 2.8: CALIFS single-rod test section (taken from Moreno [2012])

of the signal was between a few Hz to 200 Hz. These measurements were realized by translation and rotation of the rod to align it with the pressure sensor. The most important obstruction to the flow was caused by the pressure sensor. Stainless steel tubes of diameter 26.9 mm were used to represent the fuel rods. The real diameter of fuel rods in PWRs is 9.5 mm. Hence the geometric scale for this test section was 2.83. Such a scale allowed instrumentation to be inserted inside it. Midway through the canal, a spacer grid was placed along with mixing vanes. Table 2.1 lists the hydraulic features of the test section. The bulk velocities were chosen so that the flow characteristics were representative of in-core turbulent flow regime.

Length of hydraulic canal	1376 mm = 47 HD
Internal diameter of test section	56.3 mm
External diameter of the rod	26.9 mm
Hydraulic diameter of the canal	29.4 mm
Geometric scale	2.83
Water flow velocity	2-5 m/s
Reynolds number	50000-300000
Temperature	20-60°C
Pressure	<1 bar

Table 2.1: Hydraulic features of the CALIFS test section

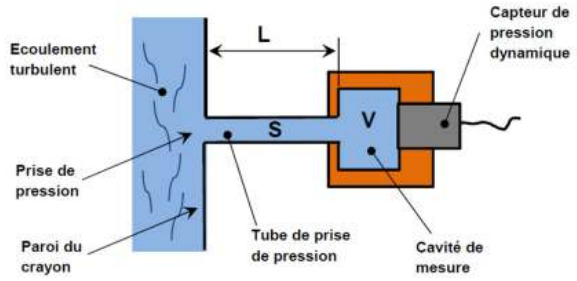

Figure 2.9: Schematic of pressure sensor module

Figure 2.10: Photo of pressure sensor module

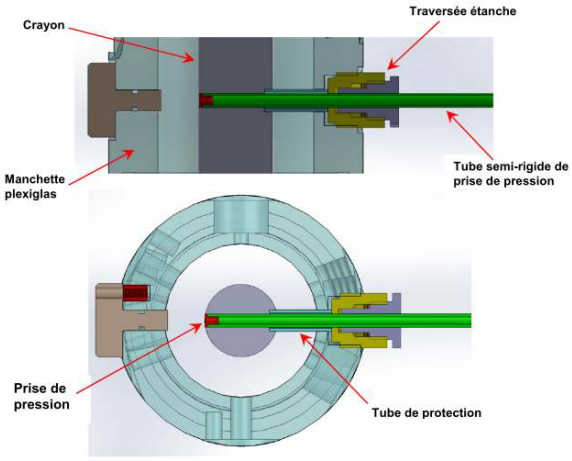

Figure 2.11: Top and oblique view of pressure sensor

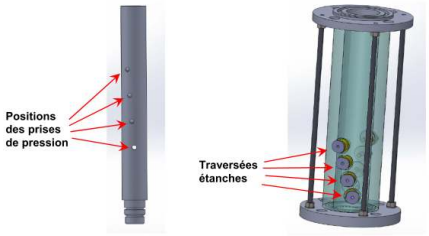

Figure 2.12: Position of pressure taps on the rod surface

In addition to the local pressure fluctuation measurements, it is interesting to determine the space-time correlations of pressure fluctuations. For that, it is necessary to make simultaneous measurements at multiple probe locations on the walls. It is extremely difficult to implant the previous device on the same rod at multiple points due to obstruction created to the flow. Therefore, a new device was designed at *LHC* to be placed outside the hydraulic canal (Figs. 2.9, 2.10 and 2.11). Each of these external modules comprised of a pressure sensor and a cavity. The modules were placed outside the hydraulic canal and linked to the pressure taps, which were fixed to the wall of the rod by means of semi-rigid polyamide tubes. The modules were filled with deaerated water. The pressure fluctuations (present in the flow at the pressure tap level) propagated along the tube to the cavity where they were measured by the sensor. The fluid was at rest in the cavity and tube. In the pressure sensor module, the semi-rigid tube radially traversed the plexiglas cover of the test section through a waterproof passage. A 2 mm pressure tap was attached to the wall at the extreme end of the semi-rigid tube. In addition, the semi-rigid tube was supported by another stainless steel tube to prevent the pressure

tap from vibrating under the turbulent flow and thereby perturbing the measurement. The frequency range of interest was between few Hz to 200 Hz. The natural frequency of the piezoelectric pressure sensor was 70 kHz. It was further connected to a charge amplifier. A piezoelectric sensor uses the piezoelectric effect, to measure changes in pressure, acceleration, strain or force by converting them to an electrical charge.

Pressure fluctuation measurements were done at different azimuths and altitudes. Four locations were selected for the pressure taps on the wall of the rod (Fig. 2.12). These were regularly separated by 1 hydraulic diameter in altitude and by 10° in azimuthal direction in order to capture the swirling flow in the wake of the mixing vanes. The taps were placed at the azimuthal locations with maximum pressure fluctuations to determine the space-time correlations. Simultaneous measurements were done at two locations and the pressure fluctuations were quantified in terms of standard deviation. The results were comparable with those obtained with the old sensor attached directly to the rod wall. Fig. 2.13 illustrates the RMS pressure fluctuations for velocity 4 m/s. At altitudes of 1, 2, 3 and 5 times HD, the peak magnitudes of fluctuation are 850 Pa, 500 Pa, 350 Pa and 200 Pa respectively. It shows that the intensity of fluctuations decrease rapidly as one moves away from the grid. Further details of the results are available in Moreno [2012] and Moreno [2014]. Chapter 5 presents comparisons of simulation data with these experimental results.

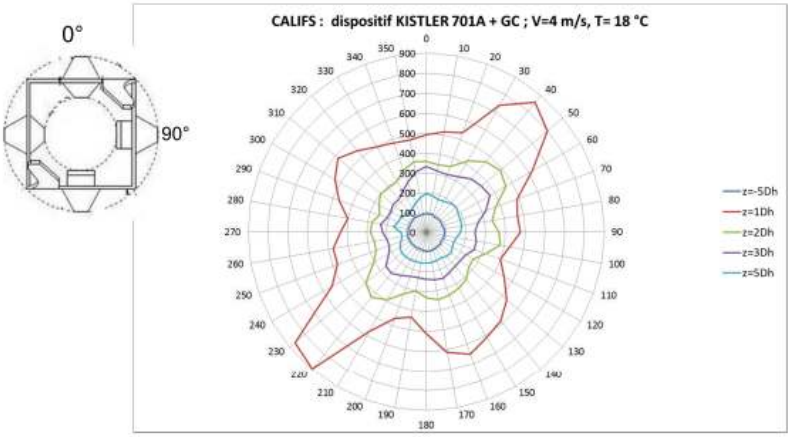

Figure 2.13: Azimuthal distribution of RMS pressure fluctuation (taken from Moreno [2012])

2.5.4 Experimental studies to measure wall pressure on cylinders

Many experiments on turbulent boundary layer (TBL) in cylindrical structures have been reported in literature. Studies on a cylinder are more representative of an annular pipe compared to a flat plate. TBL on a cylinder has many practical engineering applications like submarines, aircrafts, streamlined vehicles, sonar arrays, missiles etc. The TBL on a cylinder in axial flow is not significantly different from a flat plate if the boundary layer thickness (δ) is of the same order or smaller than the cylinder radius (a). But for $\delta/a > O(1)$, the transverse curvature of the cylinder begins to alter the flow characteristics [Bokde et al., 1999, Willmarth et al., 1976]. The flow also depends on Reynolds number which is defined as $Re_D = U_b.D/\nu$, where D is the hydraulic diameter (= diameter for a cylinder), U_b is the bulk or freestream velocity and ν is the kinematic viscosity. It should be noted that in the literature, often, the Reynolds number is expressed in terms of cylinder radius instead of diameter. Hence the reported values in the literature need to be doubled in order to be consistent with our definition. Turbulent sources in the inner region ($y+ < 30$) contribute to the high frequency band of wall pressure spectrum [Snarski and Lueptow, 1995]. Turbulent sources in the logarithmic region of the boundary layer ($y+ > 30$ *to* $y/\delta < 0.6$) contribute to the intermediate frequency range of the wall pressure. The turbulent sources in the outer region of the boundary layer ($y/\delta > 0.6$), including the interface region between the boundary layer and the potential region outside the boundary layer, contribute to the low frequency region of the wall pressure spectrum [Bokde et al., 1999, Willmarth and Woolbridge, 1963].

Willmarth and Yang [1970] and Willmarth et al. [1976] experimentally investigated the space-time characteristics of the wall pressure fluctuations for $\delta/a \approx 2$ and $\delta/a \approx 4$ respectively. They used an array of 0.15 cm mounted piezoelectric pressure transducers on a 7.6 cm diameter cylinder ($\delta/a \approx 2$) and on a 2.5 cm diameter cylinder ($\delta/a \approx 4$) in a vertical wind tunnel. Willmarth et al. [1976] further extended these measurements to boundary layers whose thickness ranged from 4 to 40 times the cylinder radius. The range of Reynolds numbers was $Re_D = 964$ to 184620. Mean air flow inside the tunnel could be varied from 0-76 m/s. The convection velocity of wall pressure fluctuations derived from the space-time wall pressure correlation was found to be nearly the same as that for a planar boundary layer increasing with streamwise separation from $0.6U_b$ to $0.8U_b$. However, since the mean velocity profile convecting the eddies is fuller because of the transverse curvature, the turbulent eddies must be smaller to result in the same convection velocity as in a plane boundary

layer. Consistent with this idea, the power spectra of the wall pressure fluctuations for a cylindrical boundary layer contain a greater energy density at higher frequencies than a planar boundary layer. The wall pressure correlation contours between a cylindrical boundary layer and a planar boundary layer suggest differences in the wavenumber spectra of wall pressure for the two cases. Wall pressure correlation contours in a cylindrical boundary layer are nearly circular in the streamwise-spanwise plane [Willmarth and Yang, 1970]. This is in contradiction to the elongation of the contours in the spanwise direction in a flat plate boundary layer. Willmarth and Yang provided the following explanation: consider a large eddy adjacent to the curved wall of a cylinder. The mean velocity at the spanwise sides of the eddy is necessarily larger in a cylindrical boundary layer than in a planar boundary layer, since the distance from the wall to the side of the eddy is more. This results in a shearing motion on the sides of the eddy and reduces its transverse scale. As noted by Blake [1986] with regard to the expression for the wavenumber spectrum of the mean-shear-turbulence interaction term, the spectrum of pressure fluctuations in the streamwise direction is enhanced relative to the spanwise direction in the planar case. This results in spatial pressure correlations that reflect smaller scales in the streamwise direction than in the spanwise direction. The larger scales in the spanwise direction are evident by the elongation of the contours in the spanwise direction [Lueptow, 1988].

Lueptow et al. [1985] experimentally measured mean velocity and Reynolds stress for a thick, turbulent boundary layer on a cylinder ($\delta/a > 1$) at the Acoustics and Vibration Laboratory wind tunnel at Massachusetts Institute of Technology, USA. All experiments were performed at free stream velocity 10-40 m/s, Re_θ = 2000-5600. Measurements were made with hot-wire anemometer probes. Whereas Willmarth et al. [1976] used different sized cylinders and measured the boundary layer at the same point physically along the cylinder to obtain values for different regimes, Lueptow et al. [1985] measured it at different points on the same cylinder. Further measurements of turbulent intensity, velocity spectra and wall shear stress for a cylindrical boundary layer with $\delta/a > 1$ on the same wind tunnel were reported by Lueptow and Haritonidis [1987] and Lueptow and Jackson [1991]. Lueptow [1988] presented a comprehensive review of the experimental work done from 1960s to 1980s. Weitrzak and Lueptow [1994] performed wall shear stress measurements in a vertical cylinder in axial air flow at Northwestern University, USA. The momentum thickness was Re_θ = 3050 and δ/a = 5.7. They reported shear stress-velocity cross-correlations.

Nepomuneco and Lueptow [1997] measured the fluctuating wall pressure, wall shear stress and streamwise velocity simultaneously in a turbulent boundary layer on the same test section and at-

tempted to understand the relationship among them. Measurements were done with a hearing aid microphone, hot wire shear stress probe and hot wire velocity probe respectively. The experiments were carried out in a wind tunnel test section with cylinder diameter = 9.53 mm. The momentum thickness Reynolds number was reported as $Re_\theta = 2160$. From the given data, the diameter Reynolds number was calculated to be $Re_D = 6430$. Cross-correlations between the three variables were studied. Spectra of the streamwise velocity and wall pressure were computed using FFT with Hanning window. It was observed that the peak for the pressure spectrum is narrower compared to that of the velocity of shear stress spectra, thereby inferring that the energy of pressure is distributed over a much smaller frequency band.

Snarski and Lueptow [1995] also reported cross-correlation spectra of the streamwise velocity and wall pressure. They measured wall pressure and streamwise velocity fluctuations on the same wind tunnel (Length of the cylinder test section = 3m, radius = 4.76 mm, Re_D=7280, Re_θ=2870, δ/a=5.04). Measuring devices were the same as in Nepomuneco and Lueptow [1997].

On the same wind tunnel test section, Bokde et al. [1999] studied the spanwise structure of wall pressure on a cylinder in axial flow for Re_D=6600, Re_θ=2530, $\delta/a = 4.81$. Measurements were made at spanwise separations of 0°, 10°, 20°, 30°, 60° and 90°. The spanwise correlation and coherence plots indicate that the wall pressure is related up to about 30°.

Cipolla and Keith [2003a] and Cipolla and Keith [2003b] performed a series of experiments and reported wall shear stress measurements using the high-speed seawater towing tank at NASA Langley Research Center, Hampton, USA. Thin cylinders of diameters 0.61, 0.89 and 2.5 mm and lengths ranging from 30 m to 150 m were used for $Re_D = 10^8 - 10^9$.

Description of the series of experiments at DIVA loop at CEA Saclay

Axisa et al. [1990] reported various experiments performed at the two-phase (DIphasique) Vibration Analysis (DIVA) loop at CEA Saclay, France in the 1970s and 80s to measure fluctuating forces on the wall. One way to measure flow induced random excitation of tube arrays is to directly measure the resultant forces on a rigid tube. The second technique is to indirectly measure the response of the flexible tubes. Taylor et al. [1986] and Taylor et al. [1988] performed experiments with water over a range of flow rate 0.007 - 0.108 m^3/s. A mixer was placed upstream of the rectangular test section (Fig. 2.14) to create a homogeneous two phase fluid. The section had a length of 300 mm and a width of 180 mm. The 30 mm diameter tubes were arranged in two configurations having pitch to diameter

Figure 2.14: (taken from Taylor et al. [1986, 1988])
Left: Schematic of DIVA loop test section,
Right: Top view of tube row within the test section

ratios 1.5 and 3. The central tube was mounted on a fixed piezoelectric force transducer. The external mounting was necessary to isolate the tube from the test section motion but it created the need for a flexible seal. Direct measurement of the fluctuating forces induced by the single-phase (water) and two phase flow were performed at various flow rates and void fractions at two different pitch to diameter ratios. Since the tests were carried out with the purpose of studying random turbulence excitation, it was necessary to suitably displace the tube natural frequency peak from the frequency range of interest (0-100 Hz). Therefore the fixed-fixed tube and support were designed such that the tube natural frequency was approximately 3 times the maximum frequency used in the tests. In water, the actual tube frequency was 280Hz.

Chen and Jendrzejczyk [1987] used the same technique of direct force measurement on a rigid tube square bundle subjected to a uniform cross flow. They observed that the results were quite similar leading to the conclusion that random excitation forces were geometry independent. Gibert et al. [1978] analyzed the random force excitation indirectly by measuring the response of the flexible tubes in a rectangular tube bundle in air cross flow. The tube response was measured with pre-calibrated strain gauges mounted on each end. Axisa et al. [1990] measured the tube response with accelerometers on a square bundle with all except the central tube clamped. It was found that direct measurement of the resultant force on a rigid tube was more convenient than measuring the response of flexible tubes. The second method leads to significant underestimation of the slope of the force spectrum in

its decreasing portion as observed by Axisa et al. [1990].

Combining all the experimental data from DIVA loop, Axisa et al. [1990] noted that turbulent force fluctuations decrease with frequency of random force acting on the rod according to a power law of the form:

$$\phi(f) \propto f^{-B}, B > 0 \tag{2.30}$$

The fluctuations are quantified in terms of power spectral density (PSD). So, Axisa et al. [1990] proposed an envelope dimensionless empirical force spectrum for a tube bundle subject to cross-flow which is plotted in Fig. 2.15 and is defined by

$$PSD_{red} = 4 \times 10^{-4} \times f_{red}^{-0.5}, 0.01 \leq f_{red} \leq 0.2 \tag{2.31}$$

$$= 3 \times 10^{-6} \times f_{red}^{-3.5}, 0.2 \leq f_{red} \leq 3. \tag{2.32}$$

where reduced frequency

$$f_{red} = \frac{fD}{V_o} \tag{2.33}$$

and reduced power

$$PSD_{red} = \frac{PSD}{\rho^2 V_o^3 D} \tag{2.34}$$

Here, f is the frequency in Hz, D is the external diameter of the rod under study in m, V_0 is average axial flow velocity in m/s, ρ is the fluid density in kg/m^3 and PSD is the power spectral density of pressure in Pa^2/Hz.

Figure 2.15: Empirical formalism of fluctuating fluid forces (taken from Axisa et al. [1990])

Axisa [2001] found that the spectra for axial flow is the same as that for cross-flow divided by 100. Being small, the vibration amplitudes do not lead to immediate failure of clad material but cause

progressive damage at the grid-rod contacts through fretting wear.

2.5.5 Empirical models for wall pressure

Let us define:

$\vec{k} = (k_x, k_z)$ wave vector in Cartesian

k_x = longitudinal wavenumber

k_z = transverse wavenumber

K = norm of $\vec{k}$

$\Gamma(x, z, \omega)$ = cross spectral density

$\phi(\omega)$ = spectral density in frequency or autocorrelation of wall pressure fluctuations, $\phi(\omega) = \Gamma(0, 0, \omega)$

$P(\vec{k}, \omega) = P(k_x, k_z, \omega)$ is the wavenumber-frequency spectrum of wall pressure fluctuating field

γ_x = coefficient of longitudinal decorrelation

γ_z = coefficient of transverse decorrelation

γ_θ = coefficient of azimuthal decorrelation

U_c = convective velocity

ω = angular frequency

- **Corcos' model**: On the basis of measurements by Corcos [1962] and Willmarth and Woolbridge [1962], Corcos [1963] proposed an empirical model for the wall pressure field in a flat plate turbulent boundary layer. He supposed that the longitudinal and transverse coherence functions of wall pressure can be represented by an exponential law. The loss of coherence are described by the exponential decay of similarity variables $(\omega x/U_c)$ and $(\omega z/U_c)$. The wavenumber-frequency spectrum of the wall pressure fluctuation field is given by

$$P(k_x, k_z, \omega) = \frac{\gamma_\theta \gamma_x \omega^2 \phi(\omega)}{\pi^2 U_c^2 \left[\left(\frac{\gamma_x \omega}{U_c}\right)^2 + \left(k_x - \frac{\omega}{U_c}\right)^2\right] \left[\left(\frac{\gamma_\theta \omega}{U_c}\right)^2 + k_z^2\right]} \tag{2.35}$$

  It can predict the convective properties of the pressure field but fails in the small wavenumber range.

- **Chase's model**: The model by Chase [1980] is applicable for a large interval of wavenumbers from small wavenumbers up to the convective zone by using a specific representation of the behavior of each source of pressure fluctuation. The model takes into account the two main con-

tributions in the generation of pressure fluctuations in equation 2.28: the mean shear-turbulence interaction T_M and the turbulence-turbulence interaction T_T. The first model by Chase [1980] was later extended to a more general formulation by Chase [1987]. The wall pressure spectrum is written as a function of terms related to mean shear-turbulence interaction $T_M(x, y, t)$ and turbulence-turbulence interaction $T_T(x, y, t)$ which forms the source terms of Poisson equation. The final spectrum in wavenumber-frequency is given by

$$P(k_x, k_z, \omega) = P_M(k_x, k_z, \omega) + P_T(k_x, k_z, \omega) \tag{2.36}$$

where

$$P_M(k_x, k_z, \omega) = \frac{\rho^2.u_\tau^3.C_M.k_x^2}{\left[\frac{(\omega - U_c.k_x)^2}{(h.u_\tau)^2} + K^2 + \frac{1}{(b.\delta)^2}\right]^{5/2}} \tag{2.37}$$

$$P_T(k_x, k_z, \omega) = \frac{\rho^2.u_\tau^3.C_T.K^2}{\left[K^2 + \frac{1}{(b\delta)^2}\right]^{\mu} \left[\frac{(\omega - U_c.k_x)^2}{(h.u_\tau)^2} + K^2 + \frac{1}{(b.\delta)^2}\right]^{(5/2)-\mu}} \tag{2.38}$$

where $\mu = 0$ gives the 1980 model and $0 < \mu \leq 1$ gives the 1987 model. C_M, C_T, b, δ are empirical constants.

2.5.6 Numerical simulations to study wall pressure

To the best of our knowledge, the earliest numerical studies on turbulent axial flow in a cylindrical configuration were by Neves et al. [1994] and Neves and Moin [1994]. These have been further dealt with by Neves et al. [1992] in detail. Neves and Moin [1994] present the detailed pressure fluctuation analysis from the numerical study of Neves et al. [1994]. Two DNS were performed at $Re_D = 622$ and 1348 for $\delta/a \approx 5$ and 11. Instead of having a spatially developing boundary layer with zero pressure gradient, Neves et al. considered a model problem: axial flow betwwen two concentric cylinders, periodic in streamwise direction, naturally periodic in azimuthal direction, with a fixed boundary layer thickness, and driven by a streamwise pressure gradient to supress the spatial growth of the boundary layer. One should note that for a laminar flow, a non-zero pressure gradient can be introduced to supress the boundary layer growth, or in other words, to fix the boundary layer thickness. However, the streamwise velocity and pressure gradient cannot be constant, but must develop either spatially downstream or in time. The gap between the cylinders correspond roughly to the thickness of the boundary layer. They compared their results to the plane channel flow DNS of Kim et al. [1987] at

a similar Reynolds number which had been subsequently characterized for wall pressure spectra by Choi and Moin [1990]. They calculated the one-dimensional wall pressure spectra as a function of the azimuthal (spanwise) and axial (streamwise) wavenumbers. It was observed that the spanwise spectra is not affected by the transverse curvature in the high wavenumber range. They also studied the temporal spectra by scaling the spectrum by $u_\tau/(\delta\tau_w^2)$.

Tutty [2008] performed numerical simulations for turbulent axial flow along a long thin cylinder. A periodic problem was solved in the streamwise direction using DNS approach for low Reynolds number (< 10000) and LES approach for higher Reynolds number (up to 100000). Circumferentially averaged wall pressure spectra were presented in physical terms (Pa^2/Hz versus Hz) for $Re_D = 500$ to 10000 with $U_b = 1$ m/s and fluid kinematic viscosity $\nu = 1.18 \times 10^{-6} m^2 s^{-1}$ which is typical of sea water. The spectra for $Re_D = 10000$ were obtained with grid sizes of 19.6 and 10.3 in the streamwise and azimuthal direction respectively in wall units. Again, pressure spectra were often scaled to non-dimensional form using either inner (friction velocity and time) or outer (free-stream or convection velocity and a measure of the boundary layer thickness) variables (refer to Farabee and Casarella [1991] and Bull [1996] for further details). The wall pressure spectra were scaled using inner variables based on friction velocity (u_τ) and time (ν/u_τ^2). This involved multiplying the non-dimensional angular frequency and spectrum by τ_w^{-1} and Re_D^2/τ_w respectively. Equivalently, the frequency in Hz and the spectra in Pa^2/Hz were multiplied by $2\pi\nu/u_\tau^2$ and $u_\tau^2/2\pi\nu\tau_w^2$ respectively. In this way, the circumferentially averaged pressure spectra are scaled by inner variables.

2.5.7 Fretting wear

Fretting is a phenomenon occurring between two surfaces having oscillatory relative motion of small amplitude. A relevant example is the slipping of fuel rods against the spring and dimple in a spacer grid. As a result, there is a loss of metal at the contact location. This is called fretting wear. It is not possible to do away with spacer grids [King et al., 2002]. Hence there exists a need to predict this fretting wear at grid-rod contact to minimize wear risk by modifying the core loading pattern. In reactor situations, fretting wear can occur in steam generators or in the reactor cores at spacer grid-fuel rod contact. Analyzing fretting wear is challenging because during reactor operation, quite a number of properties vary at beginning-of-life (BoL), middle-of-life (MoL) and end-of-life (EoL) [Pettigrew, 1993]. The factors undergoing change may be listed as:

- Mechanical properties of the fuel assembly like assembly bowing, pellet-cladding creep etc.
- Neutron irradiation on the fuel rod and spacer grid
- Variation in turbulent forces due to variation in flow pattern. The flow pattern may vary due to coupling of fuel assemblies, due to cross flow and also due to small jets or swirls created by the mixing vanes.
- Swelling of pellets due to thermal expansion and due to fission gas formation (Kr^{85}, Cs^{137}). These conditions decrease the pellet-clad gap, thereby affecting the rod stiffness and damping.

Meng and Ludema [1995] present an extensive overview of the available empirical equations for modeling fretting wear. These involve parameters like wear rate, volume loss (of materials in friction), applied load (at contact area) etc. However, such relations hold true for a specific range. Though often more accurate than analytical equations, yet they cannot be generalized to other domains. Some analytical models have also been developed; a brief introduction of which is given below.

- **Contact mechanics approach**: Kim [1999] modeled fretting wear in terms of energy dissipation by studying shear stresses at the contacts. Energy is dissipated in the form of loss of metal particles. As shear stress increases, energy dissipation increases, thereby increasing fretting damage. The energy density is calculated as the product of shear stress and slip displacement.
- **Fracture mechanics approach**: Here, fretting wear is modeled by analyzing crack propagation.
- **Monte Carlo probabilistic approach**: Since the various fuel assembly parameters vary significantly [Pettigrew, 1993], probabilistic tools can be employed for analyzing fretting wear. Rubiolo [2006] and Rubiolo and Young [2009] defined various parameters like cell clearance (or rod position), grid alignment, friction coefficient etc. as random variables and assigned probability density functions (PDF) to each one of them. The PDF is suitably chosen so that it describes the potential behavior of the variable. From the rod displacement and impact forces, the work rates (= force $\times$ displacement / time) are calculated. In order to restrict fretting wear damage, the sensitivity of wear damage to the various parameters like cell clearance size, grid misalignment or cell tilt, assembly bow pattern, fuel rod stiffness, turbulence forces etc. are to be determined first and then the important parameters are correlated with the fuel assembly

operating conditions. This model was applied on a benchmark case of Davies and Rogers [1979]. Also, it has been successfully applied for predicting fretting wear damage of fuel assemblies under controlled test conditions at Westinghouse VIPER (Vibration investigation and Pressure-drop Experimental Research) loop.

2.6 Computing resources

All simulations reported in this PhD thesis were performed on Curie and Airain supercomputers. Computing Center for Research and Technology (CCRT) facility at Bruyères-le-Chatel, France houses both Curie and Airain. Few small scale test simulations were also carried out on the 840-core Mezel supercomputer located at CEA Cadarache, France.

Curie, owned by GENCI and operated by CEA, has an aggregate peak performance of 2 PFlops. Currently, it ranks 44 on the list of most powerful supercomputers in the world [Top500 webpage]. The computer nodes are connected through a QDR InfiniBand network. The nodes run on Bullx SuperComputer Suite 4R4, based on Red Hat Enterprise Linux 6 operating system. In all, Curie has 92160 cores. Grand Équipement National de Calcul Intensif (GENCI)

The 'thin' node architecture, accessible through the standard partition, is used for regular computation. There are 5040 nodes each containing 2×8-cores SandyBridge CPU clocked at 2.7 GHz. There are 16 cores/node and 80640 cores for the whole thin node architecture. Each node has 64 GB RAM, i.e., 4 GB per core.

The 'hybrid' node architecture, accessible through the hybrid partition, is used for graphical usage. There are 144 nodes each containing 2×4-cores Westmere-EP CPU clocked at 2.67 GHz coupled to 2 Nvidia M2090 GPU. In total, there are 1152 cores + 288 GPU for the full architecture. Each node has 24 GB RAM and each GPU has 6 GB.

Airain has a peak performance of 400 TFlops [Top500 webpage]. In all, Airain has 20192 cores. The 'ivybridge' node architecture is used for regular computation. There are 360 nodes each containing 2×10-cores IvyBridge CPU clocked at 2.8 GHz. There are 20 cores/node and 7200 cores for the whole architecture. Each node has 64 GB RAM, i.e., 3.6 GB per core.

Airain also has 'hybrid' node architecture for graphical usage. There are 18 nodes each containing 2×8-cores SandyBridge CPU clocked at 2.1 GHz coupled to 2 Nvidia K20m GPU. In total, there are 288 cores + 36 GPU for the full architecture.

High performance visualization were performed on the hybrid nodes of Curie and Airain which are accessed with VisuPortal and HPC Drive environments [VisuPortal webpage]. It allows users to book a session and perform intensive graphic visualization from local workstations. Client-server remote desktop display solutions like HP RGS [HP Remote Graphics Software webpage] and VBridge [Oxalya webpage] are used for remote access to high performance workstations.

2.7 Conclusion

In this chapter, a bibliography report on the subject of the thesis is presented. The principal components of a PWR fuel assembly, the various physical phenomena occurring in it and the mathematical models and techniques to address these issues are discussed. The code TrioCFD which has been developed by CEA for unsteady, incompressible and compressible monophasic and diphasic flows and has been used for the simulations in this thesis is then briefly discussed. Its various applications over the years is also presented. Available experimental and simulation data for the flow field in rod bundles has been discussed. A detailed bibliography on experiments, numerical simulations and empirical models which have been done to study wall pressure fluctuations beneath a turbulent boundary layer is subsequently presented.

Chapter 3

Annular Pipe

3.1 Introduction

Annular pipe flows have applications not only in the field of nuclear reactors but also in heat exchangers, drilling operations in oil industry etc. In this chapter, large eddy simulation (LES) in an annular pipe for five mesh resolutions are presented. As discussed in Chapter 1, instead of reactor-scale Reynolds number 500000, simulations were done at 8900. At this lower Reynolds number, multiple simulations could be performed for different mesh resolutions and stable solutions could be obtained in a shorter time. This Reynolds number 8900 was specifically chosen due to the availability of validation data [Nouri et al., 1993, Nouri and Whitelaw, 1994, Azouz and Shirazi, 1998, Chung et al., 2002, Kaneda et al., 2003, Liu and Lu, 2004, Chung and Sung, 2005, Ould-Rouiss et al., 2009, Hadžiabdić et al., 2013]. A subsequent simulation was also performed for Reynolds number 26600 to observe the effect of Reynolds number. Mesh sensitivity study was performed to find an acceptable mesh resolution for simulating such an annular pipe and develop proper inlet boundary conditions for the complicated geometries discussed in the next chapter.

3.2 Geometry

A concentric annular pipe with outer and inner diameters 60 mm and 30 mm respectively was chosen as the computational domain. The radius ratio defined as the ratio between the inner and outer radii was 0.5. Water flowed through the pipe in axial direction as shown in Fig. 3.1. The hydraulic diameter is defined as

$$\begin{aligned} HD &= \frac{4A_{flow}}{P_{wet}} \\ &= \frac{4\left(\frac{\pi D_o^2}{4} - \frac{\pi D_i^2}{4}\right)}{\pi D_o + \pi D_i} \\ &= \frac{(D_o + D_i)(D_o - D_i)}{(D_o + D_i)} \\ &= D_o - D_i \\ &= 60\ mm - 30\ mm \\ &= 30\ mm \end{aligned}$$

where A_{flow} is the surface area of duct cross-section and P_{wet} is the wetted perimeter. The bulk velocity U_b was 0.298 m/s. Reynolds number based on the bulk velocity U_b and hydraulic diameter HD is given by

$$\begin{aligned} Re_D &= \frac{\rho \times U_b \times HD}{\mu} \\ &= \frac{U_b \times HD}{\nu} \\ &= \frac{0.298 \times 0.03}{1.006 \times 10^{-6}} \\ &= 8900 \end{aligned}$$

where ρ is the density of the working fluid, μ is the dynamic or absolute viscosity and ν is the kinematic viscosity. The total length of the domain was 0.24 m, which is equal to 8 times the hydraulic diameter. For all calculations reported here, the working fluid is water at a temperature of 20°C with kinematic viscosity $\nu = 1.004 \times 10^{-6}$ $\mathrm{m^2 s^{-1}}$ and density $\rho = 998.2$ $\mathrm{kg.m^{-3}}$.

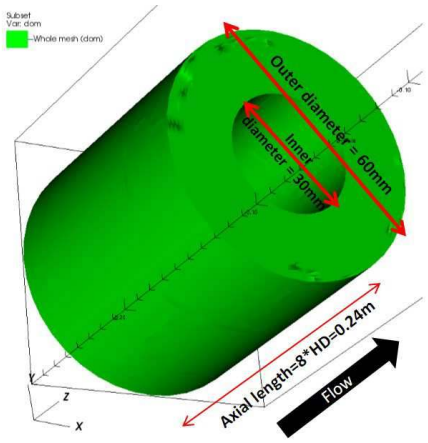

Figure 3.1: Schematic diagram of annular pipe

3.3 Mesh

Case	Grid points (N_r, N_θ, N_z)	Δ_r^+	Δ_θ^+	Δ_z^+	Elements (millions)	Cores	Physical time (days)	CPU time (hours)
C1 (Coarse)	(25,80,120)	7.7	9.2	15.3	1.3	60	3	4140
C2 (Coarse)	(25,160,120)	8.8	5.3	17.6	2.7	120	3	9315
F1 (Fine)	(73,160,480)	1.3	5.1	2.4	33	1600	2	74980
F2 (Fine)	(73,320,240)	1.3	2.7	4.9	33	1600	3	111780
UF (Ultra-fine)	(73,640,120)	1.3	1.3	9.6	33	1600	2	74980

Table 3.1: Mesh resolution for five different cases

Five different mesh resolutions were considered for the study. Table 3.1 shows the number of grid points in radial (N_r), azimuthal (N_θ) and axial (N_z) directions respectively, the mesh resolution in wall units, the number of tetrahedral elements, the number of parallel cores in the supercomputer and the physical time for each simulation case. Figs. 3.2a to 3.2e illustrate the stretching of the tetrahedral elements for each case relative to each other. The mesh was more refined near the boundary in radial direction to study the near-wall behavior. The mesh was uniform in axial and azimuthal directions. The top view and side view for the case F2 are shown in Figs. 3.3a and 3.3b respectively. The two coarse meshes C1 and C2 differ in azimuthal stretching. C1 was refined approximately 3 times in radial direction to obtain the finer meshes F1 and F2. The total number of elements was maintained for cases F1, F2, UF in order to observe the effect of azimuthal and axial stretching. Hexahedral meshes were first generated using Gmsh [Geuzaine and Remacle, 2009]. Each hexahedra was further sub-divided into 48 tetrahedra using TrioCFD (using keyword *tetrahaedriser_homogene_fin*).

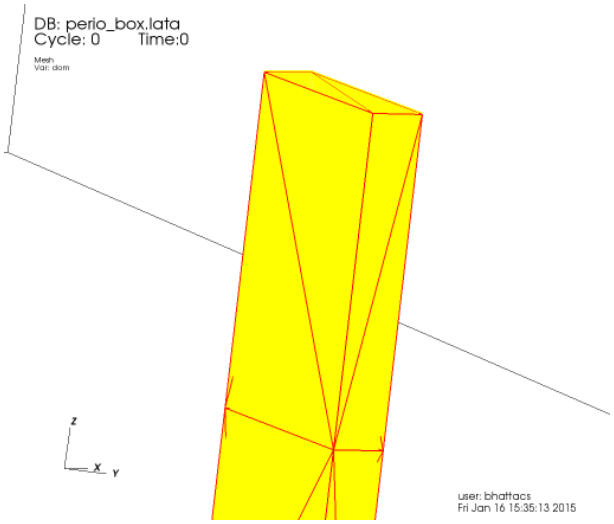

(a) C1 case

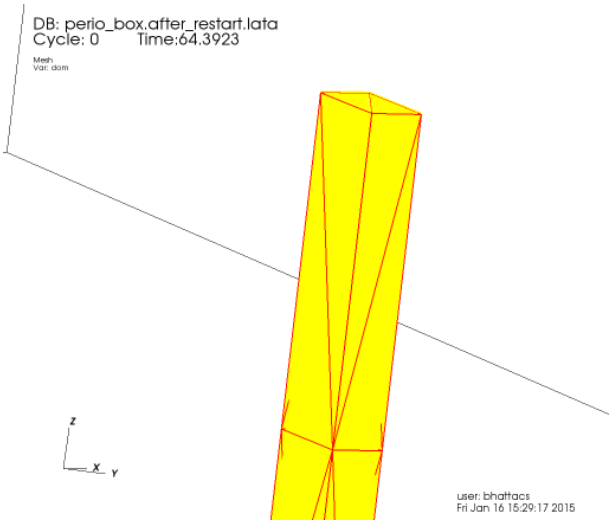

(b) C2 case

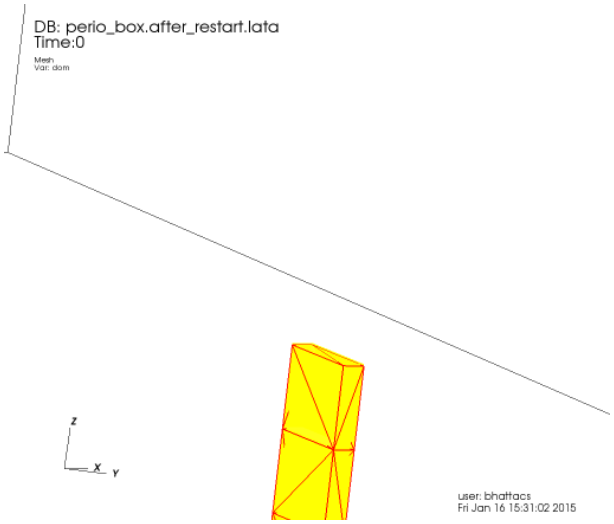

(c) F1 case

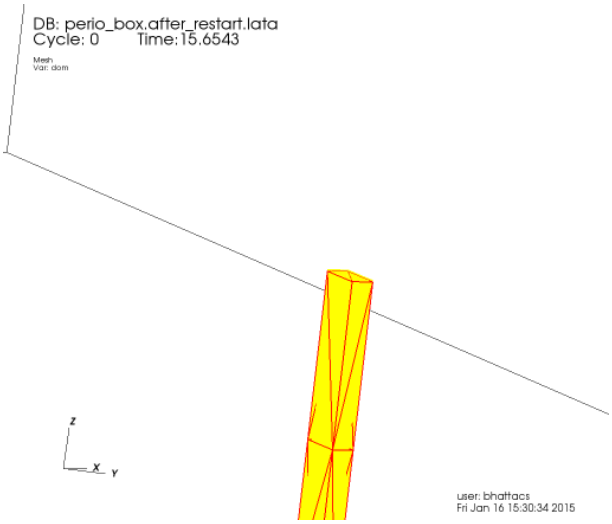

(d) F2 case

(e) UF case

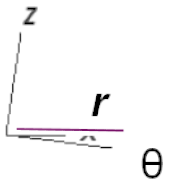

(f) Axes

Figure 3.2: Comparison of relative mesh size for the 5 different cases

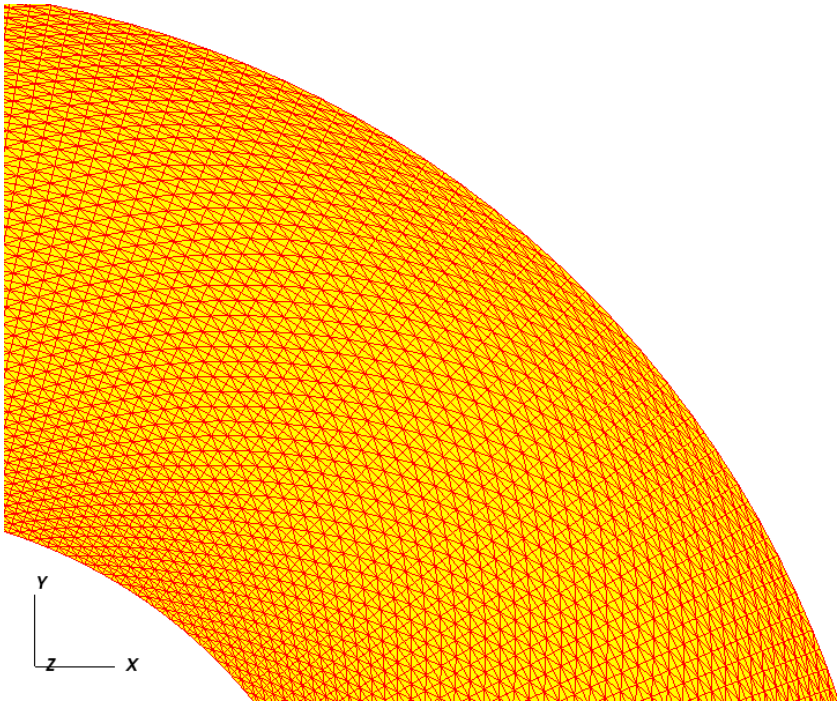

(a) Top view

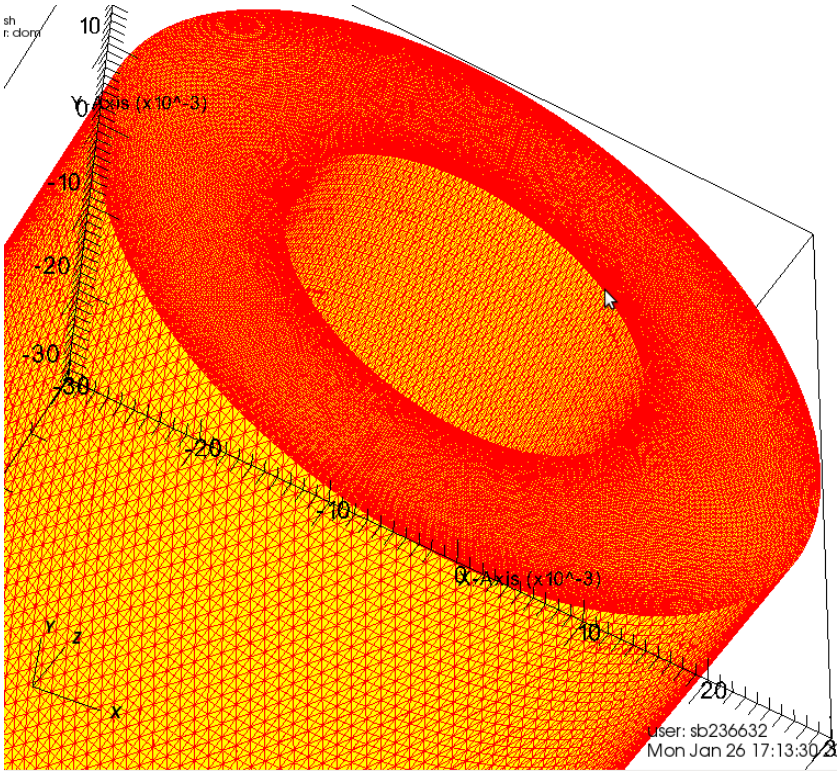

(b) Side view

Figure 3.3: Mesh for F2 case

3.4 Issues with generating turbulence

Coarse mesh (C1 case)	Fine mesh Uniform radial grid	Fine mesh Non-uniform radial grid
$N_r = 25$	$N_r = 61$	$N_r = 73$
$N_\theta = 80$	$N_\theta = 80$	$N_\theta = 80$
$N_z = 120$	$N_z = 240$	$N_z = 240$

Table 3.2: Number of grid points in all three directions

In the coarse mesh case C1, transition to turbulence occurred even when it was initialized with a constant velocity profile. However, this was not the case for the fine mesh simulations. The resultant mean velocity profile was always parabolic implying laminar flow (Fig. 3.4). This could possibly be attributed to the extreme regular pattern of the mesh.

The sensitivity of different numerical schemes were also tested. The time discretization scheme was changed from Adams-Bashforth 2nd order scheme to Adams-Bashforth 3rd order, Runge-Kutta 3rd order and Runge-Kutta 4th order. But in all cases, the flow stays laminar. Instead of the centred-stabilized EF_stab space discretization scheme, upwind scheme was employed but it was expectedly diffusive. Similar was the case with the SGS turbulence model when we switched from WALE to Smagorinsky model. The wall law was also changed from the single equation Reichardt law to the standard three layer law but it did not change the result.

Since the change in numerical schemes was not successful to generate turbulence, the initial axial velocity field was perturbed in various ways to see if there is any effect. The imposed axial velocity is given by

$$u = \overline{u} + n \times u^{'} \tag{3.1}$$

where $\overline{u}$ denotes bulk velocity, n denotes the amplitude of fluctuation (viz., 5%, 10%, 20% etc.) and $u^{'}$ denotes the behavior of fluctuation given by the following 3 expressions.

- Type 1: $u = \overline{u} + \frac{1}{10}\overline{u}\sin\left(\frac{10\pi}{R_o - R_{in}}\left[x - R_{in}\right]\right)$: *see Fig. 3.5*
- Type 2: $u = \overline{u} + \frac{1}{10}\overline{u}\sin\left(\frac{10\pi}{R_o - R_{in}}\left[x - R_{in}\right]\right)\sin\left(\frac{10\pi}{R_o - R_{in}}\left[y - R_{in}\right]\right)$: *see Fig. 3.6*
- Type 3: $u = \overline{u} + \frac{1}{10}\overline{u}\sin\left(\frac{10\pi}{R_o - R_{in}}\left[\sqrt{x^2 + y^2} - R_{in}\right]\right)$: *see Fig. 3.7*

These axial velocity fields (with 10% fluctuation) are plotted on the top plane of the annular pipe in

Figs. 3.5, 3.6, 3.7 respectively.

Figure 3.4: Parabolic mean velocity profile

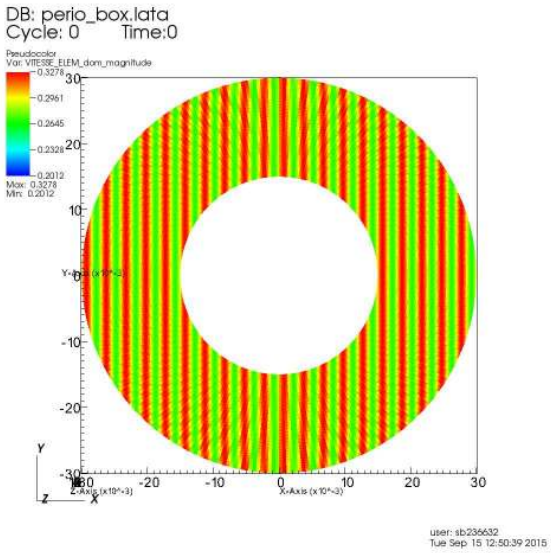

Figure 3.5: Axial velocity: type 1

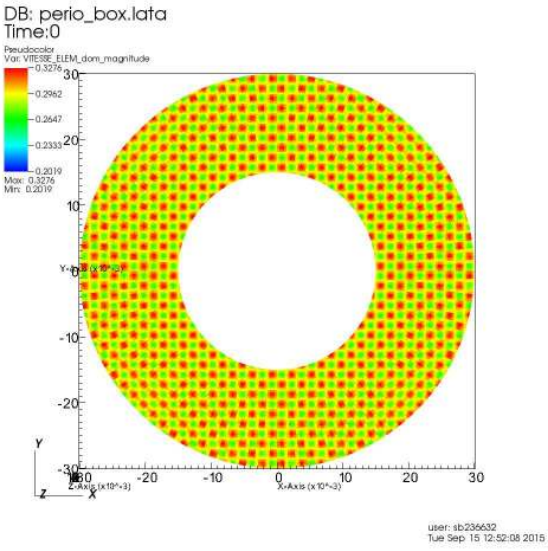

Figure 3.6: Axial velocity: type 2

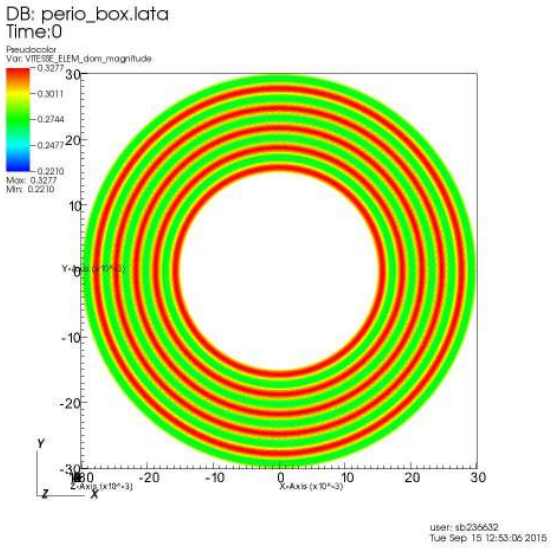

Figure 3.7: Axial velocity: type 3

Unfortunately, these sinusoidally perturbed initial velocity fields were not able to trigger transition to turbulence. The next trick was to define a parabolic field superposed by random noise in the direction of flow (axial). Like before, this velocity distribution on the top plane is plotted in Fig. 3.8c. Only random noise was defined in the other two directions (Figs. 3.8a and 3.8b). Random fluctuations were visible along the axial length. The three components of velocity are defined as:

$$V_z = V_{max} - a \times \left(\sqrt{x^2 + y^2} - 0.0225\right)^2 + R_n \tag{3.2}$$

$$V_y = R_n \tag{3.3}$$

$$V_x = R_n \tag{3.4}$$

where V_{max} represents bulk velocity ($= 0.298$ ms^{-1}), a is a constant factor ($= 5298$), R_n denotes a random number generator.

Even this strategy failed to trigger transition to turbulence. Finally, we used the fully developed turbulent flow field from the coarse mesh C1 to initiate the fine mesh simulation. TrioCFD provides the opportunity to save the field values at the last time step of a simulation in MED format using the *LataToMED* keyword. Fields stored in this format can be used to initialize any future simulation using *Champ_front_MED* keyword. The method works even if the mesh structure in the two domains is different. In case of a parallel calculation, the number of partitions for the old and new calculations need not be same. But one should ensure that the geometrical dimensions of the domain are identical. This technique successfully recreated the transition to turbulence. Turbulence was sustained in the domain and it did not die out.

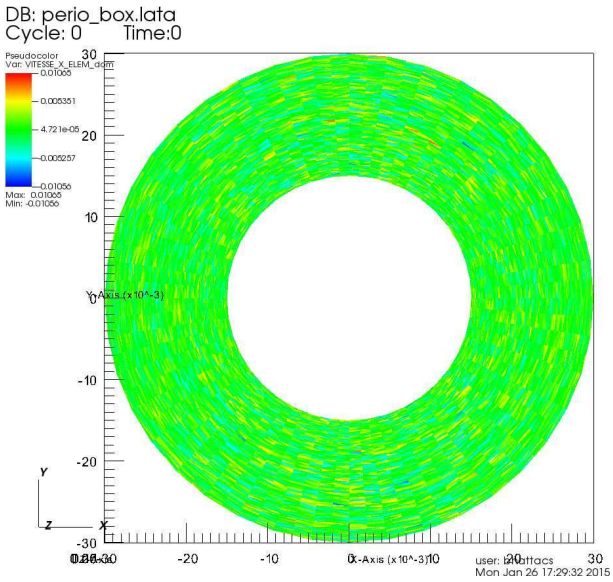

(a) Velocity V_x (Random noise)

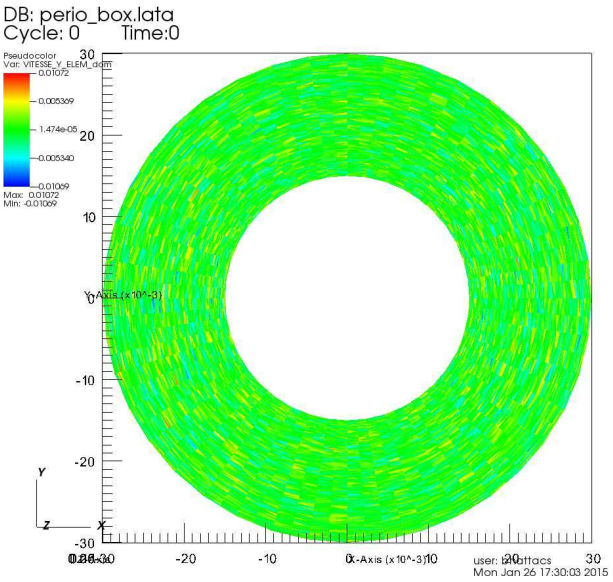

(b) Velocity V_y (Random noise)

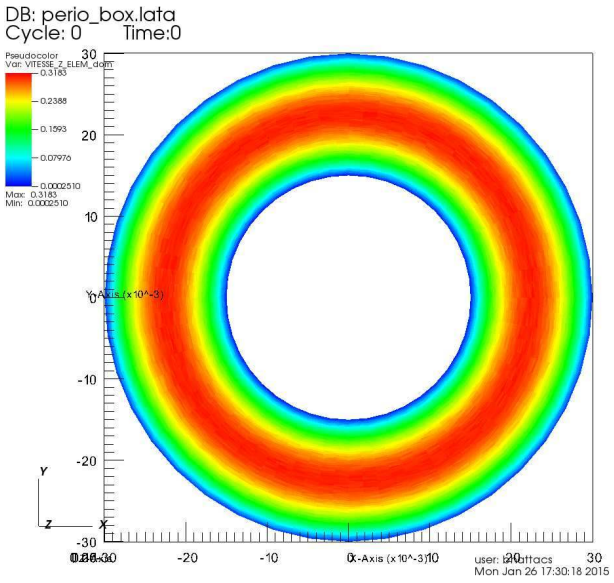

(c) Velocity V_z (Parabolic distribution superposed with random noise)

Figure 3.8: Velocity distributions in each direction

3.5 Results for Reynolds number 8900

Number of grid points	Grid spacing (m)
$N_r = 73$	$\Delta r = .00025 - .00015$
$N_\theta = 320$	$\Delta\theta = .00058 - .0003$
$N_z = 240$	$\Delta z = .00055$

Table 3.3: Mesh resolution for a fine mesh (Case F2)

In this section, the results of F2 case are presented. The number of grid points and the corresponding grid spacing are mentioned in Table 3.3. At the inner wall, axial stretching is 4 times that of radial stretching and twice the azimuthal stretching. At the outer wall, axial stretching is 4 times that of radial stretching and nearly the same as azimuthal stretching. In the bulk region, axial is twice the radial stretching. In the UF case, the ratio between axial and azimuthal stretching was increased to 4 times.

The mesh propagation factor, i.e., the change in adjacent element sizes, was well within the recommended 5% [Vandroux and Barthel, 2013]. A hexahedral mesh was first generated using the CAD tool Gmsh [Geuzaine and Remacle, 2009]. In all, there were 33 million elements. There were 73 grid points in the radial direction between the two walls. The ratio between the longest and shortest edge in an element is called the aspect ratio. Its distribution in a part of the domain is shown in Fig. 3.9: it varies from 3 in the bulk to 10 at the boundary. Metis partitioning tool [METIS webpage] was used for sub-dividing the domain into 1600 parts, i.e., approximately 20500 elements per part. For better performance, TrioCFD recommends having 20000-30000 elements per part.

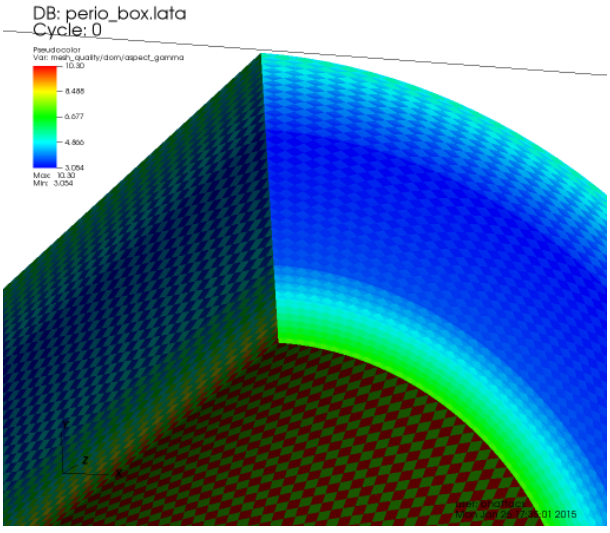

Figure 3.9: Aspect ratio distribution (Case F2)

Figure 3.10: Two point correlation for axial velocity (Case F2)

Radius ratio = D_i/D_o	0.5
Hydraulic diameter (HD)	30 mm
Re	8900
Boundary conditions	No-slip (inner & outer walls) Periodic (axial direction or flow direction)
Initial condition	Fully developed turbulent flow from a coarse mesh simulation
Time scheme	Second order explicit Adams-Bashforth
Convection scheme	Second order centered stabilized EF_stab (slightly upwind)
Diffusion scheme	Second order
Sub-grid scale (SGS) model	WALE model
Wall law (when necessary)	Reichardt function

Table 3.4: Summary of geometrical and numerical parameters

Table 3.4 presents a summary of the geometrical and numerical parameters used in the simulation. LES was performed with TrioCFD [TrioCFD (previously Trio_U) webpage] on the domain with periodic boundary condition in the direction of flow (axial). No-slip boundary condition was imposed on the inner and outer walls. Periodic boundary conditions are particularly useful in directions where the mean flow is homogeneous. They are used when the physical geometry of interest and the expected flow or thermal pattern are of periodic repeating nature. It significantly reduces computational time and effort. All properties are set to be equal at equivalent points on pairs of periodic boundaries. The distance between the two periodic boundaries must be such that two-point correlations vanish for all points on a pair of periodic boundaries. This means that the distance should be chosen to be at least twice the size of the largest eddies so that the effect of one boundary on the other is minimal [Versteeg and Malalasekara, 2007]. The axial length of the domain was 8 times the hydraulic diameter, i.e., 0.24 m. Two point correlation between the axial components of velocity is shown in Fig. 3.10 to illustrate that the computation domain length in the flow direction is adequate. The correlation coefficient falls off to zero value at separations suggesting that the domain is sufficiently large.

As discussed in the previous section, we used a fully developed turbulent flow field with bulk velocity 0.298 ms^{-1} to initialize the current simulation. This flow field was obtained from a coarse mesh simulation of the same domain (Case C1) having 1.38 million elements.

The space discretization was performed on tetrahedral elements with the second order centered stabilized EF_stab scheme (details on the scheme are discussed in Kuzmin and Turek [2004a,b]) and time discretization was done with second order Adams-Bashforth scheme. The EF_stab scheme has

a factor α to weigh the scheme centering between 0 (full centered) and 1 (mix between upwind and centered). $\alpha = 1$ tends to over dissipate kinetic energy (for further details on the factor α, refer to Ducros et al. [2010]). We used $\alpha = 0.2$ which is in fact slightly upwind. Fully upwind schemes should be avoided for LES because they are too dissipative. The PETSc Preconditioned Conjugated Gradient (PETSc PCG) iterative solver was used with SSOR preconditioning. PetSc Cholesky solver is not recommended for parallel simulation over 500 processors due to high memory requirement. For modeling the universal small scale eddies, the wall-adaptive local eddy viscosity (WALE) sub-grid scale model [Nicoud and Ducros, 1999] was used. Its advantages were previously discussed in sub-section 2.2.1. The non-dimensional parameters used to study near-wall behavior were discussed in sub-section 2.2.2. Blasius law of skin friction for pipe flow [Lesieur, 1995] was used to obtain an initial estimate of y^+. This gave an idea whether or not to use wall law.

$$\begin{aligned} Re_\tau &= 0.164 \times Re_D^{7/8}, \\ \Rightarrow u_\tau \times D/\nu &= 0.164 \times Re_D^{7/8}, \\ \Rightarrow u_\tau &= \nu/D \times 0.164 \times Re_D^{7/8}, \\ &= (1.004e-6/0.03) \times 0.164 \times (8900)^{7/8}, \\ &= 0.016 \end{aligned}$$

Using this value of friction velocity, we estimate

$$\begin{aligned} y^+ &= \frac{u_\tau \times y/2}{\nu}, \\ &= \frac{0.016 \times 0.00015/2}{1.004e-6}, \\ &= 1.2 \end{aligned}$$

Here, $Re_\tau = u_\tau \times D/\nu$ is the Reynolds number based on friction velocity and Re_D is the Reynolds number based on bulk velocity. Since $y^+ \sim O(1)$, no wall law was used for studying the near-wall behavior. A momentum source term $S(t)$ was applied to the flow to maintain constant mass flow rate:

$$S(t) = \frac{2 \times [Q(0) - Q(t)] - [Q(0) - Q(t - dt)]}{A \times D \times dt} \tag{3.5}$$

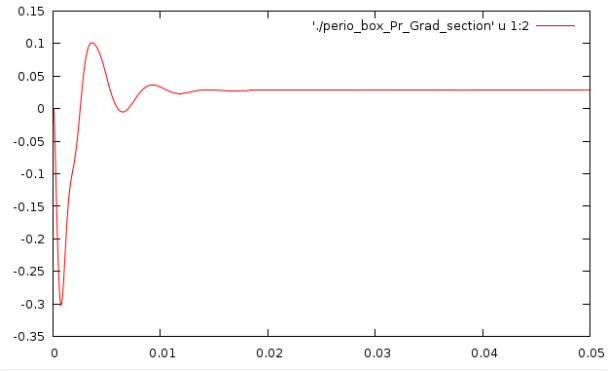

Figure 3.11: Pressure gradient (Case F2)

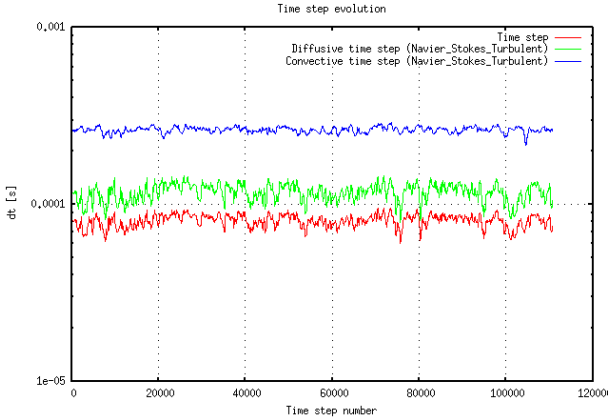

Figure 3.12: Time step evolution (Case F2)

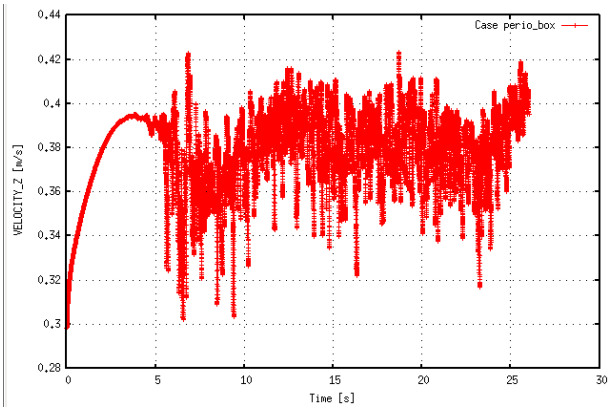

Figure 3.13: Axial velocity (Case C1)

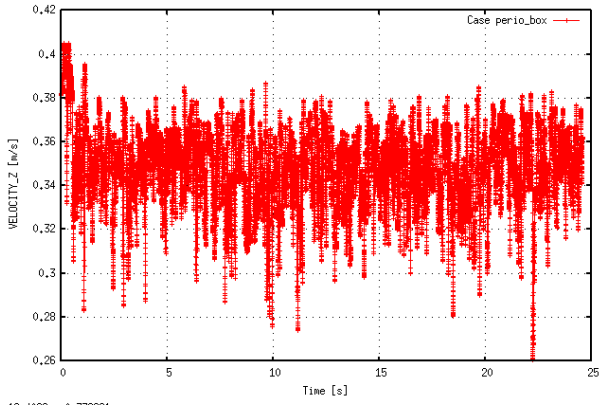

Figure 3.14: Axial velocity (Case F2)

where $Q(t)$ denotes flow rate at time t, A denotes area of cross-section, dt time step and D denotes damping coefficient. At each time step, TrioCFD writes the pressure gradient $\frac{\partial P}{\rho \partial z}$ across the periodic boundary. Its variation with time is plotted in Fig. 3.11. This axial pressure gradient was found to be constant with axial distance, i.e., $\frac{\partial P}{\rho \partial z} = 0.05$ which is 49.9 Pa. This confirmed that the flow was fully developed. The constancy of the flow rate was also verified. The time step evolution is shown in Fig. 3.12. The net calculation time step is 8×10^{-5} s; diffusive and convective time steps for the momentum equation are 1×10^{-4} s and 2×10^{-4} s respectively. The time taken by the fluid to traverse the whole domain once, i.e., the flow traversal time was 0.8s. The simulation was carried out in parallel on 1600 cores on the 'thin' nodes of Curie supercomputer at Computing Center for Research and Technology (CCRT), Bruyères-le-Chatel, France. The total CPU time was 111780 hours, i.e., 23 hours on 60 processors (for turbulent flow initialization) plus 69 hours on 1600 processors. Firstly, the transition to turbulence for C1 occurs at 5 s (Fig. 3.13). Fig. 3.14 shows the instantaneous velocity

fluctuations for F1 simulation at a point in the middle of the hydraulic canal. Clearly turbulence is sustained. The flow was fully developed and stabilized; the transient calculation was continued until we had sufficient statistics. This was collected over 28 flow traversals: from 3 s to 25 s. Typically, it is sufficient to start collecting statistics after the fluid has traversed the whole domain twice axially.

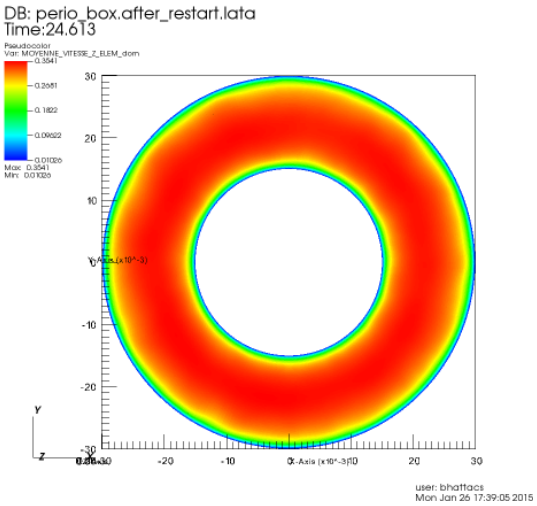

Figure 3.15: Mean axial velocity (Case F2)

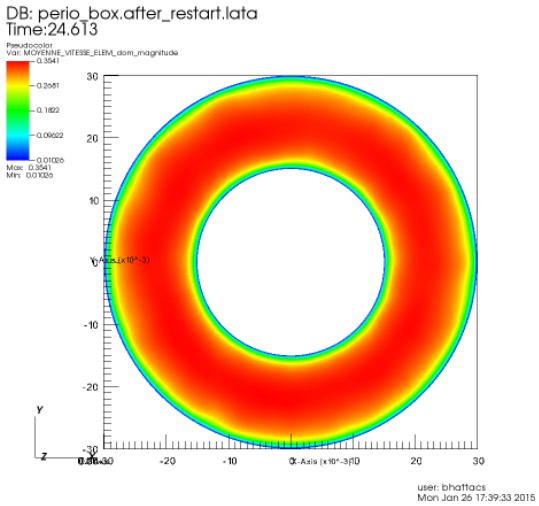

Figure 3.16: Magnitude of mean velocity (Case F2)

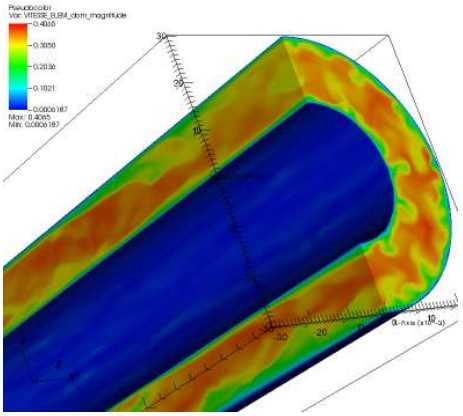

Figure 3.17: Instantaneous velocity: side view

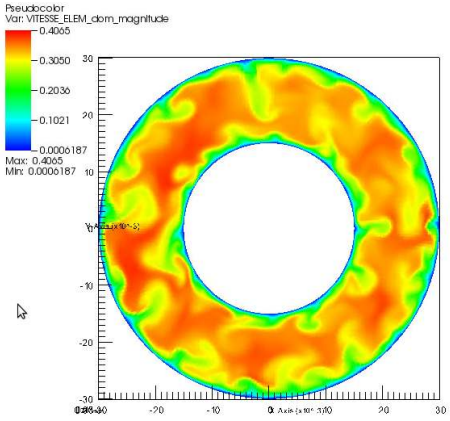

Figure 3.18: Instantaneous velocity: top view

The instantaneous and mean velocity fields are visualized using VisIt post-processing tool [Childs et al., 2012] on the VisuPortal remote visualization environment of Curie [VisuPortal webpage]. Figs. 3.15 and 3.16 illustrate the axial component and magnitude of mean velocity respectively on x-y plane. Figs. 3.17 and 3.18 show the instantaneous velocity inside the annular pipe. Fig. 3.19 illustrates the iso-surfaces of instantaneous velocity inside the pipe. The 'segment' probes in TrioCFD only calculate the time averaged values over a line segment. Since velocity is quantified at the face

center of each tetrahedron, so using TrioCFD segment probe may result in non-zero value at the boundary (violating the no-slip condition) because the face center may not be located exactly on the boundary. To avoid such non-physical results, 73 cylindrical surfaces were defined corresponding to each radial grid point. Both space- and time-averaged value was computed on each cylinder, i.e., the entire azimuthal and axial span. This was compared with the time-averaged value obtained from 'segment' probes. Both the averages were normalized by the bulk velocity and plotted along the radius in Fig. 3.20. The profiles are in good agreement to the benchmark DNS of Chung et al. [2002]. The mean velocity profile can also be represented in wall units to better understand the near wall behavior. The velocity and length scales are re-written in terms of the non-dimensional parameters y^+ and u_+ and plotted on a semi-log scale (Fig. 3.21).

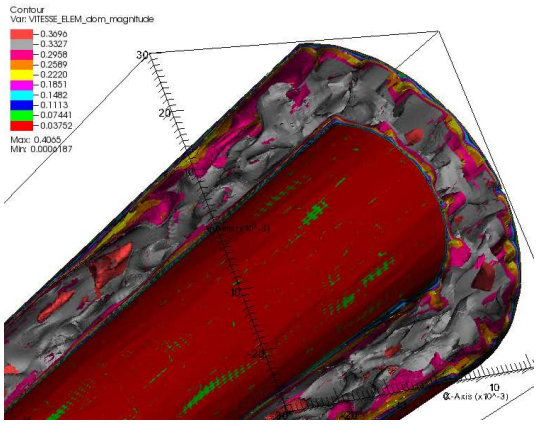

Figure 3.19: Iso-surfaces of instantaneous velocity (F2 case)

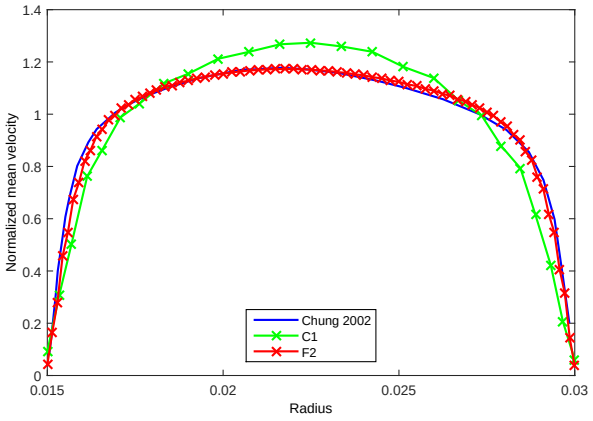

Figure 3.20: Mean axial velocity for C1 and F2 cases

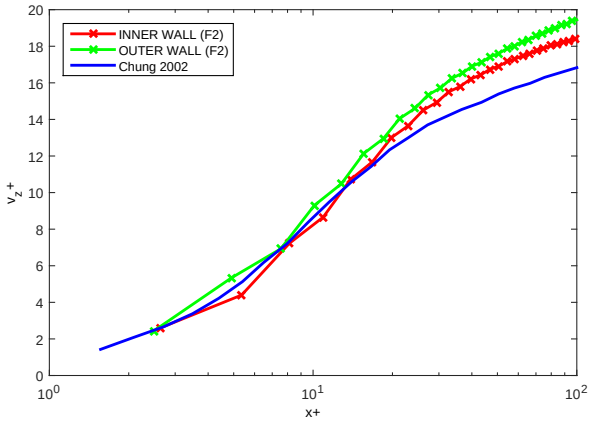

Figure 3.21: Mean axial velocity for F2 case in wall units

Calculation of friction velocity

The friction velocity was calculated from the friction drag exerted by the fluid on the inner and outer walls. The x- and y- components were negligible compared to the z-component.

$$\begin{aligned}\vec{F} &= \int (-\mu \nabla u) \times n dS \\ F_z &= 7.974 \times 10^{-3}\,\mathrm{N} \text{ (inner wall)} \\ &= 1.377 \times 10^{-2}\,\mathrm{N} \text{ (outer wall)}\end{aligned}$$

Total surface area of the inner and outer walls are respectively

$$\begin{aligned}A_i &= 2.2618 \times 10^{-2}\,\mathrm{m}^2 \\ A_o &= 4.5236 \times 10^{-2}\,\mathrm{m}^2\end{aligned}$$

Friction velocity

$$\begin{aligned}u_\tau &= \sqrt{\frac{\tau_w}{\rho}} \\ &= \sqrt{\frac{F_z}{\rho \times A}} \\ &= 0.0188 \text{ (inner wall)} \\ &= 0.0175 \text{ (outer wall)}\end{aligned}$$

These values are quite close to the Blaisius law estimate 0.016. Using these values of friction velocity,

$$\begin{aligned}y^+ &= \frac{u_\tau \times y/2}{\nu} \\ &= 1.4 \text{ (inner wall)} \\ &= 1.3 \text{ (outer wall)}\end{aligned}$$

The non-dimensional velocity profile too agrees well with Chung et al. [2002] except in the logarithmic region. We have to accept this error of around 10% while comparing to a DNS because LES has a significantly less number of grid points compared to DNS.

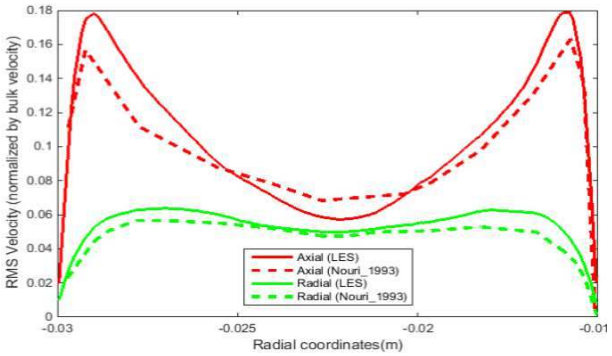

Figure 3.22: RMS axial and radial velocity (Case F2)

RMS distribution of axial and radial component of fluctuating velocities on a segment probe normalized by the friction velocity are displayed in Fig. 3.22. In order to ascertain the reliability of this simulation, a comparison is made with the LDV measurements of Nouri et al. [1993]. It is in good agreement; it expectedly reaches a minimum at the middle of the hydraulic canal and peaks close to the boundary.

3.6 Mesh sensitivity analysis for Reynolds number 8900

A mesh sensitivity study was proposed following LES on five mesh resolutions mentioned previously in Table 3.1. A comparison of mean velocity profiles for the fine and coarse meshes is presented in Figs. 3.23 and 3.24 respectively. Comparison of the C1 profile with F1 shows an obvious improvement due to the refinement in all directions. The F2 mesh was created with the same number of elements but the resolution in azimuth was doubled and that in axial was halved. Clearly the mean velocity profile for F2 agrees well with the DNS of Chung et al. [2002]. The UF mesh also shows similar result as F2. Thus it can be inferred that the meshes F2 and UF have an acceptable mesh resolution to reproduce the DNS result considering a compromise between accuracy and cost. In terms of wall units, one could go up to resolution of the order of 10 in axial, 3 in azimuthal and 1.3 in radial direction. It should be noted that the total number of elements was the same for cases F1, F2 and UF. The above sensitivity analysis shows that the mean velocity profile has a stronger dependence on the azimuthal resolution compared to axial resolution for the 4 meshes presented here. A similar test was performed with the coarse mesh. The azimuthal resolution in C1 was doubled to create C2. Again, Fig. 3.24 shows a significant improvement in the profile of C2. The mean velocity was plotted in non-dimensional units to observe the near-wall behavior (Fig. 3.25). It shows that the result from

F2 mesh is closest to benchmark.

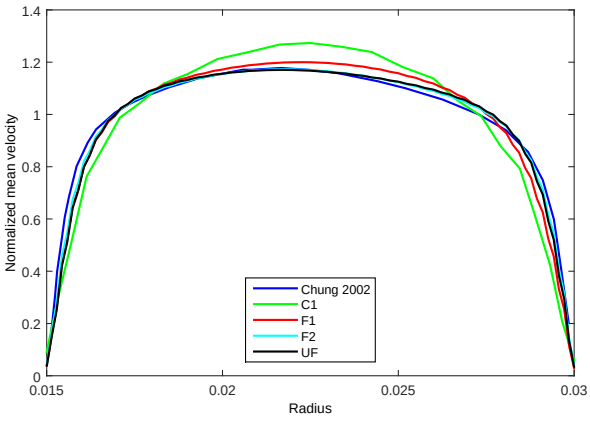

Figure 3.23: Comparison of mean axial velocity among fine meshes

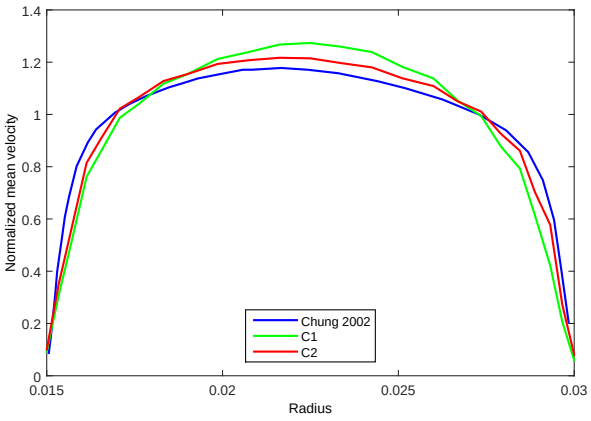

Figure 3.24: Comparison of mean axial velocity among coarse meshes

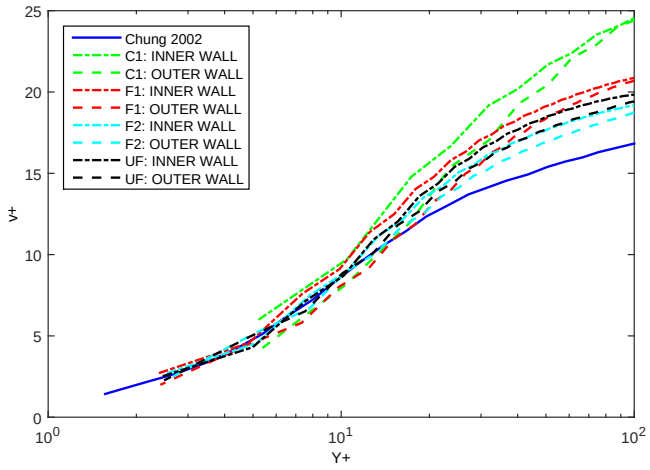

Figure 3.25: Mean axial velocity in wall units

3.7 Results for Reynolds number 26600

In order to observe the effect of Reynolds number, the LES was repeated for a higher Reynolds number 26600. One coarse mesh C1 and one fine mesh F2 were chosen for comparison. Understandably, the CPU time increases. The bulk velocity was $0.89\,\mathrm{ms}^{-1}$ and the axial domain length 8 times the hydraulic diameter. Two point correlation curve confirms the adequacy of the computational domain (Fig. 3.26). The simulation was initialized with the flow field from a simulation in the coarse mesh C1. Figs. 3.27 and 3.28 show the pressure gradient and time step evolution respectively. The pressure gradient in the axial direction is found to be $\frac{\partial P}{\partial z} = 0.27 \times 998.2 = 269.5$ Pa.

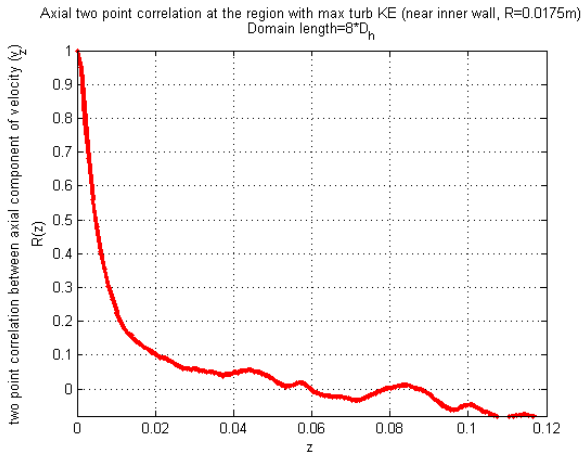

Figure 3.26: Two point correlation for axial velocity (Case F2)

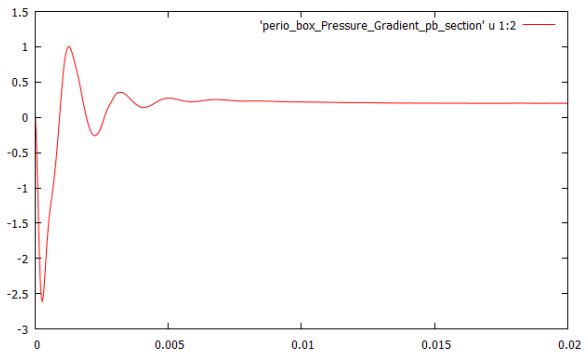

Figure 3.27: Pressure gradient (Case F2)

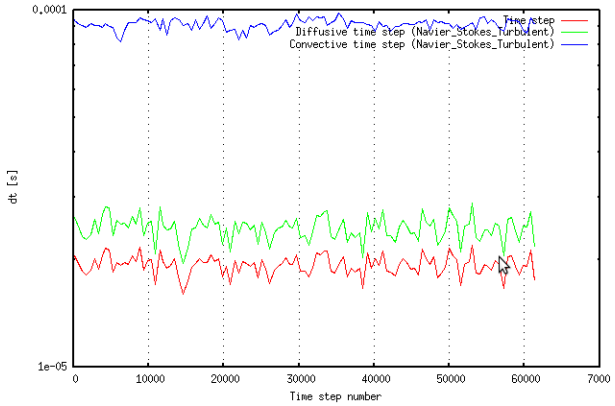

Figure 3.28: Time step evolution (Case F2)

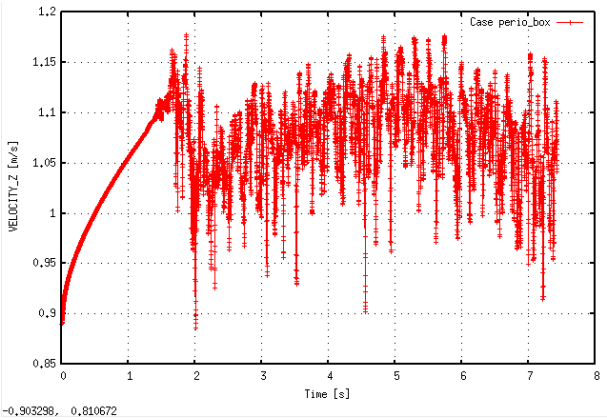

Figure 3.29: Axial velocity (Case C1)

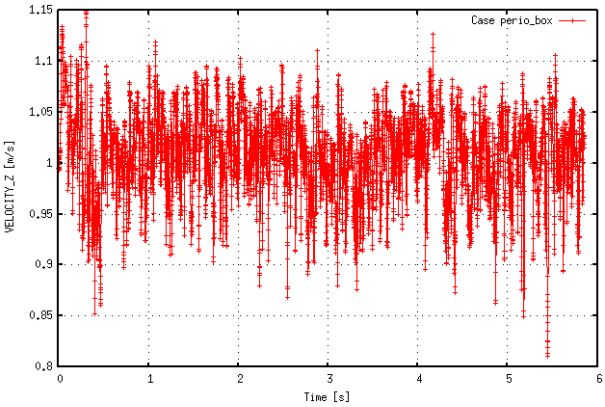

Figure 3.30: Axial velocity (Case F2)

Figs. 3.29 and 3.30 show the instantaneous axial velocity evolution with time for the coarse mesh C1 and fine mesh F2 respectively. Time for one flow traversal was 0.27 s. Statistics were collected from 2 to 5.8 s which is equal to approximately 14 flow traversals. A total of 185020 CPU hours on Airain supercomputer were used.

Calculation of friction velocity

Friction drag exerted by the fluid on the inner and outer walls is:

$$\begin{aligned} F_z &= 5.153 \times 10^{-2}\,\text{N (inner wall)} \\ &= 8.769 \times 10^{-2}\,\text{N (outer wall)} \end{aligned}$$

The total surface area remains unchanged since the domain is same. Therefore, friction velocity is

$$\begin{aligned} u_\tau &= 0.048 \text{ (inner wall)} \\ &= 0.044 \text{ (outer wall)} \\ y^+ &= \frac{u_\tau \times y/2}{\nu} \\ &= 3.59 \text{ (inner wall)} \\ &= 3.29 \text{ (outer wall)} \end{aligned}$$

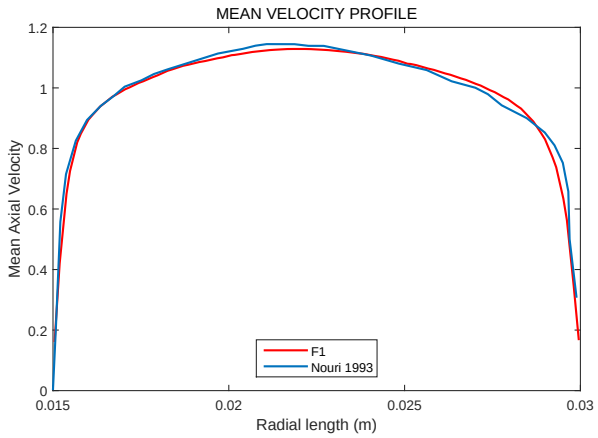

Figure 3.31: Mean axial velocity for case F2

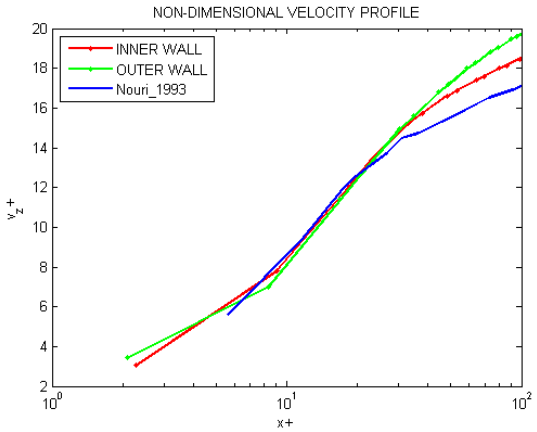

Figure 3.32: Mean axial velocity for case F2 in wall units

Time averaged velocities were computed on segment probes and normalized with bulk velocity. Its comparison with the experimental measurements of Nouri et al. [1993] is shown in Fig. 3.31. The non-dimensional profile (Fig. 3.32) normalized by the friction velocity was also in good agreement with the experiment of Nouri et al. [1993]. The data of Nouri et al. [1993] was properly scaled as per the observation of Azouz and Shirazi [1998].

RMS velocities were plotted on a segment probe in Fig. 3.33. The fluctuations behaved as expected with the magnitude decreasing in the order of axial, azimuthal and radial components. The profiles have a minima corresponding to the mean velocity maxima.

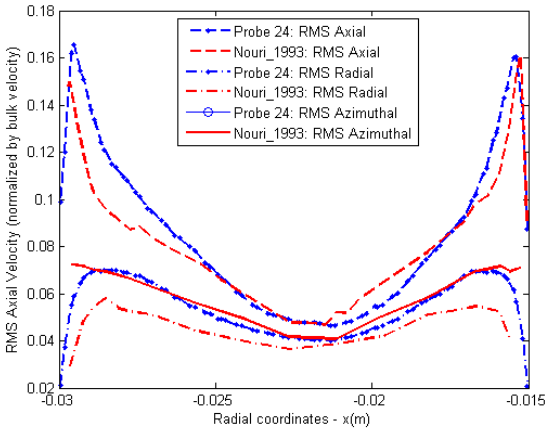

Figure 3.33: RMS velocity for case F2

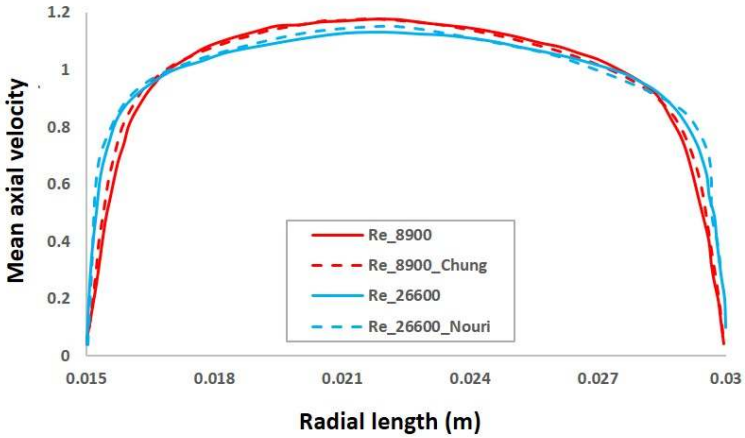

Figure 3.34: Comparison of mean axial velocity for $Re_D = 8900$ and 26600 (F2 case)

In Fig. 3.34, the mean axial velocity for Reynolds numbers 8900 (F2 case) and 26600 (F2 case) are plotted. It should be noted that the same mesh F2 was used for both cases. To make the comparison more meaningful, the mesh should be further refined for $Re_D = 26600$ so that the non-dimensional y^+ are approximately the same for both cases. Nevertheless, the curves show good agreement with the data of Chung et al. [2002] and Nouri et al. [1993]. Table 3.5 summarizes the CPU time required for carrying out these simulations.

Case	Cores	Physical time (days)	CPU time (hours)
$Re_D = 8900$	1600	3	111780
$Re_D = 26600$	1600	5	185020

Table 3.5: Comparison of CPU time for $Re_D = 8900$ and 26600 (F2 mesh)

3.8 Conclusion

Large eddy simulation was performed in an annular pipe of radius ratio 0.5 for five mesh resolutions at Reynolds number 8900. All meshes were structured and tetrahedral. Two coarse meshes and three fine meshes were studied. The goal of this chapter was three-fold: firstly to get an idea of the mesh resolution necessary to perform computation in an annular pipe; secondly to build confidence in using the code TrioCFD; and thirdly to develop proper input conditions for the complex geometries discussed in the next chapter. Due to the regular mesh, it was not possible to generate turbulence using flat profile initial conditions or mathematically perturbed profiles (sinusoidal, parabolic, random

noise etc.). So, a fully developed turbulent flow from a coarse mesh simulation was used as initial condition. A mesh sensitivity study was performed for the five meshes and it was found that the mean velocity profile has a stronger dependence on the azimuthal resolution compared to the axial resolution. For these five meshes, one can conclude that a resolution of the order of 1 in radial, 3 in azimuthal and 10 in axial direction in wall units is an acceptable mesh resolution for simulating such an annular pipe considering a compromise between accuracy and computational cost. The sensitivity analysis presented here was published by Bhattacharjee et al. [2015a]. The simulation was repeated with the same mesh for a higher Reynolds number 26600 and the result was comparable to standard literature data.

Chapter 4

Hydrodynamic Field

4.1 Introduction

This chapter is dedicated to the behavior of the flow field inside a annular pipe in the presence of 3 types of perturbations - two mixing vanes (MV), circular grid (CG) and square grid with two mixing vanes (SQ). The last case is the closest representative to a realistic PWR fuel assembly. However, unlike a realistic situation, none of these configurations contain the spring - dimple configuration which introduces additional perturbation to the fluid flow. This was done to simplify the mesh generation. The 3 different configurations are first introduced. Next, the procedure of mesh generation is discussed for each case along with the numerical schemes used. Finally, the characteristics of the velocity field at different upstream and downstream locations are discussed. All simulations were performed at $Re_D = 8900$ (based on hydraulic diameter and bulk velocity). The reasons behind choosing this Reynolds number have been explained previously in Chapters 1 and 3. The availability of simulation and experimental data for an annular pipe at this Reynolds number allowed us to compare the flow characteristics upstream of the obstacles and hence have confidence in the simulation results. Also, the effect of the geometrical obstacles on the flow could be studied by comparing with the annular pipe simulations in Chapter 3.

4.2 Geometrical configuration

4.2.1 Case of mixing vanes (MV)

Figure 4.1: Schematic diagram of the pipe with mixing vanes (1)

Schematic diagrams of the pipe with the mixing vanes and their dimensions are shown in Figs. 4.1 and 4.2. The outer (OD) and inner diameters (ID) of the pipe were 56.3 mm and 26.9 mm respectively. The radius ratio of the pipe was 0.48. Note that the dimensions have been slightly modified compared to the annular pipe case (Chapter 3) where the outer diameter, inner diameter and radius ratio were 60 mm, 30 mm and 0.5 respectively. This modification was necessary because the idea was to compare these simulations with the results from 'CALIFS single rod' experiment at CEA Cadarache (discussed in Chapter 2). Thus the geometrical dimensions were exactly the same as in the experiment except that the rounded edges of the mixing vane were ignored. The mixing vanes were modeled as parallelepiped (the edges being sharp). The two mixing vanes were placed symmetrically opposite to each other close to the fluid inlet at an inclination of 30° to the axis (Fig. 4.2). This angle of inclination was used in CALIFS experiment by Moreno [2012, 2014] and has also been used elsewhere [Lee and Choi, 2007, Chang et al., 2008, Smith et al., 2013, Peña Monferrer et al., 2014, Chatelain, 2014, Agbodemegbe et al., 2016]. Since the radius ratio 0.48 is very close to 0.5, it was possible to compare the velocity

profiles upstream with the reported literature of Chung et al. [2002] and Nouri et al. [1993] and hence, gain confidence in the current simulations. Water flowed through the annular gap of 14.7 mm.

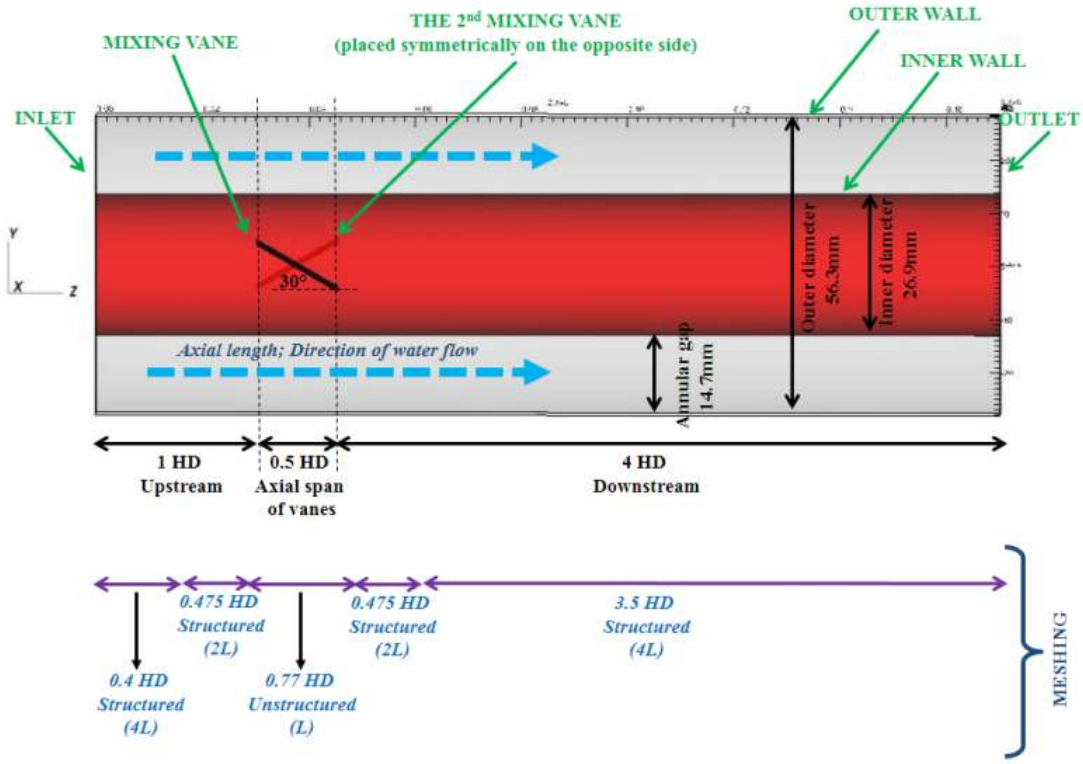

Figure 4.2: Schematic diagram of the pipe with mixing vanes (2)

4.2.2 Case of circular grid (CG)

A realistic PWR core has a square spacer grid as shown in Fig. 4.3a. The circular spacer grid design was studied due to the following reasons:

- mesh generation was simple because of the inherent symmetry,
- it was possible to create structured mesh,
- less simulation time and hence faster computation, and
- easy post-processing.

The equivalent circular grid is also shown in Fig. 4.3b. The white portion represents the spacer grid and the red portion represents the flow areas (designated as 1 and 2). To retain the physics of the problem, the circular grid was designed with the same ratio of hydraulic diameters of flow areas 1 and 2 as in the case of the square grid. This calculation is illustrated below. The dimensions of the

square grid were imported from the CALIFS experimental setup. A schematic diagram of the domain is shown in Fig. 4.4. The radial dimensions of the pipe were identical to the case of mixing vanes.

Let us define:

Width of the inner grid surface, $L_i = 36.4$ mm,

Width of the outer grid surface, $L_o = 39.8$ mm,

Thickness, $T = 1.2$ mm,

Inner radius of the pipe, $R_i = 13.45$ mm,

Outer radius of the pipe, $R_o = 28.15$ mm,

Inner radius of the new circular grid= RG_i,

Outer radius of the new circular grid= RG_o,

Hydraulic diameter of flow area i= HD_i, (i:1,2),

Surface area of duct cross-section of flow area i= A_i, (i:1,2),

Wetted perimeter of flow area i=P_i, (i:1,2).

To keep the thickness of the circular grid same as in the square grid, the following relations will hold true: $L_o - L_i = 2T$ and $RG_o - RG_i = T$.

(a) (b)

Figure 4.3: Transformation from a square to circular spacer grid

Figure 4.4: Schematic diagram of the pipe with circular grid

For the square grid,

$$\begin{aligned} HD_1 &= \frac{4A_1}{P_1} \\ &= \frac{4\left(L_i^2 - \pi R_i^2\right)}{4L_i + 2\pi R_i} \\ HD_2 &= \frac{4A_2}{P_2} \\ &= \frac{4\left(\pi R_o^2 - L_o^2\right)}{4L_o + 2\pi R_o} \end{aligned}$$

For the circular grid,

$$\begin{aligned} HD_1 &= \frac{4A_1}{P_1} \\ &= 2RG_i - 2R_i \\ HD_2 &= \frac{4A_2}{P_2} \\ &= 2R_o - 2RG_o \end{aligned}$$

To have the same ratio HD_1/HD_2 for both grids,

$$\frac{4\left(L_i^2-\pi R_i^2\right)}{4L_i+2\pi R_i}\cdot\frac{4L_o+2\pi R_o}{4\left(\pi R_o^2-L_o^2\right)}=\frac{2RG_i-2R_i}{2R_o-2RG_o}$$

$$\Rightarrow\frac{4\left(36.4^2-\pi 13.45^2\right)}{4\times 36.4+2\pi\times 13.45}\cdot\frac{4\times 39.8+2\pi\times 28.15}{4\left(\pi 28.15^2-39.8^2\right)}=\frac{2RG_i-2\times 13.45}{2\times 28.15-2RG_i-2\times 1.2}$$

$$\Rightarrow RG_i=20.9\ mm$$

$$\Rightarrow RG_o=22.1\ mm$$

4.2.3 Case of square grid with mixing vanes (SQ)

Detailed diagrams of the domain with exact dimensions are presented in Figs. 4.5 and 4.6. Two symmetrically opposite mixing vanes (as in MV case) and a square spacer grid were introduced close to the fluid inlet. The location and inclination (30°) of the vanes were the same as in the case of mixing vanes (MV) to ensure proper comparison. The radial dimensions were identical to the previous 2 cases. The total length of the pipe was 226.15 mm: the net axial span of the grid and vanes was 76.1 mm $\approx$ 2.5 HD; upstream and downstream sections were 1 and 4 HD long respectively. The vanes were parallelepiped and their dimensions were imported from those of CALIFS experiment except that the rounded edges were ignored. Also, the spring and dimple on the spacer grid surface were ignored. The dimensions of the grid conforms to that of the CALIFS experiment except that the length of the grid was reduced from 4 HD (in the experiment) to 2 HD (in the simulation). Since the grid surface was smooth without any spring or dimple, so an additional 2 HD of this grid would not significantly affect the behavior of the flow but only be an additional cost on the computational resources. In addition, although the previous simulation was done with a 4 HD long circular spacer grid, a small test simulation of the case of circular grid with a 2 HD long grid showed that the flow pattern is the same for both 2 HD and 4 HD grid. The uniform thickness, width of the inner grid surface and width of the outer grid surface were 1.2 mm, 36.4 mm and 39.8 mm respectively. Unlike the experiment, the vanes were slightly detached from the grid for simplifying mesh generation. A gap equal to 2 mesh elements was kept in between the two structures.

Figure 4.5: Schematic diagram of the pipe with square grid and mixing vanes (1)

Figure 4.6: Schematic diagram of the pipe with square grid and mixing vanes (2)

4.3 Meshing strategy

4.3.1 Case of mixing vanes (MV)

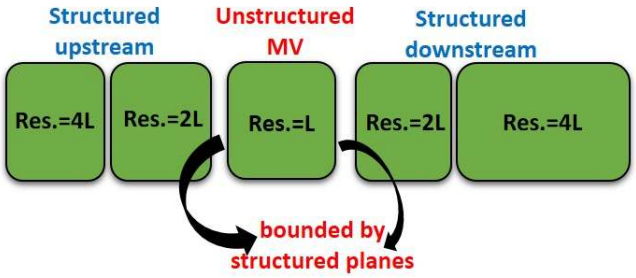

Figure 4.7: Meshing strategy (MV case)

The meshing strategy is illustrated in Fig. 4.7. The presence of geometrical obstacles complicate the mesh generation. The idea was to keep the mesh as structured as possible. However, generation of structured mesh in the vicinity of vanes was not possible. So a hybrid mesh was implemented: unstructured around the vanes and structured in the rest of the domain. This is illustrated in Fig. 4.2 (previously) and Fig. 4.8. Again, Figs.4.9 and 4.10 illustrate the orientation of the vanes with 2D meshing pattern on the inner wall at the background. Fig. 4.11 illustrates the position of the vanes from top. In order to reduce the number of elements and computational cost, gradient stretching was implemented in axial direction keeping in mind the allowable mesh resolutions obtained in Chapter 3. Table 4.1 illustrates the mesh resolution in wall units.

The final domain comprised of 5 sub-domains. At first, we tried to create the sub-domains by extruding the inlet and outlet plane of the unstructured sub-domain using TrioCFD. Although the extrusion worked fine, we observed a significant number of largest angle of an element in the range $120-150°$. A test simulation was run and it was observed that the simulation slows down by 15 times due to the large number of obtuse angles. Finally, it was decided to create each sub-domain separately using Gmsh [Geuzaine and Remacle, 2009] and generate tetrahedra in them with Gmsh. This helped to reduce the largest angle size. Default meshing algorithms in Gmsh were chosen: Delaunay for 2D plane surfaces, MeshAdapt for 2D curved surfaces and Delaunay for 3D volumes. Gmsh's in-built mesh optimizer and Netgen mesh optimizer were used to improve mesh quality. The 5 sub-domains were constructed as follows:

- Unstructured sub-domain was created around the vanes with element size 0.3 mm (in all 3 directions) bounded by structured inlet and outlet planes to ensure conformity with the first

Boundary	Direction	Mesh resolution (in wall units)	Mesh resolution (in mm)
Inner wall	Radial (wall normal)	3.18	0.30
Inner wall	Azimuthal	2.76	0.26
Inner wall	Axial (unstructured)	3.18	0.30
Inner wall	Axial (structured)	12.75	1.20
Outer wall	Radial (wall normal)	3.00	0.30
Outer wall	Azimuthal	5.50	0.55
Outer wall	Axial (unstructured)	3.00	0.30
Outer wall	Axial (structured)	12.00	1.20
Mixing vanes	All directions	5.59	0.30

Table 4.1: Mesh resolutions in case of mixing vanes

upstream and the first downstream sub-domains. This element size will henceforth be denoted as L. The resolution at the vane surface was 5.59 wall units. The structured mesh on the inlet and outlet planes is shown in Fig. 4.12. The radial direction had uniform grid spacing ($=L$). The axial resolution was 3.18 and 3.00 at inner and outer walls respectively. The azimuthal resolution was 2.76 and 5.5 at the inner and outer walls respectively. Box function in Gmsh was used to force the same element size throughout the sub-domain. It was 0.77 HD long.

- Using Gmsh, the inlet plane was extruded axially 0.475 times the hydraulic diameter HD with axial mesh resolution of $2L \approx 6$ wall units to create the first upstream sub-domain.

- The second upstream sub-domain was similarly extruded 0.4 times HD axially using Gmsh with axial mesh resolution of $4L \approx 12$ wall units. The acceptable mesh resolution in an annular pipe obtained in the previous chapter was ≈ 10 which was slightly exceeded here.

- The first downstream sub-domain was created by extruding the outlet plane 0.475 times HD using Gmsh with axial mesh resolution $2L \approx 6$ wall units.

- The second downstream sub-domain was similarly created by extruding the outlet plane 3.5 times HD using Gmsh with axial mesh resolution $4L \approx 12$ wall units.

Each of these sub-domains were meshed in 3D with Gmsh and exported as .med files [Code_Aster webpage]. These .med files were read by TrioCFD (using 'lire_med'). The common boundary surfaces were deleted from each sub-domain using 'supprime_bord'. Finally the 5 sub-domains were joined together with TrioCFD (using 'mailler') to create a conforming mesh while maintaining the original

mesh structure. The total axial length of the domain was 170 mm which corresponds to about 6 hydraulic diameters. The domain consisted of 19.36 million tetrahedrons. There were 50 grid points in the radial direction between the two walls.

Figure 4.8: Hybrid structured-unstructured mesh (MV case)

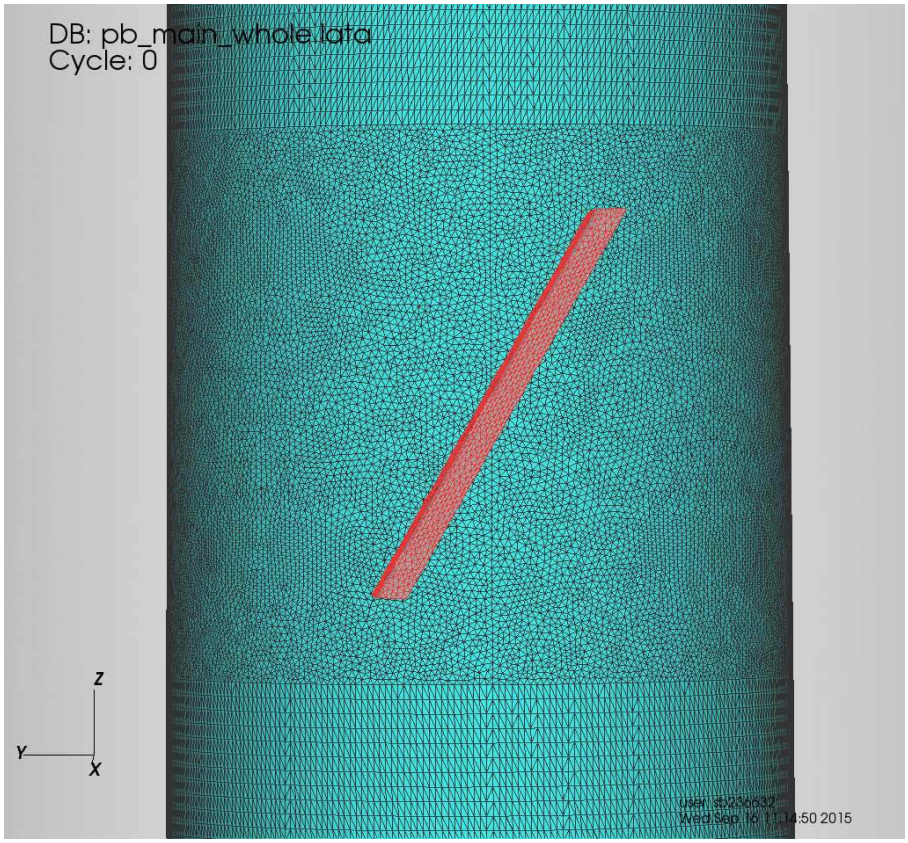

Figure 4.9: Orientation of vane with inner wall on the background (1) (MV case)

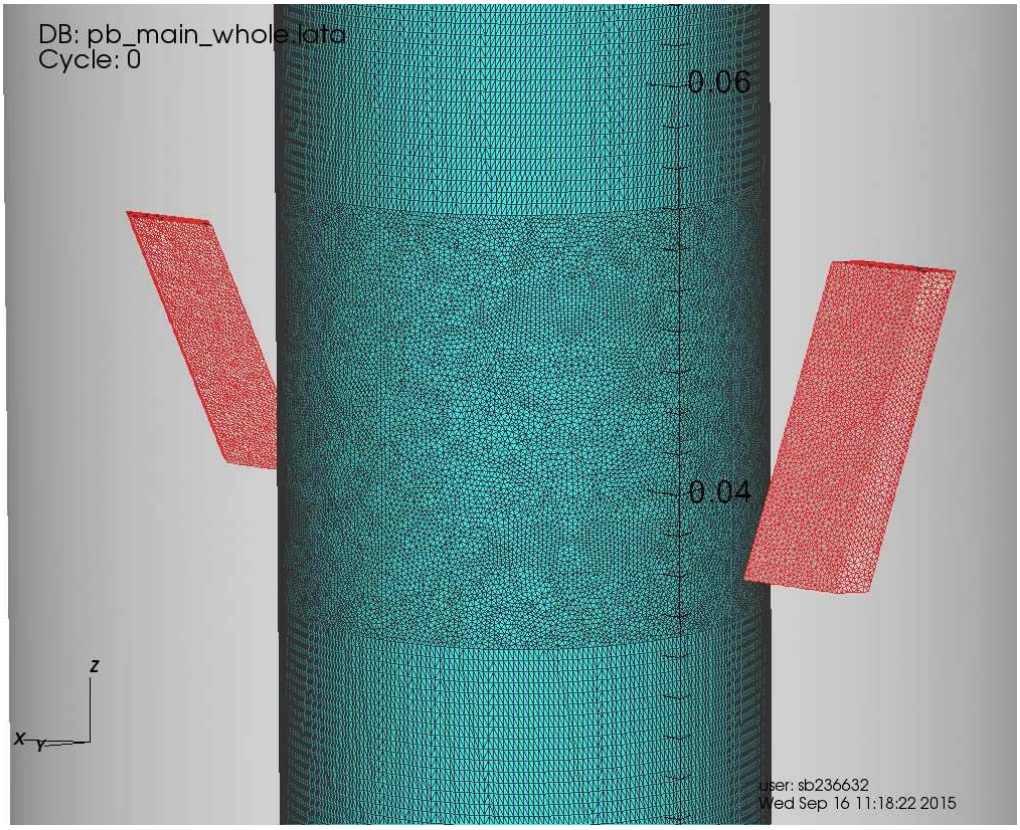

Figure 4.10: Orientation of vane with inner wall on the background (2) (MV case)

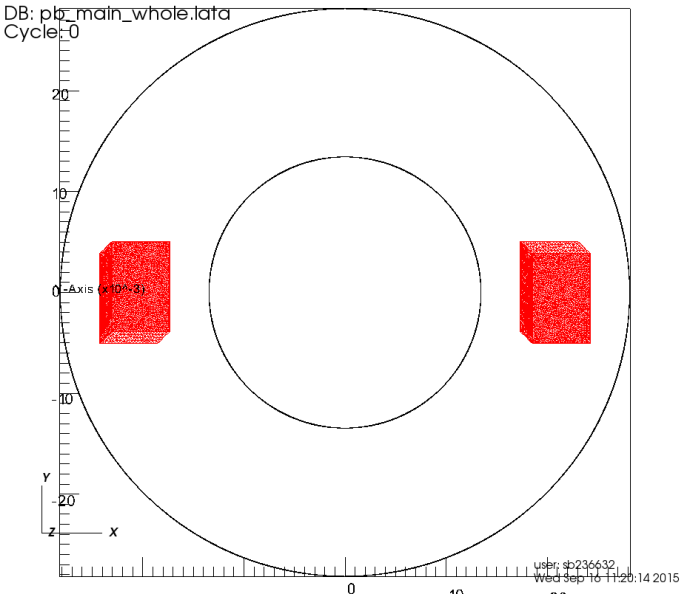

Figure 4.11: View of mixing vanes from top

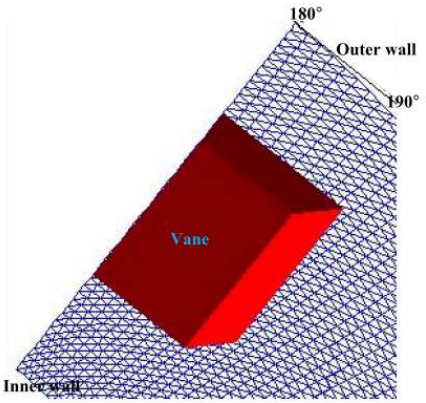

Figure 4.12: Structured mesh on inlet and outlet plane (MV case)

4.3.2 Case of circular grid (CG)

Figure 4.13: Meshing strategy for circular grid case

Boundary	Direction	Mesh resolution (in wall units)	Mesh resolution (in mm)
Inner wall	Radial (wall normal)	3.18	0.30
Inner wall	Azimuthal	2.76	0.26
Inner wall	Axial	12.75	1.20
Outer wall	Radial (wall normal)	2.94	0.30
Outer wall	Azimuthal	5.39	0.55
Outer wall	Axial	11.76	1.20
Circular grid	Radial (wall normal)	3.64	0.30
Circular grid	Azimuthal	4.85	0.40
Circular grid	Axial	14.55	1.20

Table 4.2: Mesh resolutions for circular grid case

Due to the inherent symmetry of the configuration, it was possible to create a structured mesh. The adopted strategy was to split up the domain into 8 sub-domains, mesh them separately and then merge them using TrioCFD. A rectangular plane could be visualized as made up of 9 planes as shown in Fig. 4.13. 8 of these planes were defined in separate .geo files. Each of these planes were extruded azimuthally to 360° with the mesh resolution presented in Table 4.2 (by defining layers in Gmsh). Hexahedral meshes were created in each of these 8 sub-domains with Gmsh and exported as .med files. These were then merged with TrioCFD (using 'mailler') to obtain the whole domain. The hollow part at the center represented the spacer grid (indicated by 0 in Fig. 4.13). After merging, surfaces which ceased to be boundaries were deleted (using 'Supprime_Bord') and those which retained their boundary character were merged and renamed as a single boundary (using 'Regroupebord'). Each hexahedra was sub-divided into 48 tetrahedra (using 'Tetraedriser_homogene_fin'). The total axial length of the domain was 268.8 mm which is ≈ 9 times the hydraulic diameter. Some compromise had to be made in the mesh resolutions presented in Table 4.2 due to lack of computational resources. The

final domain had 20.7 million tetrahedra. There were 51 grid points in the radial direction between the two walls.

4.3.3 Case of square grid with mixing vanes (SQ)

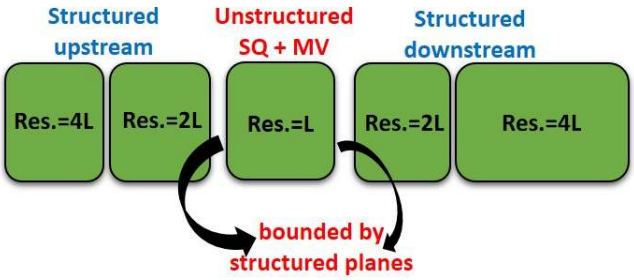

Figure 4.14: Meshing strategy (SQ case)

The meshing strategy is illustrated in Fig. 4.14. In this case, the principle of mesh generation was the same as in the case of mixing vanes, i.e., unstructured around the grid and vanes and structured elsewhere as shown in Fig. 4.16. The unstructured part is shown in further detail in Fig. 4.17. In CALIFS experimental setup, the external surface of the spacer grid was in contact with the outer wall of the pipe. But Gmsh could not create 3D mesh in this configuration due to intersecting faces. So it became necessary to keep a small gap in between the wall and spacer grid. A gap equal to 2 times the element length was introduced: this is well illustrated in Fig. 4.15. Similarly, a gap of 2 element lengths is kept in between the spacer grid and vanes. To reduce the number of elements and computational time, gradient stretching was implemented in axial direction keeping in mind the allowable mesh resolutions obtained in Chapter 3. Table 4.3 presents the mesh resolutions at all the boundary surfaces in each direction.

Figure 4.15: Gap between spacer grid and outer wall (SQ case)

Like the mixing vane case, whole domain was divided into 5 sub-domains. Each individual sub-domain was meshed separately with Gmsh. For 2D meshing, 'Delaunay' algorithm was used for

Boundary	Direction	Mesh resolution (in wall units)	Mesh resolution (in mm)
Inner wall	Radial (wall normal)	3.46	0.30
Inner wall	Azimuthal	3.00	0.26
Inner wall	Axial (unstructured)	3.46	0.30
Inner wall	Axial (structured)	13.85	1.20
Outer wall	Radial (wall normal)	3.18	0.30
Outer wall	Azimuthal	5.82	0.55
Outer wall	Axial (unstructured)	3.18	0.30
Outer wall	Axial (structured)	12.71	1.20
Mixing vanes	All directions	5.73	0.30
Spacer grid	All directions	4.57	0.30

Table 4.3: Mesh resolutions in the case of square grid with mixing vanes

plane surfaces and 'MeshAdapt' algorithm was used for curved surfaces. For 3D meshing, 'Delaunay' algorithm was used. Gmsh's built-in mesh optimizer and Netgen mesh optimizer were used to improve mesh quality. The 5 sub-domains were constructed as follows:

- Unstructured sub-domain was created around the vanes with element size L=0.3 mm (in all 3 directions) bounded by structured inlet and outlet planes to ensure conformity with the first upstream and first downstream sub-domains. The resolutions at vane and spacer grid boundary were 5.7 and 4.6 respectively in wall units. The structured mesh pattern on the inlet and outlet planes is shown in Fig. 4.16. The radial direction had uniform grid spacing (=L). In wall units, it was 3.5 and 3.2 at the inner and outer walls respectively. The value is slightly higher at the inner wall due to higher friction velocity (tabulated for all boundaries in Table 4.7). In the azimuthal direction, the mesh resolution was 3 at the inner wall and 5.82 at the outer wall. Box function in Gmsh was used to force the same element size throughout the sub-domain except the plane surfaces. This unstructured sub-domain was 83.7 mm long,≈ 2.8 HD, compared to 0.77 HD only in the case of mixing vanes. It contained 22.7 million cells.

- Using Gmsh, the inlet plane was extruded axially 0.475 times HD with axial mesh resolution $2L$ ≈ 6 wall units, to create the first upstream sub-domain. This had 2.2 million cells.

- The second upstream sub-domain was similarly extruded 0.4 times HD axially using Gmsh with axial mesh resolution $4L \approx 12$ wall units. It had 0.9 million cells. It exceeds the acceptable mesh resolution (≈ 10) obtained in Chapter 3 slightly.

- Similar to the first upstream sub-domain, the first downstream sub-domain was created by extruding the outlet plane 0.475 times HD using Gmsh with axial mesh resolution $2L \approx 6$ wall units. This had 2.2 million cells.

- Again, the second downstream sub-domain was similarly created by extruding the outlet plane 3.4 times HD using Gmsh with axial mesh resolution $4L \approx 12$ wall units. This had 8 million cells.

Each of these sub-domains were meshed in 3D with Gmsh and exported as .med files. These .med files were then read by TrioCFD, the common boundary surfaces were deleted from each sub-domain and finally the 5 sub-domains were joined together to create a conforming mesh while maintaining the original mesh structure. The axial length of the whole domain added up to 226.15 mm, i.e., $\approx$ 7.5 HD. The domain consisted of 36.1 million tetrahedrons. There were 50 grid points in the radial direction between the two walls.

Figure 4.16: Hybrid structured-unstructured mesh (SQ case)

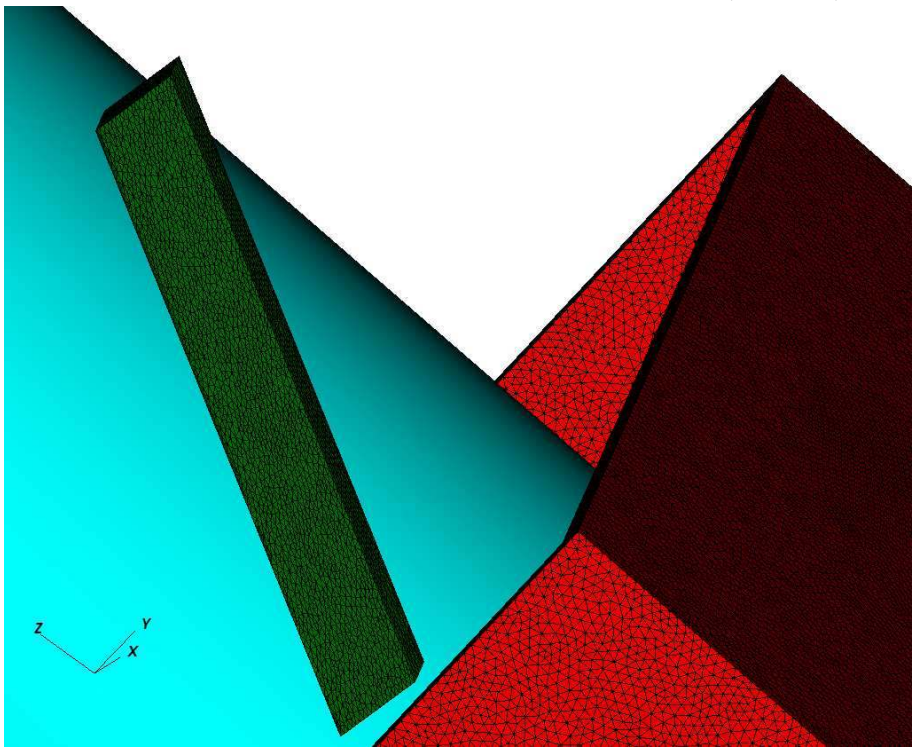

Figure 4.17: Mesh in unstructured sub-domain (SQ case)

4.4 General simulation strategy

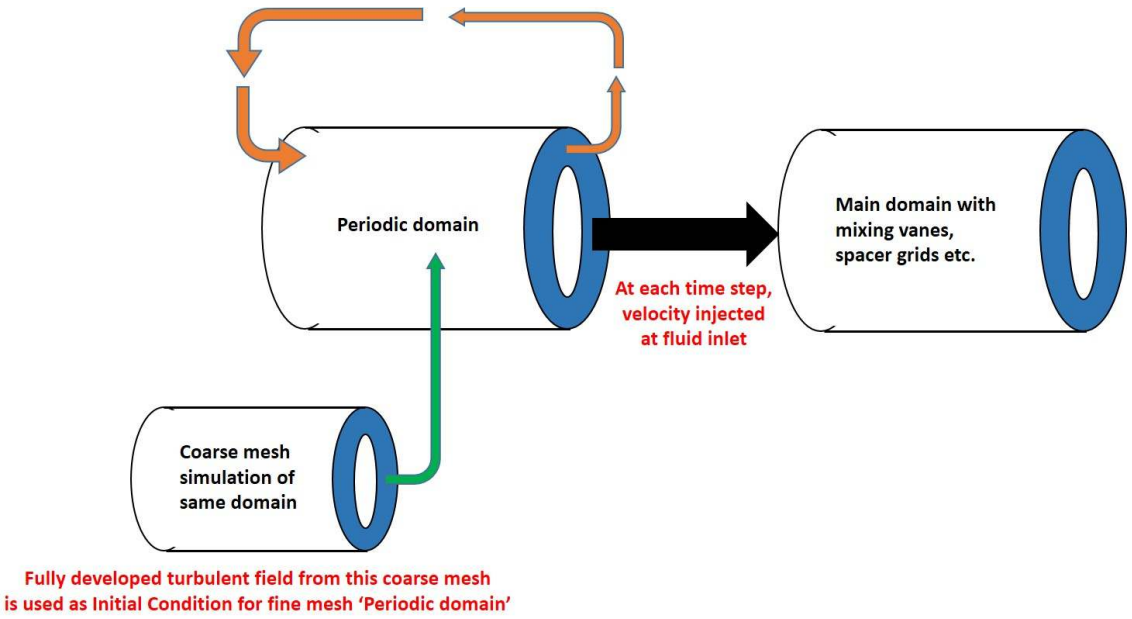

Figure 4.18: Coupled calculation in TrioCFD

The general simulation strategy adopted in all the three cases is illustrated above (Fig. 4.18) and then discussed in this section. In order to have proper inlet boundary conditions quickly, a LES was performed on a domain extruded axially to a length 6 times the hydraulic diameter from the inlet plane (=180 mm). Inlet and outlet boundaries of this extruded domain were regrouped into one boundary with the same name. TrioCFD gives the option of coupling two domains and running a computation on both in parallel using the keyword 'probleme_couple'. Periodic boundary conditions were applied axially in the new extruded domain. Henceforth this domain would be called the periodic domain. A momentum source term was added to maintain constant mass flow rate. During extrusion, the axial element length was maintained at $4L$ in the periodic domain (same as in the second upstream and downstream sub-domains mentioned in the previous sections). This extruded domain consisted of 14.11 million tetrahedrons. It was divided in to 490 parts. To ensure that the periodic domain is physical, its axial length must be such that the two-point correlation coefficient goes to zero on half a period. In general, correlation coefficient between any two variables f and g is defined by

$$R_{fg} = \frac{\Sigma(f_i - \overline{f})(g_i - \overline{g})}{\sqrt{\Sigma(f_i - \overline{f})^2}\sqrt{\Sigma(g_i - \overline{g})^2}} \tag{4.1}$$

which upon simplification becomes

$$R_{fg} = \frac{\Sigma(fg) - N\overline{f}\ \overline{g}}{(N-1)\sigma_f \sigma_g} \tag{4.2}$$

where $\overline{f}$, $\overline{g}$, σ_f and σ_g denote the means and standard deviations of the variables f and g respectively. For the present case, let us define the variables

vz_{t1} = Axial velocity at time t, position 1;

vz_{tS} = Axial velocity at time t, position S;

$\overline{vz_1} = \frac{1}{N}\Sigma(vz_{t1}),\ t:1\ to\ N$ = Mean axial velocity at position 1;

$\overline{vz_S} = \frac{1}{N}\Sigma(vz_{tS}),\ t:1\ to\ N$ = Mean axial velocity at position S;

$\sigma_{vz1} = \sqrt{\frac{1}{N-1}\Sigma(vz_{t1} - \overline{vz_1})^2},\ t:1\ to\ N$ = RMS axial velocity at position 1;

$\sigma_{vzS} = \sqrt{\frac{1}{N-1}\Sigma(vz_{tS} - \overline{vz_S})^2},\ t:1\ to\ N$ = RMS axial velocity at position S;

where the first and second subscripts in a variable represent time and space respectively. 'Mean' represents time averaging. The two point correlation coefficient between axial velocity at positions 1 and S is calculated for each S using

$$R_{1S} = \frac{\Sigma(vz_{t1}.vz_{tS}) - N\ \overline{vz_1}\ \overline{vz_S}}{(N-1)\ \sigma_{vz1}\ \sigma_{vzS}},\ t:1\ to\ N \tag{4.3}$$

and it is plotted in Fig. 4.19 where axial positions S are on x-axis and the correlation coefficient on the y-axis. The coefficient falls to zero at separations confirming that the domain length 6× HD is sufficiently long.

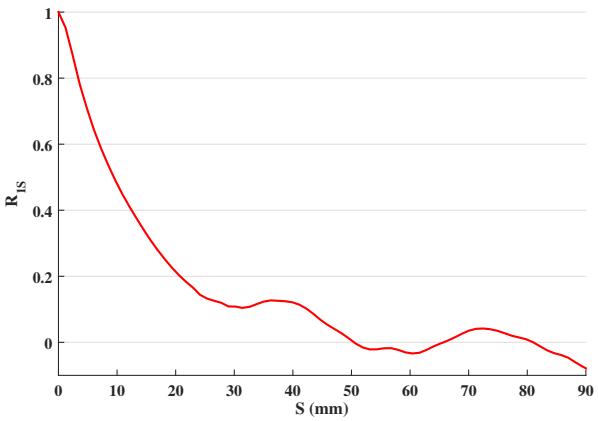

Figure 4.19: Two point correlation for axial velocity in case of the periodic domain

The velocities obtained on the periodic boundary were injected at the inlet of the main domain at each time step (using the coupling technique of TrioCFD). In order to accelerate the formation of a physically correct solution, a fully turbulent flow developed in another separate periodic box was used as initial condition. This particular simulation was done on a relatively coarse mesh to save computational resource and time, while maintaining the same domain size. This coarse simulation was performed for 13 hours on 36 cores of Airain, which is equal to 468 hours or 19.5 CPU days.

Second order centered stabilized 'EF_stab' scheme [Kuzmin and Turek, 2004a,b] was used as convection scheme. The EF_stab scheme has a factor α to weigh the scheme centering between 0 (full centered) and 1 (mix between upwind and centered). Fully upwind schemes should be avoided for LES because they are too dissipative. Ducros et al. [2010] observed that $\alpha = 1$ tends to over dissipate the kinetic energy. This behavior was verified. Best practice guidelines for TrioCFD recommend the use of $\alpha = 0.2$. Hence we used $\alpha = 0.2$ which is in fact slightly upwind. Second order diffusion scheme was used. Time discretization was done with second order explicit Adams-Bashforth scheme. The PETSc Preconditioned Conjugated Gradient (PETSc PCG) iterative solver was used with SSOR preconditioning [PETSc webpage]. Constant zero pressure was imposed at the outlet. No-slip boundary conditions were imposed on the inner and outer walls and the surface of the two vanes. Various sub-grid scale models like the Smagorinsky-Lille model, WALE model, dynamic sub-grid scale model etc. are available in TrioCFD for modeling the universal small scale eddies. The wall-adaptive local eddy viscosity (WALE) sub-grid scale model [Nicoud and Ducros, 1999] was chosen because of reasons discussed earlier in Chapter 2. Mesh resolution of the order of 1 is required near the wall. But this was not the case here as shown in Tables 4.1, 4.2 and 4.3 previously. So Reichardt wall law [Reichardt, 1951] was used to model the near wall behavior. These parameters, same for all the 3 cases, are again tabulated in Table 4.4.

Parameter	Scheme
Time scheme	2^{nd} order explicit Adams-Bashforth
Convection scheme	2^{nd} order centered stabilized EF_stab ($\alpha = 0.2$; slight upwind)
Diffusion scheme	2^{nd} order
Solver	PetSc Preconditioned Conjugated Gradient (PCG)
SGS model	WALE
Wall law	Reichardt law
Domain partitioning tool	Metis

Table 4.4: Summary of simulation parameters

4.4.1 Case of mixing vanes (MV)

Since TrioCFD uses a domain decomposition method, Metis partitioning tool [METIS webpage] was used to decompose the domain into 670 parts, each part having approximately 28800 elements. The total domain had 19.36 million elements. For a coupled problem, TrioCFD requires both domains to have equal number of partitions. So 180 empty partitions were created for the periodic domain so that both domains involved in the coupled simulation have 670 parts each. The simulation was launched on 670 cores (thin nodes) in parallel on Curie supercomputer located at Computing Center for Research and Technology (CCRT). It ran for 7 days 14 hours on 670 cores which amounts to 121940 hours or 5080.8 CPU days. Adding it to the initial coarse simulation on Airain makes it 6000 CPU days in total. It is not possible to run such long simulations at one go. So 'reprise' feature of TrioCFD was used to restart the simulation from the last time at which the fields were saved. Fields could be saved in binary format (N .sauv files where N is the number of parallel processes) or xyz format (single .xyz file). While restarting from .sauv files, each process reads in a specific file whereas from a .xyz file, each process reads sequentially from the same file. It is better to resume from .sauv files because reading the same file by multiple processes is not efficient. The calculation time step was $1 \times 10^{-5}s$; diffusive and convective time steps for the momentum equation were $1.5 \times 10^{-5}s$ and $7.5 \times 10^{-5}s$ respectively. It was continued for 3.76 s physical time to collect sufficient statistics. The time required for one flow traversal was $0.17/0.298 = 0.57s$. Upon studying the velocity fluctuations locally at different regions of the domain, it was observed that fluctuations arise much faster downstream of the vanes compared to the other regions. So we waited until we had fully turbulent flow in all regions and then collected statistics from 0.5 s to 3.76 s, i.e., 5.7 flow traversals. Statistics were calculated in two ways. TrioCFD's internal 'moyenne' and 'ecart_type' operators calculated the mean and RMS respectively from velocity values at each simulation time step. Secondly, velocity values were stored in probes every 100 time steps to save disk space and then post-processed manually using Matlab to obtain the mean and RMS quantities. It was observed that using TrioCFD's operators slows down the simulation. Both methods were used. Comparing the results obtained using the two methods, it was verified that saving values every 100 time steps did not result in any loss of information.

Boundary	Surface area (m^2)	Friction drag (N)	Friction velocity ($m^3.s^{-2}$)
Inner wall	1.44×10^{-2}	6.53×10^{-3}	2.13×10^{-2}
Outer wall	3.01×10^{-2}	1.21×10^{-2}	2.01×10^{-2}
Mixing vanes	2.75×10^{-4}	3.85×10^{-4}	3.75×10^{-2}

Table 4.5: Friction velocities (MV case)

The surface area, friction drag and friction velocity for each boundary are printed in Table 4.5. The friction drag

$$F_z = -\int \mu \nabla u.ndS \tag{4.4}$$

is integrated on each surface by TrioCFD where μ is dynamic viscosity (Pa.s), u is velocity (m/s), n is the unit normal on surface dS. The friction velocity u_τ and non-dimensional wall unit y^+ are respectively calculated by

$$u_\tau = \sqrt{\frac{F_z}{\rho A}}\ , \tag{4.5}$$

$$y^+ = \frac{u_\tau y_1}{\nu} \tag{4.6}$$

where ρ is density, A is surface area, ν is kinematic viscosity and y_1=$y/2$, y being the size of the first element in wall normal direction. The friction drag is maximum at the outer wall due to its maximum surface area. Friction velocity is higher at the inner wall compared to the outer wall but maximum at the vane surface. TrioCFD calculates friction velocity at body centers and so y_1 represents the distance to the body center of the first element. By default in TrioCFD, y^+ values are initialized as -1. To analyze y^+ using probes, the probe point should be moved to the center of gravity of the boundary element and not any other element. Otherwise, the code returns -1. To visualize in VisIt, y^+ field was post-processed in LATA format on each boundary element. Its distribution on outer wall of the pipe is shown in Fig. 4.20. Its spatial evolution in axial direction at 180° and 90° is shown in Fig. 4.21.

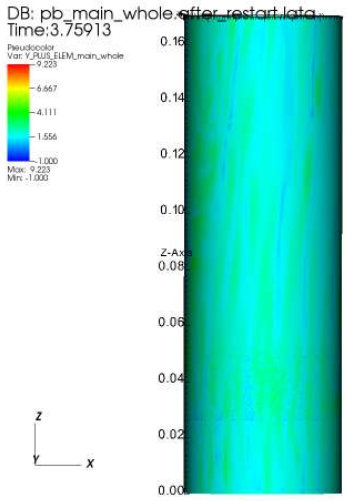

Figure 4.20: y^+ distribution on outer wall

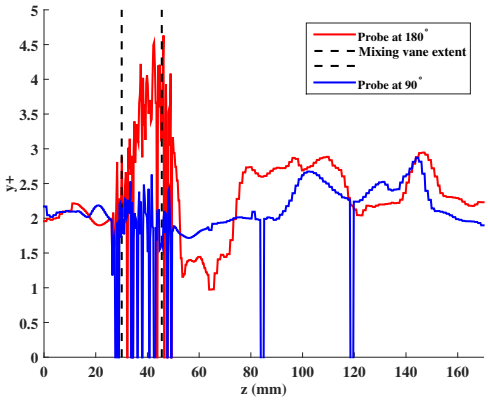

Figure 4.21: y^+ distribution on 2 axial probes on the outer wall

4.4.2 Case of circular grid (CG)

This domain was divided in to 710 parts and the simulation was run for 5 days and 13 hours on 710 cores (thin nodes) of Curie (= 94430 hours or 3935 CPU days). Adding it to the initial coarse mesh simulation makes it 3955 CPU days. The diffusive and convective time steps for the periodic domain (first) were 2×10^{-4} s and 3.2×10^{-4} s respectively. The same for the main domain (second) were 3.4×10^{-5} s and 1.6×10^{-4} s respectively. The overall calculation time step is determined by the second problem and it is 2.6×10^{-5} s. This calculation was 2.6 times faster than the other two due to the structured nature of the grid. The overall time step for the other two cases of mixing vanes and the square grid with mixing vanes was 1×10^{-5} s. The simulation was continued for 5.69 s physical time. The time required for 1 flow traversal was 0.2688/0.298=0.9 s. Statistics were averaged from 0.5 s to 5.69 s ,i.e., $\approx$ 5.8 flow traversals. Velocity data was stored at every 100 time steps, pressure at every 10 time steps and integrated pressure force on ring surfaces at every 1000 time steps. These were post-processed with Matlab. The surface area, friction drag and friction velocity for each boundary are printed in Table 4.6.

Boundary	Surface area (m^2)	Friction drag (N)	Friction velocity ($m^3.s^{-2}$)
Inner wall	2.27×10^{-2}	1.03×10^{-2}	2.13×10^{-2}
Outer wall	4.75×10^{-2}	1.84×10^{-2}	1.97×10^{-2}
Circular grid	3.30×10^{-2}	1.96×10^{-2}	2.44×10^{-2}

Table 4.6: Friction velocities (CG case)

4.4.3 Case of square grid with mixing vanes (SQ)

The domain of 36.1 million elements was divided into 1280 parts, i.e., ≈ 28200 elements per part. Empty parts were created corresponding to the periodic domain so that it has 1280 parts and a coupled simulation was done using TrioCFD. It was run for 11 days and 11 hours on 1280 cores (thin nodes) of Curie, which is equal to 352000 hours or 14667 CPU days. Adding it to the initial coarse mesh simulation makes it 14686 CPU days. The diffusive and convective time steps for the periodic domain (first) were 2×10^{-4} s and 3×10^{-4} s respectively. The same for the main domain (second) were 1.2×10^{-5} s and 6.5×10^{-5} s respectively. The overall calculation time step is determined by the second problem and it is 1×10^{-5} s. The simulation was continued for 4.66 s physical time. The time required for 1 flow traversal was 0.22615/0.298=0.75 s. Statistics were averaged from 0.5 s to 4.66 s which is approximately equal to 5.5 flow traversals. Velocity data was stored at every 100 time steps, pressure at every 10 time steps and integrated force on ring surfaces at every 1000 time steps. These were post-processed with Matlab. The surface area, friction drag and friction velocity for each boundary are printed in Table 4.7. y^+ field was post-processed in LATA format on the body center of each boundary element and its distribution on the outer wall is shown in Fig. 4.22.

Boundary	Surface area (m^2)	Friction drag (N)	Friction velocity $(m^3.s^{-2})$
Inner wall	1.91×10^{-2}	1.03×10^{-2}	2.32×10^{-2}
Outer wall	4.00×10^{-2}	1.81×10^{-2}	2.13×10^{-2}
Mixing vanes	2.75×10^{-4}	4.03×10^{-4}	3.83×10^{-2}
Spacer grid	1.86×10^{-2}	1.74×10^{-2}	3.06×10^{-2}

Table 4.7: Friction velocities (SQ case)

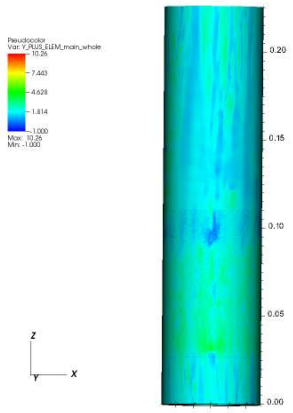

Figure 4.22: y+ distribution on outer wall (SQ case)

4.5 Analysis of the velocity field

4.5.1 Case of mixing vanes (MV)

The velocity field upstream of the vanes should be identical to that in an annular pipe without any vanes. This was verified by examining the velocity profiles at 0.66 HD upstream of the vanes ($z = 10$ mm). Figs. 4.23a and 4.23b show the mean and RMS axial velocities respectively. Segment velocity probes were put at 4 azimuthal locations 0°, 90°, 180° and 270° on the $x-y$ plane. Values were time-averaged at each of these 4 locations. Then, the values at these 4 locations were averaged to obtain the spatial average and these were plotted against the radius. The mean and RMS velocities were normalized by bulk velocity to compare with Chung et al. [2002] and Nouri et al. [1993] respectively. The profiles agree well with these standard results. Mean velocity has a peak value $1.17U_b = 0.35$ m/s

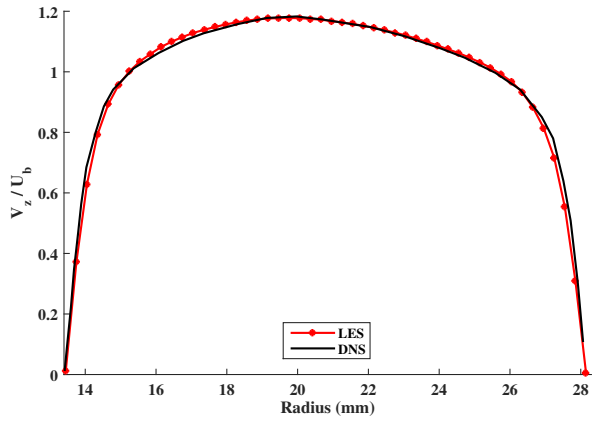

(a) Mean axial velocity

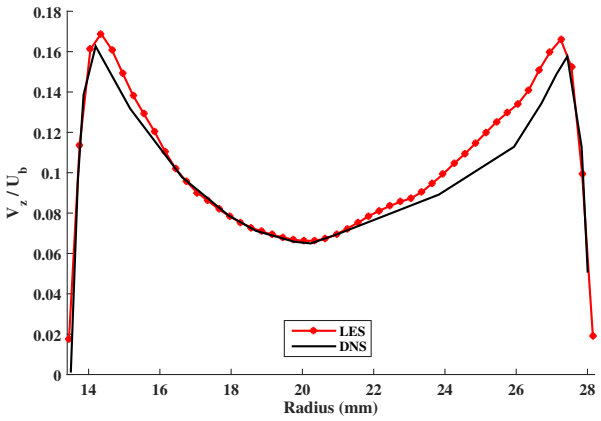

(b) RMS axial velocity

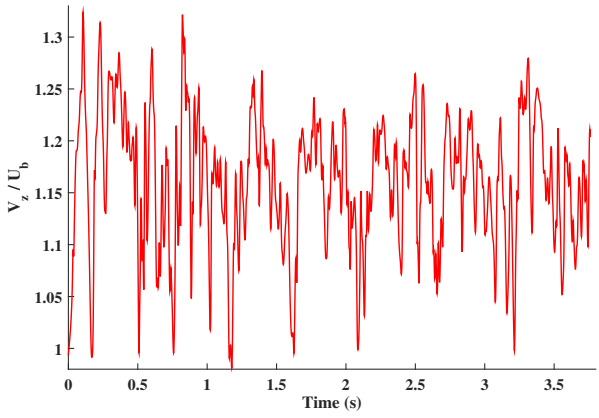

(c) Velocity fluctuation with time

Figure 4.23: Flow characteristics at -0.66 HD (MV case)

at radius 19.5 mm. This peak is shifted towards the inner wall (which is at $x = 13.4$ mm) from the mid-point of the annular gap 20.8 mm. The RMS profile peaks close to the walls and reaches a minimum close to the middle of the gap at 20.2 mm. Fig. 4.23c shows the turbulent velocity fluctuations at the midpoint of the canal at the same height -0.66 HD.

Instantaneous axial velocity was stored at the mid-point of the annular canal (radius = 20.8 mm) in line with the mixing vanes. Data was stored in probes at four positions: -0.66 HD, 0.015 HD, 1 HD and 2 HD at a frequency of 1 kHz. PSD was computed for each probe. Welch's PSD estimator [Welch, 1967] was used with a Hanning window of size 512 and the result is plotted in Fig. 4.24. For this plot, the data samples were not normalized with bulk velocity. No peaks are found in the spectra, although one can observe that the amplitude increases by a decade approximately downstream of the vanes compared to the spectrum upstream.

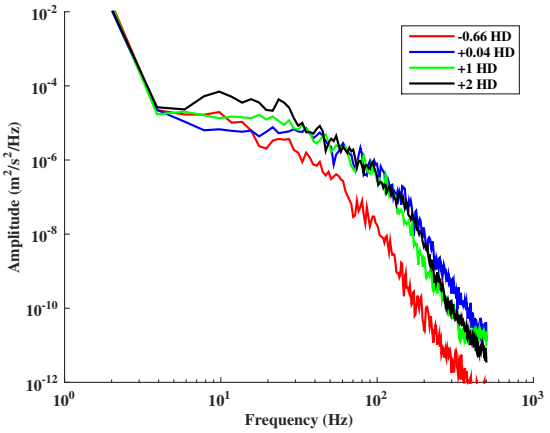

Figure 4.24: PSD of instantaneous axial velocity at the mid-point of the canal (MV case)

Segment probes were placed at two downstream locations 1 HD and 2 HD to analyze the flow characteristics. Four probes were placed at 0°, 90°, 180° and 270° at each of the two heights. A representative diagram of the four locations is shown in Fig. 4.25. Real view of the position of the mixing vanes was previously shown in Fig. 4.11. Mixing vanes were located at 0° and 180°. The simulations were done in Cartesian coordinates x, y, z. So at 0° and 180°, the azimuthal component was y and at 90° and 270°, it was x. From Figs. 4.26a and 4.27a, it can be observed that the axial component of mean velocity is significantly perturbed only downstream of the vanes at 0° and 180°. As expected, the perturbation to the flow is less at 2 HD compared to 1 HD. The perturbed profiles at 0° and 180° are asymmetric. The peak of the curves corresponding to 90° and 270° for both axial and azimuthal components is shifted towards inner wall. The azimuthal profiles give information about the

Figure 4.25: Location of 4 probes placed on azimuthal plane

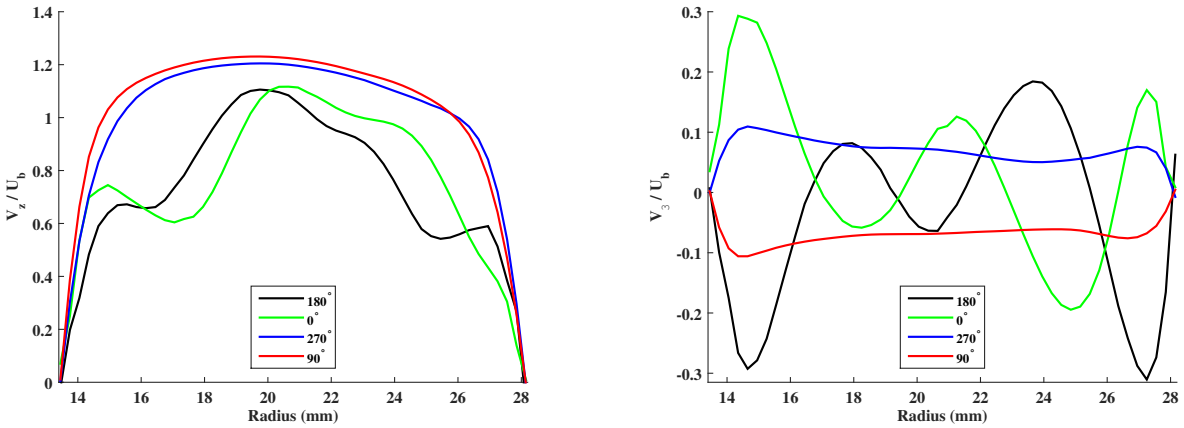

(a) Mean axial velocity

(b) Mean azimuthal velocity

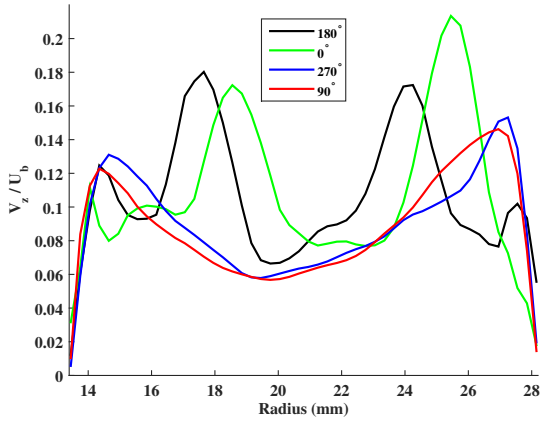

(c) RMS axial velocity

Figure 4.26: Flow characteristics at 1 HD (MV case)

azimuthal separation introduced in the flow due to the presence of the vanes. In Fig. 4.26b, the peak at 180° and 0° is 3 times higher than that at 270° and 90° (0.3 m/s compared to 0.1 m/s) whereas in Fig. 4.27b (2 HD), the same is 2 times higher. This azimuthal separation can also be seen in the mean velocity plot in Fig. 4.29c. This point is further emphasized in the vector plot in Fig. 4.28. Mean

velocity vectors on x-y plane are shown at 0.015 HD and 1 HD. The vectors are uniformly located throughout the mesh and not adapted to the mesh resolution. This azimuthal separation could also explain the peak in RMS pressure force on the inner wall at a location 1 HD downstream (8th ring) as shown in Fig. 5.3b (in Chapter 5). The profiles at 270° and 90° are smooth. At 270°, the mean azimuthal velocity is positive whereas it is negative at 90°.

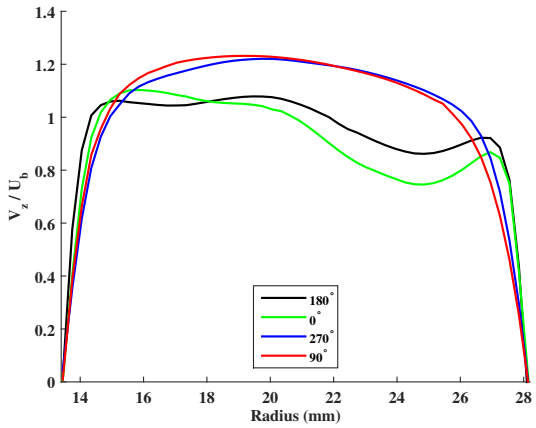

(a) Mean axial velocity

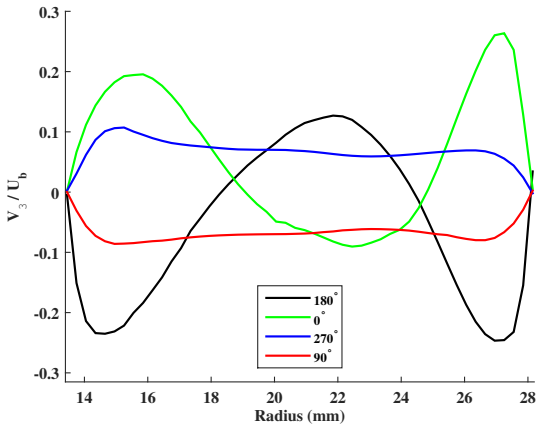

(b) Mean azimuthal velocity

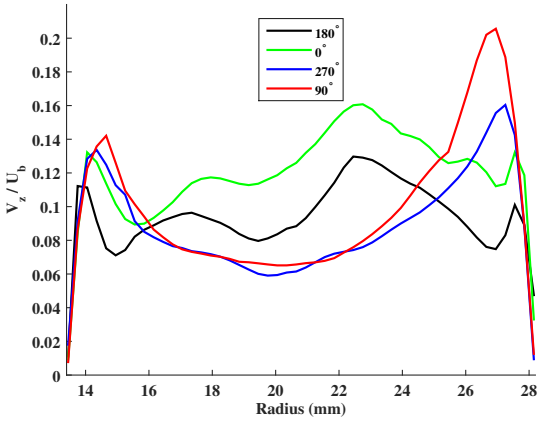

(c) RMS axial velocity

Figure 4.27: Flow characteristics at 2 HD (MV case)

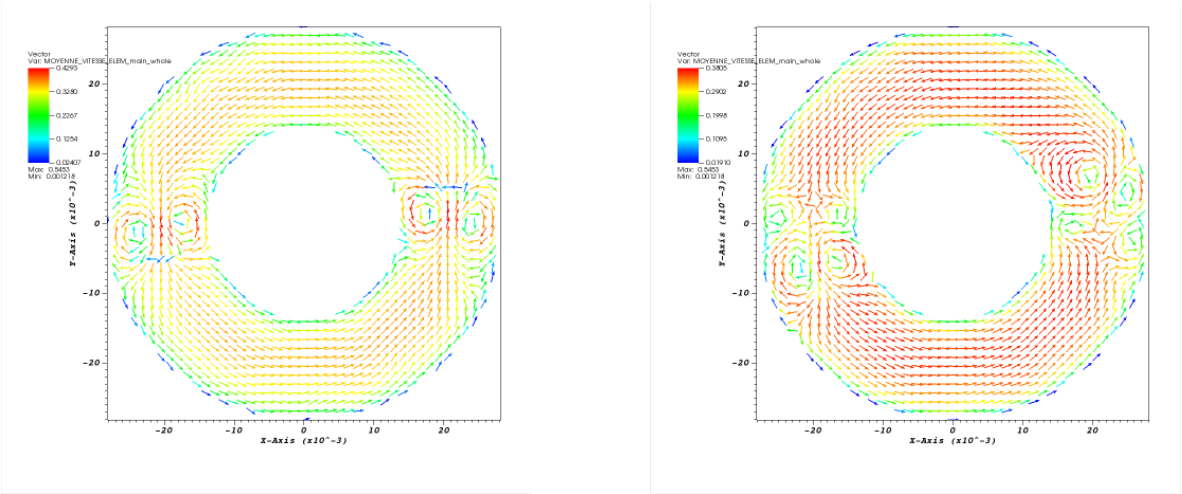

(a) at 0.015 HD

(b) at 1 HD

Figure 4.28: Vector plots of magnitude of mean velocity on x-y plane (MV case)

Fields were post-processed to LATA format and then visualized using VisIt [Childs et al., 2012] on the VisuPortal remote visualization environment of Curie. Magnitude of mean velocity on the x-y plane at 4 different values of z are shown in Fig. 4.29. Upstream of the vanes, profile is homogeneous with peak 0.35 m/s. Immediately downstream, the mean velocity varies from 0.11 - 0.43 m/s. At 1 HD, it reduces to 0.1 - 0.38 m/s. Similar pattern is observed at 1 HD, 2 HD and 3 HD. It is observed that the field was perturbed only in the vicinity of the vanes. Thus the flow field shows a deviation in the flow pattern downstream of the vanes. This is because the vanes generate strong swirls in the annular gap. In a realistic reactor situation, these swirls increase heat transfer between the fuel rod cladding (the inner wall of the pipe) and coolant (water).

Magnitude of RMS velocity on the x-y plane at 4 different values of z are shown in Fig. 4.30. This gave an idea on the effect of the vanes on the fluctuating field. At 1 HD, the maximum amplitude of RMS velocity is 0.11 m/s in the swirl region; it goes down to 0.04 m/s in the vicinity of the swirl; and in the bulk region, it is 0.03 m/s.

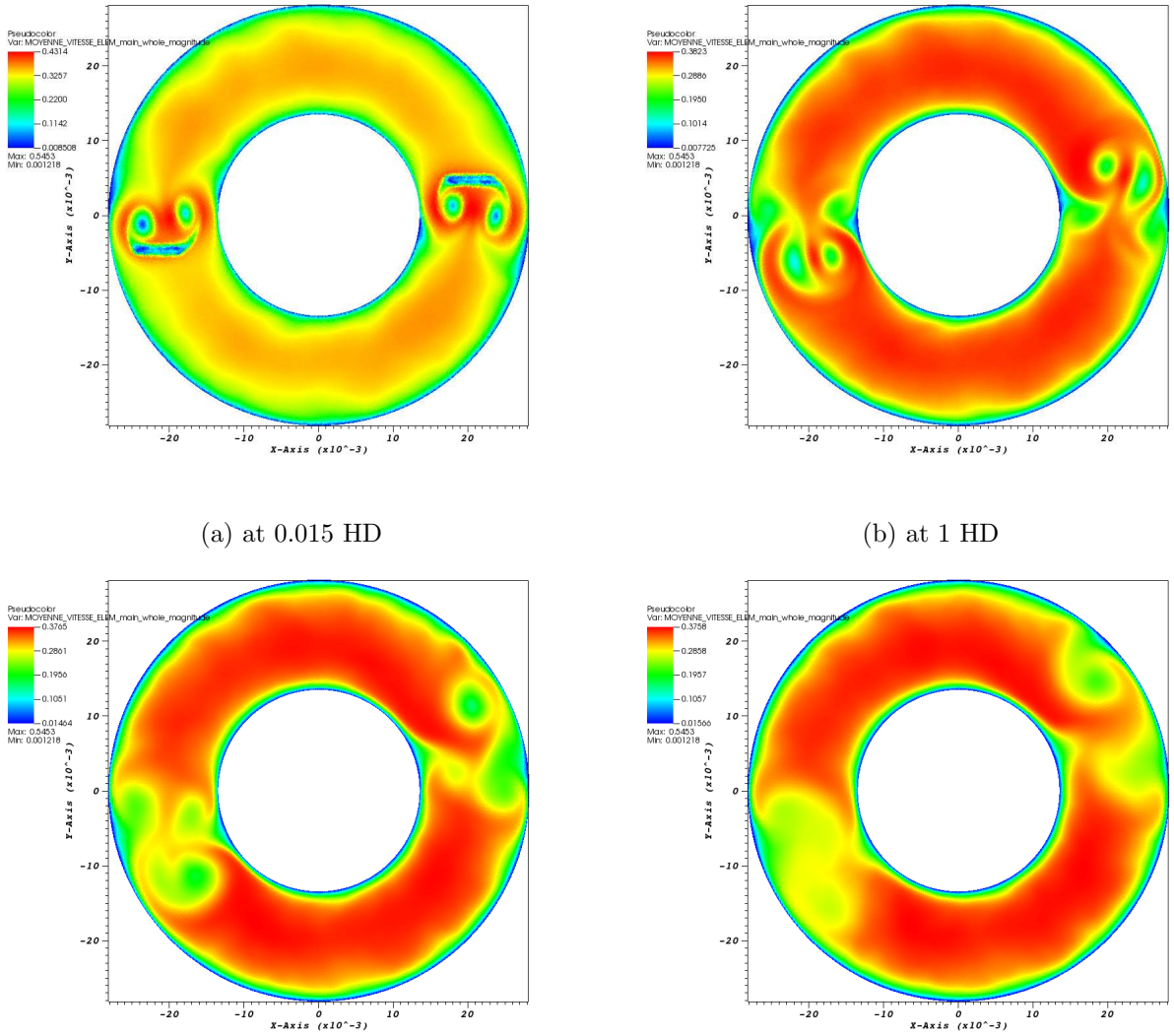

(a) at 0.015 HD

(b) at 1 HD

(c) at 2 HD

(d) at 3 HD

Figure 4.29: Magnitude of mean velocity field on x-y plane at increasing altitudes (MV case)

Magnitude of instantaneous velocity on the x-y plane at 4 different values of z are shown in Fig. 4.31. Upstream of the vanes at -0.66 HD, the peak instantaneous velocity is 0.39 m/s. The turbulent fluctuations are distributed homogeneously. Just at the exit of the vanes (0.015 HD), the velocity variation in the azimuthal direction is very large 0 - 0.45 m/s. Further downstream at 1 HD, the variation range is 0.1 - 0.4 m/s. Further downstream, the flow tends to be homogeneous with the variation ranging from 0.2 - 0.4 m/s.

The magnitude of instantaneous and RMS velocity on x-z plane are shown in Fig. 4.32a and 4.32b respectively. One observes that the RMS velocity fluctuations are asymmetric. The main reason could be the slightly oblique design of the mixing vanes (represented by *white* blocks) on both sides of the

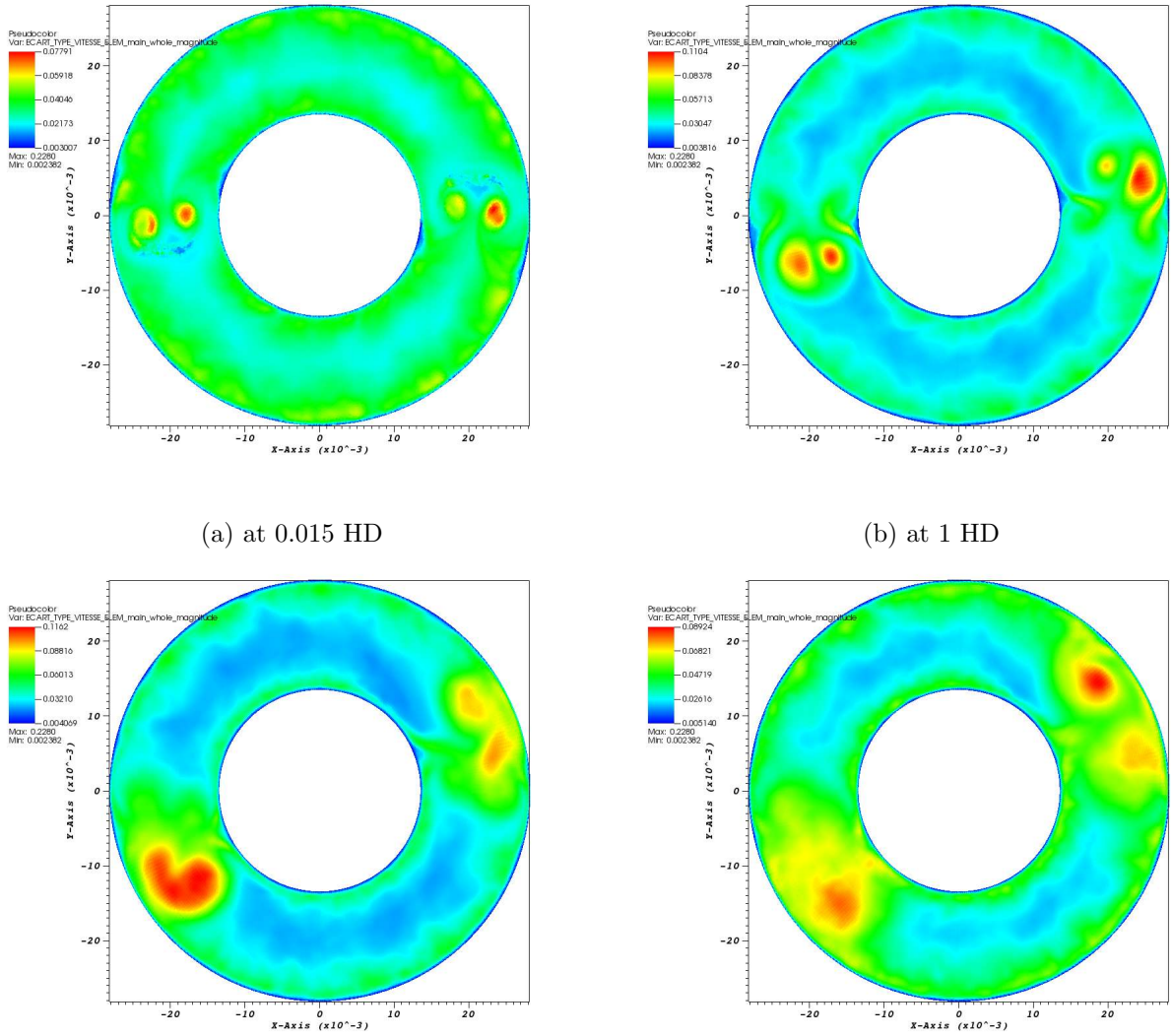

(a) at 0.015 HD

(b) at 1 HD

(c) at 2 HD

(d) at 3 HD

Figure 4.30: Magnitude of RMS velocity on x-y plane at increasing altitudes (MV case)

annular canal. This is again observed in the RMS pressure fluctuations in Fig. 5.36a. Secondly, this may be attributed to the fact that there is unstructured mesh in the vicinity of the vane which is not the same on both sides of the pipe. The unstructured region extends from -0.13 HD to +0.13 HD. Similar asymmetric pattern is observed for RMS pressure and it is further investigated in Section 5.8.

For further visualization, one can refer to the Appendix A where Figs. A.1 and A.2 show how the flow evolves with time at two downstream locations 1 HD and 2 HD on the x-y plane. Similarly, time evolution on x-z plane is shown in Fig. A.3.

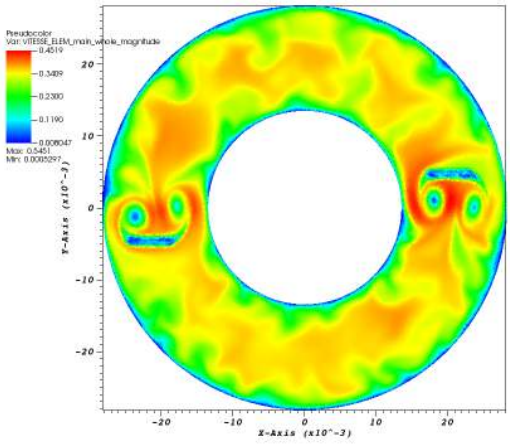

(a) at 0.015 HD

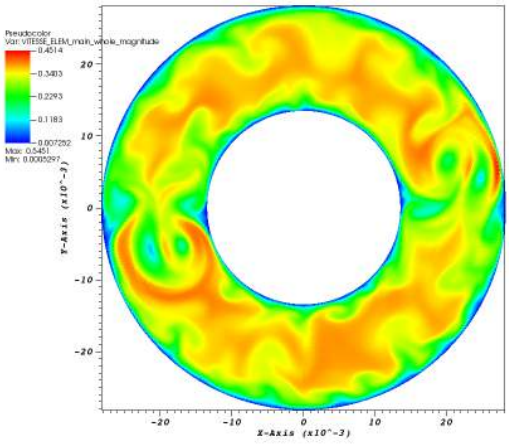

(b) at 1 HD

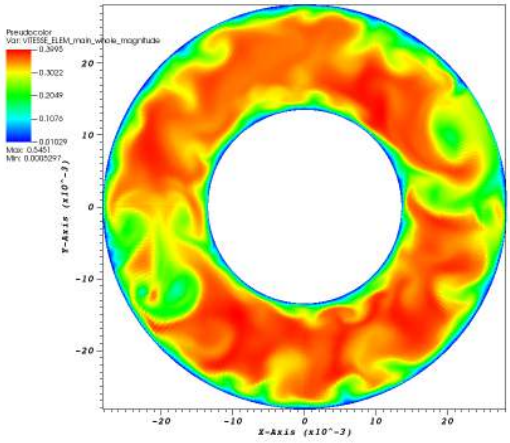

(c) at 2 HD

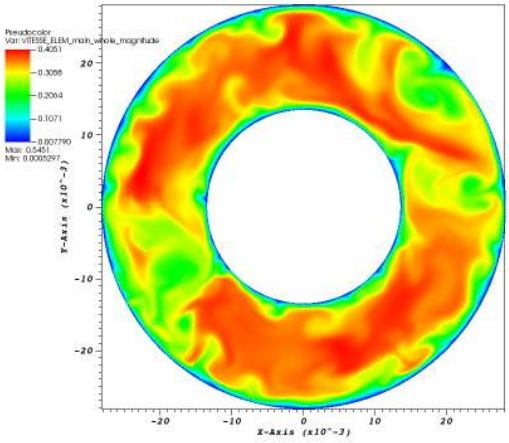

(d) at 3 HD

Figure 4.31: Magnitude of instantaneous velocity field on x-y plane at increasing altitudes (MV case)

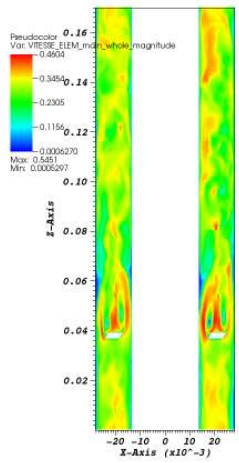

(a) Instantaneous velocity

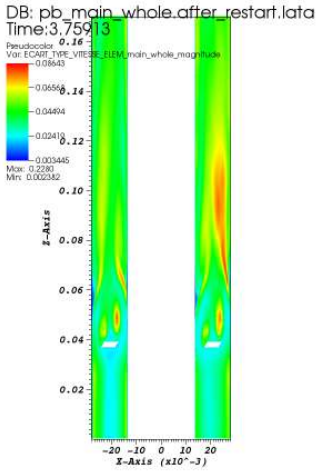

(b) RMS velocity

Figure 4.32: Magnitude of velocity on x-z plane (MV case)

4.5.2 Case of circular grid (CG)

All analysis were performed at 5 axial positions: -0.66 HD, 0.04 HD, 1 HD, 2 HD and 3 HD. The time evolution of velocity at the mid-point of the canal at these 5 positions were studied in terms of PSD. The length of the signal was 5189 and sample frequency 1 kHz. Welch's PSD estimator [Welch, 1967] was used with a Hanning window of size 512 and the results plotted in Fig. 4.33. The velocity data samples were not normalized with bulk velocity only for this plot. Due to the strong fluctuations present at 0.04 HD and 1 HD, peaks are observed at 30 Hz and 60 Hz in the spectra. Comparing the spectra downstream and at 1 HD, one observes a 1 decade increase in power due to the presence of the circular grid. At 2 HD, this difference reduces to half a decade.

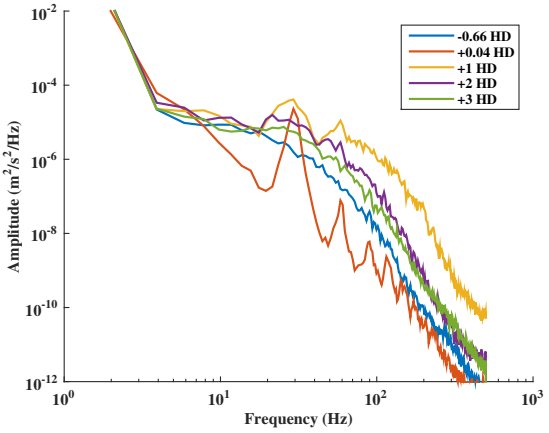

Figure 4.33: PSD of instantaneous axial velocity at mid-point of the canal (CG case)

Mean and RMS velocities on the x-z plane are shown in Figs. 4.34 and 4.35. Smooth flow is observed along the grid due to the absence of any spring or dimple-like structures. So, instead of a 4 HD long grid, a 2 HD long grid could have been used without any loss of physical information.

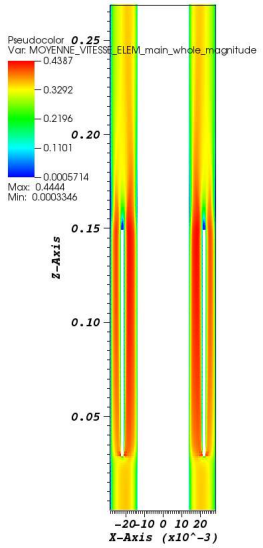

Figure 4.34: Magnitude of mean velocity on x-z plane (CG case)

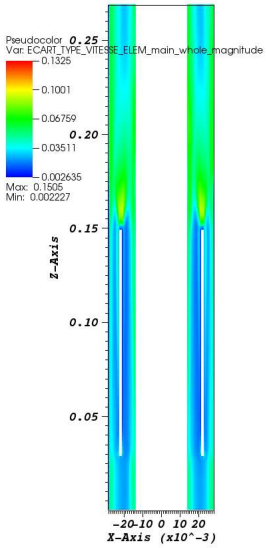

Figure 4.35: Magnitude of RMS velocity on x-z plane (CG case)

Similarly, mean and RMS velocity fields on the x-y plane at 4 different downstream positions are shown in Figs. 4.37 and 4.38 respectively. These figures complement the velocity profile behavior on the segments in Fig. 4.36a. The upstream profile has an expected behavior similar to that in the mixing vane case, i.e., peak $1.15U_b$ at 19.5 mm. This peak is slightly shifted towards the inner wall which is typical of annular pipe flow. All the downstream profiles also follow this behavior with varying magnitudes. Immediately downstream of the grid at 0.04 HD, the mean velocity reaches zero at the position of the grid. Two peaks of magnitude $1.42U_b$ and $1.32U_b$ are observed towards the inner and outer walls respectively. There is a 7% difference amongst the two peak magnitudes. Compared to the upstream profile, there is a 20% increase in the peak magnitude. At 1 HD, the profile has a dip in the region of the grid and two peaks at $1.25U_b$ and $1.12U_b$ towards the inner and outer walls respectively; magnitude difference being 10%. The same behavior could be seen in Fig. 4.37b. The peak magnitude decreases as we go downstream from 0.04 HD to 3 HD. But it is still higher than the magnitude upstream. The RMS velocity profiles on the same segments are plotted in Fig. 4.36b.

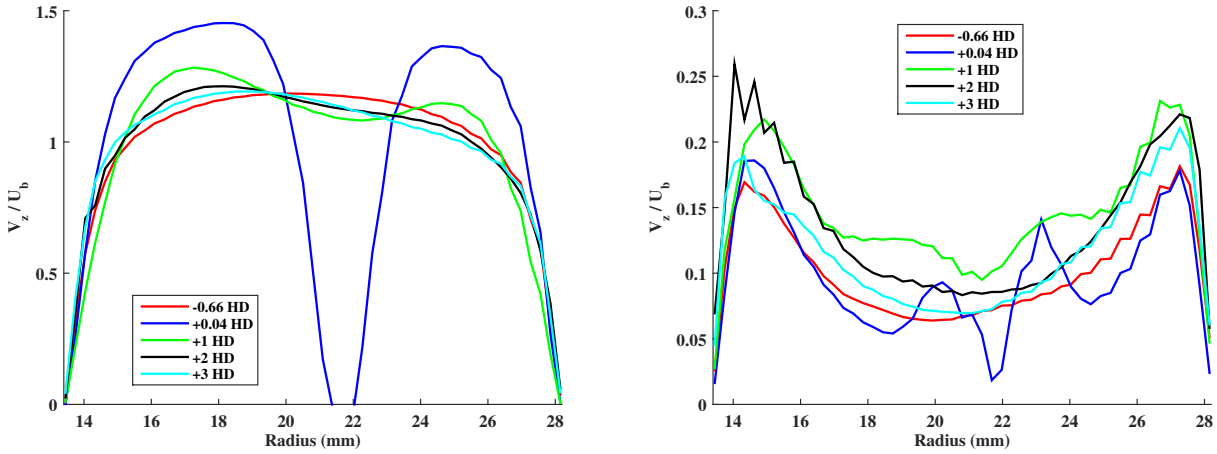

(a) Mean axial velocity

(b) RMS axial velocity

Figure 4.36: Flow characteristics along the length of the pipe (CG case)

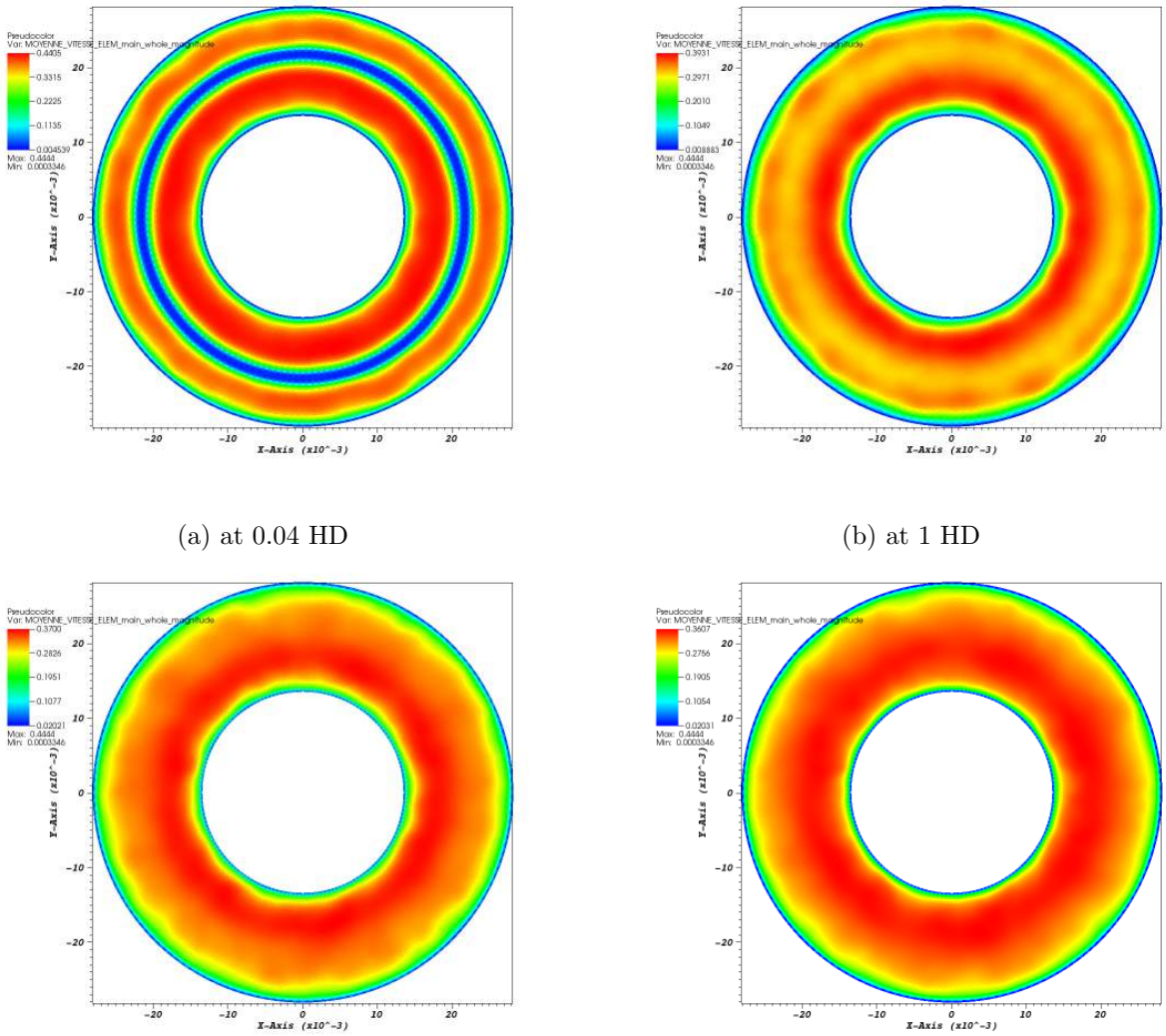

(a) at 0.04 HD

(b) at 1 HD

(c) at 2 HD

(d) at 3 HD

Figure 4.37: Magnitude of mean velocity on x-y plane at increasing altitudes (CG case)

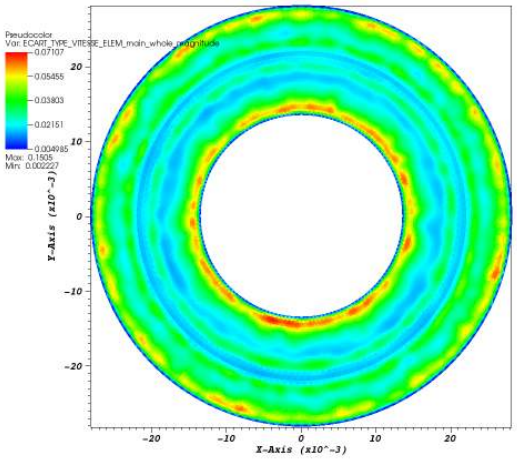

(a) at 0.04 HD

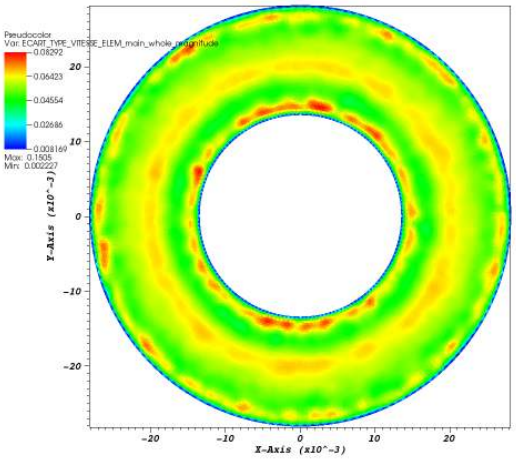

(b) at 1 HD

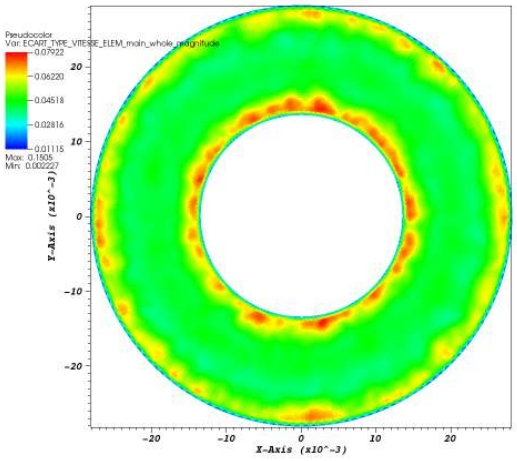

(c) at 2 HD

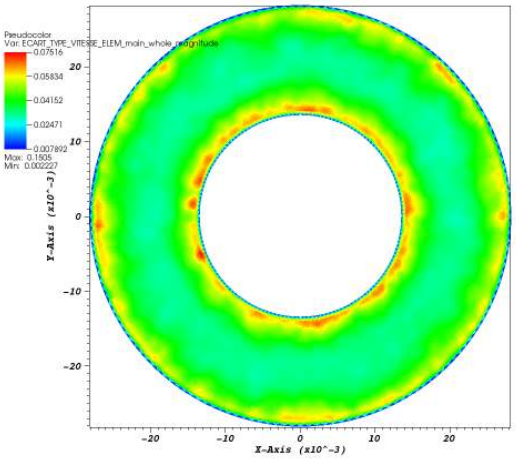

(d) at 3 HD

Figure 4.38: Magnitude of RMS velocity on x-y plane at increasing altitudes (CG case)

4.5.3 Case of square grid with mixing vanes (SQ)

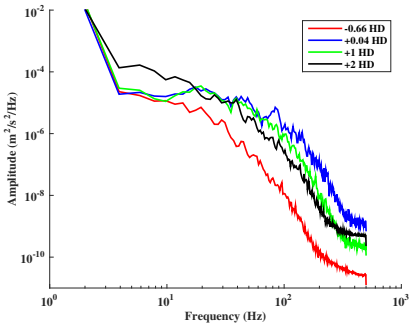

(a) R=20.8 mm (Probe in line with MV)

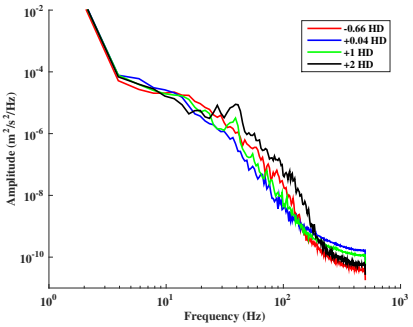

(b) R=16.4 mm (Probe out of line with MV)

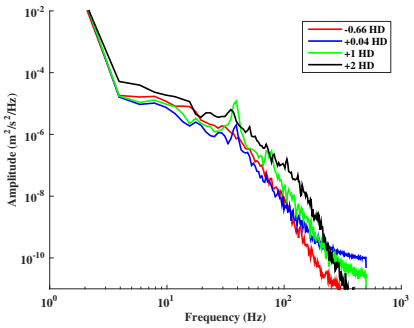

(c) R=19.3 mm (Probe out of line with MV)

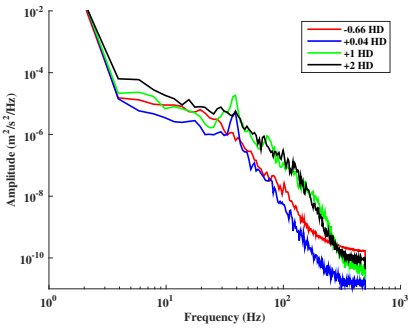

(d) R=20.8 mm (Probe out of line with MV)

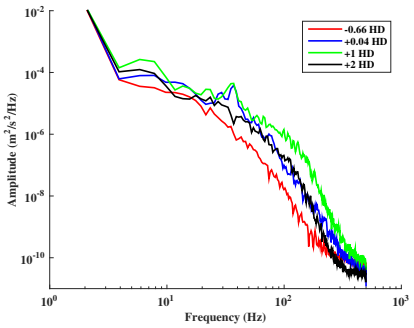

(e) R=23.7 mm (Probe out of line with MV)

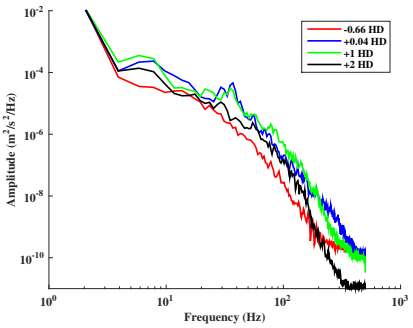

(f) R=24.3 mm (Probe out of line with MV)

Figure 4.39: PSD of instantaneous axial velocity at radial positions denoted by R (SQ case)

PSD of instantaneous axial velocity was calculated at different positions to study the velocity spectra. Data was examined for 4 positions: -0.66 HD, 0.015 HD, 1 HD and 2 HD at a frequency of 1 kHz. Welch's PSD was computed with a Hanning window of size 512 and the result is plotted in Figs. 4.39a to 4.39f. No significant peaks are observed on a probe placed in line with the MV. However, for a probe placed out of line of the MV (with the spacer grid in upstream or downstream as the case may be), one observes a frequency peak at 38 Hz. Velocity spectra was examined at different radial positions R = 16.4 mm, 19.3 mm, 20.8 mm (mid-point), 23.7 mm and 24.3 mm. It should be noted that the

spacer grid was located near the outer wall (radial coordinates from 26.35 mm to 27.55 mm). It is interesting to note that in case of the probe in line with MV, the spectra upstream and downstream are separated by one decade. But in the case of the probe out of line with MV, the spectra are more merged together.

Figure 4.41: Color coding of the 4 probes placed on azimuthal plane (SQ case)

Figure 4.40: View of mixing vanes (RED) and spacer grid (GREEN) from the top (SQ case)

Next, velocity profiles were examined at two downstream locations 1 HD and 2 HD. Four segment probes were placed at 0°, 90°, 180° and 270° at each of these two locations. The relative position of the mixing vanes and spacer grid is shown in Fig. 4.40. Mixing vanes were located upstream of the probes at 0° and 180°. The position of the four probes and their color codes are shown in Fig. 4.41. The time-averaged axial and azimuthal velocities at 1 HD and 2 HD respectively are shown in Figs. 4.42a, 4.42b, 4.43a and 4.43b.

In the axial velocity profiles, a pronounced dip is observed near the outer wall. This can be explained by the presence of the grid corners as seen in Fig. 4.40. At 1 HD, the peak axial velocity at 90° and 270° is $1.35U_b = 0.4m/s$ at 19.2 mm. Near the outer wall at 27 mm, it drops 50% to $0.7U_b$. Only the effect of the grid can be observed here. This is around 15% higher than the peak value $1.17U_b$ at the same position upstream. Radial extent of the vanes is 18.55 mm to 25.25 mm. Probes at 0° and 180° illustrate an additional effect of vanes; leading to a 15% decrease in peak value from $1.35U_b$ to $1.15U_b$. At 2 HD, the peak axial velocity at 19.2 mm at 90° and 270° goes down by 5% to $1.28U_b$.

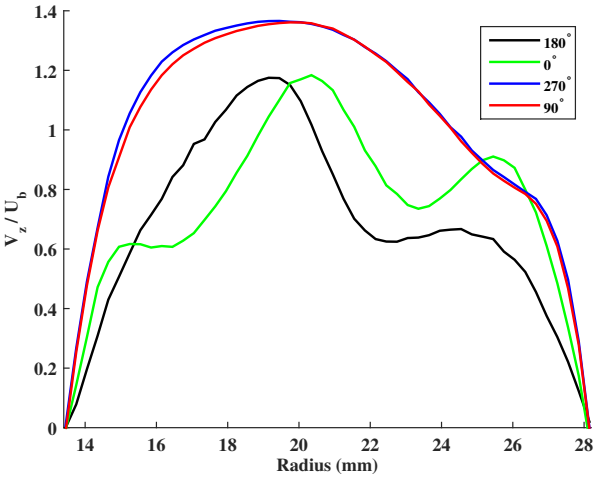

(a) Mean axial velocity

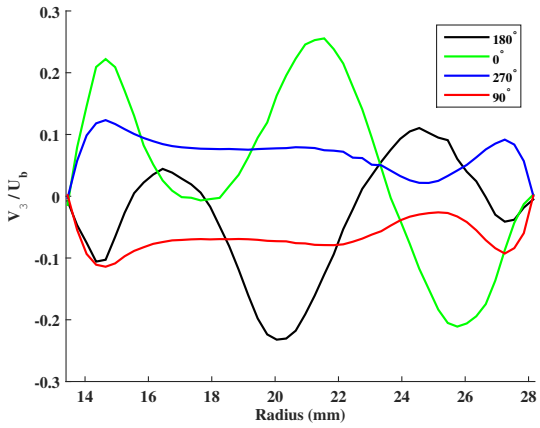

(b) Mean azimuthal velocity

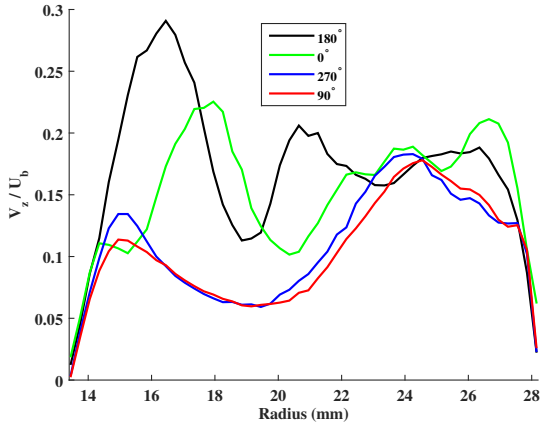

(c) RMS axial velocity

Figure 4.42: Flow characteristics at 1 HD (SQ case)

In the case of azimuthal velocity profiles, the behavior is symmetric at 90° and 270° with dips observed at 25 mm which can be attributed to the presence of the spacer grid. However, the profiles at 0° and 180° are not symmetric. This asymmetry is due to the configuration and not due to insufficient simulation time because the ones at 90° and 270° are symmetric. The azimuthal separation discussed above can be visualized in the mean velocity vector plots in Fig. 4.44. The vectors are uniformly located throughout the mesh and not adapted to the mesh resolution.

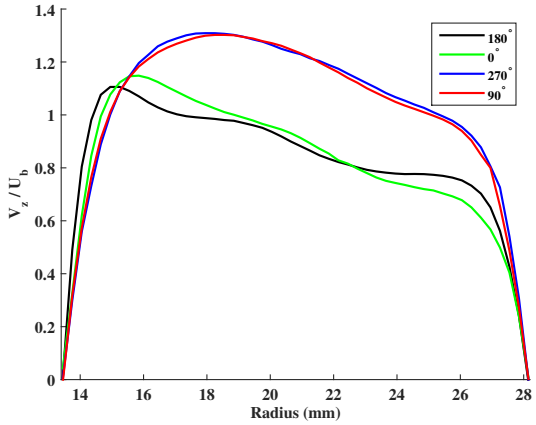

(a) Mean axial velocity

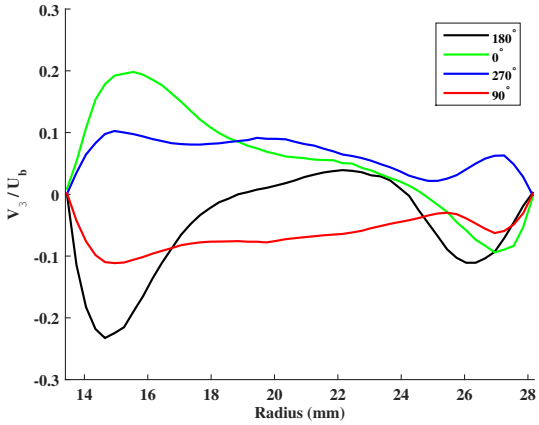

(b) Mean azimuthal velocity

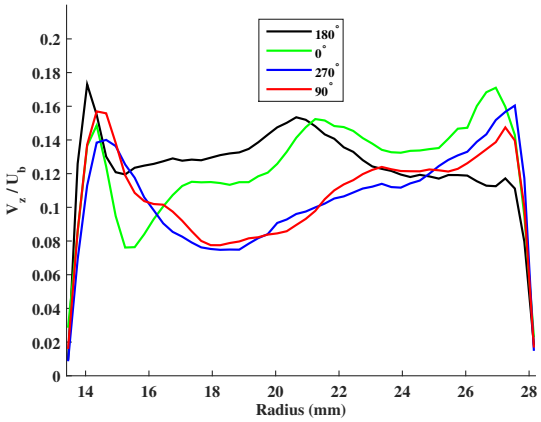

(c) RMS axial velocity

Figure 4.43: Flow characteristics at 2 HD (SQ case)

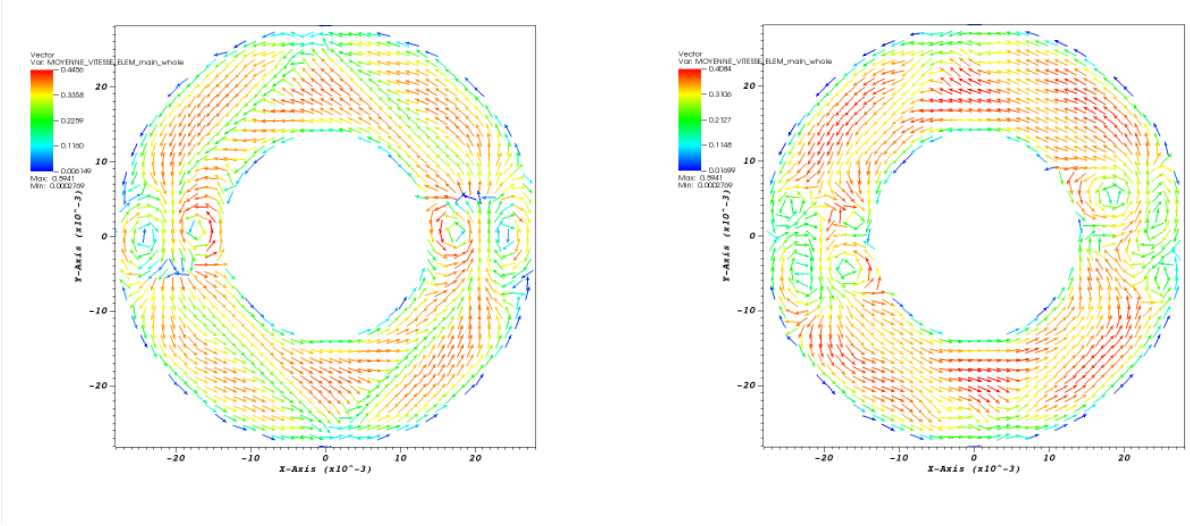

(a) at 0.015 HD

(b) at 1 HD

Figure 4.44: Mean velocity vector plots on x-y plane (SQ case)

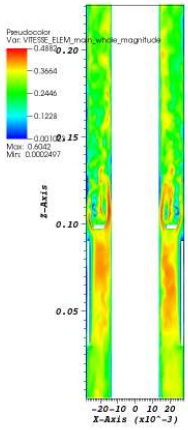

Figure 4.45: Magnitude of instantaneous velocity on x-z plane (SQ case)

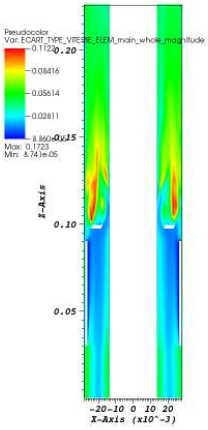

Figure 4.46: Magnitude of RMS velocity on x-z plane (SQ case)

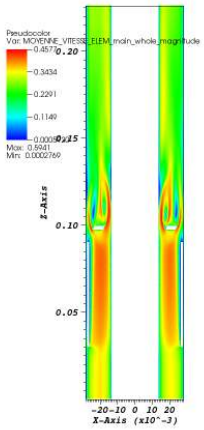

Figure 4.47: Magnitude of mean velocity on x-z plane (SQ case)

The instantaneous, RMS and mean velocity (their magnitudes) on the x-z plane are shown in Figs. 4.45, 4.46 and 4.47 respectively. Magnitude of mean and RMS velocity fields on the x-y plane at 4 different downstream positions are shown in Figs. 4.48 and 4.49 respectively. The RMS plot at 0.015 HD clearly delineates the regions downstream of the vanes and grid. Strong, symmetric swirls with peak fluctuation 0.11 m/s are observed downstream of the vanes. At 1 HD and 2 HD, the fluctuation reduces slightly and the swirl on the right is increasingly shifted upwards and the swirl on the left is increasingly shifted downwards. This is due to the 30° inclination of the vanes. Similarly, magnitude of instantaneous velocity at the same positions are shown in Fig. 4.50.

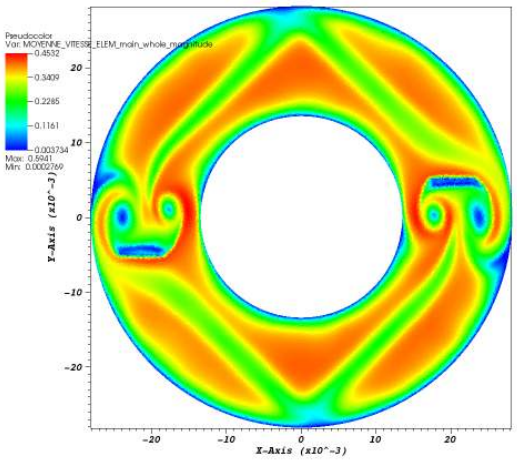

(a) at 0.015 HD

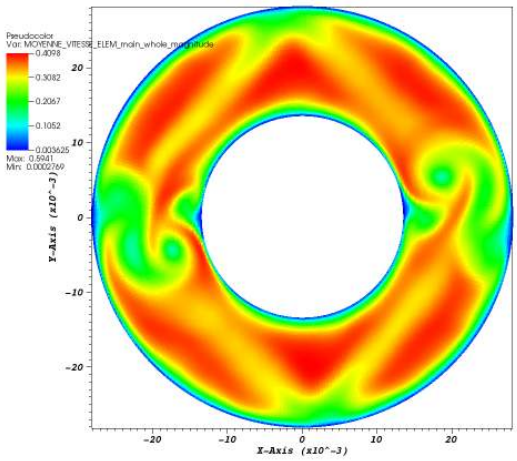

(b) at 1 HD

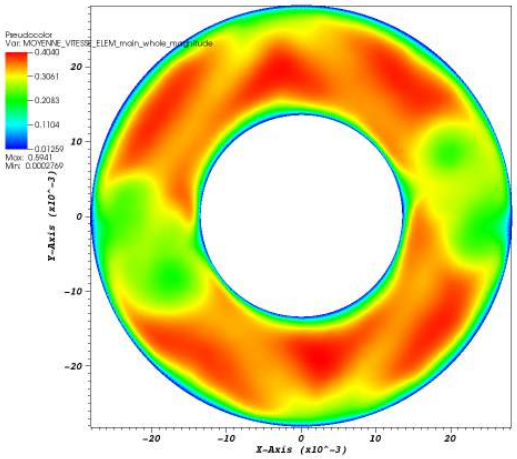

(c) at 2 HD

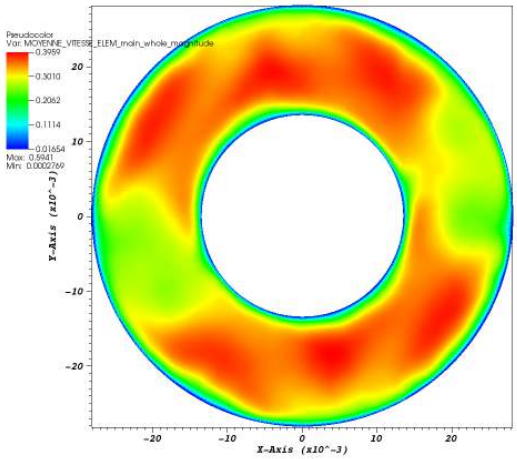

(d) at 3 HD

Figure 4.48: Magnitude of mean velocity on x-y plane at increasing altitudes (SQ case)

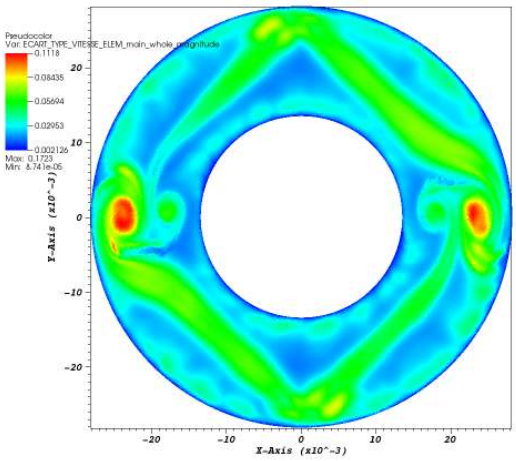

(a) at 0.015 HD

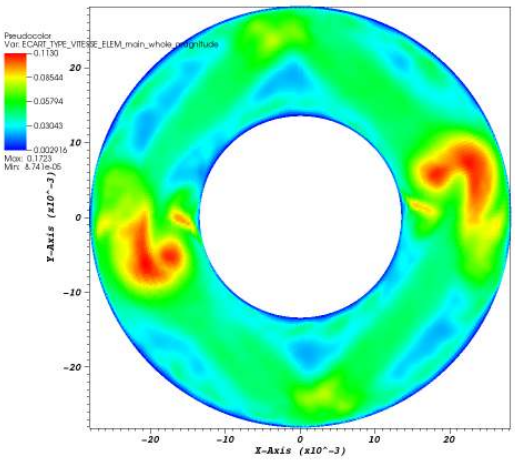

(b) at 1 HD

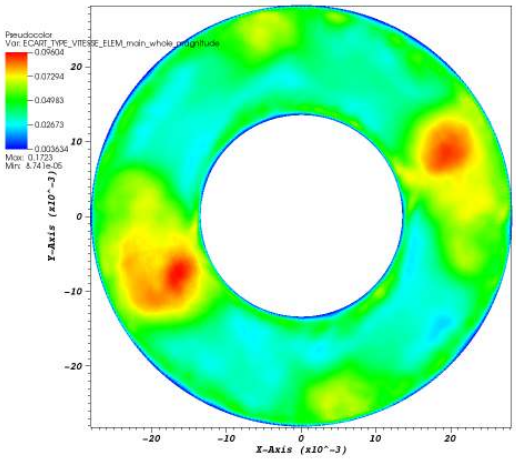

(c) at 2 HD

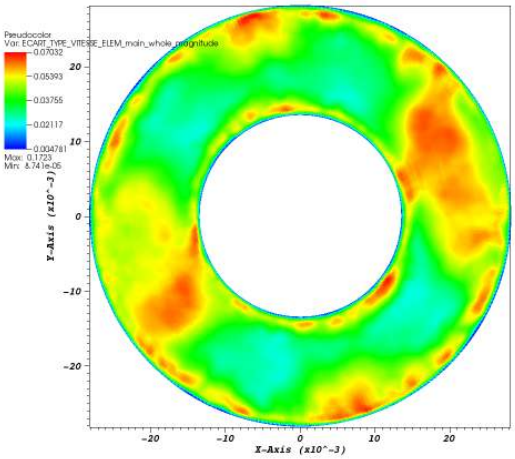

(d) at 3 HD

Figure 4.49: Magnitude of RMS velocity on x-y plane at increasing altitudes (SQ case)

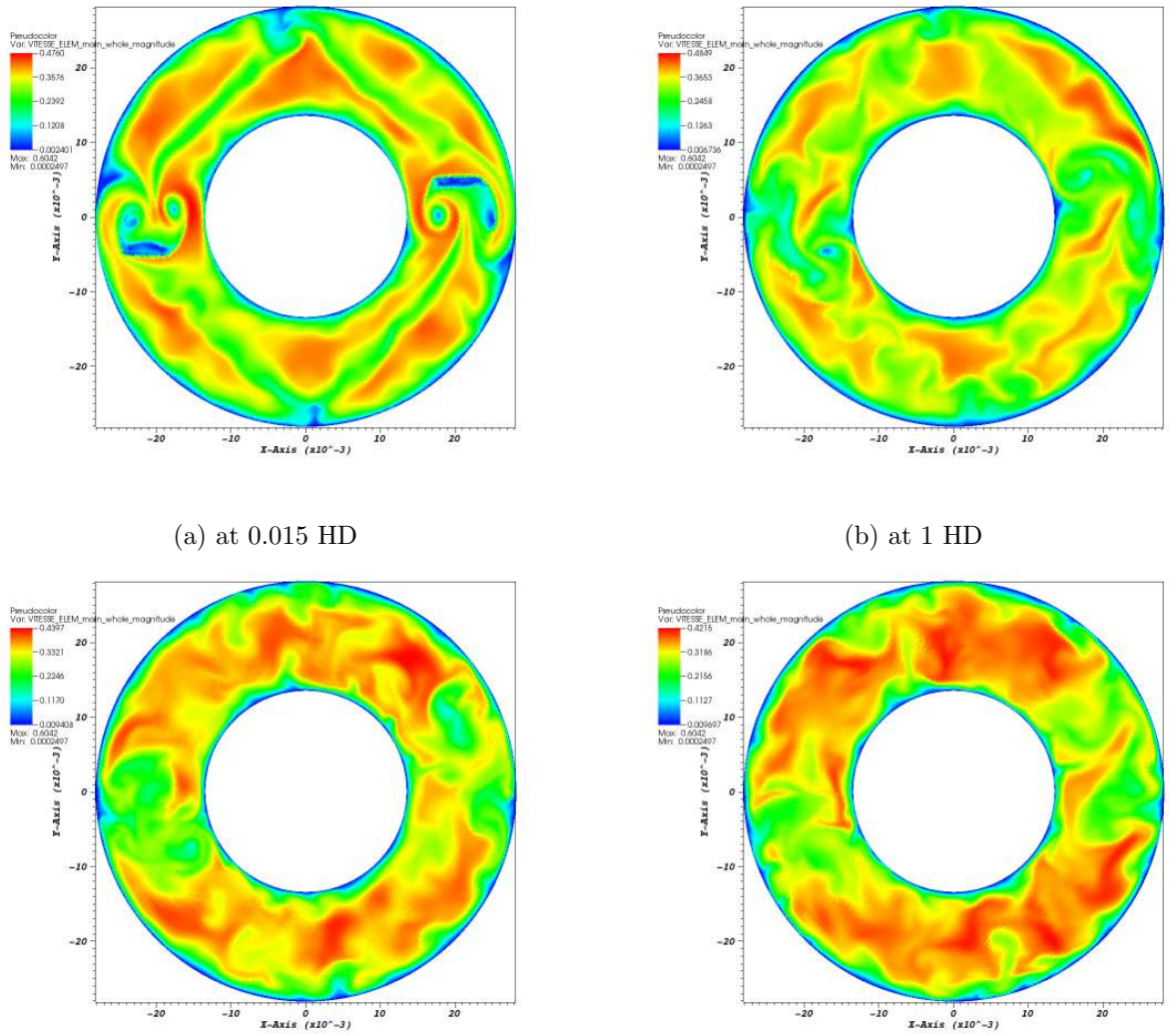

(a) at 0.015 HD

(b) at 1 HD

(c) at 2 HD

(d) at 3 HD

Figure 4.50: Magnitude of instantaneous velocity on x-y plane at increasing altitudes (SQ case)

4.6 Conclusion

In this chapter, three different geometrical obstacles were introduced inside the annular pipe, namely, mixing vanes (MV), circular grid (CG) and a square grid with mixing vanes (SQ). A hybrid mesh was used for the MV and SQ cases: unstructured mesh around the vanes and structured mesh in the rest of the domain. A fully structured mesh was used for the CG case due to its symmetry. Table 4.8 presents a comparison of the y^+ mesh resolution and CPU time required for each simulation.

Case	y^+ (inner wall)	y^+ (outer wall)	Cores	Physical time (days)	CPU time (hours)
MV	3.5	3.2	670	8	122408
CG	3.2	2.9	710	6	94898
SQ	3.5	3.2	1280	12	352468

Table 4.8: Comparison of y^+ and CPU time for MV, CG and SQ cases

The complex swirling flow was analyzed in detail to understand the flow structures in these different configurations. In the MV case, swirling flow was observed close to the vanes whereas it was more or less homogeneous in the rest of the domain. In the SQ case, in addition to the swirl due to the vanes, acceleration of flow was observed on either side of the grid due to the presence of the grid. In the CG case, symmetric flow pattern was observed due to the inherent symmetry of the design.

A comparison of mean and RMS axial velocity profile at 1 HD and 2 HD for each case is shown from Figs. 4.51a to 4.54b. By comparing the probes in line with MV and out of line with MV, it is clear that the mixing vanes introduce the larger fluctuations. From Figs. 4.51b and 4.52b (probes out of line with MV), it is seen that the presence of the square grid near the inner wall accelerates the flow in that region and decelerates it near the outer wall due to conservation of mass. From these probes, it seems that the SQ case is a combination of the MV and CG cases. From the probes in line with the MV (Figs.4.53a and 4.54a), it is observed that the fluctuations are stronger at 1 HD downstream compared to 2 HD.

A look at the azimuthal component of mean velocity shows strong destabilization of the flow (Figs. 4.26b, 4.27b, 4.42b, 4.43b). Positive and negative velocity components were observed for the probes in line with MV, whereas for probes out of line with MV, the mean azimuthal velocity components were more or less uniform.

Looking at the velocity spectra for the three cases at different upstream and downstream locations, frequency peaks were observed at 30 Hz and 38 Hz for CG and SQ cases respectively. These peaks were observed for probes out of line with the vanes and not for the ones in line with the vanes. Also, no peak was observed for MV case. These frequencies could be related to the Strouhal number Strouhal [1878] used to describe oscillating flows. This has been further discussed in the next chapter.

The analyses presented in this chapter for the mixing vane (MV) case were published by Bhattacharjee et al. [2015b].

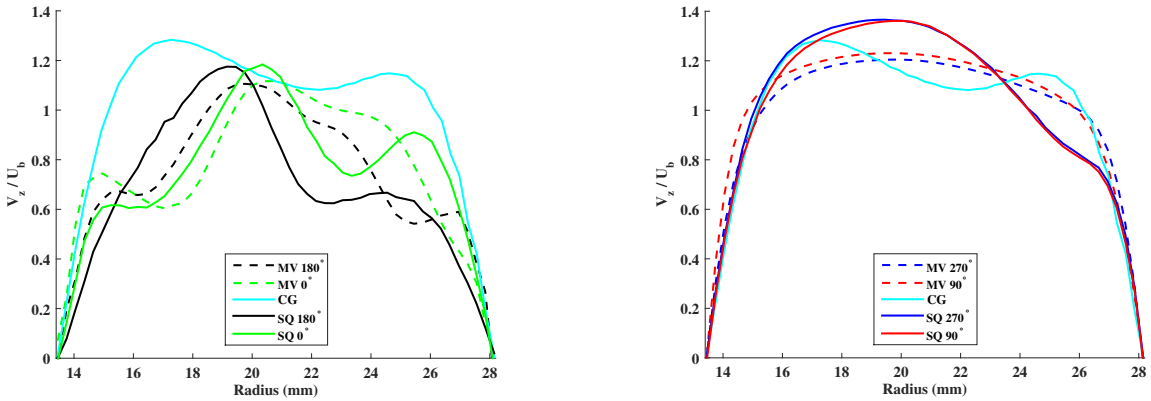

(a) Probes in line with MV

(b) Probes out of line with MV

Figure 4.51: Comparison of mean axial velocity of the 3 cases at 1 HD

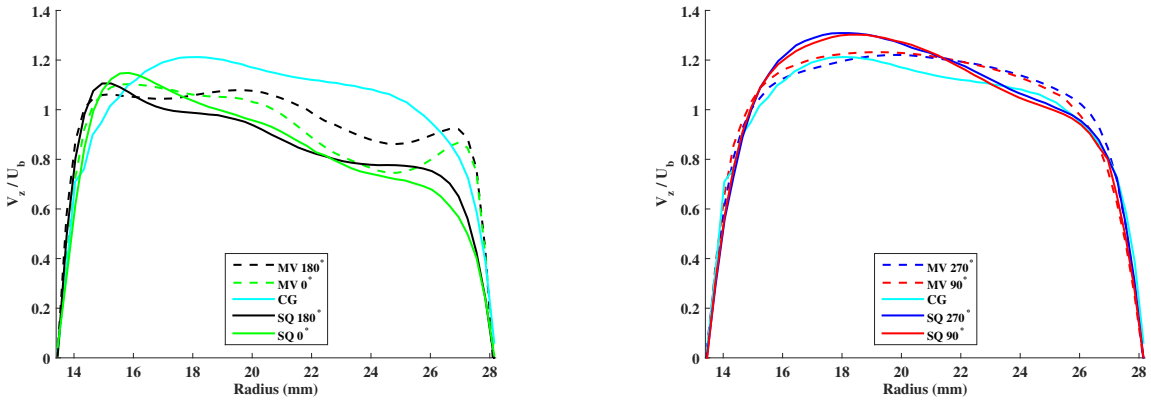

(a) Probes in line with MV

(b) Probes out of line with MV

Figure 4.52: Comparison of mean axial velocity of the 3 cases at 2 HD

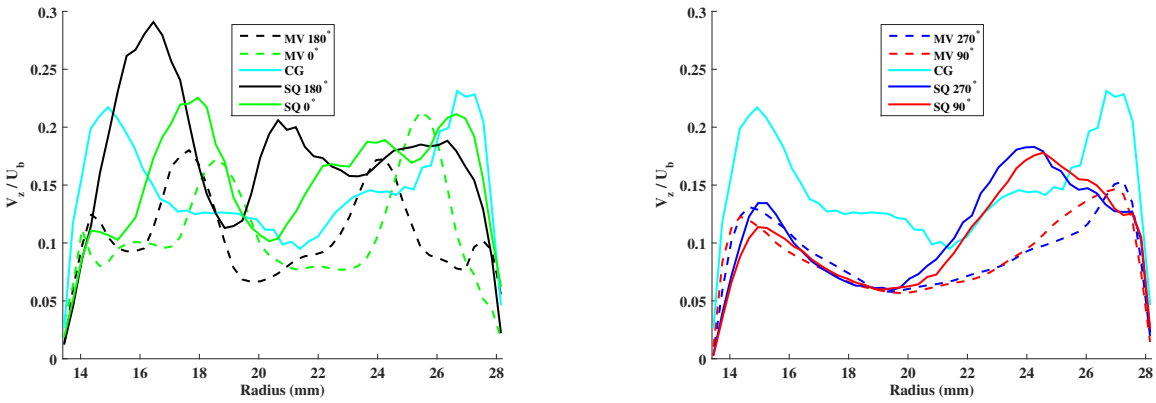

(a) Probes in line with MV

(b) Probes out of line with MV

Figure 4.53: Comparison of RMS axial velocity of the 3 cases at 1 HD

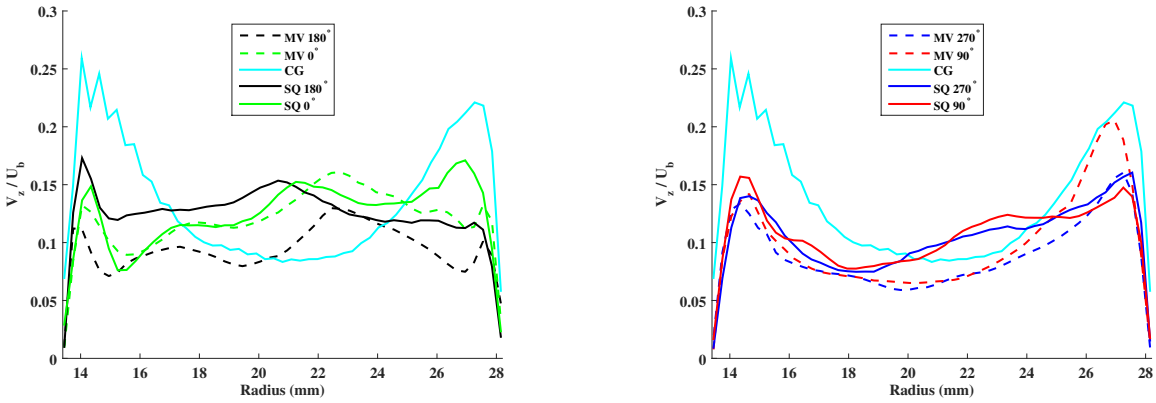

(a) Probes in line with MV

(b) Probes out of line with MV

Figure 4.54: Comparison of RMS axial velocity of the 3 cases at 2 HD

Chapter 5

Wall Pressure Field

5.1 Introduction

This chapter is dedicated to the analysis of the pressure field on the inner wall of the annular pipe. This fluctuating pressure field is likely to vibrate the fuel rod. In total, five cases are studied. For the pipe without any geometrical obstacles, two simulation cases ($Re_D = 8900$) were chosen from the ones discussed in Chapter 3: fine mesh case F1 (denoted as PF in this chapter) and a coarse mesh case C1 (denoted as PC in this chapter). The three cases MV, CG and SQ presented in Chapter 4 were also analyzed. All the simulations reported here were performed at $Re_D = 8900$. Firstly, the lateral fluid forces acting on the inner wall were analyzed for each case. Next, two-point spatial correlation was plotted. Proper Orthogonal Decomposition (POD) was applied to the pressure signal to get an idea about the spatial behavior of the system. This is followed by spectral analysis of wall pressure and finally, the simulations are compared with experimental data from CALIFS ($Re_D = 58500$ and above) and classical semi-empirical models.

5.2 Lateral fluid forces on the wall

To analyze the lateral fluid forces, the inner wall of the pipe was divided into 17, 27 and 23 equal rings of height 10 mm (one-third of a hydraulic diameter HD) respectively for the 3 cases MV, CG, SQ as shown in Figs. 5.1 and 5.2. TrioCFD allows a user to extract a surface mesh from a volume mesh.

Figure 5.1: Decomposition of inner wall into 17 rings (MV case)

Figure 5.2: Decomposition of inner wall into 23 rings (SQ case)

Surface meshes were extracted corresponding to the rings and created on the inner wall boundary. The x- and y- pressure force time histories were then time-averaged to obtain the mean and RMS force on each ring. The fluctuating pressure force provides a reasonable representation of the forces acting on the inner wall. Figs. 5.3 and 5.4 plot the x and y components respectively of pressure force corresponding to mid-point of each ring for the mixing vanes case. The vertical dotted lines represent the axial bounds of the mixing vanes. A decrease in RMS pressure force was observed by Caraghiaur et al. [2009] and Nourgaliev et al. [2013] downstream of the vanes as no energy production takes place there. However, it should be noted that the domain of Nourgaliev et al. [2013] had a downstream section 300 mm whereas in our case, it is only 120 mm (=4 HD). A clear decay of RMS pressure force is observed only in the case of circular grid. In the other two cases, it decreases even though the profile is not as smooth. The reason could be that the domain length downstream is not sufficient to observe the decreasing behavior of RMS force.

In the MV case (Figs. 5.3 and 5.4), the x-component of RMS fluctuation peaks at the 8th ring which is $\approx$ 1 HD downstream of the vanes. This peak is higher at 1 HD than at 2 HD. This behavior agrees well with the higher azimuthal separation observed at 1 HD than at 2 HD in the mean azimuthal velocity profiles presented previously in Chapter 4 (Figs. 4.26b and 4.27b). For the y-component, the RMS peak is observed at the 6th ring. The mean force plots show that the maximum force act on the wall near the vanes.

In the CG case, Figs. 5.5 and 5.6 plot the mean and RMS of x and y components of pressure force respectively corresponding to the mid-point of each ring. Vertical dotted lines represent the axial bounds of the circular grid. Due to the symmetry of the structure, the x and y components overlap. The mean force is of the order of 1×10^{-5} N which is one decade less than that observed for the mixing vanes or the square grid case. From the RMS curves, one observes a peak in fluctuation at the 4th ring (z=30-40 mm) which is the entrance to the circular grid. The second peak occurs at the 17th ring (around 1 HD). Further downstream, the RMS force decreases.

Finally, in the SQ case, Fig. 5.8 shows the x and y components of pressure force respectively corresponding to the mid-point of each ring. From the mean curves, it is clear that the maximum force on the wall occurs in the region where the vanes end. From the RMS curves, one observes a peak in fluctuation at the 4th ring (z=30-40 mm) which is the entrance of spacer grid. The second peak occurs at around 1 HD (for x-component, the peak is from 135-155 mm, i.e., 14th-16th ring and for y-component, the peak is from 125-135 mm, i.e., 12th-13th ring).

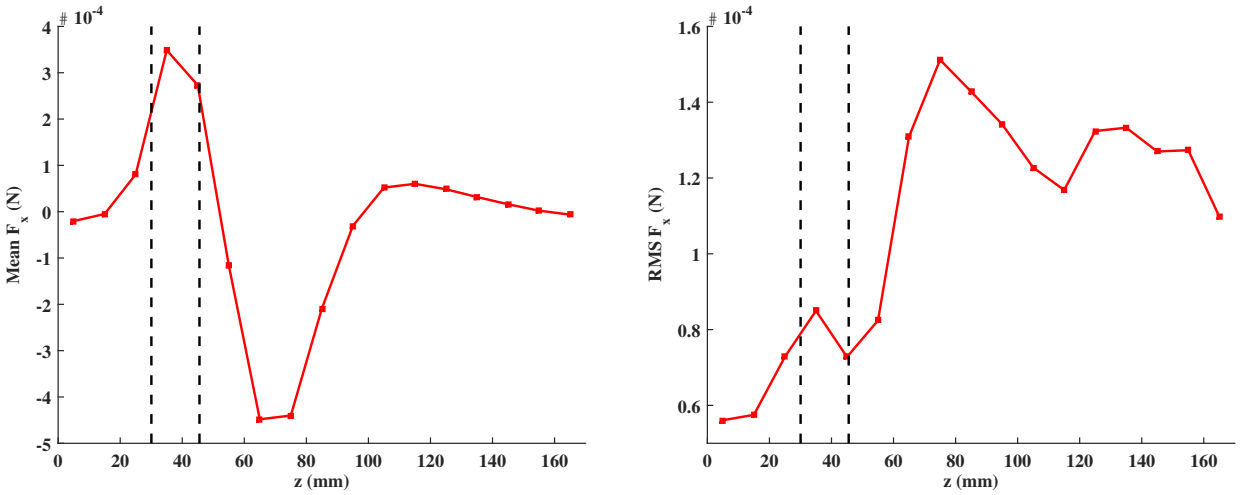

(a) (b)

Figure 5.3: Mean and RMS of x- pressure force respectively on inner wall (MV case)

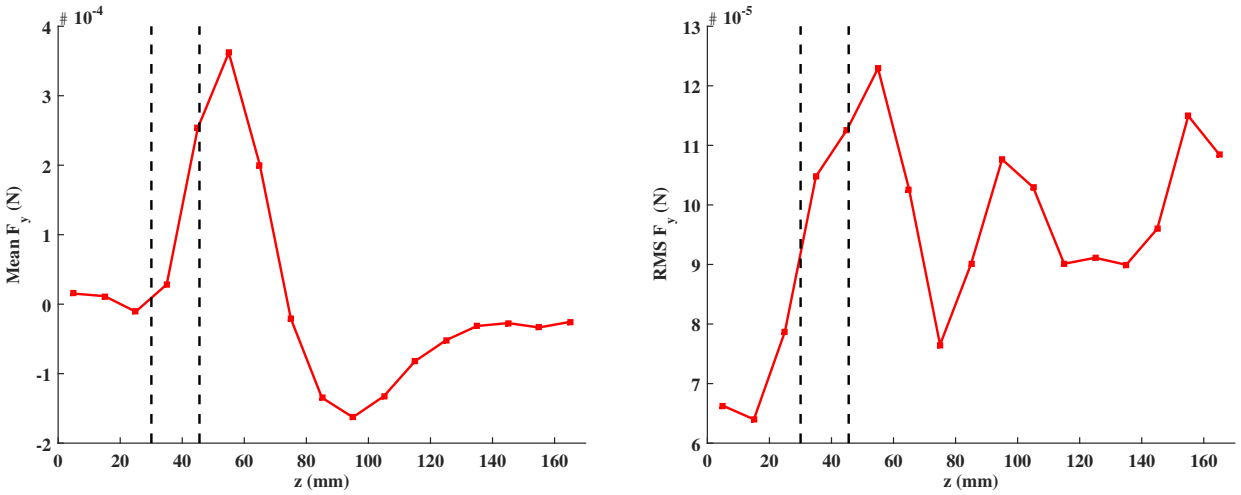

(a) (b)

Figure 5.4: Mean and RMS of y- pressure force respectively on inner wall (MV case)

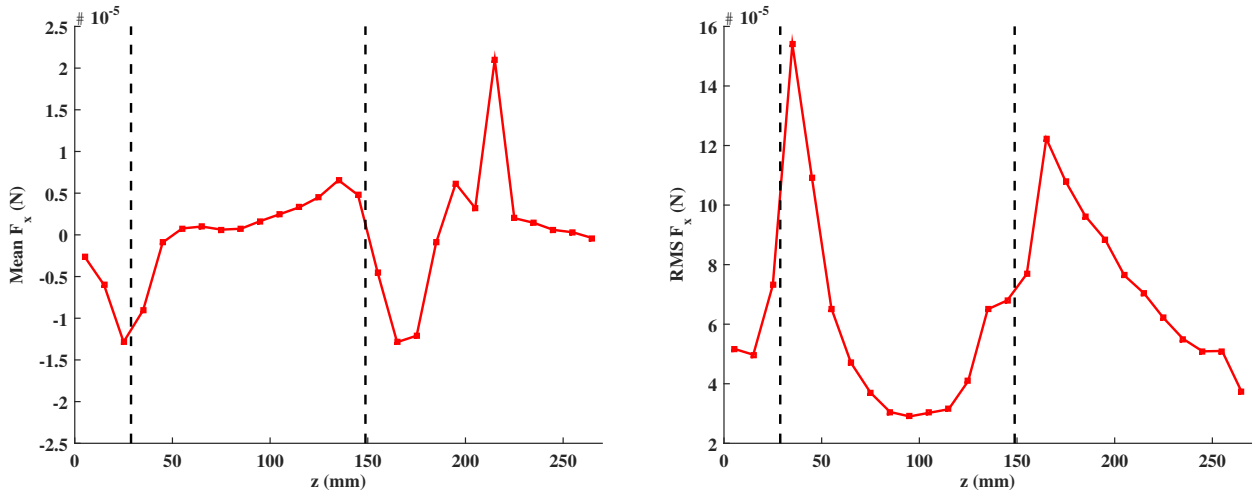

(a) (b)

Figure 5.5: Mean and RMS of x- pressure force respectively on inner wall (CG case)

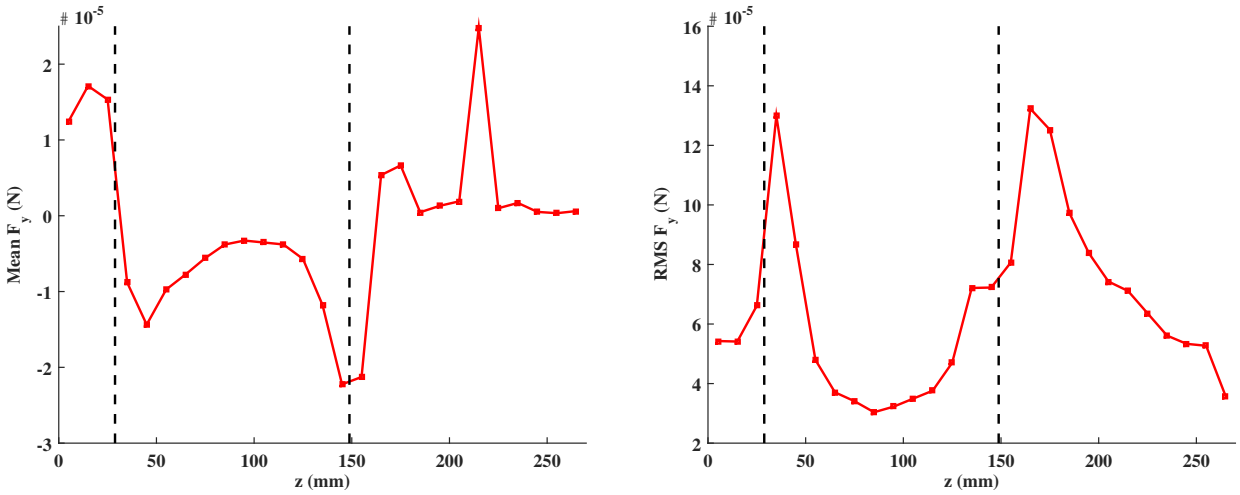

(a) (b)

Figure 5.6: Mean and RMS of y- pressure force respectively on inner wall (CG case)

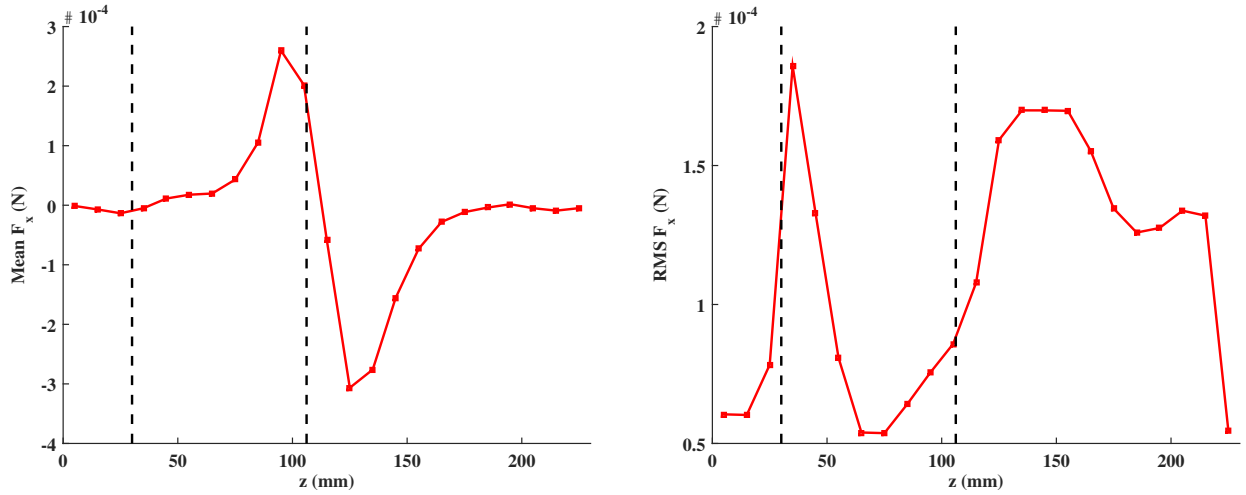

(a) (b)

Figure 5.7: Mean and RMS of x- pressure force acting on the inner wall respectively (SQ case)

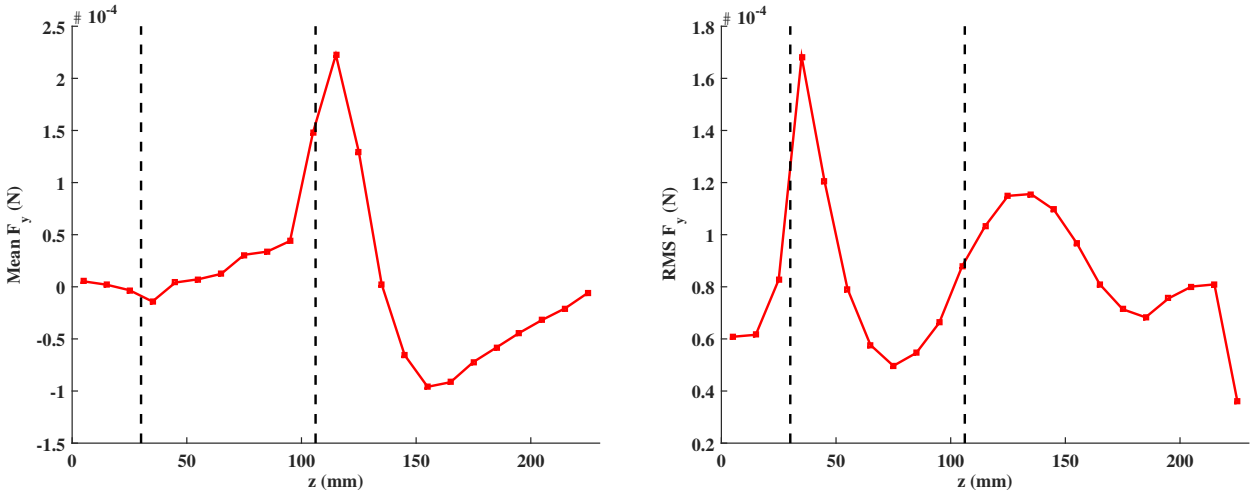

(a) (b)

Figure 5.8: Mean and RMS of y- pressure forces acting on the inner wall respectively (SQ case)

5.3 Description of probes for wall pressure analysis

To avoid too much data, pressure field was stored at every 10 time steps (calculation time step $\approx 1 \times 10^5$). In spatial terms, data is stored in axial and azimuthal probes as shown in Fig. 5.9. An axial probe saves pressure at 240 uniformly spaced points along a line parallel to the axis of the inner wall and located on the inner wall. So, an axial probe is defined by an angle or azimuthal position. For the annular pipe and circular grid cases, axial probes at 0° and 180° were defined. For the remaining two cases, axial probes were defined at 0°, 90°, 180° and 270°. Azimuthal probes save pressure on 80 uniformly spaced points (4.5° apart) on a circle located on the inner wall. So, an azimuthal probe is defined by its axial position. For the annular pipe case, two azimuthal probes are considered: one in the middle and another at one fourth of the axial length. For the other cases, five azimuthal probes are considered at upstream positions -0.66 HD and downstream positions 0.015, 1, 2 and 3 HD.

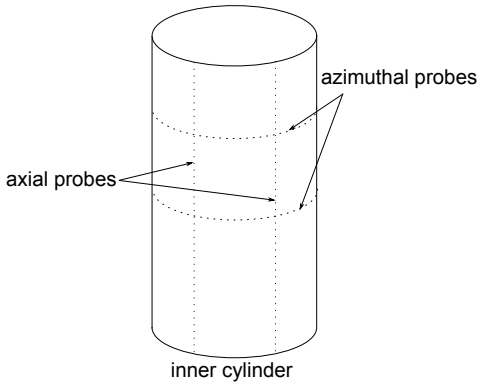

Figure 5.9: Location of axial and azimuthal probes on inner cylinder

5.4 Pressure drop calculation

Since the hydrostatic pressure at the outlet is fixed at zero, the calculated inlet pressure determines the pressure drop over the whole domain. In Fig. 5.10, time-averaged pressure on two probes placed at 180° and 90° were plotted for the MV case. The dotted lines indicate the axial bounds of the vanes. For the probe at 90°, the mean pressure decreases monotonically. But for the one at 180°, there was a steep drop in the vicinity of the vanes. A large drop in mean pressure through the mixing vanes indicates that most of the pressure loss is due to the vanes. The maximum pressure drop is 20 Pa. Additional insight into the fluctuating velocity field is found by examining the turbulent kinetic energy (TKE). In Fig. 5.11, the streamwise spatial evolution of time-averaged TKE is plotted for two probes placed at 180° and 90°. Like the variation of mean pressure, TKE peaks in the vicinity of the vanes to $1.7 \times 10^{-3}\,\mathrm{m}^2/\mathrm{s}^2$. A hump is observed around z=90 mm with a peak value $0.4 \times 10^{-3}\,\mathrm{m}^2/\mathrm{s}^2$ and further downstream the curve dips to $0.2 \times 10^{-3}\,\mathrm{m}^2/\mathrm{s}^2$. This behavior of TKE is similar to the one observed by Nourgaliev et al. [2013] for an LES on 3×3 fuel sub-assembly for a reactor scale Reynolds number 4.01×10^5. The TKE at 90° (no vanes present upstream) is uniform $0.2 \times 10^{-3}\,\mathrm{m}^2/\mathrm{s}^2$ except some small fluctuations around the vanes. This shows that the highest level of TKE occurs near the mixing vanes. Also, from the TKE curves for different mesh refinements by Nourgaliev et al. [2013], it is seen that the result from the most refined mesh is similar to the current result (Fig. 5.11).

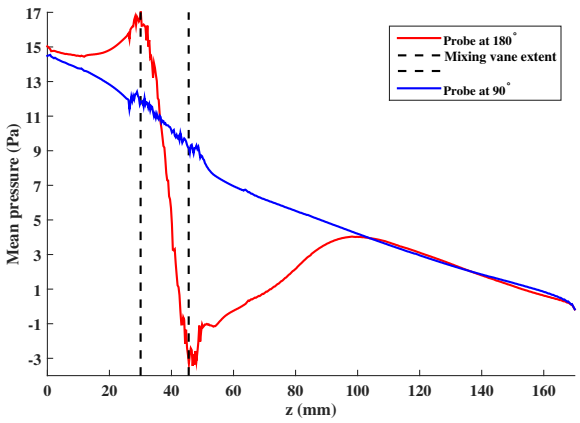

Figure 5.10: Pressure drop along the pipe (MV case)

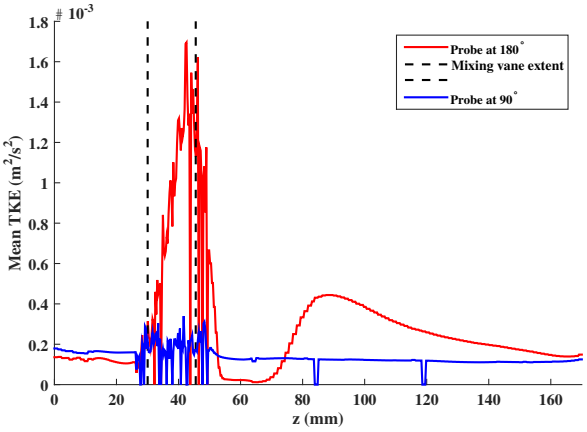

Figure 5.11: Variation of TKE along the pipe (MV case)

Instantaneous pressure distribution on the inner wall is shown in Figs. 5.12 and 5.13 for the circular grid case and square grid case respectively. This gives us an idea of the pressure drop.

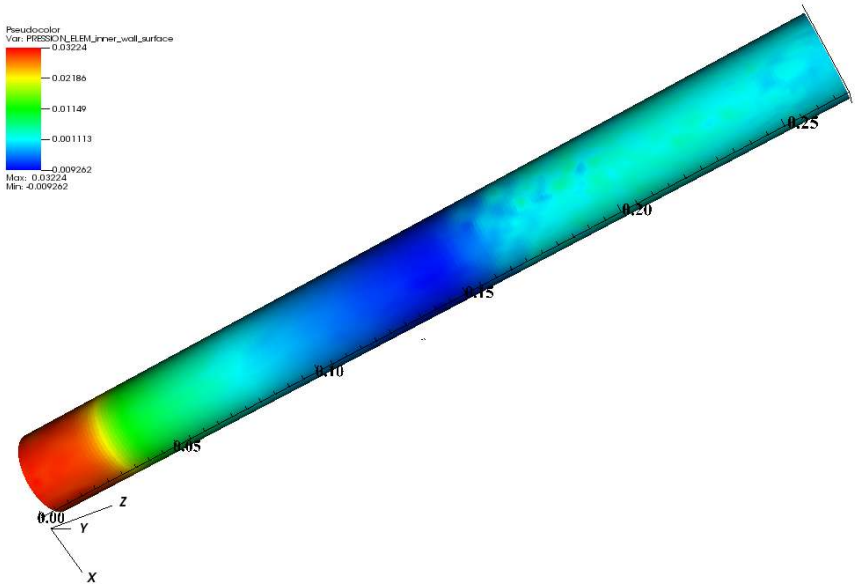

Figure 5.12: Instantaneous pressure field on inner wall for circular grid case (*the values are normalized by density; so it should be multiplied by 998.2 ≈ 1000 to obtain the values in Pa*)

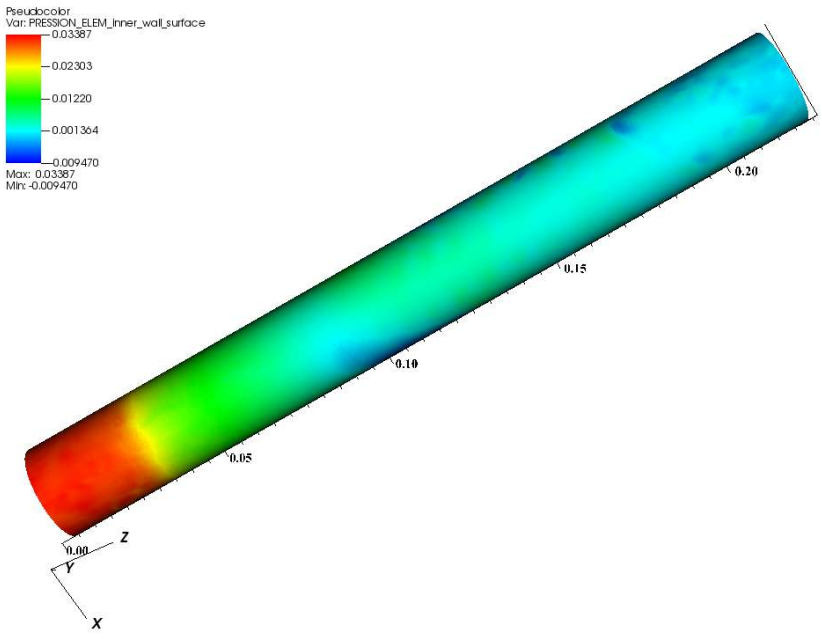

Figure 5.13: Instantaneous pressure field on inner wall for square grid case (*the values are normalized by density; so it should be multiplied by 998.2 ≈ 1000 to obtain the values in Pa*)

5.5 Correlation length

From the rod vibration point of view, it is important to know the correlation length of the fluid forces acting on a rod. In this section, the axial and azimuthal spatial correlation of pressure are analyzed.

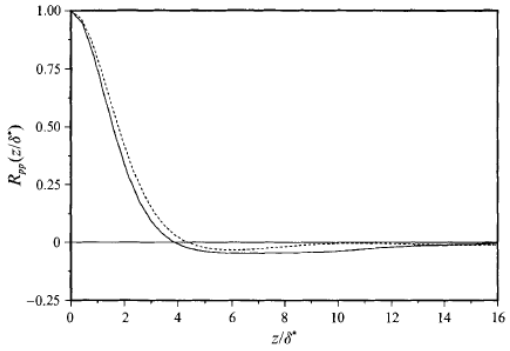

FIGURE 8. Axial (streamwise) two-point correlations of the wall pressure fluctuations: ——, $\gamma = 5$ and – – – –, $\gamma = 11$.

Figure 5.14: Streamwise wall pressure correlation (taken from Neves and Moin [1994])

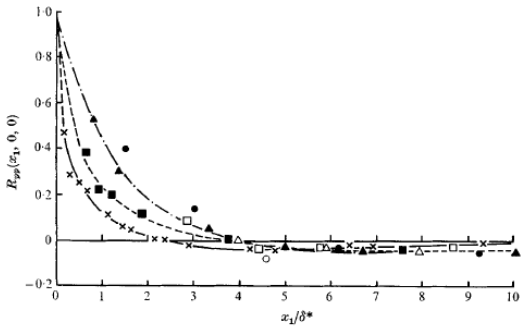

FIGURE 14. Longitudinal wall-pressure correlation in a broad frequency band. ×, $\delta/a = 2$, all others, $\delta/a = 0$. ■, $R_\theta = 38{,}000$, Willmarth & Wooldridge; ●, $R_\theta = 10{,}000$, Bull; ▲, $R_\theta = 19{,}500$, Bull; ○, $R_\theta = 11{,}000$, Bull; △, $R_\theta = 24{,}300$, Bull; □, $R_\theta = 33{,}800$, Bull.

Figure 5.15: Streamwise wall pressure correlation (taken from Willmarth and Yang [1970])

As shown in Fig. 5.15 (*bold black triangles*), Bull [1963] and Bull [1967] presented experimental data (wind tunnel) for streamwise wall pressure correlation on a flat plate and Willmarth and Yang [1970] presented the same data on a cylinder. The streamwise length was normalized by the boundary layer displacement thickness. They observed that the correlation length is less for a cylindrical surface (approximately 2) compared to a flat plate (approximately 4). Similar results were presented by Willmarth et al. [1976] as well. As shown in Fig. 5.14, Neves and Moin [1994] presented the streamwise spatial correlations for the DNS of an annular pipe (discussed in detail in Chapter 2) for two Reynolds number. They found a correlation length of 3.9. It was observed that the correlation length decreases with increase in Reynolds number. The Reynolds numbers corresponding to the curves $\gamma = 5$ and 11 are 1348 and 622 respectively.

In Figs. 5.16 and 5.17, spatial correlation of pressure in axial (streamwise) and azimuthal directions are presented for the annular pipe (coarse and fine mesh cases). In Fig. 5.16, the correlation decreases quickly in both axial and azimuthal directions. One could also note that the coarse mesh overestimates the correlation length in the azimuthal direction (Fig. 5.17). Hence, this coarse mesh is not suitable for wall pressure analysis. The fine mesh case in Fig. 5.17 gives a correlation length of about 5 mm for annular pipe flow.

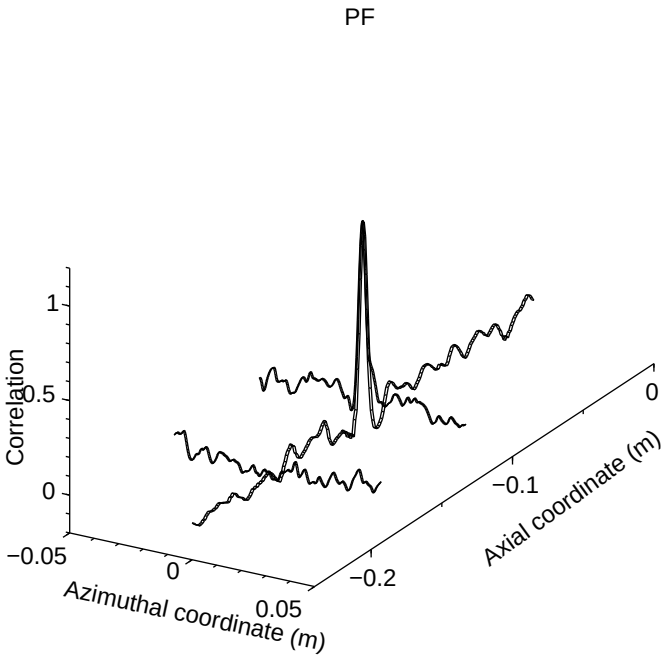

Figure 5.16: Spatial correlation in annular pipe (fine mesh PF)

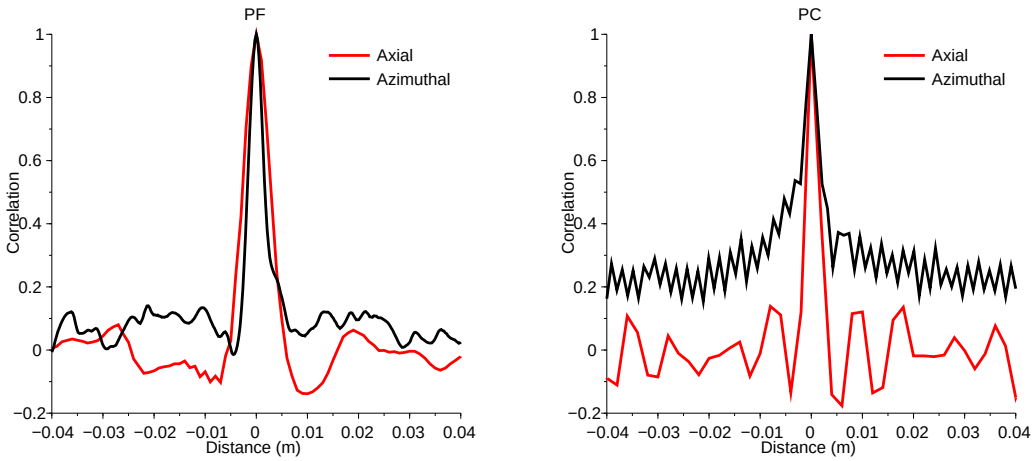

Figure 5.17: Spatial correlation in annular pipe: comparison between fine (PF, left) and coarse mesh (PC, right)

In order to compare with the above literature values, an approximate estimation of boundary layer thickness is made using Blasius' relation for turbulent flow [Pope, 2000]. The boundary layer thickness is

$$\delta = \frac{0.37D}{Re_D^{1/5}} \tag{5.1}$$

where D denotes hydraulic diameter and Re_D denotes Reynolds number. This thickness is found to be 1.8 mm giving a z/δ ratio 2.7. Neves and Moin [1994] found the same ratio to be 3.9 for an annular pipe and that it decreases with increase in Reynolds number. The current fine mesh annular pipe simulation agrees well with this behavior.

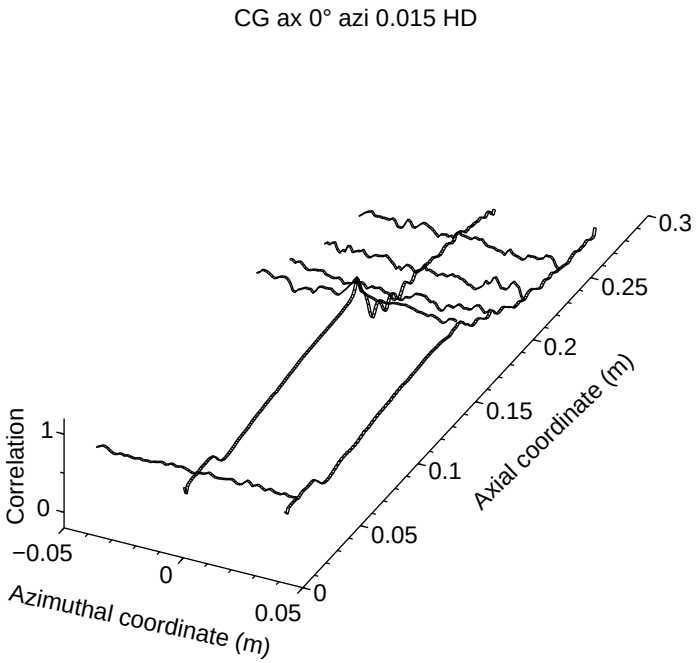

Figure 5.18: 3D view of spatial correlation for CG case

The circular grid case shows different behavior with a high correlation value close to the grid (Figs. 5.18 and 5.19). This is due to a lower Reynolds number close to the grid since the hydraulic diameter is smaller. Nevertheless after 2 HD downstream of the grid, we obtain the same behavior as in case of annular flow (correlation length = 5 mm).

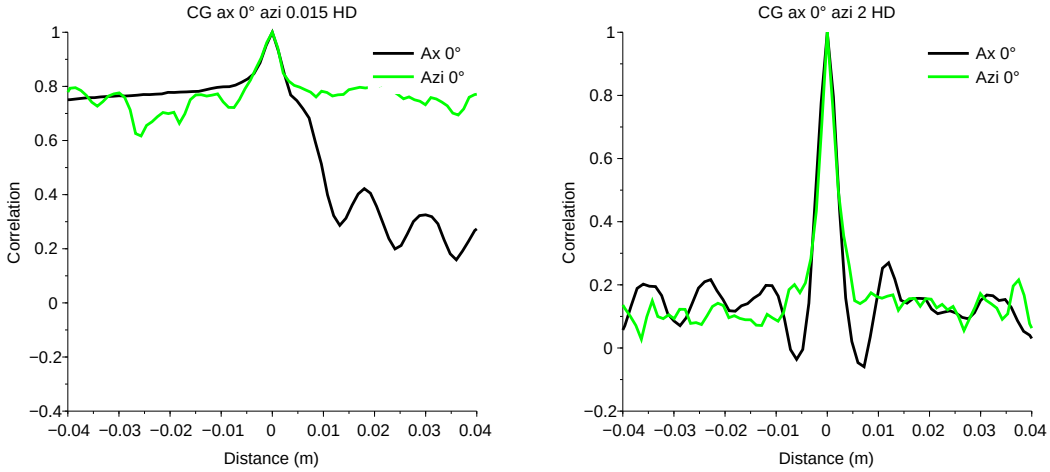

Figure 5.19: 2D view of spatial correlation for CG case

In the mixing vanes case (Fig. 5.20), one can observe that the correlation length is higher at 90° than at 0° which is in line with a mixing vane. This makes sense since the mixing vane induces more turbulence and therefore, a smaller correlation length. But it is surprising to observe that for 90°, the correlation length is higher than in the case of an annular flow. This illustrates that the mixing vanes strongly modify the flow structure.

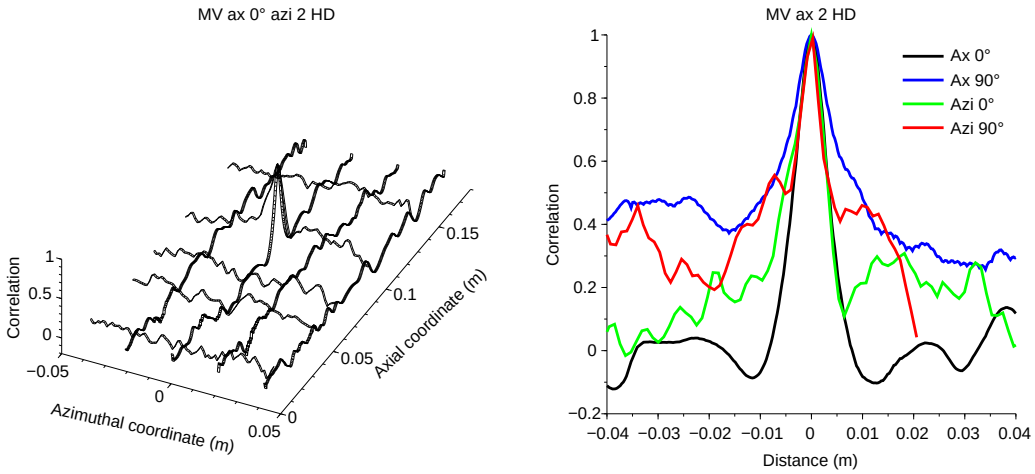

Figure 5.20: Spatial correlation for MV case

The case of the square grid with mixing vanes (Figs. 5.21 and 5.22) shows a combination of the cases of mixing vanes and circular grid with a higher correlation length close to the grid and a smaller correlation length in line with MV (*black* and *green* curves in Fig. 5.22). This low correlation is due to strong turbulence. Also, it is seen that correlation length is smaller in axial direction compared to azimuthal direction as the flow is convected axially. Overall, the analysis of correlation lengths reflect strong destabilization of flow by the vanes. For more pressure correlation curves, one can refer to Appendix B.

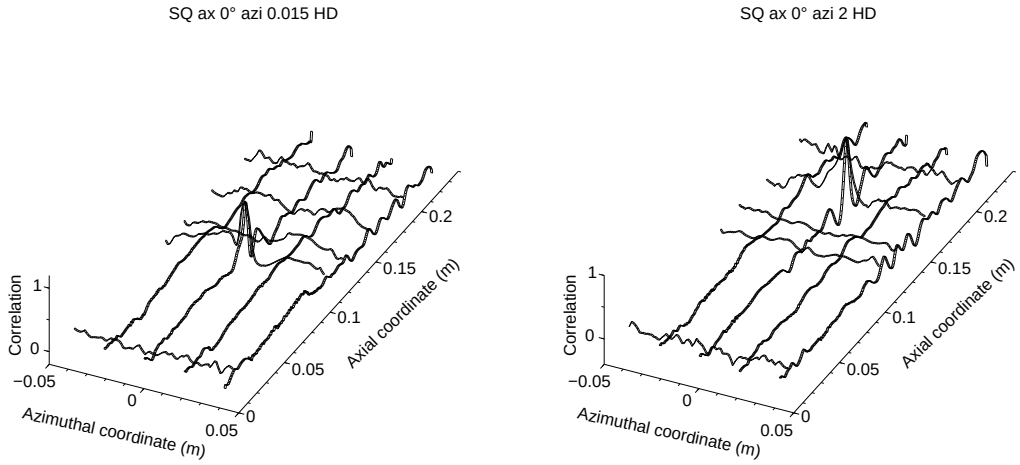

Figure 5.21: 3D view of spatial correlation for SQ case

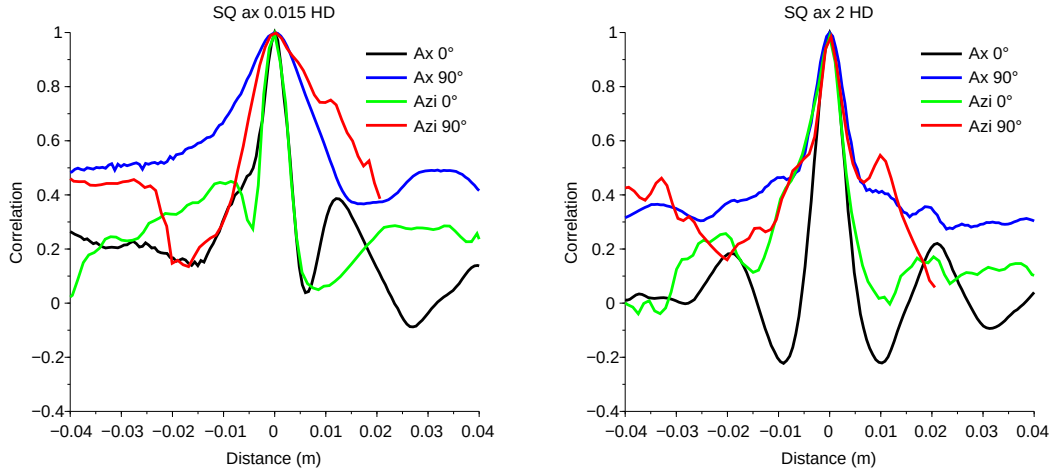

Figure 5.22: Spatial correlation for SQ case

Figs. 5.23 and 5.24 illustrate the coherence of the pressure between one location and five other locations within a hydraulic diameter in the azimuthal and axial directions. As for the correlation, one can observe that the coarse mesh overestimates the coherence in the azimuthal direction (Fig. 5.23).

In general, one can observe that the coherence decreases with the distance and the frequency and that it decreases faster in the azimuthal direction than in the axial one.

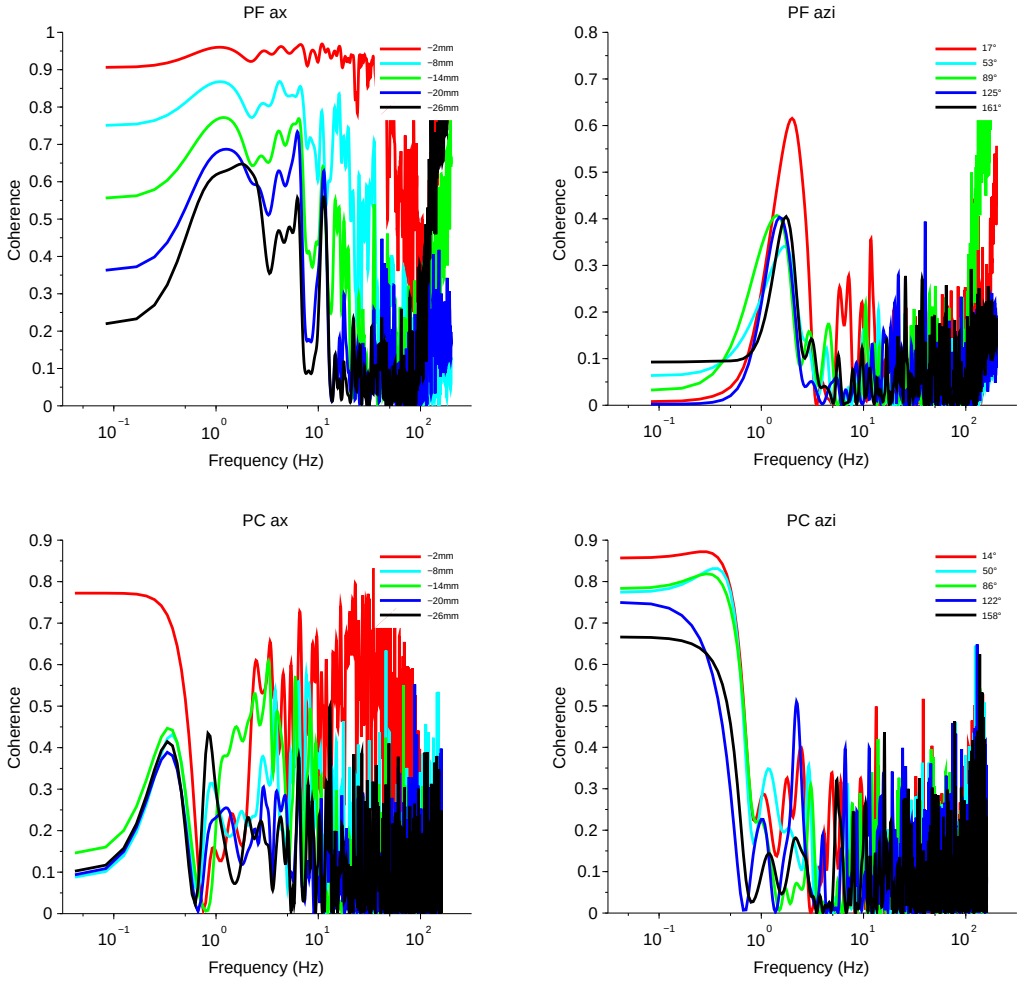

Figure 5.23: Transfer function for annular pipe fine and coarse mesh around 0° in axial direction (left) and azimuthal direction (right)

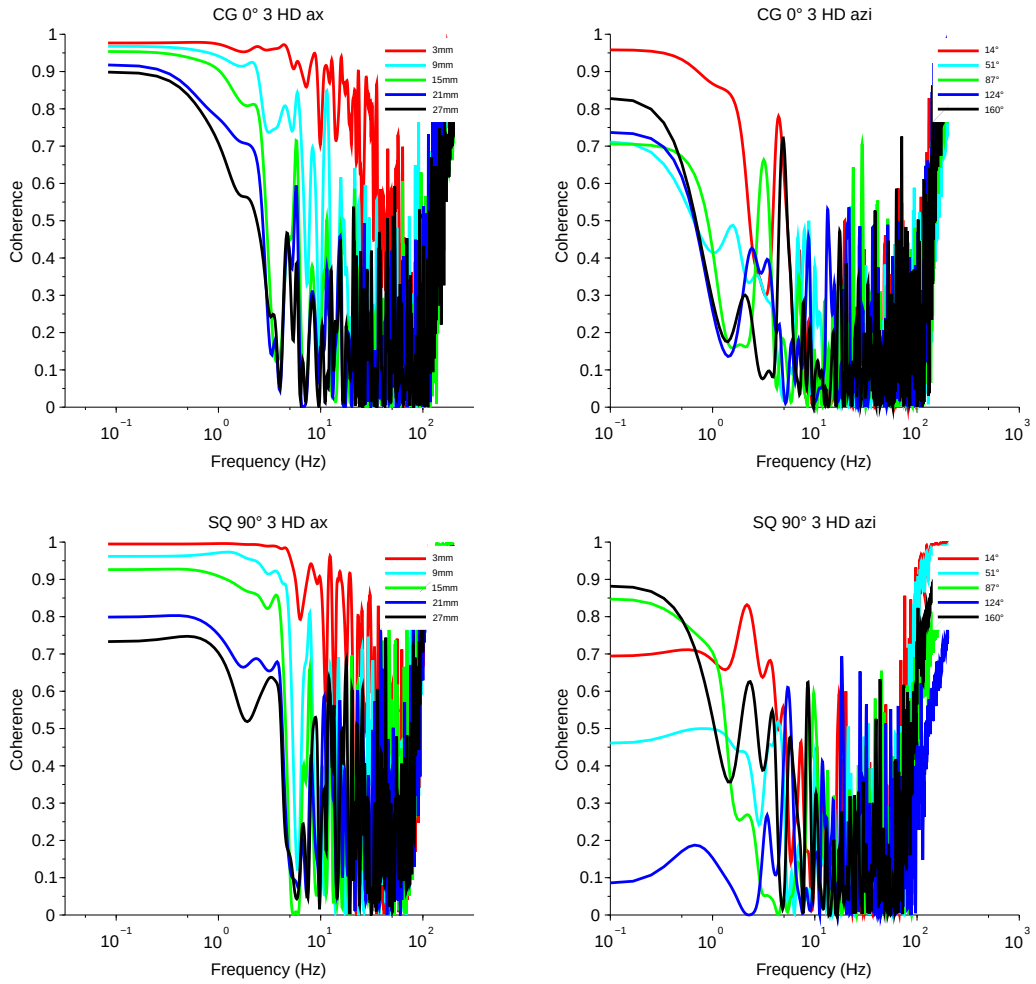

Figure 5.24: Transfer function for SQ and CG case around 0° (3 HD downstream) in axial direction (left) and azimuthal direction (right)

5.6 POD analysis

In this section, a Proper Orthogonal Decomposition (POD) (or Karhunen-Loève decomposition) method is applied to all the probes described previously for the pressure field. It provides an optimum basis for modeling fields. It has been used successfully to analyze complex spatial-temporal fields [Païdoussis et al., 2005] and for model reduction purposes [Graham and Kevrekidis, 1996]. A detailed description of the method can be found in Kerschen et al. [2005].

In the current study, the POD method is applied to the spatially discretized field:

$$\mathbf{P}(t) = (\mathbf{p}(x_1, t)^T, \cdots, \mathbf{p}(x_{N_n}, t)^T)^T, \tag{5.2}$$

where N_n denotes the number of modes. Starting with the time-averaged correlation matrix :

$$\mathbf{R} = \frac{1}{N_s} \sum_{i=1}^{N_s} \bar{\mathbf{P}}(t_i) \bar{\mathbf{P}}(t_i)^T, \tag{5.3}$$

where $\bar{\mathbf{P}}(t_i) = \mathbf{P}(t_i) - \sum_{i=1}^{N_s} \bar{\mathbf{P}}(t_i)$, and solving the eigenproblem $\mathbf{R}\mathbf{\Phi} = \lambda\mathbf{\Phi}$, the field $\mathbf{P}$ can be decomposed into

$$\bar{\mathbf{P}}(t) = \sum_j \alpha_j(t) \mathbf{\Phi}_j, \tag{5.4}$$

where the eigenvectors $\mathbf{\Phi}_j$ have been numbered based on the associated eigenvalues λ_i in decreasing order. Classically, $\mathbf{\Phi}_j$ denotes the j^{th} Proper Orthogonal Mode (POM), $\alpha_j(t)$ the associated Proper Orthogonal Component (POC) and λ_i the associated Proper Orthogonal Value (POV). Due to the symmetry of $\mathbf{R}$, the POMs are orthogonal and the POVs (with $\lambda_i > 0$) characterize the energy of the modal component and satisfy $||P||^2 = \sum_j \lambda_j$. It should be noted that POMs have no physical significance apart from the fact that they give a good idea of the spatial behavior of the system. However, after making some assumptions about the system (the linearity, proportional viscous damping, etc.), the POMs have been found to converge with the physical modes of the system [Bellizzi and Sampaio, 2006].

Taking the Discrete Fourier Transform (DFT) of each $\alpha_j(t)$ allows us to plot a frequency POM number diagram (Fig. 5.25). One can observe that for every case the first POMs present a low frequency range and that as the number of the POM increases the predominant frequency shift toward higher frequencies. This effect is less marked for the circular grid and periodic box coarse mesh cases.

Coarse and refined mesh show very different behaviors: in case of the coarse mesh, the first POM catches more than 12 % of the energy compared to only 4 % in the refined case (Fig. 5.26), whereas it takes less than 200 POM to capture 95 % of the energy in the refined mesh case and more than 250 in the coarse mesh case (Fig. 5.27).

The square grid with mixing vanes (SQ) case seems to be a combination of the mixing vanes (MV) and circular grid (CG) cases as the frequency POM diagram seems to be the sum of the two cases, even the percentage of energy captured by the first POMs seem to be the average of the two cases.

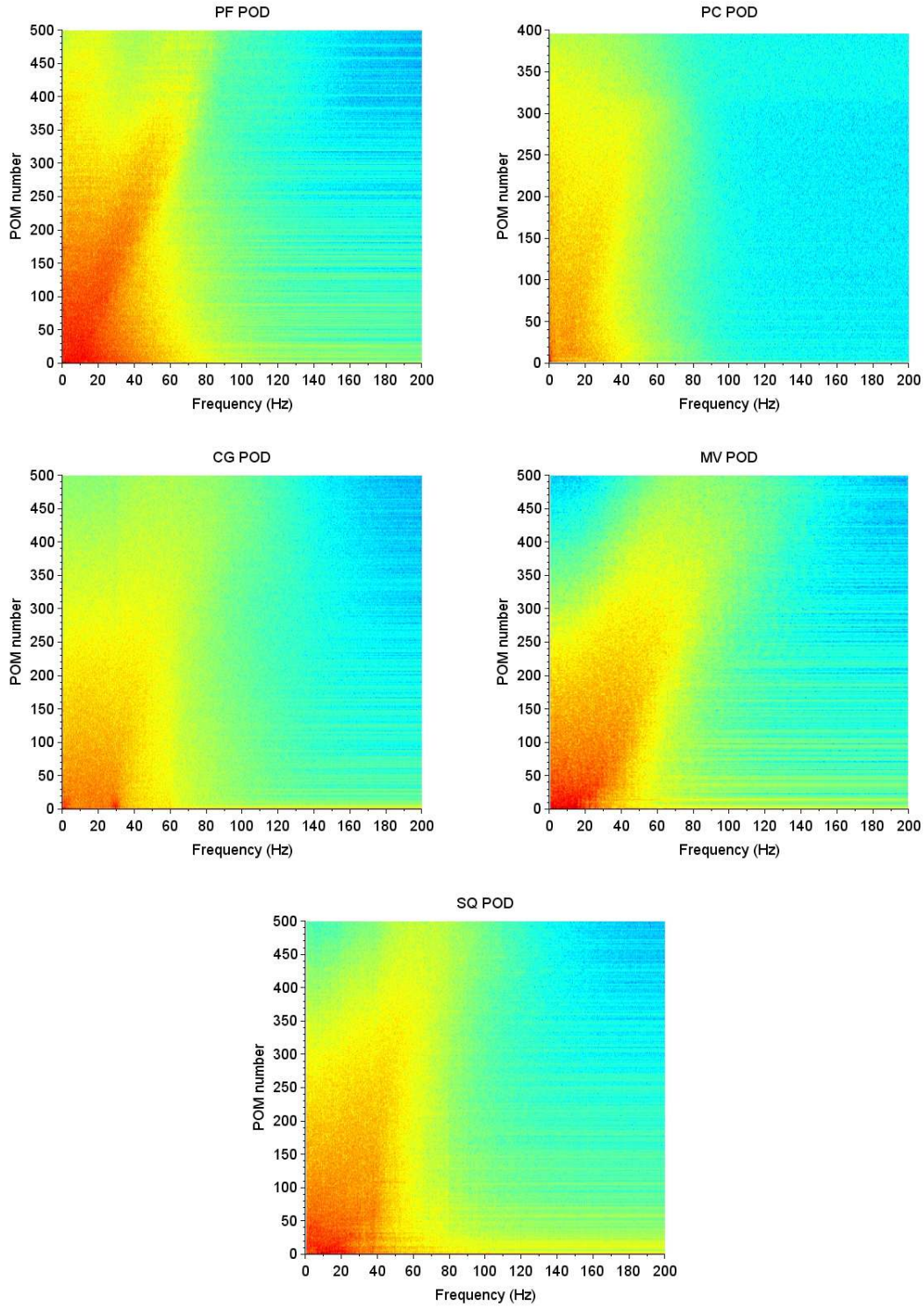

Figure 5.25: Frequency POM diagrams for different cases

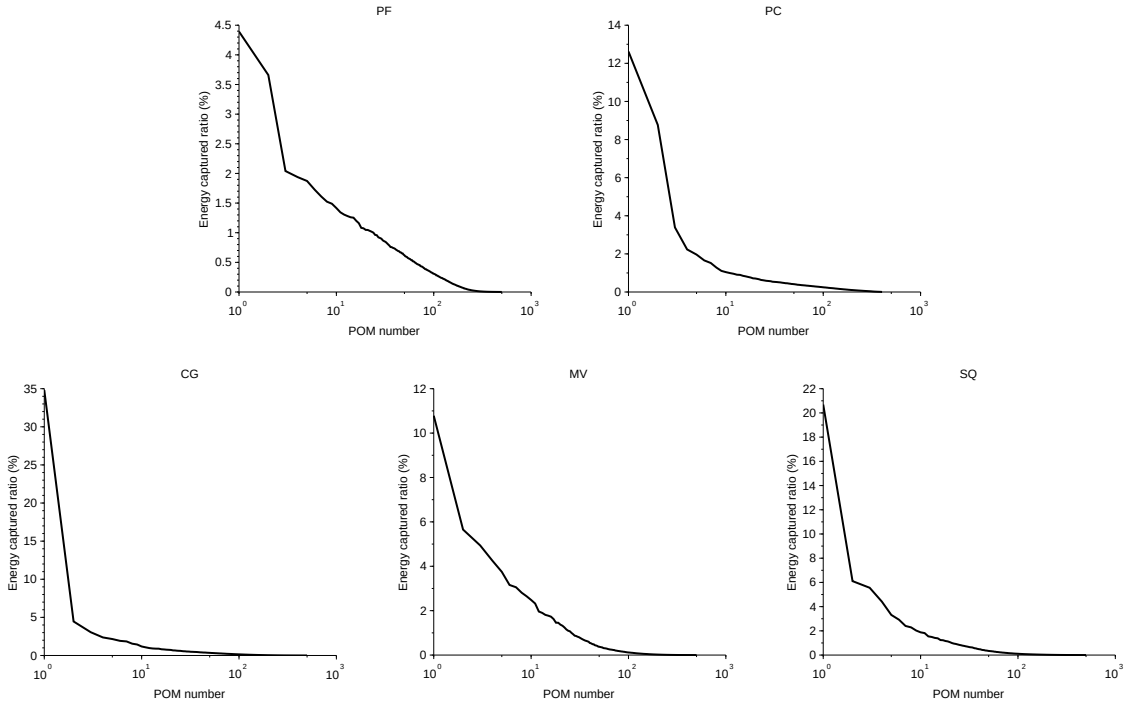

Figure 5.26: Percentage of energy captured per mode for different cases

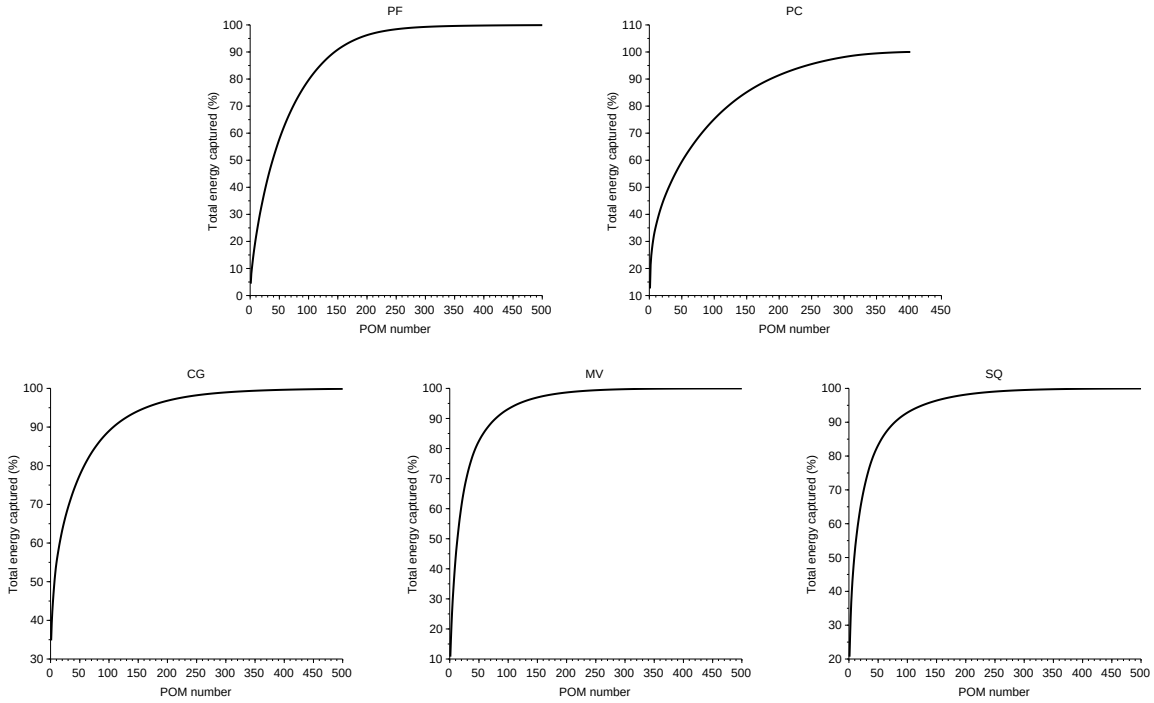

Figure 5.27: Total percentage of energy captured per mode for different cases

As done for $\alpha_j(t)$, DFT is applied on some part of each $\mathbf{\Phi}_j(x)$. This gives wave number POM diagrams for each axial and azimuthal probes.

In Fig. 5.28, the wavenumber POM diagrams for azimuthal probes 2 HD downstream of the grid or the vanes show very different behavior. In the periodic box (PF) and circular grid (CG) cases, the DFT shows a peak of which the frequency seems to linearly increase with the POM number, whereas for the mixing vanes (MV) and square grid (SQ) cases, the frequency range just become larger as the POM number increases.

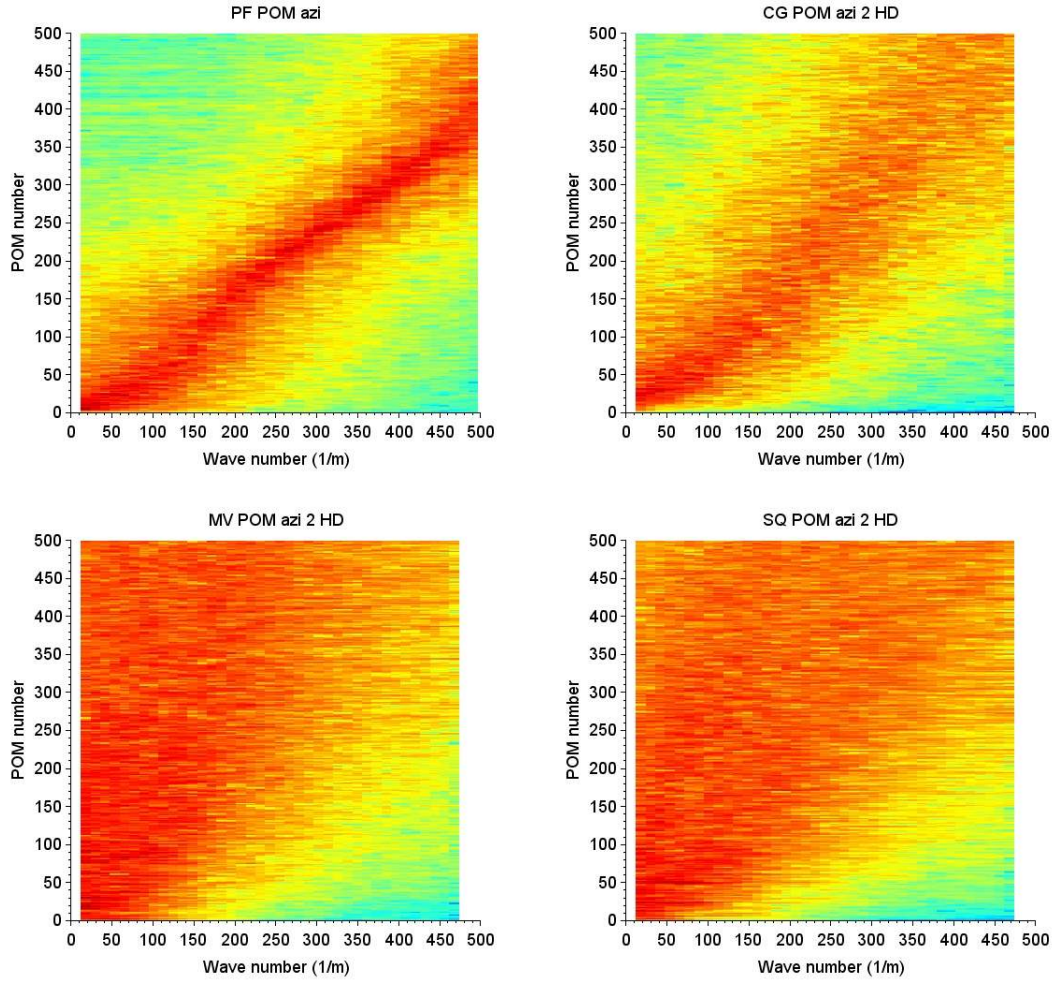

Figure 5.28: Wave number POM diagrams in azimuthal direction at 2 HD downstream

In case of the axial probes (Fig. 5.29), the periodic box (PF) case shows different behavior than the circular grid (CG) case which is closer to the square grid (SQ) case. The SQ case again seems to be a combination of the CG and MV cases.

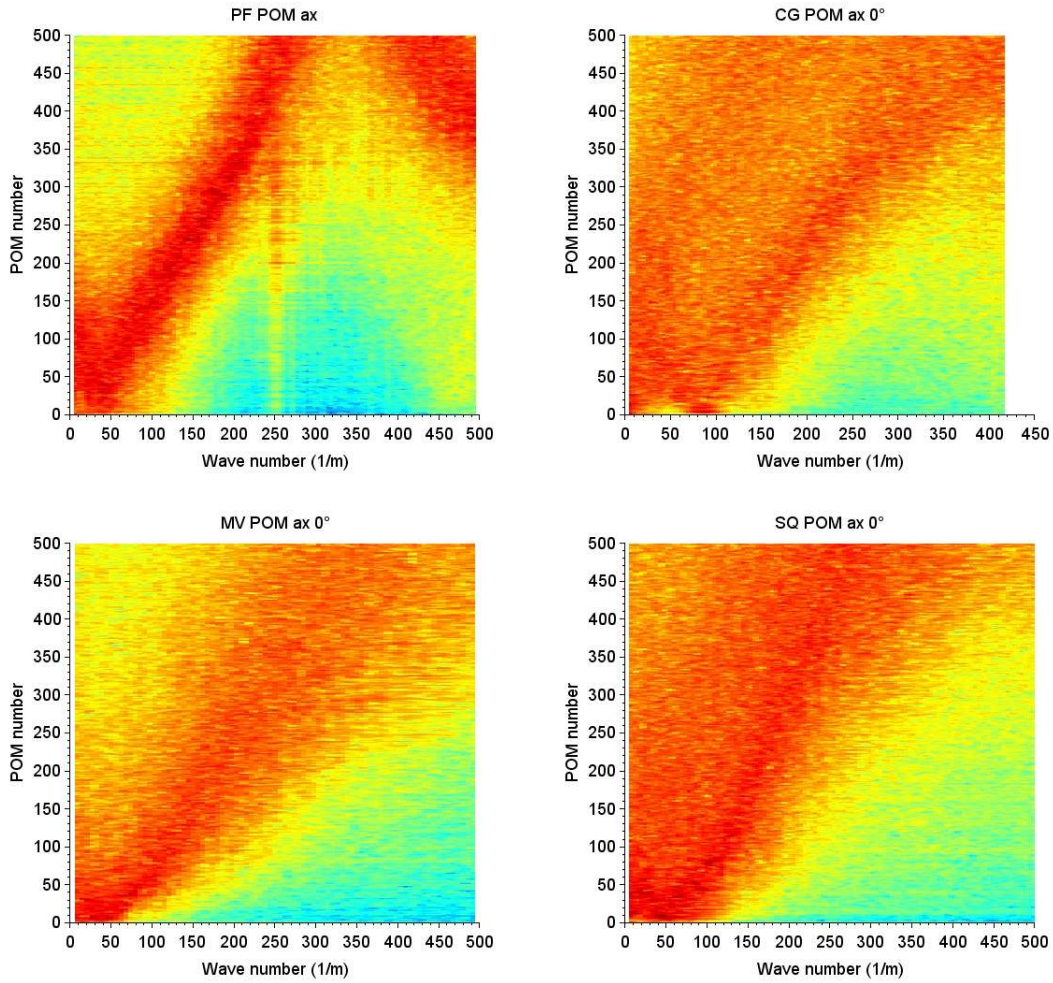

Figure 5.29: Wave number POM diagrams in axial direction at 0°

The POMs for each of the cases PC, PF, MV, CG and SQ both in axial and azimuthal directions have been presented in Appendix D. The frequency - POM and wavenumber - POM diagrams have also been presented.

5.7 Spectral analysis

Figs. 5.30, 5.31 and 5.32 show the Power Spectral Density (PSD) of the pressure at different axial and azimuthal locations for the circular grid (CG), mixing vanes (MV) and square grid with mixing vanes (SQ) cases. The data sampling frequency was 10 kHz and the PSD was calculated with a Hanning window. For the axial probes, data is presented for 5 equidistant locations along the length of the domain. For the azimuthal probes, data is presented at 5 equidistant locations on a semi-circle (0° to 180°).

The axial evolution of wall pressure spectra along the rod is presented in Fig. 5.30. The axial probes were located at 0° in line with the vanes. It should be recalled that the vanes are located at 0° and 180°. In case of the circular grid, a peak is observed at 30 Hz corresponding to axial location 162 mm which is 0.4 HD downstream of the grid. In case of the square grid, strong variations are observed at axial locations 136 mm and 182 mm which corresponds to 1 HD and 2.5 HD downstream of the vanes. Of all 3 cases, SQ has the most variations whereas the MV case is the most homogeneous.

The azimuthal evolution (Fig. 5.31) of wall pressure spectra at the two axial positions 0.015 HD and 1 HD shows different behavior for each case. In the circular grid case, a homogeneous repartition of the spectra is observed. Due to the symmetric geometry, all the spectra collapse and overlap. A prominent frequency peak is observed at 30 Hz. The area under the curve is higher for the spectra at 1 HD than at 0.015 HD. Since the integrated area under a PSD curve gives variance, so the wall pressure fluctuation is higher at 1 HD than at 0.015 HD. This is because the distance 0.015 HD is insufficient for fluctuations to propagate to the wall. In the mixing vanes case, the spectra for 0° is clearly separated out whereas those for the other azimuths collapse. This implies that fluctuations are concentrated in the vicinity of the vanes. The slope of the spectra changes at approximately 30 Hz. Once again, the strongest variations are observed in the square grid case among the 3 cases. The variations are stronger at 1 HD than at 0.015 HD. A peak is observed at 38 Hz for all azimuths. The magnitude of the peak is maximum at azimuth 37° and it decreases monotonically for the azimuths 73°, 110° and 146°. The occurrence of the maximum peak at 37° could be explained as follows. Due to the 30° inclination of the vanes (previously shown in Fig. 4.40 of Chapter 4), the swirl structures tend to propagate in anti-clockwise direction on x-y plane as one progresses downstream. This shift of the swirl structures is also observed in the RMS velocity and RMS pressure fluctuations plotted in Figs. 4.49 and 5.39 respectively. Overall, one can observe the presence of sharp peaks in the circular

grid and square grid cases respectively at 30 and 38 Hz. In the circular grid case, the peak is observed at every altitude and azimuth although its amplitude decreases as the distance from the grid increases. On the other hand,in case of the square grid, the peak is present only for azimuthal positions out of line with the vanes, i.e., around 90° and 270°, and vanishes quickly after 1 hydraulic diameter. Strouhal number [Strouhal, 1878] is a dimensionless number used to describe oscillating flow mechanisms. It is defined as

$$St = \frac{fL}{U} \tag{5.5}$$

where f is the frequency of vortex shedding, L is the characteristic length (for example, hydraulic diameter) and U is the flow velocity. Considering the smaller distance between the inner wall and the spacer grid as the characteristic length, the Strouhal number is calculated to be 0.63 and 0.46 respectively for circular grid and square grid cases (Table 5.1). These values can be related to vortex shedding in confined flow [Pettigrew and Taylor, 2003]. The lower Strouhal number for square grid indicates that while the vortices are generated by the spacer grid, the vanes change the flow structure and make the vortices vanish faster. It should be noted that similar frequency peaks were previously observed for the velocity spectra in Chapter 4.

Case	f (Hz)	St
CG	30	0.63
SQ	38	0.46

Table 5.1: Strouhal number

Fig. 5.32 shows the axial evolution of pressure spectra at 5 different positions along the inner wall. Comparisons were made for the square grid (SQ) and mixing vane (MV) cases for probes placed in line with MV (0°) and those placed out of line with the MV (90°). In the MV case, the presence of the vane at 0° does not seem to generate a lot of variation along the inner wall compared to 90°, whereas in the SQ case, the mixing vanes clearly generate strong variations along the wall. This illustrates the combined effect of the square spacer grid and the vane. The presence of the spacer grid reduces the cross-section of flow and hence accelerates the flow just upstream of the mixing vanes, thereby amplifying the effect of the vanes.

More PSD analyses have been presented in Appendix F.

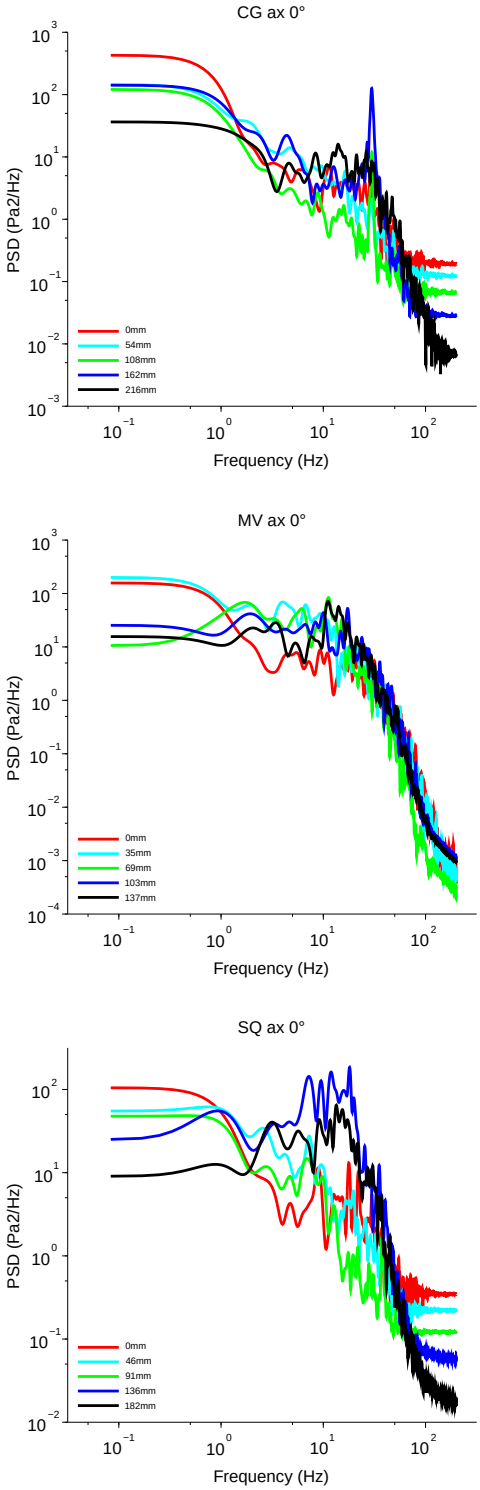

Figure 5.30: PSD of the pressure at upstream and downstream locations on an axial probe placed at 0° for CG, MV and SQ cases respectively

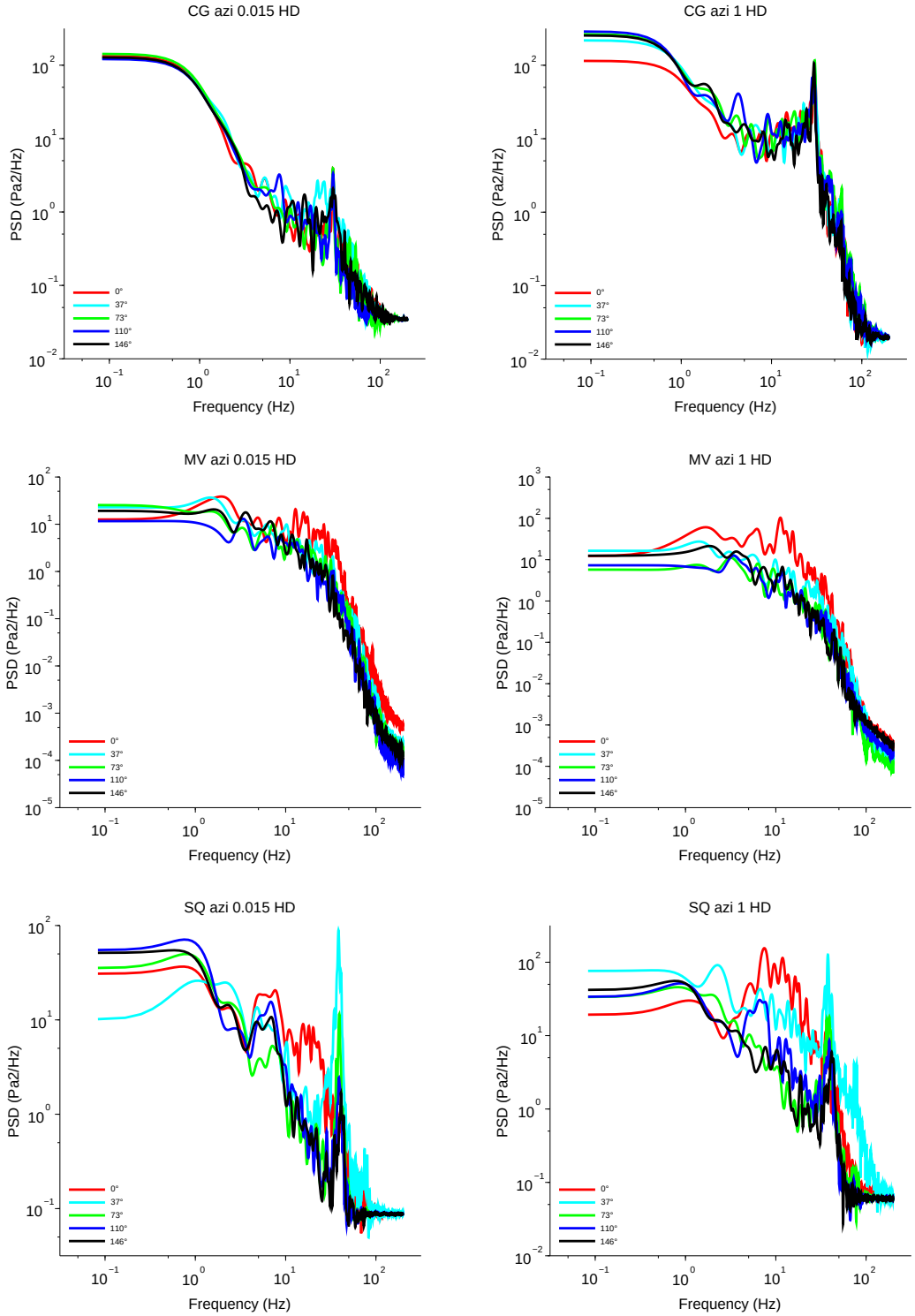

Figure 5.31: PSD of the pressure on an azimuthal probe placed at downstream locations 0.015 HD (left) and 1 HD (right) for three cases

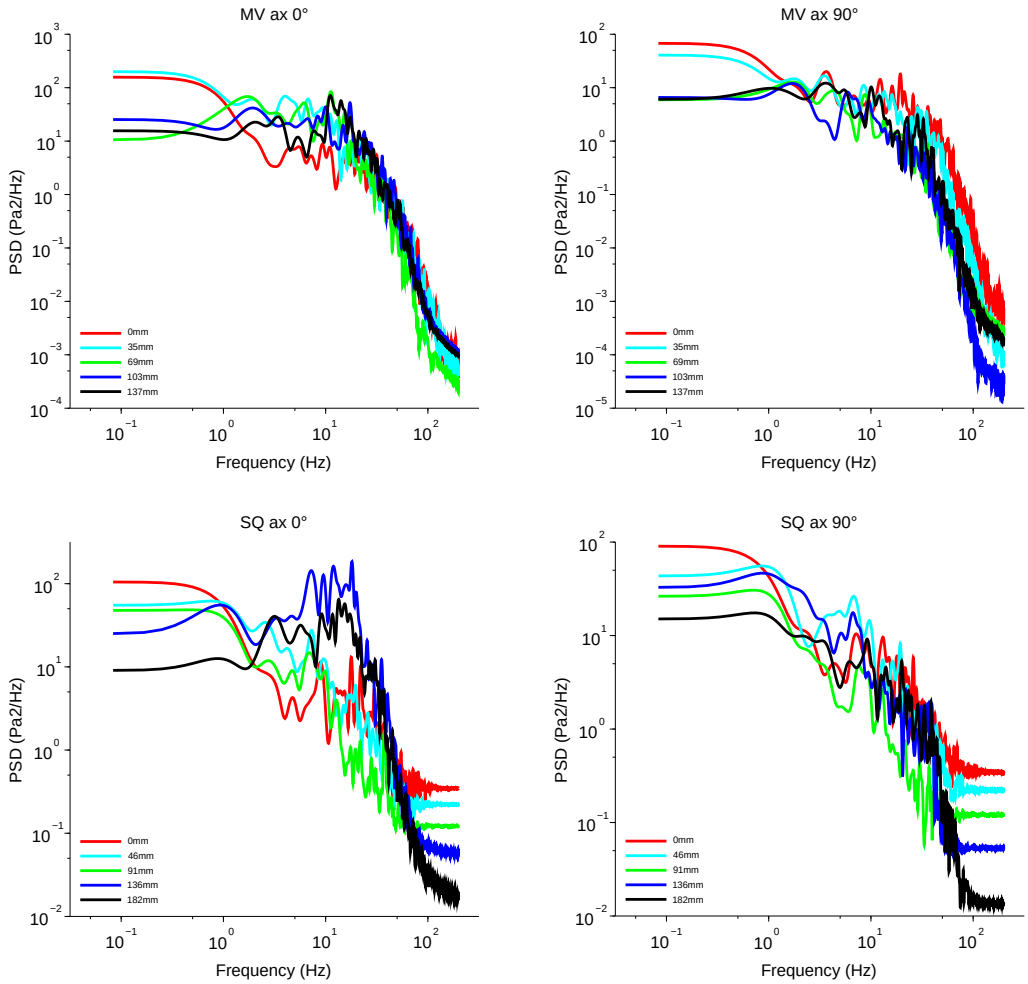

Figure 5.32: PSD of the pressure at upstream and downstream locations on an axial probe placed at 0° (in line with MV) and 90° (out of line with MV) for MV and SQ cases respectively

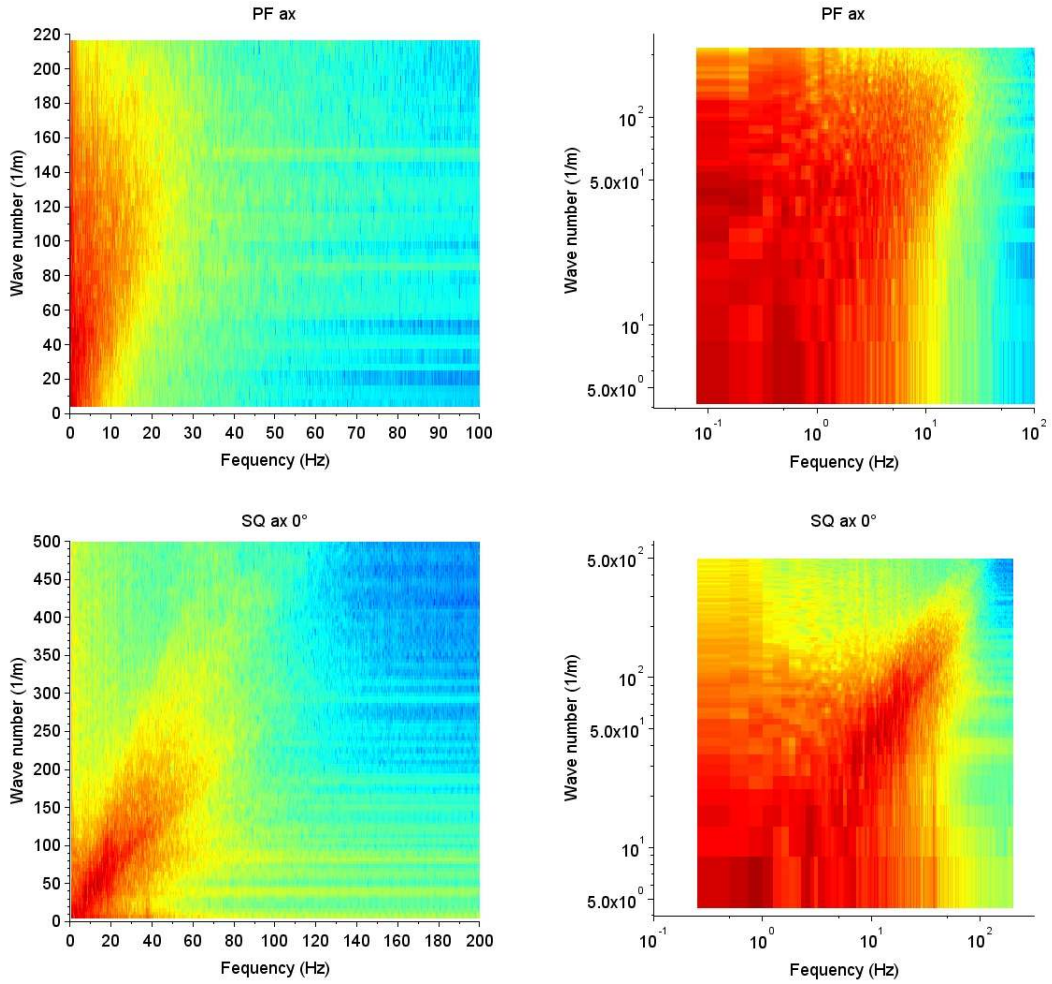

Figure 5.33: Frequency wave number diagrams on an axial probe placed at 0° for annular pipe fine mesh (PF) and square grid (SQ) cases [linear scale on the left and logarithmic scale on the right]

Frequency wavenumber diagrams are illustrated in Figs. 5.33 and 5.34 in linear and logarithmic scales. As in case of POM decomposition, direct Fourier transform (DFT) is applied in space to each axial and azimuthal probe at each time step to obtain a space spectrum for each time step. Then DFT is applied in time for each wave number to obtain a frequency wave number diagram for each axial and azimuthal probe.

From the axial probes (Fig. 5.33), one can observe that the wave length seems to be an approximate linear function of the frequency; thereby implying a convection driven structure. On the other hand, from the azimuthal probes (Fig. 5.34), one can observe broad range frequency domain for each wave number.

More frequency - wavenumber analyses have been presented in Appendix E.

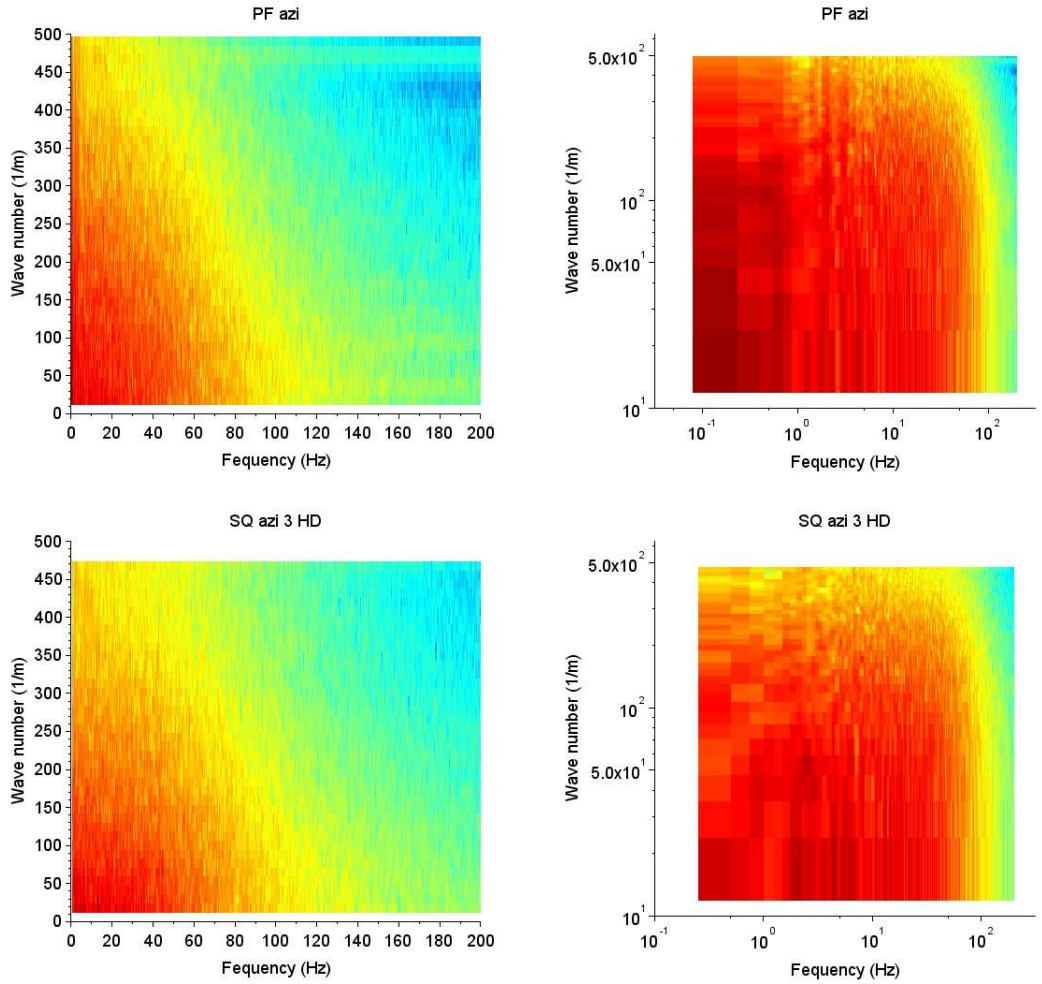

Figure 5.34: Frequency wave number diagrams on an azimuthal probe placed at 3 HD downstream for annular pipe fine mesh (PF) and square grid (SQ) cases [linear scale on the left and logarithmic scale on the right]

5.8 Comparison with experiment

In this section, comparison of simulations to CALIFS experimental results are presented. The experimental setup was described in Chapter 2. Simulations were done for a Reynolds number of 8900 (0.298 m/s $\approx$ 0.3 m/s) whereas experiments were conducted for Reynolds numbers of 58500 (2 m/s), 87800 (3 m/s), 117100 (4 m/s) and 146400 (5 m/s). This is tabulated in Table 5.2. Despite the fact that the lowest CALIFS Reynolds number is about 6 times than that of the simulations, the goal was to perform qualitative comparisons. The reasons for choosing this low Reynolds number 8900 have been explained in Chapters 1 and 3. For current comparison, Reynolds numbers 58500, 87800 and 146400

Flow velocity (m/s)	Reynolds number Re_D
5	146400
4	117100
3	87800
2	58500
0.3 (simulations)	8900

Table 5.2: Reynolds numbers for the CALIFS experiment

were chosen. The pressure, frequency, and PSD were non-dimensionalized with bulk velocity (U_b) as discussed previously in Chapter 2 [Axisa et al., 1990]. The reduced pressure, reduced frequency and reduced PSD are respectively defined as:

$$p_{red} = \frac{p}{\rho U_b^2}, \tag{5.6}$$

$$f_{red} = \frac{fD}{U_b}, \tag{5.7}$$

$$PSD_{red} = \frac{PSD}{\rho^2 U_b^3 D}, \tag{5.8}$$

where p is the pressure in Pa, U_b is the bulk velocity, f is the frequency in Hz, D is the diameter of the inner rod in m, ρ is the density in kg/m^3 and PSD is the power spectral density of pressure in Pa^2/Hz.

Fig. 5.35 shows the azimuthal distributions of the RMS fluctuations of reduced pressure at various altitudes (upstream denoted as -HD and downstream denoted as 1 HD, 2 HD and 3 HD). These were compared to experimental data at the lowest available Reynolds number 58500. Overall, one can observe that the order of magnitude is reproduced upstream and downstream the spacer grid, even though there are some discrepancies. RMS pressure peaks are observed close to the azimuthal locations in line with the mixing vanes (0° and 180°). It is interesting to observe that at 1 HD, the square grid case is the closest to the experimental results but at 2 HD, it is the mixing vane case. In fact for the mixing vane case (MV), the peak magnitude at 0° increases from 0.02 at 1 HD to 0.025 at 2 HD and then decreases to 0.016 at 3 HD whereas in SQ case, it decreases monotonically. It is also seen that the increase magnitude of reduced pressure from upstream to downstream is more pronounced in the experiment than in the simulations. For instance, in the experiment, it increases from 0.007 to 0.03 (considering the lowest value) whereas in CG case, it increases from 0.01 to 0.015. At 1 HD, difference in peak value between SQ and MV case is 0.04 and 0.0175, i.e., an increase of 2.3 times. At 2 HD, peak values of both cases almost overlap (≈ 0.025). The RMS pressure fluctuations

for the CG case is expectedly uniform due to its symmetric structure. At 1 HD, considering the area under the curve, SQ is an approximate summation of MV and CG cases. At 2 HD, CG looks more of an average between SQ and MV cases. Nevertheless, the SQ case, which is in fact geometrically closest to the experimental setup, reproduces well the increase in pressure fluctuations at 0° and 180° induced by the presence of the grid and vanes.

Comparing the cases accounting for mixing vanes (SQ and MV) and the circular grid case (CG), one could say that the mixing vanes tend to concentrate the pressure fluctuations at the two azimuths in line with the mixing vanes (0° and 180°) at the expense of other azimuthal positions.

It is also important to observe that in case of the simulations, the magnitude of RMS pressure is higher at 0° than at 180° even though the relative position of the vanes and grid are symmetric. This is explained in the following paragraph.

The RMS pressure on the x-z plane for the 3 cases are shown in Fig. 5.36. The same is plotted on the x-y plane at increasing altitudes in Figs. 5.37, 5.38 and 5.39 respectively for MV, CG, SQ cases. The asymmetric behavior of RMS pressure at 0° and 180° is more pronounced in MV case.

The main reason could be the slightly oblique structure of the mixing vanes (represented by the *white* blocks in Fig. 5.36a) on both sides of the annular canal. On the left canal of the annulus, the pressure fluctuations are diverted towards the inner wall whereas on the right side, those are diverted towards the outer wall. This can again be viewed in Fig.5.37 where the RMS pressure on x-y plane is plotted at increasing values of z. At 0.015 HD, 1 HD and 2 HD, it can be seen that the stronger fluctuations on the left side are towards the inner wall and those on the right side are towards the outer wall. At 1 HD, the maximum pressure fluctuation is 22 Pa and mimimum is 14 Pa. In general, larger fluctuations were observed in the vicinity of the vanes whereas the field was homogeneous in the rest of the canal. Another reason for the asymmetric profile could be due to the unstructured mesh around the vanes which leads to asymmetry in the mesh on either side. The unstructured region extends from -0.13 HD to 0.13 HD. But the probes are located in the structured region at 0.15 HD, 1 HD, 2 HD and 3 HD. The third reason could have been the length of the downstream section where the zero outlet pressure may affect the flow pattern inside. The current simulation was performed with 4 HD length downstream. A test simulation was performed for 2 hydraulic diameter downstream length and it was observed that the profiles at 0.15 HD, 1 HD and 2 HD are respectively similar to the current case. So length of downstream section does not seem to be responsible for the asymmetric fluctuations. Similar asymmetric pattern was observed in case of RMS velocity fluctuations as well

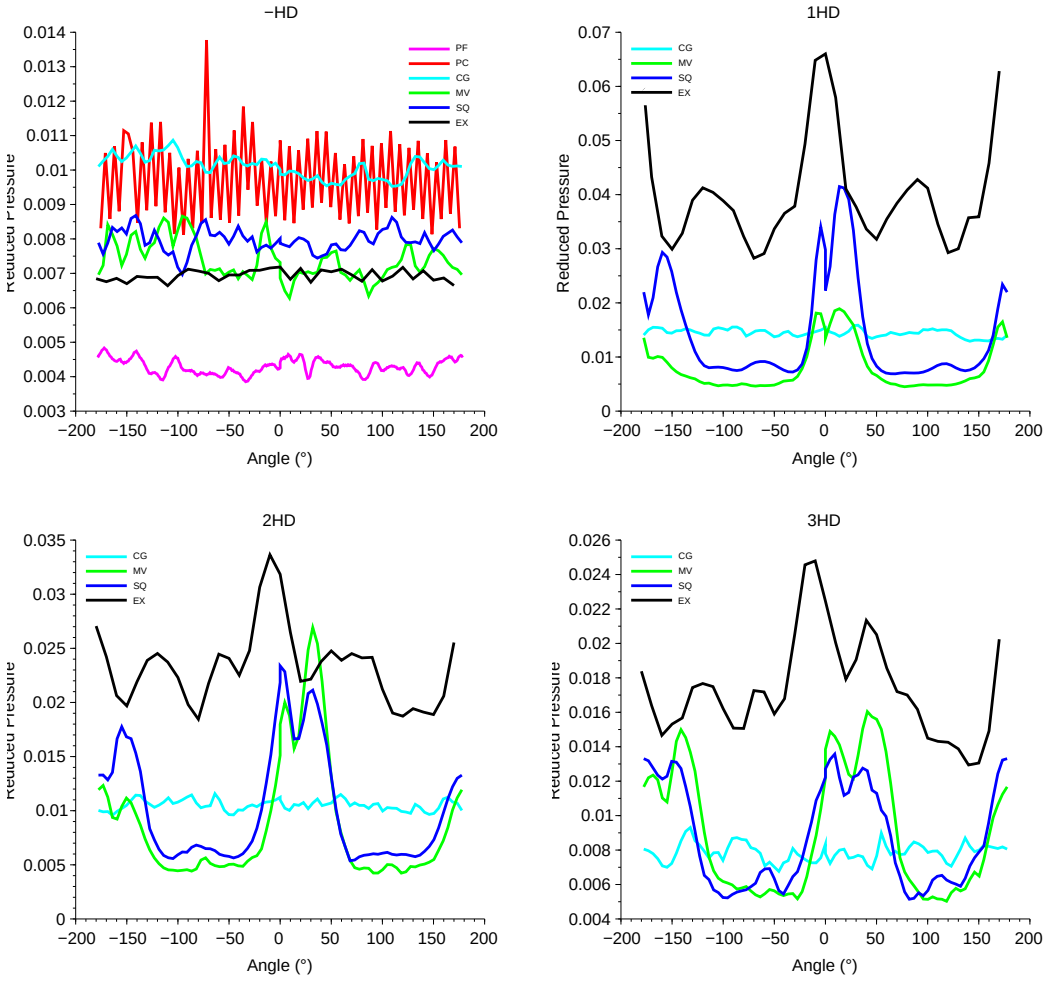

Figure 5.35: RMS of reduced pressure upstream and downstream of the spacer grid and/or vanes as the case may be (CG, MV, SQ). EX denotes CALIFS experimental data at $Re_D = 58500$

(discussed previously in Section 4.5.1). Also, the fact that the vanes were modeled as parallelepiped instead of rounded edges (as in CALIFS experiment) could have a likely effect on the flow.

One can observe that the simulations fail to reproduce the pressure fluctuations ('secondary' peaks) seen in the experiment in the region between the mixing vanes at 90° and 270°. This difference could be attributed to the absence of spring and dimple configuration in the simulation. Previously, it was observed that the square grid accelerated the flow. Therefore, introduction of spring and dimple on the spacer grid should further accelerate the flow. So, it seems that the effect of the spring and dimple is not negligible. Similar discrepancy between simulation and experiment was reported by Bieder [2013] for LES with TrioCFD on a 5×5 rod bundle where spring and dimple was not considered in the simulation.

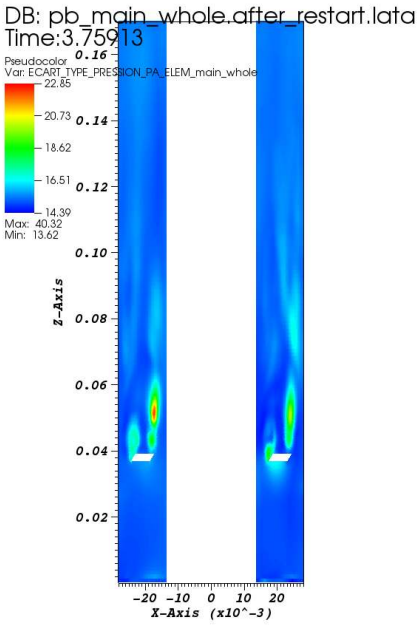

(a) MV case

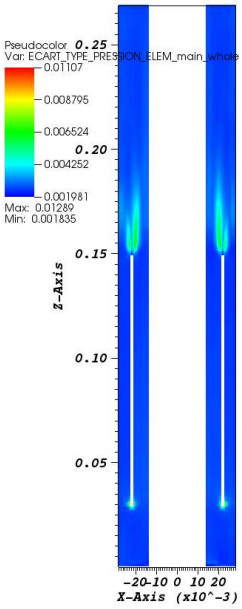

(b) CG case

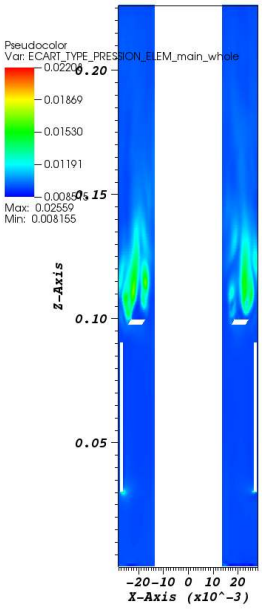

(c) SQ case

Figure 5.36: RMS pressure fluctuations as seen from x-z plane (y=0)

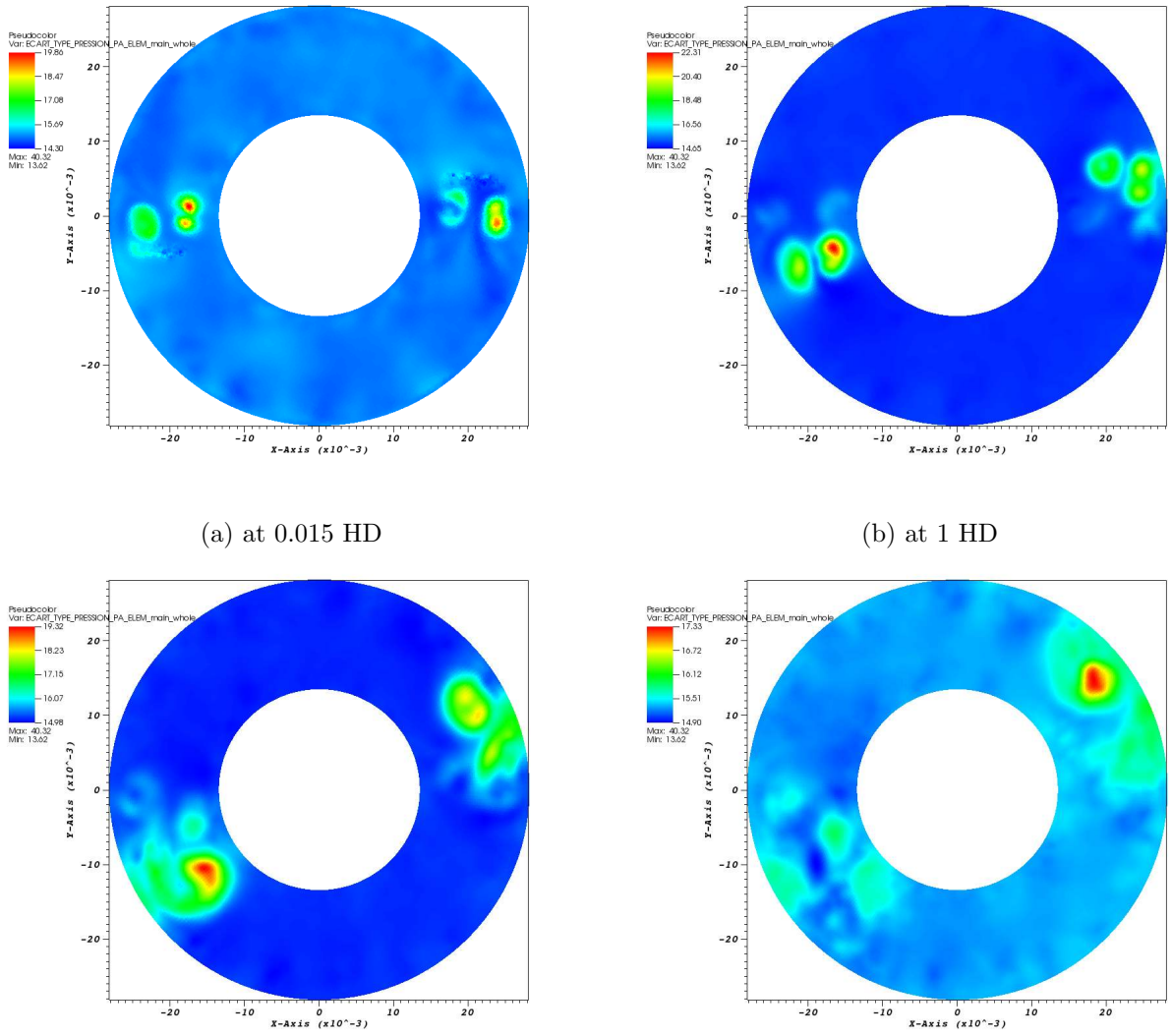

(a) at 0.015 HD

(b) at 1 HD

(c) at 2 HD

(d) at 3 HD

Figure 5.37: RMS pressure field on x-y plane at increasing altitudes (MV case)

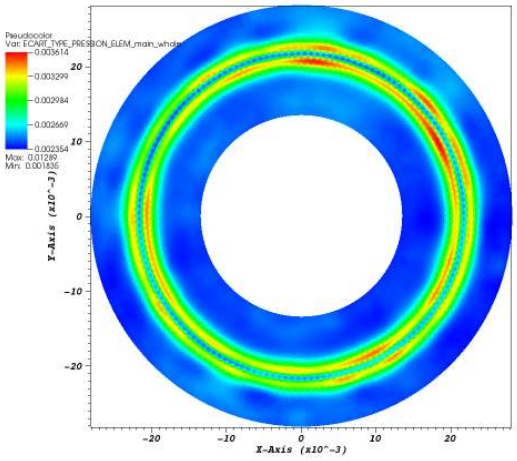

(a) at 0.04 HD

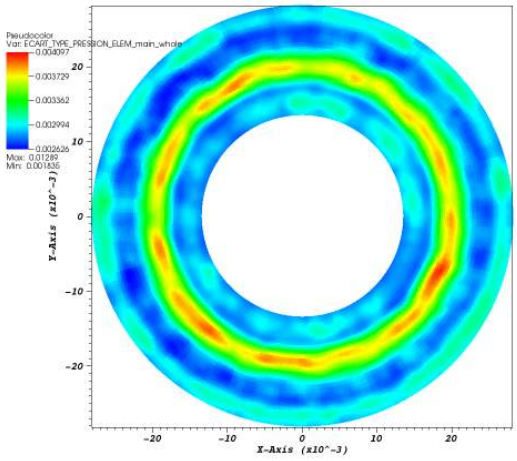

(b) at 1 HD

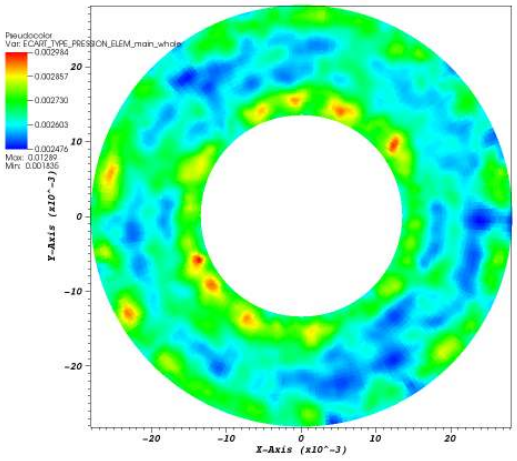

(c) at 2 HD

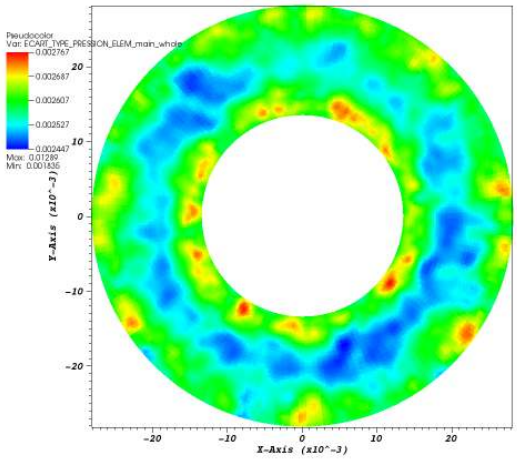

(d) at 3 HD

Figure 5.38: RMS pressure field on x-y plane at increasing altitudes (CG case)

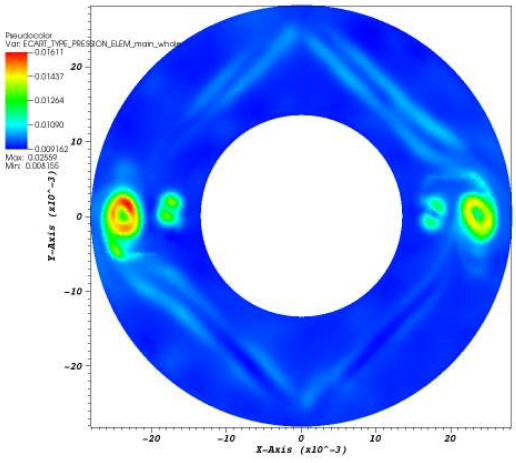

(a) at 0.015 HD

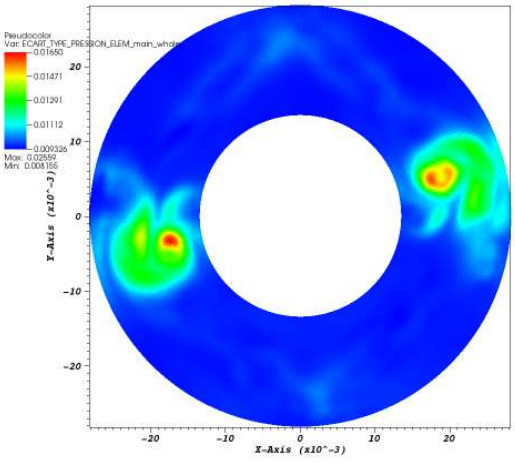

(b) at 1 HD

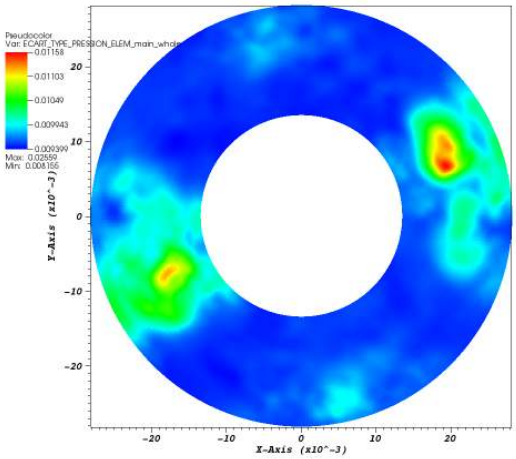

(c) at 2 HD

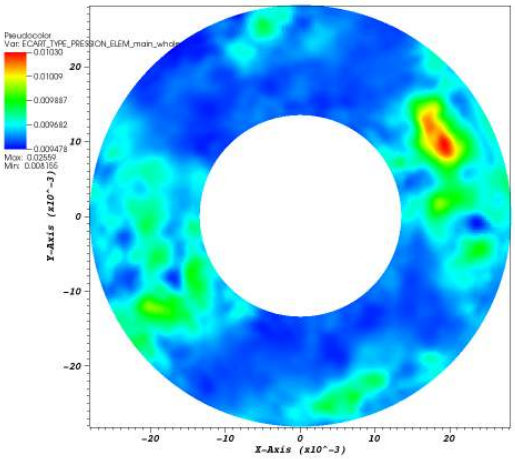

(d) at 3 HD

Figure 5.39: RMS pressure field on x-y plane at increasing altitudes (SQ case)

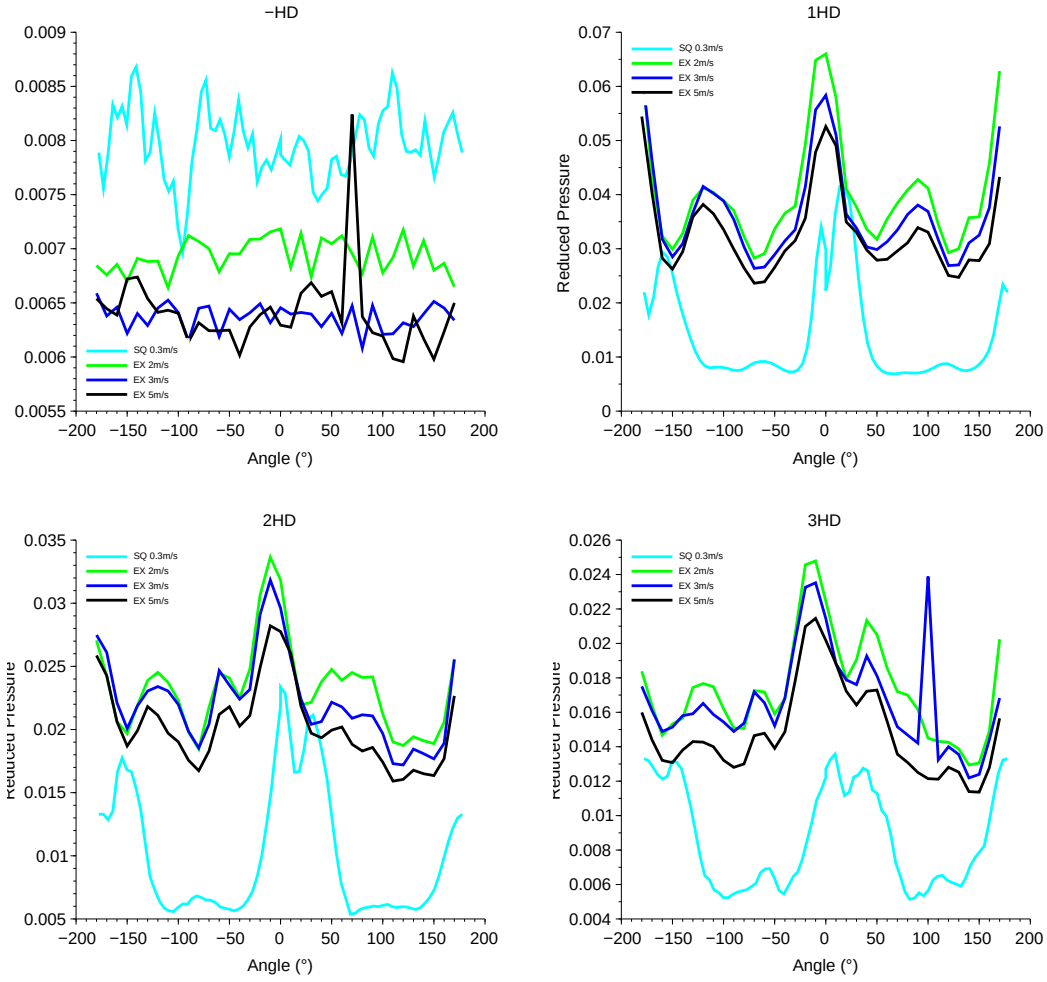

Figure 5.40: Comparison of RMS reduced pressure for SQ case with experiment at 3 velocities

Fig. 5.40 shows the effect of Reynolds number on RMS reduced pressure fluctuation for experimental results. Experimental data was plotted for three different velocities 2 m/s, 3 m/s and 5 m/s. This was compared to simulation result for SQ case for velocity 0.298 m/s ≈ 0.3 m/s. One can observe that the Reynolds number introduces some changes. As Reynolds number increases, the RMS reduced pressure decreases. But it is not enough to explain the differences between simulations and experiment. So, this could be attributed to the geometrical simplifications which were considered in the model.

Next, the comparison between simulations and experiment is presented in terms of power spectral density (PSD). Fig. 5.41 shows the reduced PSD upstream of the grid for experiment and simulations. Similar to the case of RMS fluctuations, the spectra are reproduced with a good order of magnitude. Looking at the case of the annular pipe with fine mesh (PF in the left figure or PF 0.3 m/s in the

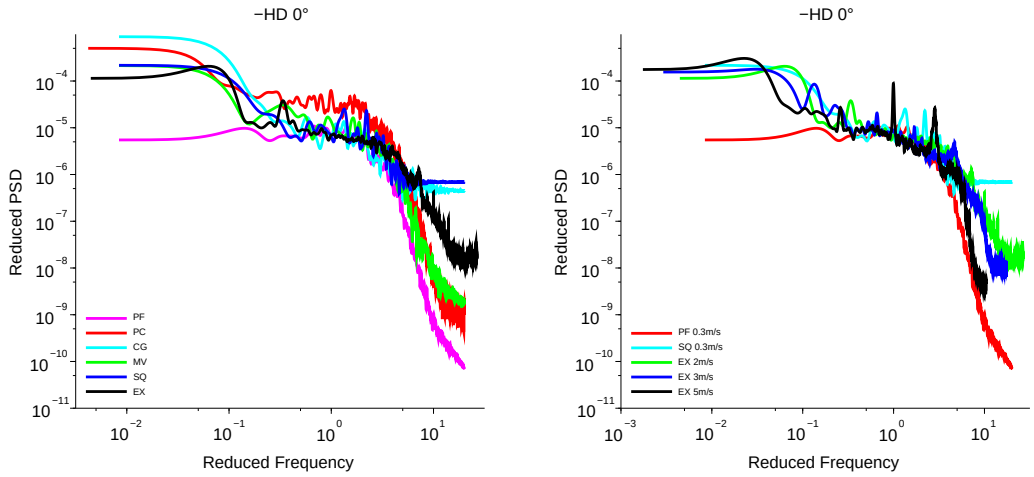

Figure 5.41: Comparison of PSD for experiment and simulation upstream of the grid or vanes

right figure), the slope of the spectrum changes at $f_{red} = 3$.

The reduced PSD of pressure at 1, 2 and 3 HD downstream of the grid are presented in Fig. 5.42. In line with the mixing vanes (0°), the simulations are close to the experiments specially the SQ case at 2 and 3 HD, even though there are some discrepancies at lower frequencies. But out of line with the vanes (at 60° azimuthal location), the differences between experiment and simulation are more stronger. These strong differences could be due to the simplification in simulation model (absence of spring and dimple). Here at 1 HD, peaks are observed for SQ and CG cases. Peaks are more prominent out of line with MV. Since the effect of the vanes do not extend upto 60° azimuthal location, no such peak is observed for MV case. At 2 HD, a less prominent peak is observed only for CG case. This could lead to the conclusion that the presence of the vanes in SQ case accelerates the decay of pressure fluctuations. At 3 HD, the spectra almost collapse.

Moreover, the peaks observed in the simulations are not present in the experimental results. And again the effect of Reynolds number is not enough to explain the differences between experiments and simulations (Fig. 5.43). The spectra in line with MV (left) match well in the high frequency range f_r = 1 - 10. The differences observed in the spectra out of line with MV (right) could again be attributed to the absence of spring and dimple.

More pressure spectra to compare experiment and simulations have been presented in Appendix G.

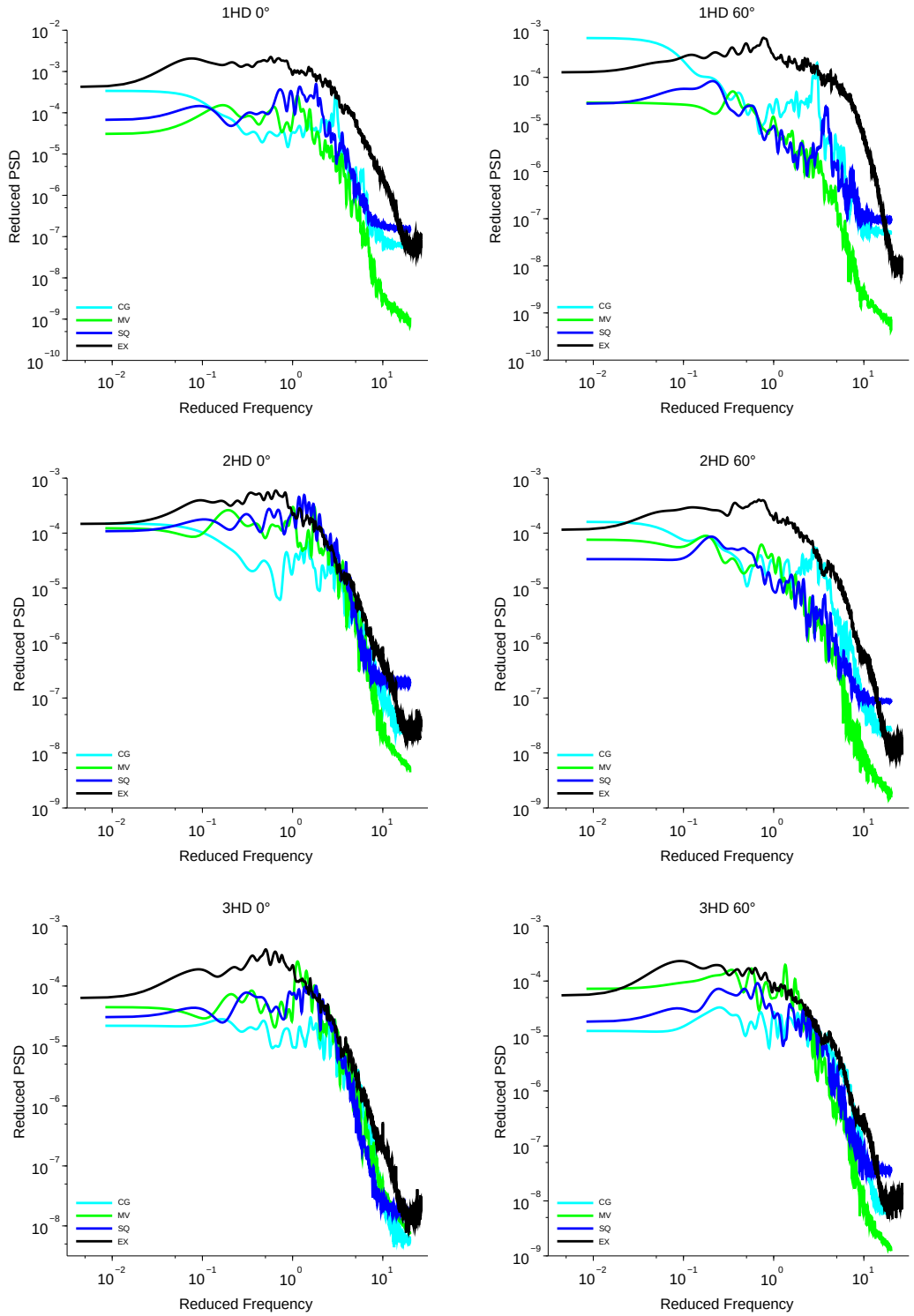

Figure 5.42: Comparison of PSD for experiment and simulation downstream of the grid or vanes [left: in line with MV; right: out of line with MV]

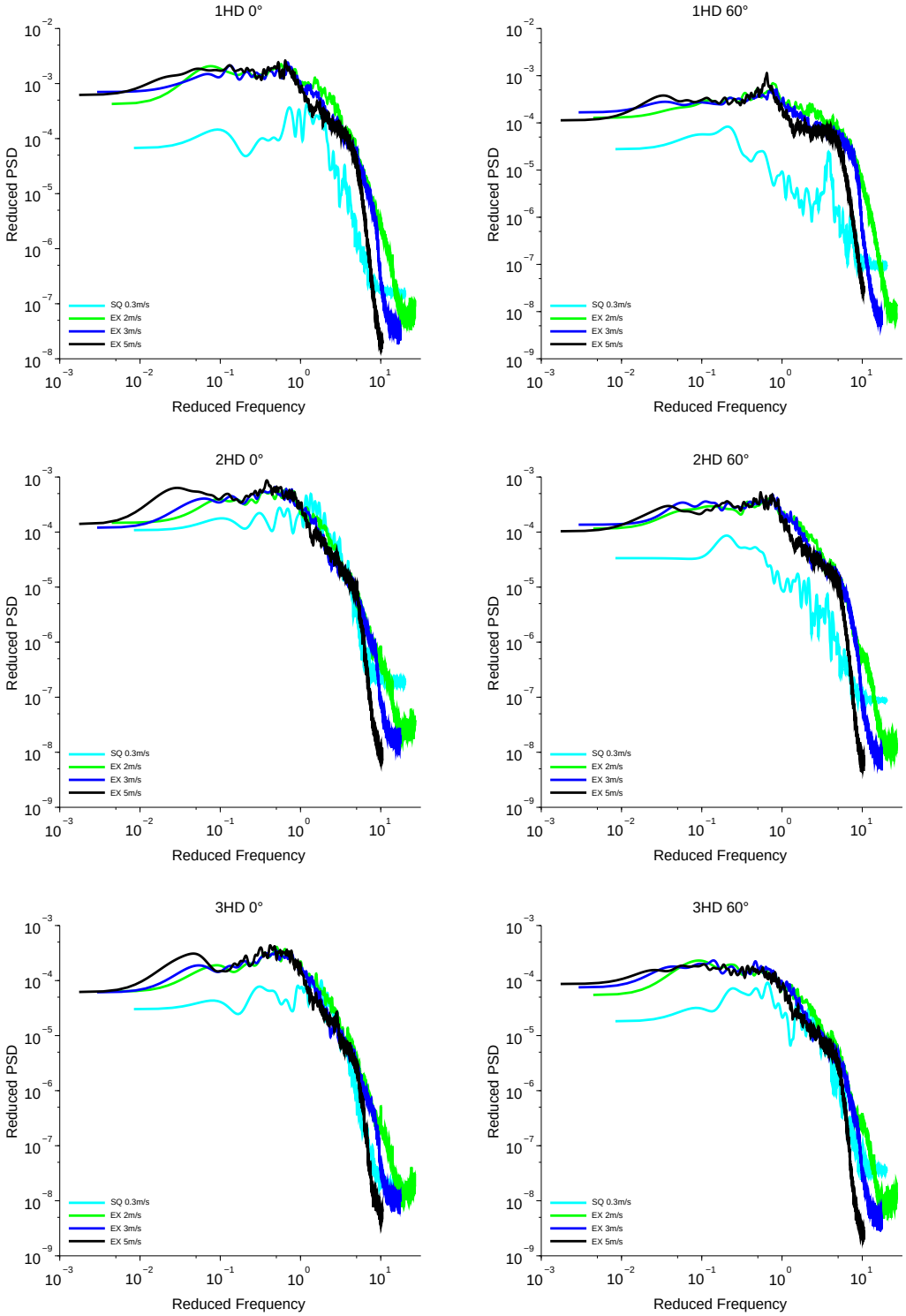

Figure 5.43: Comparison of PSD for SQ case with experiment at 3 velocities [left: in line with MV; right: out of line with MV]

5.9 Comparison with empirical models

In this section, some preliminary comparisons are made between the simulations and classical semi-empirical models discussed previously in Chapter 2. The empirical models by Corcos [1963] and Chase [1987] are valid for studying wall pressure field beneath a turbulent boundary layer on a flat plate. Comparisons are made for the annular pipe fine mesh case (PF) and square grid case (SQ). Table 5.3 lists out the constants used in Chase's model.

Constant	Annular pipe (PF)	Square grid (SQ)
C_M	0.1840	5.628×10^{-6}
C_T	0.0075	5.628×10^{-4}
U_c	0.5 U_b	0.6 U_b
b	3	3
h	7	10

Table 5.3: Constants for Chase's model

Fig. 5.44 shows the behavior of the pressure spectra using Chase's and Corcos' models on the annular pipe fine mesh case (PF). The continuous lines denote the model and dashed lines denote the simulation results. Data for the axial probe at 0° was considered for this purpose. The curves show some resemblance at lower wavenumbers. But no further interpretation can be made. Similarly, Fig. 5.45 shows the behavior of the pressure spectra upon using Chase's and Corcos' models on the square grid case (SQ). Data for an axial probe at 90° (out of line with the vanes) was considered for this purpose. It is interesting to see that the square grid gives better comparison to the models than the annular pipe. This may be due to the presence of obstacles which changes the flow structure with regards to the wall pressure field. However, it seems that the wavenumber resolution is bad; a much larger spatial extent of the domain is needed to better characterize the spectra in wavenumbers.

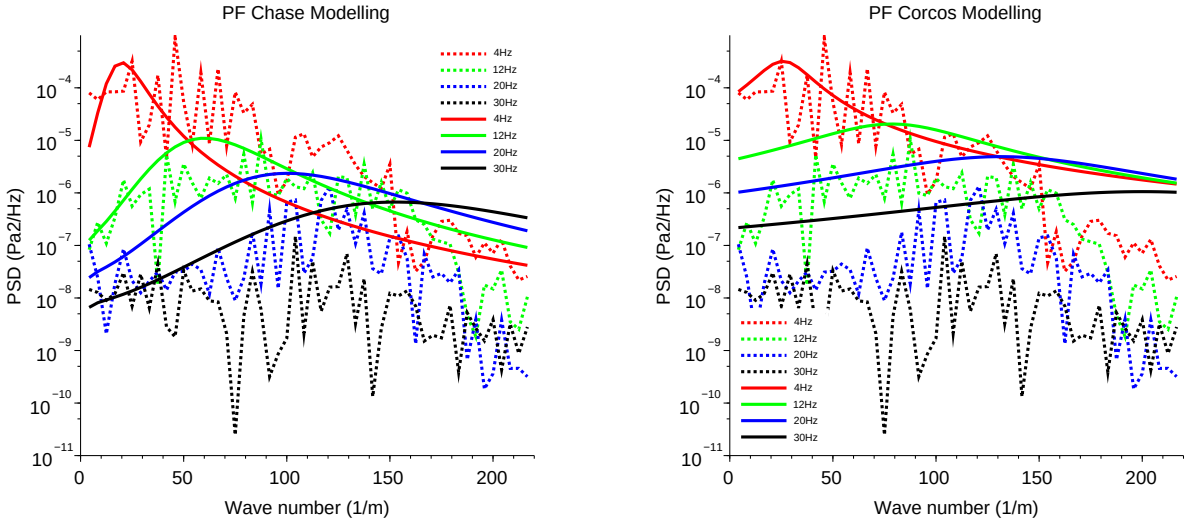

Figure 5.44: Chase's (left) and Corcos' (right) models applied to the annular pipe case (PF) [*Continuous* lines denote the model and *dashed* lines denote the simulation]

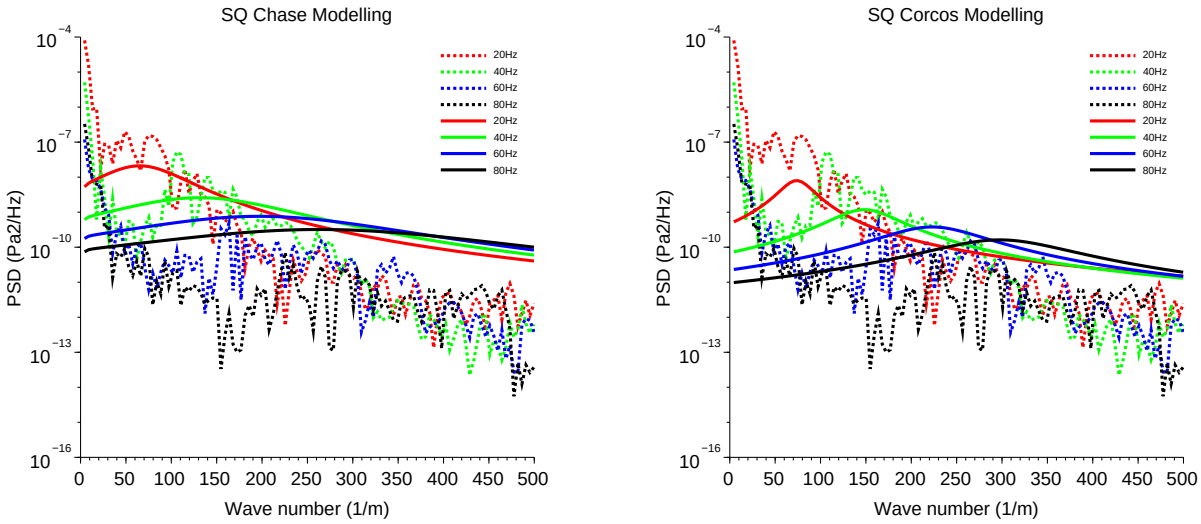

Figure 5.45: Chase's (left) and Corcos' (right) models applied to the square grid case (SQ) [*Continuous* lines denote the model and *dashed* lines denote the simulation]

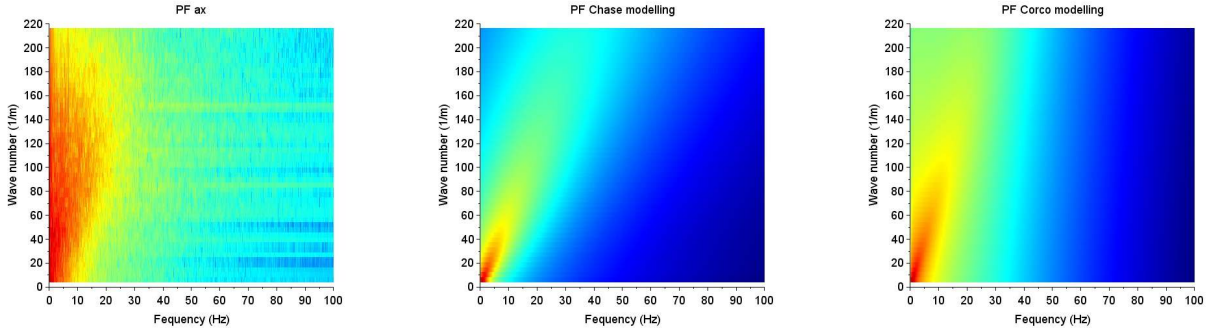

(a) Simulation result (b) Chase's model (c) Corcos' model

Figure 5.46: Comparison of simulation (repeated from Section 5.7) with empirical models (PF case)

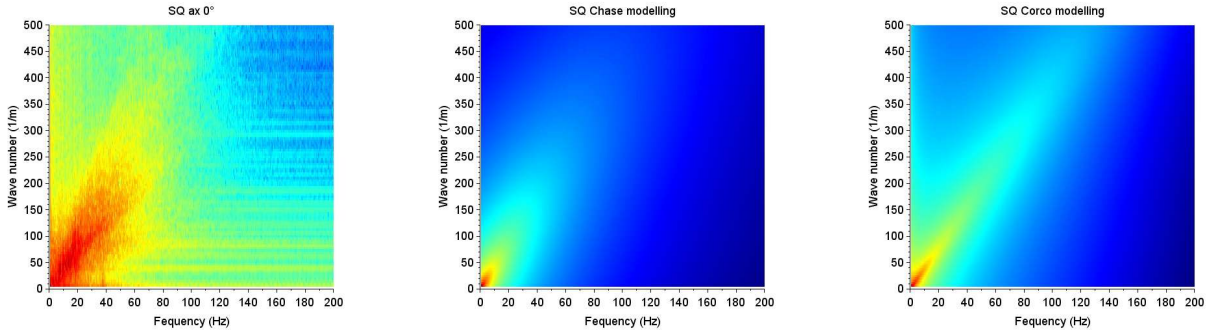

(a) Simulation result (b) Chase's model (c) Corcos' model

Figure 5.47: Comparison of simulation (repeated from Section 5.7) with empirical models (SQ case)

Figs. 5.46a to 5.46c compare the wave-number-frequency diagrams of the simulation (previously discussed in Section 5.7) to the Chase's and Corcos' models in case of the annular pipe (PF). Figs. 5.47a to 5.47c compare the wave-number-frequency diagrams of the simulation to the Chase's and Corcos' models in case of the square grid (SQ). Once again, one observes better matching of the square grid results compared to the annular pipe results.

Goody [2004] proposed an empirical model for representing the pressure spectra in frequency domain for a flat plate taking into account the influence of Reynolds number. A preliminary comparison is presented in Fig. 5.48 for the annular pipe and square grid cases. For the annular pipe, data corresponds to an axial probe at 0° whereas for the square grid case, data corresponds to an axial probe at 90° (out of line with the vanes).

Finally, it should be kept in mind that these comparisons with empirical models were a preliminary investigation. Further comparison should be done by developing more appropriate models for such complex structures.

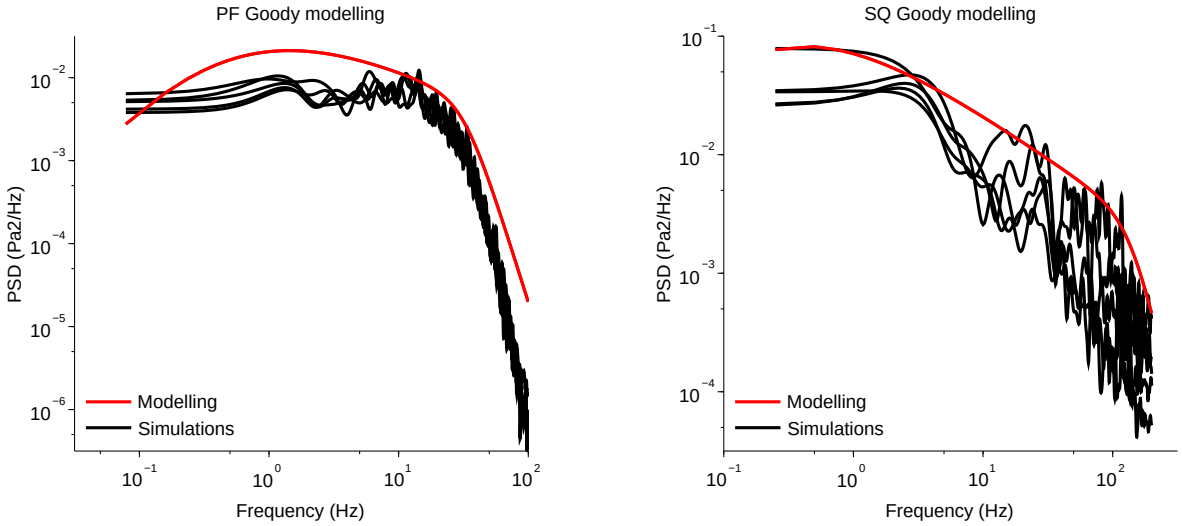

Figure 5.48: Application of Goody's model to the annular pipe PF case (left) and square grid SQ case (right)

5.10 Conclusion

In this chapter, the wall pressure field was analyzed for various simulations and compared to experiments and semi-empirical models. In all the cases, the lateral fluid forces show high fluctuation immediately downstream of the vanes or grid as the case may be. Pressure correlation length was calculated for each case. Comparison of correlation length for annular pipe with literature values showed good agreement. The coarse mesh for the annular pipe is not sufficient for studying wall pressure field. It leads to wrong prediction of the wall pressure field. Smaller correlation lengths were observed close to the vanes due to strong turbulence. The grid and the mixing vanes have a combined effect; the grid accelerates the flow and amplifies the fluctuations induced by the vanes. A POD analysis showed that the coarse and fine meshes predict very different behavior with respect to the energy captured by the POMs.

Spectral analysis of axial and azimuthal wall pressure fields shows that SQ case generates the most inhomogeneous spectra (both axially and azimuthally). Frequency peaks of 30 and 38 Hz were observed in the pressure spectra of CG and SQ cases respectively. These could be related to Strouhal number for oscillating flows.

The comparison with experiment illustrated that the simulations were comparable to some degree in spite of the simplification made to the geometry by ignoring the spring and dimple. Nevertheless some discrepancies remain and may be due to the absence of springs and dimples. Further simulations

could be performed with simplified springs and dimples to see their effect. In this study, pressure was non-dimensionalized with bulk velocity. In the future, non-dimensionalization with other parameters like friction velocity could be attempted. In this case, the friction velocity was not available for the experiment. Moreover simulations should be done at higher Reynolds number to see if the frequency peak observed in the simulations are due to vortex shedding.

Preliminary comparisons were made with some semi-empirical models developed for turbulent boundary layer on a flat plate. It was interesting to note that the square grid case was more close to the model than the annular pipe. This may be attributed to the presence of the geometrical obstacles which changes the flow structure thereby modifying the wall pressure field. However, to obtain some definitive conclusions, further comparisons with more appropriate models should be made.

Chapter 6

General Conclusion

The goal of the thesis was to study hydrodynamic forces exerted on fuel rods by the fluid in a pressurized water reactor (PWR). LES turbulence modeling technique was chosen to study the transient behavior. Due to the very complex structure inside a PWR fuel assembly, certain simplifications were considered in the simulation model before carrying out the transient calculations. The objective was to use simple 3D geometries in order to understand the interaction between the fluid forces and the structures. Instead of reactor-scale Reynolds number $Re_D = 500000$, a lower value $Re_D = 8900$ was chosen for the simulations because the idea was to perform multiple simulations with different 3D geometries in a limited time, obtain stable solutions and then do comparative studies.

In Chapter 3, calculations were performed on an annular pipe of radius ratio 0.5 with fully structured tetrahedral meshes using the CFD code TrioCFD (previously Trio_U). Meshes were generated using Gmsh. Five different mesh resolutions were chosen with increasing order of refinement. A stronger dependence on the azimuthal mesh resolution was observed compared to the axial resolution among the five meshes. Considering a compromise between accuracy and computational cost, a mesh resolution of the order of 1 in radial, 3 in azimuthal and 10 in axial direction (in wall units) was found to be acceptable to simulate such an annular pipe. The simulations were validated with numerous data available in the literature. These simulations helped us to develop proper inlet boundary conditions for the subsequent complex geometries and also increase confidence in TrioCFD code.

In Chapter 4, three geometrical singularities were introduced inside the annular pipe: two symmetrically placed mixing vanes (MV), a circular spacer grid (CG) and a square spacer grid with the two symmetrically placed mixing vanes (SQ). These domains were designed by taking into account the exact dimensions of the CALIFS experimental setup with a few exceptions: spring and dimple

on the grid surface and rounded edges of the mixing vanes were ignored. A hybrid meshing strategy was adopted for the cases with mixing vanes (i.e., MV and SQ): unstructured mesh around the vanes and structured mesh in the upstream and downstream regions. The axial mesh resolution became poorer as one moved away from the unstructured region. The circular grid was designed by taking into account the ratio of the hydraulic diameters of the inner and outer flow areas. Although it was a theoretical design, the inherent symmetry allowed one to generate fully structured tetrahedral mesh which led to faster computation and easy post-processing. The concept of maintaining a structured mesh as far as possible improved the speed of the simulation and also reduced numerical errors which may arise due to interpolation by the code from the calculation node to the probe location. In the three cases MV, CG and SQ, the mesh resolution in wall normal direction was approximately 3 (in wall units). Reichardt's wall function was used to model the near wall behavior.

The comparison of flow characteristics at 1 HD and 2 HD downstream locations between the MV case and SQ case showed a higher peak velocity for the SQ case. This was caused by the acceleration of the flow near the inner wall. The presence of the grid led to deceleration near the outer wall. This effect reduced as one went further downstream. Comparing the velocity profiles for the probes in line with MV and out of line with MV, it was clear that the mixing vanes introduced maximum fluctuations. The mixing vanes created a deflection in the flow pattern creating a swirl structure which evolved in the axial direction. Also, it seemed that the SQ case is a summation effect of the MV and CG cases. RMS velocity fluctuations were stronger at 1 HD compared to 2 HD. Azimuthal component of mean velocity showed strong destabilization of the flow by the vanes.

In Chapter 5, various ways of characterization of the wall pressure field on the inner wall of the pipe were presented and the simulations were compared to experimental data. Looking at the axial and azimuthal spatial correlations for pressure, it was observed that the chosen coarse mesh resolution was not sufficient to characterize the wall pressure field in an annular pipe. Similar to the hydrodynamic analysis, the summing effect of the SQ case was observed individually more or less with the mixing vanes case and circular grid case for the pressure field as well. Spectral analysis of axial and azimuthal wall pressure fields showed that the square grid (SQ) case generates the most inhomogeneous spectra. Frequency peaks were observed in the pressure and velocity spectra in CG and SQ cases respectively. These could be related to Strouhal number. Although the numerical simulations were carried out at Reynolds number 8900 which is about 6 times lower than that of CALIFS experiment (58500 and above), yet the simulation and experimental results were qualitatively comparable. The discrepancies

observed could be attributed to the absence of spring and dimple on the square grid surface which would lead to further acceleration of the flow. For this comparative study, pressure was non-dimensionalized with bulk velocity. In the future, non-dimensionalization could be carried out with friction velocity. This was not possible for the present case because friction velocity data was not available for CALIFS experiment. Overall, the mixing vanes and the circular spacer grid seemed to have a cumulative effect equivalent to the square spacer grid.

Preliminary comparisons were performed with some classical semi-empirical models (valid for turbulent boundary layer on a flat plate) and it was found that the square grid case was more close to the model than the annular pipe case. This may be attributed to the presence of the geometrical obstacles which changed the flow structure thereby modifying the wall pressure field. However, in the future, more appropriate models for such complex structures should be developed to obtain definitive conclusions.

Finally, one can conclude that the simplified approach demonstrated interesting results on the effect that different structural components have on the hydrodynamic and wall pressure characteristics. However, these simplified models do not seem to be sufficient enough to predict the realistic behavior of fluid forces inside a PWR fuel assembly. Nevertheless, this initial study opens up interesting perspectives towards improving the modeling strategy and understanding the complex phenomena leading to wear in fuel rods.

So, in the future, from a structural point of view, it would be important to add spring and dimple to the spacer grid surface. It should be noted that similar discrepancies between simulation and experimental results were reported by Bieder [2013] who carried out LES on a 5×5 rod bundle without taking into account spring and dimple.

From a simulation point of view, the following computations should throw up interesting results in the future.

- Perform mesh sensitivity tests near the mixing vanes.
- Perform wall-resolved LES with $y^+ \approx 1$ (this resolution was attained only for the annular pipe configuration).
- Simulate for higher Reynolds number as close to the experimental value as possible (for MV, CG and SQ cases). Although looking at the CALIFS experimental results, change in Reynolds number does not seem to have a significant effect on wall pressure fluctuations. In this thesis,

effect of Reynolds number has been reported only for the annular pipe case. Also, it would be interesting to see if the frequency peaks observed at $Re_D = 8900$ are reproduced at higher Re_D. It should be noted that no frequency peaks were observed in the experimental results.

- Effect of Reichardt's wall function on the wall pressure field should be investigated by either refining the mesh close to the walls or by simulating a lower Reynolds number for the same mesh. In this way, use of wall functions could be avoided.

On the other hand, from an experimental point of view, the following could be performed:

- experiment at a lower Reynolds number (in the CALIFS experiment, due to the lower threshold limit of the pump flow rate, measurements could not be done for Reynolds number less than 58500);
- experiment with such simplified structures.

After obtaining the spectra of fluid force or pressure from CFD simulations, this spectra could be fed into a structural dynamics code to obtain the rod vibration characteristics like modes, amplitude etc. by modeling the rod as a beam constrained at the spacer grid locations. From the fluid force and amplitude of rod displacement, one could obtain work rates which could subsequently be used to estimate wear rates and scar depth at contact locations. Few developments in this regard are cited below. Rubiolo [2006], Rubiolo and Young [2008, 2009] developed a probabilistic non-linear vibration model VITRAN to predict fretting wear by taking into account the dynamic response of the fuel rod and spacer grid. Meng and Ludema [1995] reported some empirical models to study fretting wear and Kim [1999] discussed the modeling of fretting wear in terms of energy dissipation by analyzing shear stresses at contact locations between the rod and grid.

List of Figures

List of Tables

References

I. Abalakin and B. Koobus. The behavior of two near wall models for k-ϵ prediction of stall. Technical Report RR-4075, Institut National de Recherche en Informatique et en Automatique (INRIA), Sophia-Antipolis, France, November 2000. URL `https://hal.archives-ouvertes.fr/file/index/docid/72558/filename/RR-4075.pdf`.

ADTSC Science Highlights. *Associate Directorate for Theory, Simulation and Computation (ADTSC), Los Alamos National Laboratory (LANL), USA*. 2013. URL `http://www.lanl.gov/orgs/adtsc/publications/science_highlights_2013/docs/2013BookFile.pdf`.

V. Y. Agbodemegbe, X. Cheng, E. H. K. Akaho, and F. K. A. Allotey. An investigation of the effect of split-type mixing vane on extent of crossflow between subchannels through the fuel rod gaps. *Annals of Nuclear Energy*, 88:174–185, 2016.

J. S. An and Y. D. Choi. A study of heat transfer characteristics of large scale vortex flow mixing vane of nuclear fuel rod bundle. *Transactions of the Korean Society of Mechanical Engineers - B (in Korean)*, 30(1(WN.244)):24–31, 2006a.

J. S. An and Y. D. Choi. A study of turbulence generation characteristics of large scale vortex flow mixing vane of nuclear fuel rod bundle. *Korean Journal of Air-conditioning and Refrigeration Engineering (in Korean)*, 18(10):811–818, 2006b.

J. D. Anderson Jr. *Computational Fluid Dynamics: An Introduction*. Springer Berlin Heidelberg, 3rd edition, 2009. Chapter 2.

P.-E. Angeli. Large-Eddy Simulation of thermal striping in WAJECO and PLAJEST experiments with TrioCFD. In *Proceedings of 16th International Topical Meeting on Nuclear Reactor Thermal Hydraulics (NURETH-16)*, Chicago, USA, August 2015.

P.-E. Angeli, U. Bieder, and G. Fauchet. Overview of the TrioCFD code: Main features, V& V procedures and typical applications to nuclear engineering. In *Proceedings of 16th International Topical Meeting on Nuclear Reactor Thermal Hydraulics (NURETH-16)*, Chicago, USA, August 2015.

F. Axisa. *Modélisation des systèmes mécaniques: Vibrations sous écoulements*, volume 4. HERMES Sciences Publications, Paris, France, 2001.

F. Axisa, J. Antunes, and B. Villard. Random excitation of heat exchanger tubes by cross flows. *Journal of Fluids and Structures*, 4(3):321–341, 1990.

I. Azouz and S. A. Shirazi. Evaluation of several turbulence models for turbulent flow in concentric and eccentric annuli. *Journal of Energy Resources Technology*, 120(4):268–275, 1998.

J. Bakosi, M. A. Christon, R. B. Lowrie, L. A. Pritchett-Sheats, and R. R. Nourgaliev. Large eddy simulations of turbulent flow for grid-to-rod fretting in nuclear reactors. *Nuclear Engineering and Design*, 262:544–561, 2013.

R. Bavière, N. Tauveron, F. Perdu, E. Garré, and S. Li. A first system / CFD coupled simulation of a complete nuclear reactor transient using CATHARE2 and TRIO_U. Preliminary validation on the Phénix Reactor Natural Circulation Test. *Nuclear Engineering and Design*, 277:124–137, 2014.

S. Bellizzi and R. Sampaio. POMs analysis of randomly vibrating systems obtained from Karhunen-Loève expansion. *Journal of Sound and Vibration*, 297(3-5):774–793, 2006.

S. Benhamadouche and D. Laurence. LES, coarse LES, and transient RANS comparisons on the flow across a tube bundle. *International Journal of Heat and Fluid Flow*, 24(4):470–479, 2003.

S. Bhattacharjee, G. Ricciardi, and S. Viazzo. LES in a concentric annular pipe: Analysis of mesh sensitivity and wall pressure fluctuations. In *Proceedings of the ERCOFTAC Workshop Direct and Large Eddy Simulation 10 (DLES10)*, Limassol, Cyprus, May 2015a.

S. Bhattacharjee, G. Ricciardi, and S. Viazzo. Modeling of fluctuating fluid forces exerted on the walls of a concentric annular pipe using large eddy simulation. In *Proceedings of 16th International Topical Meeting on Nuclear Reactor Thermal Hydraulics (NURETH-16)*, Chicago, USA, August 2015b.

U. Bieder. Analysis of the flow down- and upwind of split type mixing vanes. In *Proceedings of the CFD for Nuclear Reactor Safety Applications (CFD4NRS-4) Conference on Experimental Validation and Application of CFD and CMFD Codes in Nuclear Reactor Technology, OECD/NEA and IAEA Workshop*, Daejeon, South Korea, 2012.

U. Bieder. Analysis of the flow field in a simplified PWR assembly with mixing grid. Technical Report DEN/DANS/DM2S/STMF/LMSF/RT/12-011/A, CEA Cadarache, France, 2013.

U. Bieder. CFD ANALYSIS OF NON-AXIAL FLOW IN FUEL ASSEMBLIES. In *Proceedings of 16th International Topical Meeting on Nuclear Reactor Thermal Hydraulics (NURETH-16)*, Chicago, USA, August 2015.

U. Bieder and E. Graffard. Qualification of the CFD code Trio_U for full scale reactor applications. *Nuclear Engineering and Design*, 238(3):671–679, 2008.

U. Bieder, C. Calvin, and P. Emonot. PRICELES: A parallel CFD 3-dimensional code for industrial large eddy simulations. In *Proceedings of Parallel Computational Fluid Dynamics - Trends and Applications*, Trodheim, Norway, 2000a. URL `http://www.elsevier.com/books/parallel-computational-fluid-dynamics-2000/jenssen/978-0-444-50673-3`.

U. Bieder, C. Calvin, and P. Emonot. PRICELES: An object oriented code for industrial LES. In *Proceedings of CFD2K: 8th Annual Conference of CFD Society of Canada*, pages 439–444, Montreal, Canada, 2000b. URL `ftp://rcom.univie.ac.at/mirrors/lib.stat.cmu.edu/imsbull/mirror/ims/bulletin/march00/node26.html`.

U. Bieder, C. Calvin, and H. Mutelle. Detailed thermal hydraulic analysis of induced break severe accidents using the massively parallel CFD code Trio_U / PRICELES. In *Proceedings of the International Conference on Supercomputing in Nuclear Applications (SNA-2003)*, Paris, France, 2003.

U. Bieder, G. Fauchet, S. Bétin, N. Kolev, and D. Popov. Simulation of mixing effects in a VVER-1000 reactor. *Nuclear Engineering and Design*, 237(15-17):1718–1728, 2007. Special issue: 11th International Topical Meeting on Nuclear Reactor Thermal Hydraulics (NURETH-11).

U. Bieder, F. Falk, and G. Fauchet. LES analysis of the flow in a simplified PWR assembly with mixing grid. *Progress in Nuclear Energy*, 75:15–24, 2014a.

U. Bieder, G. Fauchet, C. Calvin, and P. Ledac. High performance Large Eddy Simulation of turbulent flows around PWR mixing grids. In *Proceedings of 16th IEEE International Conference on High Performance Computing and Communications (HPCC)*, Paris, France, 2014b.

U. Bieder, F. Falk, and G. Fauchet. CFD analysis of the flow in the near wake of a generic PWR mixing grid. *Annals of Nuclear Energy*, 82:169–178, 2015.

W. K. Blake. *Mechanics of Flow-induced Sound and Vibration: Complex Flow-Structure Interactions*, volume 2. Academic Press, New York, USA, 1986.

A. L. W. Bokde, R. M. Lueptow, and B. Abraham. Spanwise structure of wall pressure on a cylinder in axial flow. *Physics of Fluids*, 11(1):151–161, 1999.

P. Bradshaw. Irrotational fluctuations near a turbulent boundary layer. *Journal of Fluid Mechanics*, 27(2):209–230, 1967.

M. K. Bull. Properties of the fluctuating wall-pressure field of a turbulent boundary layer. Technical Report AGARD-455, NATO Science and Technology Organization, USA, 1963.

M. K. Bull. Wall-pressure fluctuations associated with subsonic turbulent boundary layer flow. *Journal of Fluid Mechanics*, 28(4):719–754, 1967.

M. K. Bull. Wall pressure fluctuations beneath turbulent boundary layers: Some reflections on forty years of research. *Journal of Sound and Vibration*, 190(3):299–315, 1996.

C. Calvin, O. Cueto, and P. Emonot. AN OBJECT-ORIENTED APPROACH TO THE DESIGN OF FLUID MECHANICS SOFTWARE. *Mathematical Modelling and Numerical Analysis*, 36(5): 907–921, 2002.

D. Caraghiaur. Licentiate Thesis: Experimental study and modeling of spacer grid influence on flow in nuclear fuel assemblies. *KTH - The Royal Institute of Technology, Stockholm, Sweden*, page 39, 2009.

D. Caraghiaur, H. Anglart, and W. Frid. Experimental investigation of turbulent flow through spacer grids in fuel rod bundles. *Nuclear Engineering and Design*, 239(10):2013–2021, 2009.

M. Chandesris, A. D'Hueppe, B. Mathieu, D. Jamet, and B. Goyeau. Direct numerical simulation of turbulent heat transfer in a fluid-porous domain. *Physics of Fluids*, 25(12):125110, 2013.

S. K. Chang, S. K. Moon, W. P. Baek, and D. C. Young. Phenomenological investigations on the turbulent flow structures in a rod bundle array with mixing devices. *Nuclear Engineering and Design*, 238(3):600–609, 2008.

D. M. Chase. Modeling the wavevector-frequency spectrum of turbulent boundary layer wall pressure. *Journal of Sound and Vibration*, 70(1):29–67, 1980.

D. M. Chase. The character of the turbulent wall pressure spectrum at subconvective wavenumbers and a suggested comprehensive model. *Journal of Sound and Vibration*, 112(1):125–147, 1987.

A. Chatelain. 1-phase CFD - Validation of Pressure Fluctuations on the Rods (CALIFS experiment) and Analysis of Excitation Forces by Unsteady CFD Approaches. Technical Report FS1-0019929, AREVA, France, 2014.

A. Châtelain, F. Ducros, and O. Métais. LES of turbulent heat transfer: proper convection numerical schemes for temperature transport. *International Journal for Numerical Methods in Fluids*, 44(9): 1017–1044, 2004.

S. S. Chen and J. A. Jendrzejczyk. Fluid excitation forces acting on a square tube array. *Journal of Fluids Engineering*, 109(4):415–423, 1987.

M.-S. Chenaud, S. Li, M. Anderhuber, L. Matteo, and A. Gerschenfeld. COMPUTATIONAL THERMAL HYDRAULIC SCHEMES FOR SFR TRANSIENT STUDIES. In *Proceedings of 16th International Topical Meeting on Nuclear Reactor Thermal Hydraulics (NURETH-16)*, Chicago, USA, August 2015.

H. Childs, E. Brugger, B. Whitlock, J. Meredith, S. Ahern, D. Pugmire, K. Biagas, M. Miller, C. Harrison, G. H. Weber, H. Krishnan, T. Fogal, A. Sanderson, C. Garth, E. W. Bethel, D. Camp, O. Rübel, M. Durant, J. M. Favre, and P. Navrátil. VisIt: An End-User Tool For Visualizing and Analyzing Very Large Data. In *High Performance Visualization–Enabling Extreme-Scale Scientific Insight*, pages 357–372, October 2012. URL `https://wci.llnl.gov/simulation/computer-codes/visit/`.

H. Choi and P. Moin. On the space-time characteristics of wall pressure fluctuations. *Physics of Fluids A*, 2(8):1450–1460, 1990.

M. A. Christon, J. Bakosi, N. Barnett, M. Francois, and R. Lowrie. Initial assessment of Hydra-TH on Grid-to-Rod Fretting Problems (L2 Milestone THM.CFD.P4.01). Technical Report CASL-U-2011-0242-001, LA-UR-11-07034, Los Alamos National Laboratory (LANL), Los Alamos, USA, 2011. URL `http://www.casl.gov/docs/CASL-U-2011-0242-001.pdf`.

S. Y. Chung and H. J. Sung. Large-eddy simulation of turbulent flow in a concentric annulus with rotation of an inner cylinder. *International Journal of Heat and Fluid Flow*, 26(2):191–203, 2005.

S. Y. Chung, G. H. Rhee, and H. J. Sung. Direct numerical simulation of turbulent concentric annular pipe flow Part 1: Flow field. *International Journal of Heat and Fluid Flow*, 23(4):426–440, 2002.

O. Cioni, M. Marchand, G. Geffraye, and F. Ducros. 3D thermal-hydraulic calculations of a modular block-type HTR core. *Nuclear Engineering and Design*, 236(5-6):565–573, 2006.

K. M. Cipolla and W. L. Keith. High reynolds number thick axisymmetric turbulent boundary layer measurements. *Experiments in Fluids*, 35(5):477–485, 2003a.

K. M. Cipolla and W. L. Keith. Momentum thickness measurements for thick axisymmetric turbulent boundary layers. *Journal of Fluids Engineering*, 125(3):569–575, 2003b.

Code_Aster webpage. URL `http://www.code-aster.org/V2/spip.php?article275`.

Code_Saturne. *Computational Fluid Dynamics code, EDF, France*. URL `http://code-saturne.org/cms/`.

Computing Center for Research and Technology (CCRT). *Bruyères-le-Chatel, France*. URL `http://www-hpc.cea.fr/en/complexe/tgcc-curie.htm`.

M. E. Conner, B. E, and A. M. Elmahdi. CFD methodology and validation for single-phase flow in PWR fuel assemblies. *Nuclear Engineering and Design, Journal Topical Issue: Experiments and CFD code applications to nuclear reactor safety (XCFD4NRS)*, 240(9):2088–2095, 2010.

M. E. Conner, Y. A. Hassan, and E. E. Dominguea-Otiveros. Hydraulic benchmark data for PWR mixing vane grid. *Nuclear Engineering and Design, Journal Topical Issue: The 14th International Topical Meeting on Nuclear Reactor Thermal Hydraulics (NURETH-14)*, 264(2013):97–102, 2013.

Consortium for Advanced Simulation of Light water reactors (CASL). URL `http://www.casl.gov`.

G. M. Corcos. Pressure fluctuations in shear flows. Technical Report Ser. 183, No. 2, University of California Institute of Engineering, USA, 1962.

G. M. Corcos. Resolution of pressure in turbulence. *The Journal of the Acoustical Society of America*, 35(2):192–199, 1963.

H. G. Davies and R. J. Rogers. The vibrations of structures elastically constrained at discrete points. *Journal of Sound and Vibration*, 63(3):437–447, 1979.

J. W. Deardorff. A numerical study of three-dimensional turbulent channel flow at large Reynolds numbers. *Journal of Fluid Mechanics*, 41(2):453–480, 1970.

S. Delafontaine and G. Ricciardi. Fluctuating pressure calculation induced by axial flow through mixing grid. *Nuclear Engineering and Design*, 242:233–246, 2012.

E. E. Dominguez-Ontiveros and Y. A. Hassan. Experimental study of a simplified 3 x 3 rod bundle using DPTV. *Nuclear Engineering and Design*, 279(2014):50–59, 2014.

E. E. Dominguez-Ontiveros, Y. A. Hassan, M. E. Conner, and Z. Karoutas. Experimental benchmark data for PWR rod bundle with spacer-grids. In *Proceedings of CFD for Nuclear Reactor Safety Applications (CFD4NRS-3) Workshop*, Bethesda, USA, 2010.

F. Ducros, U. Bieder, O. Cioni, T. Fortin, B. Fournier, G. Fauchet, and P. Quéméré. Verification and validation considerations regarding the qualification of numerical schemes for LES for dilution problems. *Nuclear Engineering and Design*, 240(9):2123–2130, 2010.

A. M. Elmahdi, R. Lu, M. E. Conner, Z. Karoutas, and E. Baglietto. Flow induced vibration forces on a fuel rod by LES CFD analysis. In *Proceedings of The 14th International Topical Meeting on Nuclear Reactor Thermal Hydraulics (NURETH-14)*, Toronto, Canada, 2011. URL `http://www.casl.gov/docs/NURETH14-365.pdf`.

T. M. Farabee and M. J. Casarella. Spectral features of wall pressure fluctuations beneath turbulent boundary layers. *Physics of Fluids A*, 3(10):2410–2420, 1991.

FLUENT. *Computational Fluid Dynamics code, ANSYS, USA*. URL `https://caeai.com/ansys-software-support/ansys-software/computational-fluid-dynamics-ansys-cfx-and-fluent-cfd-software`.

T. Frank, S. Jain, A. A. Matyushenko, and A. V. Garbaruk. The OECD/NEA Matis-H benchmark - CFD analysis of water flow through a 5x5 rod bundle with spacer grids using ANSYS FLUENT and ANSYS CFX. In *Proceedings of the CFD for Nuclear Reactor Safety Applications (CFD4NRS-4) Conference on Experimental Validation and Application of CFD and CMFD Codes in Nuclear Reactor Technology, OECD/NEA and IAEA Workshop*, Daejeon, South Korea, 2012.

M. Germano, U. Piomelli, P. Moin, and W. H. Cabot. A dynamic sub-grid scale eddy viscosity model. *Physics of Fluids A: Fluid Dynamics*, 3(7):1760–1765, 1991.

C. Geuzaine and J. F. Remacle. Gmsh: A three dimensional finite element mesh generator with built-in pre- and post-processing facilities. *International Journal for Numerical Methods in Engineering*, 79(11):1309–1331, 2009.

R. Gibert, J. Chabrerie, and M. Sagner. Tube bundle vibrations in transversal flow. In *Proceedings of BNES International Conference on Vibration in Nuclear Plant*, volume 1, pages 205–209, Keswick, UK, 1978.

M. Goody. Empirical Spectral Model of Surface Pressure Fluctuations. *AIAA Journal*, 42(9):1788–1794, 2004.

M. D. Graham and I. G. Kevrekidis. Alternative approaches to the Karhunen-Loève decomposition for model reduction and data analysis. *Computers and Chemical Engineering*, 20(5):495–506, 1996.

Grand Équipement National de Calcul Intensif (GENCI). *France*. URL `http://www.genci.fr/en`.

M. Hadžiabdić, K. Hanjalić, and R. Mullyadzhanov. LES of turbulent flow in a concentric annulus with rotating outer wall. *International Journal of Heat and Fluid Flow*, 43(October):74–84, 2013.

J. O. Hinze. *Turbulence*. Mc-Graw Hill, New York, USA, 1959.

T. Höhne, S. Kliem, and U. Bieder. Modeling of a buoyancy-driven flow experiment at the {ROCOM} test facility using the {CFD} codes CFX-5 and Trio_U. *Nuclear Engineering and Design*, 236(12): 1309–1325, 2006.

HP Remote Graphics Software webpage. URL `http://www8.hp.com/us/en/campaigns/workstations/remote-graphics-software.html`.

K. Ikeda and M. Hoshi. Development of rod-embedded fiber LDV to measure velocity in fuel rod bundles. *Journal of Nuclear Science and Technology*, 43(2):150–158, 2006.

T. Ikeno and T. Kajishima. Decay of swirling turbulent flow in rod-bundle. *Journal of Fluid Science and Technology*, 1(1):36–47, 2006.

M. Kaneda, B. Yu, H. Ozoe, and S. W. Churchill. The characteristics of turbulent flow and convection in concentric circular annuli. Part I: Flow. *International Journal of Heat and Mass Transfer*, 46 (26):5045–5057, 2003.

G. Kerschen, J. C. Golinval, A. F. Vakakis, and L. A. Bergman. The method of proper orthogonal decomposition for dynamical characterization and order reduction of mechanical systems: An overview. *Nonlinear Dynamics*, 41(1):147–169, 2005.

H.-K. Kim. Mechanical analysis of fuel fretting problem. *Nuclear Engineering and Design*, 192(1): 81–93, 1999.

J. Kim, P. Moin, and R. D. Moser. Turbulence statistics in fully developed channel flow at low reynolds number. *Journal of Fluid Mechanics*, 177:133–166, 1987.

S. J. King, M. Y. Young, D. D. Seel, M. E. Conner, R. Y. Lu, and D. V. Paramov. Flow induced vibration and fretting wear in PWR fuel. In *Proceedings of the 10th International Conference on Nuclear Engineering*, Arlington, VA, USA, 2002.

A. N. Kolmogorov. Dissipation of Energy in the Locally Isotropic Turbulence. *Dokl. Akad. Nauk SSSR (in Russian)*, 32(1):16–19, 1941a.

A. N. Kolmogorov. The local structure of turbulence in incompressible viscous fluid for very large Reynolds numbers. *Dokl. Akad. Nauk SSSR (in Russian)*, 30(4):9–13, 1941b.

F. Kreith and O. K. Sonju. The decay of a turbulent swirl in a pipe. *Journal of Fluid Mechanics*, 22 (2):257–271, 1965.

D. Kuzmin and S. Turek. Multidimensional FEM-TVD paradigm for convection-dominated flows. In *Proceedings of the European Congress on Computational Methods in Applied Sciences and Engineering (ECCOMAS)*, Jyvaskyla, Finland, 2004a. URL `http://www.mathematik.uni-dortmund.de/~kuzmin/keps.pdf`.

D. Kuzmin and S. Turek. High-resolution FEM-TVD schemes based on a fully multidimensional flux limiter. *Journal of Computational Physics*, 198(1):131–158, 2004b.

C. M. Lee and Y. D. Choi. Comparison of thermo-hydraulic performances of large scale vortex flow (LSVF) and small scale vortex flow (SSVF) mixing vanes in 17 x 17 nuclear rod bundle. *Nuclear Engineering and Design*, 237(24):2322–2331, 2007.

M. Lesieur. *Turbulence in Fluids*. Kluwer Academic Publishers, Dordrecht, Netherlands, 3rd edition, 1995.

E. Leveque, F. Toschi, L. Shao, and J.-P. Bertoglio. Shear-improved Smagorinsky model for large-eddy simulation of wall-bounded turbulent flows. *Journal of Fluid Mechanics*, 570:491–502, 2007.

D. K. Lilly. On the Application of the Eddy Viscosity Concept in the Inertial Sub-range of Turbulence. Technical Report 123, NCAR, USA, 1966.

D. K. Lilly. The Representation of Small-scale Turbulence in Numerical Simulation Experiments. In *Proceedings of the IBM Scientific Computing Symposium on Environmental Sciences*, page 195, 1967.

D. K. Lilly. A proposed modification of the Germano subgrid scale closure method. *Physics of Fluids A: Fluid Dynamics*, 4(3):633–635, 1992.

N. S. Liu and X. Y. Lu. Large eddy simulation of turbulent concentric annular channel flows. *International Journal for Numerical Methods in Fluids*, 45(12):1317–1338, 2004.

R. M. Lueptow. Turbulent boundary layer on a cylinder in axial flow. Technical Report 8389, Naval Underwater Systems Center (NUSC), USA, 1988.

R. M. Lueptow and J. H. Haritonidis. The structure of the turbulent boundary layer on a cylinder in axial flow. *Physics of Fluids*, 30(10):2993–3005, 1987.

R. M. Lueptow and C. P. Jackson. Near wall streaky structure in a turbulent boundary layer on a cylinder. *Physics of Fluids*, 3(11):2822–2824, 1991.

R. M. Lueptow, P. Leehey, and T. Stellinger. The thick, turbulent boundary layer on a cylinder: Mean and fluctuating velocities. *Physics of Fluids*, 28(12):3495–3505, 1985.

J. Mahaffy, B. Chung, F. Dubois, F. Ducros, E. Graffard, M. Heitsch, M. Henriksson, E. Komen, F. Moretti, T. Morii, P. Mühlbauer, U. Rohde, M. Scheuerer, B. L. Smith, C. Song, T. Watanabe, and G. Zigh. Best practice guidelines for the use of CFD in nuclear reactor safety applications. Technical Report NEA/CSNI/R(2007)5, OECD/NEA, France, 2007. URL `http://www.oecd-nea.org/nsd/docs/2007/csni-r2007-5.pdf`.

H. L. McClusky, M. V. Holloway, D. E. Beasley, and M. E. Connor. Development of swirling flow in a rod-bundle sub-channel. *Journal of Fluids Engineering*, 124(3):747–755, 2002.

H. C. Meng and K. C. Ludema. Wear models and predictive equations: their form and content. *Wear*, 181-183(2):443–457, 1995.

METIS webpage. URL `http://glaros.dtc.umn.edu/gkhome/metis/metis/overview`.

F. Moreno. CALIFS Experimental: Présentation de l'avancement des essais de faisabilité des mesures de fluctuations de pression. Technical Report CEA/DEN/CAD/DTN/STRI/LHC/DO 60, CEA Cadarache, France, 2012.

F. Moreno. CALIFS Experimental: Essais de faisabilité des mesures de longueur de corrélation des fluctuations de pression. Technical Report CEA/DEN/CAD/DTN/STCP/LHC/NT/2014-32-INDICE A, CEA Cadarache, France, 2014.

H. Nepomuneco and R. M. Lueptow. Pressure and shear stress measurements at the wall in a turbulent boundary layer on a cylinder. *Physics of Fluids*, 9(9):2732–2739, 1997.

J. C. Neves and P. Moin. Effects of convex transverse curvature on wall bounded turbulence. Part 2. The pressure fluctuations. *Journal of Fluid Mechanics*, 272:383–406, 1994.

J. C. Neves, P. Moin, and R. D. Moser. Numerical study of axial turbulent flow over long cylinders. Technical Report 54, Department of Mechanical Engineering, Stanford University, Stanford, USA, 1992.

J. C. Neves, P. Moin, and R. D. Moser. Effects of convex transverse curvature on wall bounded turbulence. Part 1. The velocity and vorticity. *Journal of Fluid Mechanics*, 272:349–381, 1994.

F. Nicoud and F. Ducros. Subgrid-scale stress modeling based on the square of the velocity gradient tensor. *Flow, Turbulence and Combustion*, 62(3):183–200, 1999.

R. R. Nourgaliev, M. A. Christon, J. Bakosi, R. B. Lowrie, and L. A. Pritchett-Sheats. Hydra-TH: A Thermal-Hydraulics code for Nuclear Reactor Applications. In *Proceedings of The 15th International Topical Meeting on Nuclear Reactor Thermal Hydraulics (NURETH-15)*, Pisa, Italy, 2013. URL `http://www.casl.gov/docs/CASL-U-2013-0100-000.pdf`.

J. M. Nouri and J. H. Whitelaw. Flow of Newtonian and Non-Newtonian Fluids in a Concentric Annulus With Rotation of the Inner Cylinder. *Journal of Fluids Engineering*, 116(4):821–827, 1994.

J. M. Nouri, H. Umur, and J. H. Whitelaw. Flow of Newtonian and non-Newtonian fluids in concentric and eccentric annuli. *Journal of Fluid Mechanics*, 253:617–641, 1993.

M. Ould-Rouiss, L. Redjem-Saad, and G. Lauriat. Direct numerical simulation of turbulent heat transfer in annuli: Effect of heat flux ratio. *International Journal of Heat and Fluid Flow*, 30(4): 579–589, 2009.

Oxalya webpage. URL `http://www.oxalya.com`.

M. P. Païdoussis, A. Sarkar, and C. Semler. A horizontal fluid-conveying cantilever : spatial coherent structures, beam modes and jumps in stability diagram. *Journal of Sound and Vibration*, 280(1-2): 141–157, 2005.

C. Peña Monferrer, J. Muñoz Cobo, and S. Chiva. CFD Turbulence Study of PWR Spacer-Grids in a Rod Bundle. *Science and Technology of Nuclear Installations*, 2014(635651):1–15, 2014.

PETSc webpage. URL `http://www.mcs.anl.gov/petsc/`.

M. J. Pettigrew. The vibration behavior of nuclear fuel under reactor conditions. *Nuclear Science and Engineering*, 114(3):179–189, 1993.

M. J. Pettigrew and C. E. Taylor. Vibration analysis of shell-and-tube heat exchangers: an overview-Part 2: vibration response, fretting-wear, guidelines. *Journal of Fluids and Structures*, 18(5):485–500, 2003.

S. B. Pope. *Turbulent Flows*. Cambridge University Press, Cambridge, UK, 2000.

H. Reichardt. Vollständige Darstellung der turbulenten Geschwindigkeitsverteilung in glatten Leitungen. *ZAMM - Journal of Applied Mathematics and Mechanics / Zeitschrift für Angewandte Mathematik und Mechanik (in German)*, 31(7):208–219, 1951.

L. F. Richardson. *Weather Prediction by Numerical Process.* Cambridge University Press, Cambridge, UK, 1922.

R. S. Rogallo and P. Moin. Numerical simulation of turbulent flows. *Annual Review of Fluid Mechanics*, 16:99–137, 1984.

P. R. Rubiolo. Probabilistic prediction of fretting-wear damage of nuclear fuel rods. *Nuclear Engineering and Design*, 236(14-16):1628–1640, 2006.

P. R. Rubiolo and M. Y. Young. VITRAN: an Advance Statistic Tool to Evaluate Fretting-wear Damage. *Journal of Power and Energy Systems*, 2(1):57–66, 2008.

P. R. Rubiolo and M. Y. Young. On the factors affecting the fretting-wear risk of PWR fuel assemblies. *Nuclear Engineering and Design*, 239(1):68–79, 2009.

P. Sagaut. *Large eddy simulations for incompressible flows.* Springer-Verlag, Berlin Heidelberg, 3rd edition, 2005.

A. Saxena. PhD Thesis: Thermal-hydraulic numerical simulation of fuel sub-assembly for Sodium-cooled Fast Reactor. *Université Aix-Marseille, Marseille, France*, 2014.

A. Saxena, U. Bieder, T. Cadiou, and S. Viazzo. Large Eddy Simulation of turbulent flow in wire wrapped fuel pin bundles cooled by sodium. In *Proceedings of 3rd International Conference on Advancements in Nuclear Instrumentation, Measurement Methods and their Applications (ANIMMA)*, Marseille, France, 2013.

J. Smagorinsky. General Circulation Experiments with the Primitive Equations. *Monthly Weather Review*, 91(3):99–164, 1963.

B. L. Smith, C.-H. Song, S.-K. Chang, J. R. Lee, and J. W. Kim. Report of the OECD/NEA - KAERI rod bundle CFD benchmark exercise. Technical Report NEA/CSNI/R(2013)5, OECD/NEA, France, 2013.

B. L. Smith, M. Andreani, U. Bieder, F. Ducros, E. Graffard, M. Heitsch, M. Henriksson, T. Höhne, M. Houkema, E. Komen, J. Mahaffy, F. Menter, F. Moretti, T. Morii, P. Mühlbauer, U. Rohde, M. Scheuerer, C. H. Song, T. Watanabe, and G. Zigh. Assessment of CFD Codes for Nuclear

Reactor Safety Problems. Technical Report NEA/CSNI/R(2014)12, OECD/NEA, France, 2014. URL https://www.oecd-nea.org/nsd/docs/2014/csni-r2014-12.pdf.

S. R. Snarski and R. M. Lueptow. Wall pressure and coherent structures in a turbulent boundary layer on a cylinder in axial flow. *Journal of Fluid Mechanics*, 286:137–171, 1995.

STAR-CCM+. *Computational Fluid Dynamics code, CD-adapco, USA*. URL http://www.cd-adapco.com/products/star-ccm.

V. Strouhal. Ueber eine besondere Art der Tonerregung (in German). *Annalen der Physik*, 241(10): 216–251, 1878.

C. E. Taylor, M. J. Pettigrew, F. Axisa, and B. Villard. Experimental determination of single and two-phase cross flow-induced forces on tube rows. In *Proceedings of ASME Pressure Vessels and Piping Conference: Volume 104: Flow-induced Vibrations*, pages 31–39, Chicago, USA, 1986.

C. E. Taylor, M. J. Pettigrew, F. Axisa, and B. Villard. Experimental determination of single and two-phase cross flow-induced forces on tube rows. *Journal of Pressure Vessel Technology*, 110(1): 22–28, 1988.

L. Temmerman, M. A. Leschziner, C. P. Mellen, and J. Fröhlich. Investigation of wall function approximations and subgrid scale models in large eddy simulation of separated flow in a channel with streamwise periodic constrictions. *International Journal of Heat and Fluid Flow*, 24(2):157–180, 2003.

Top500 webpage. URL http://www.top500.org/list/2015/06.

TrioCFD (previously Trio_U) webpage. *Computational Fluid Dynamics code, CEA, France*. URL http://www-trio-u.cea.fr/scripts/home/publigen/content/templates/show.asp?L=EN&P=55&vTicker=alleza&ITEMID=3.

TrioCFD User's Manual. *Computational Fluid Dynamics code, CEA, France*. 2015.

O. R. Tutty. Flow along a long thin cylinder. *Journal of Fluid Mechanics*, 602:1–37, 2008.

S. Vandroux and V. Barthel. Trio_U code validation database: Best practice guidelines. Technical Report CEA/DEN/DANS/DM2S/STMF/LMSF/NT/13-008/A, CEA Saclay, France, 2013.

H. K. Versteeg and W. Malalasekara. *An Introduction to Computational Fluid Dynamics: The Finite Volume Method*. Pearson Prentice Hall, London, 2nd edition, 2007.

VisuPortal webpage. URL `http://www.visuportal.com`.

A. Weitrzak and R. M. Lueptow. Wall shear stress and velocity in a turbulent, axisymmetric boundary layer. *Journal of Fluid Mechanics*, 259:191–218, 1994.

W. Welch. The use of fast Fourier transform for the estimation of power spectra: A method based on time averaging over short, modified periodograms. *IEEE Transactions on Audio and Electroacoustics*, AU-15(2):70–73, 1967.

W. W. Willmarth and C. E. Woolbridge. Measurement of the fluctuating pressure at the wall beneath a thick turbulent boundary layer. Technical Report ORA 02920-1-T, University of Michigan, USA, 1962.

W. W. Willmarth and C. E. Woolbridge. Measurements of the correlation between the fluctuating velocities and the fluctuating wall pressure in a thick turbulent boundary layer. Technical Report AGARD-456, NATO Science and Technology Organization, USA, 1963.

W. W. Willmarth and C. S. Yang. Wall pressure fluctuations beneath turbulent boundary layers on a flat plate and a cylinder. *Journal of Fluid Mechanics*, 41(1):47–80, 1970.

W. W. Willmarth, R. E. Winkel, L. K. Sharma, and T. J. Bogar. Axially symmetric turbulent boundary layers on cylinders: mean velocity profiles and wall pressure fluctuations. *Journal of Fluid Mechanics*, 76(1):35–64, 1976.

S. K. Yang and M. K. Chung. Turbulent Flow Through Spacer Grids in Rod Bundles. *Journal of Fluids Engineering*, 120(4):786–791, 1998.

Appendix A

Velocity Field

The time evolution of magnitude of instantaneous velocity at different altitudes for MV case is presented here.

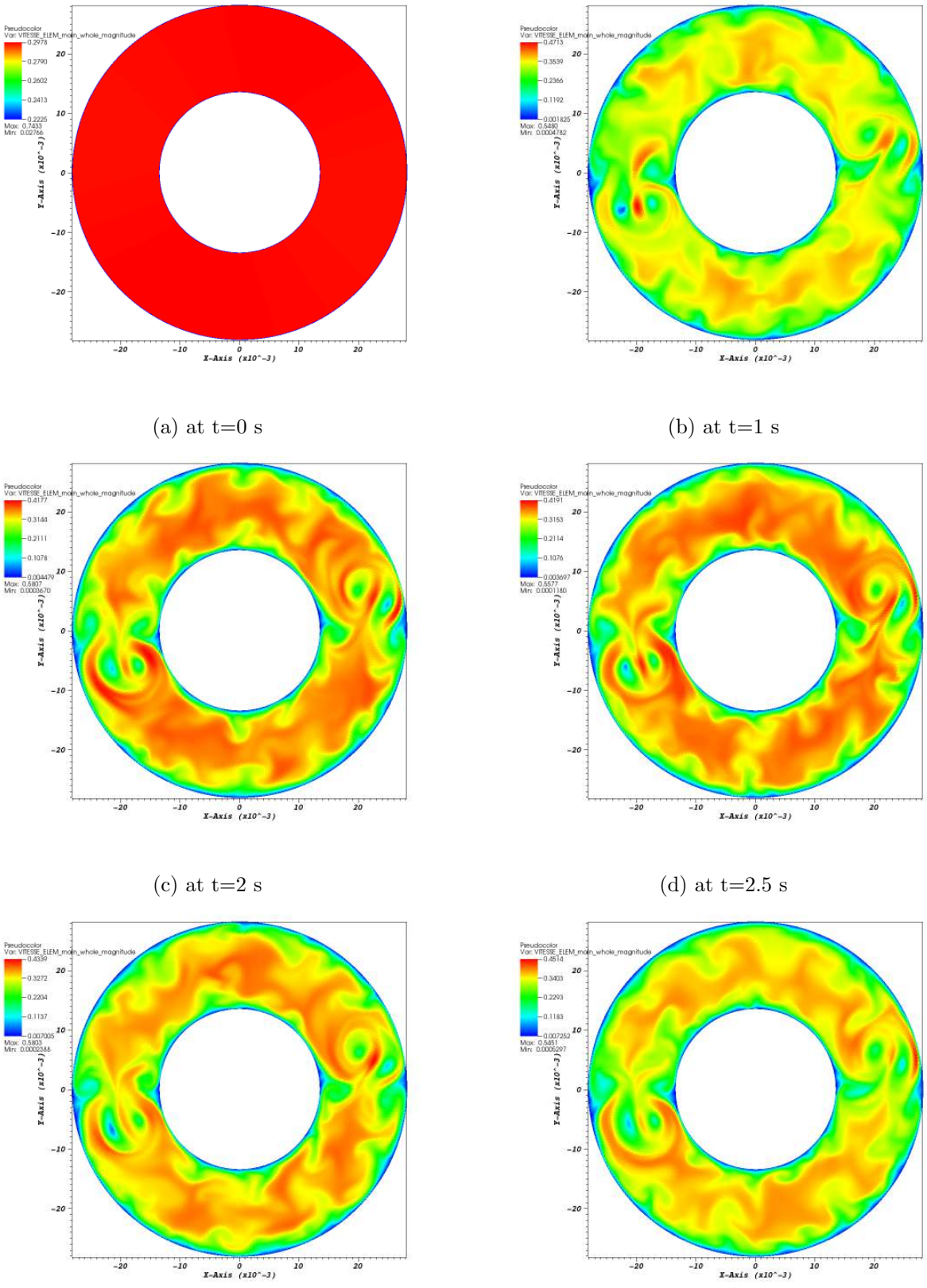

(a) at t=0 s

(b) at t=1 s

(c) at t=2 s

(d) at t=2.5 s

(e) at t=3 s

(f) at t=3.75 s

Figure A.1: Time evolution of magnitude of instantaneous velocity at 1 HD for MV case (on x-y plane)

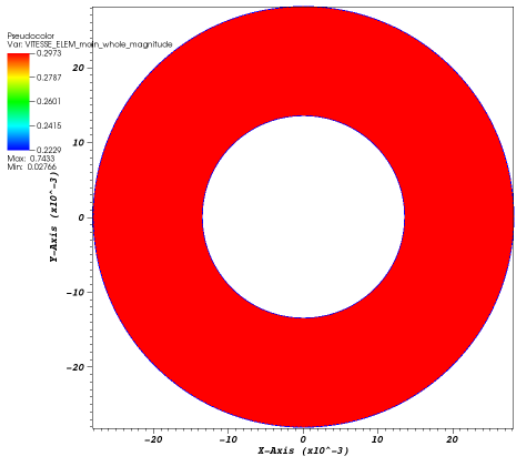

(a) at t=0 s

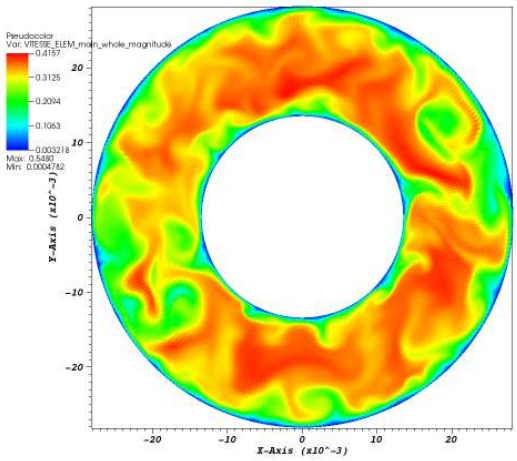

(b) at t=1 s

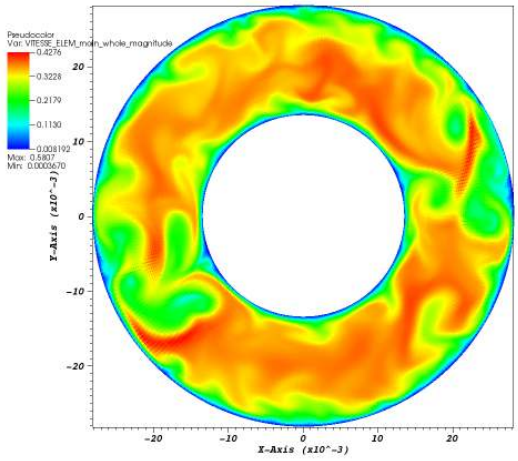

(c) at t=2 s

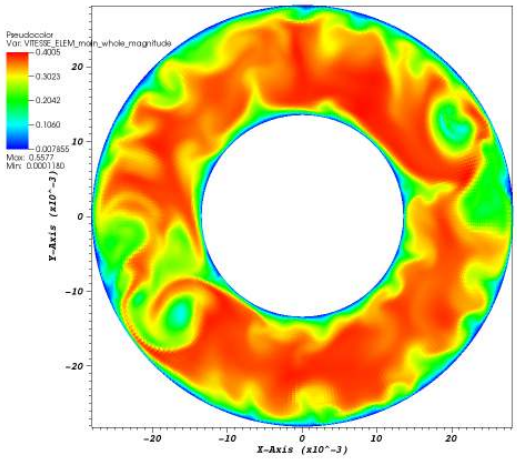

(d) at t=2.5 s

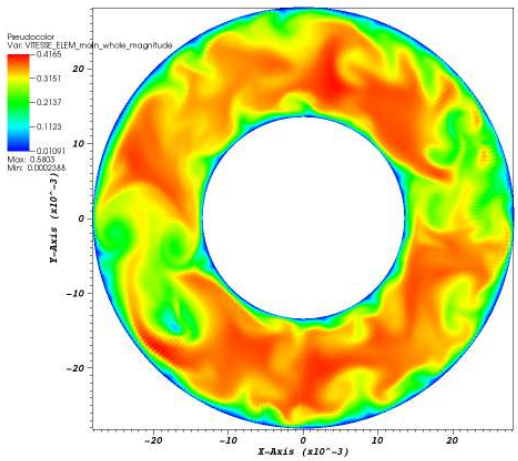

(e) at t=3 s

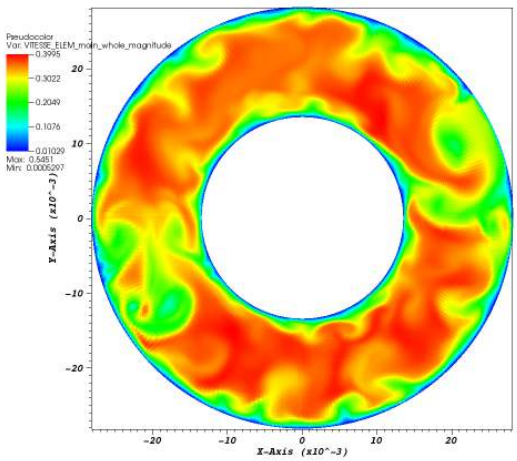

(f) at t=3.75 s

Figure A.2: Time evolution of magnitude of instantaneous velocity at 2 HD for MV case (on x-y plane)

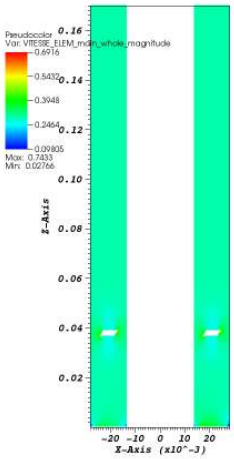

(a) at t=0 s

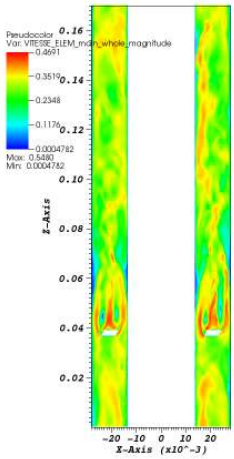

(b) at t=1 s

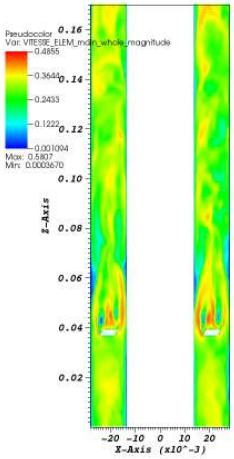

(c) at t=2 s

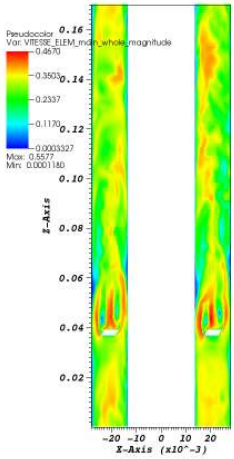

(d) at t=2.5 s

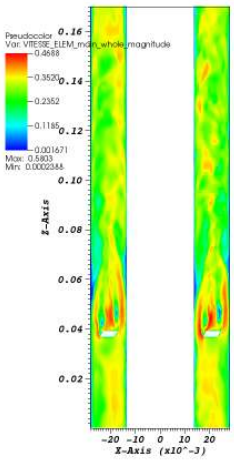

(e) at t=3 s

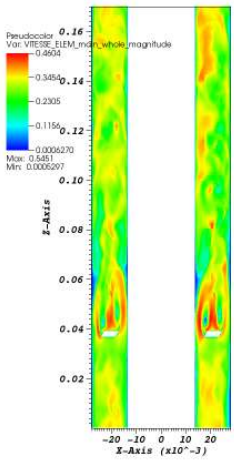

(f) at t=3.75 s

Figure A.3: Time evolution of magnitude of instantaneous velocity for MV case on x-z plane

Appendix B

Pressure Correlation

The pressure correlation in the axial and azimuthal directions is presented here for the two annular pipe cases (PC and PF) and the MV, CG, SQ cases.

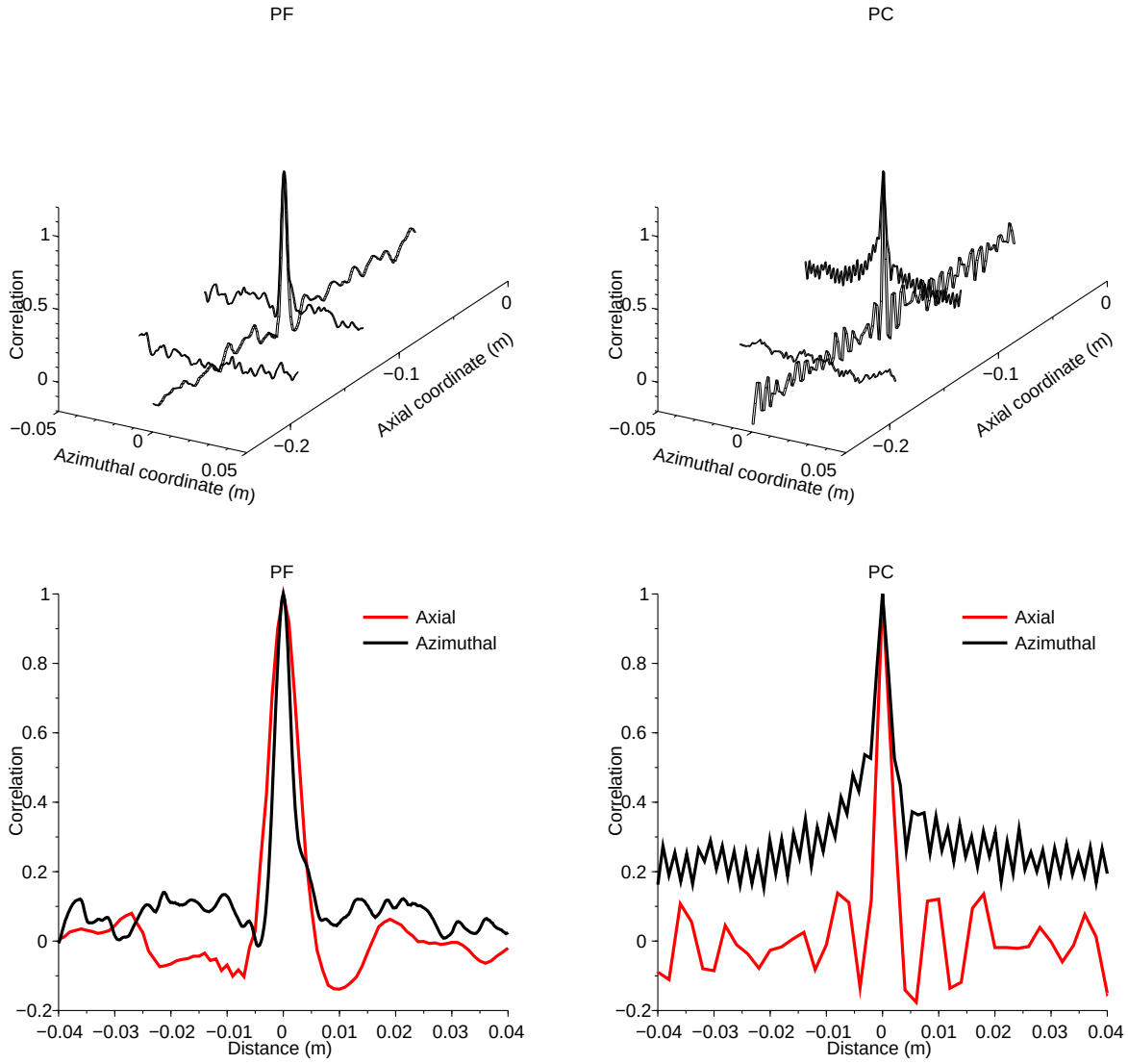

Figure B.1: Correlation for annular pipe case - fine mesh (left) coarse mesh (right)

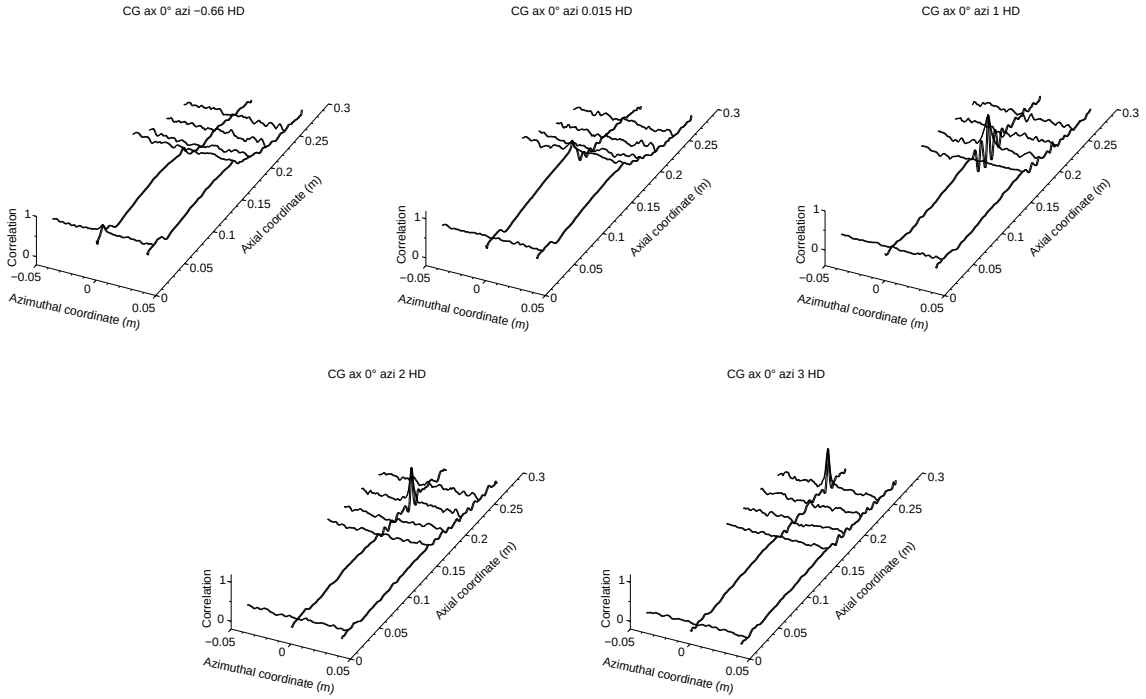

Figure B.2: Correlation for circular grid case

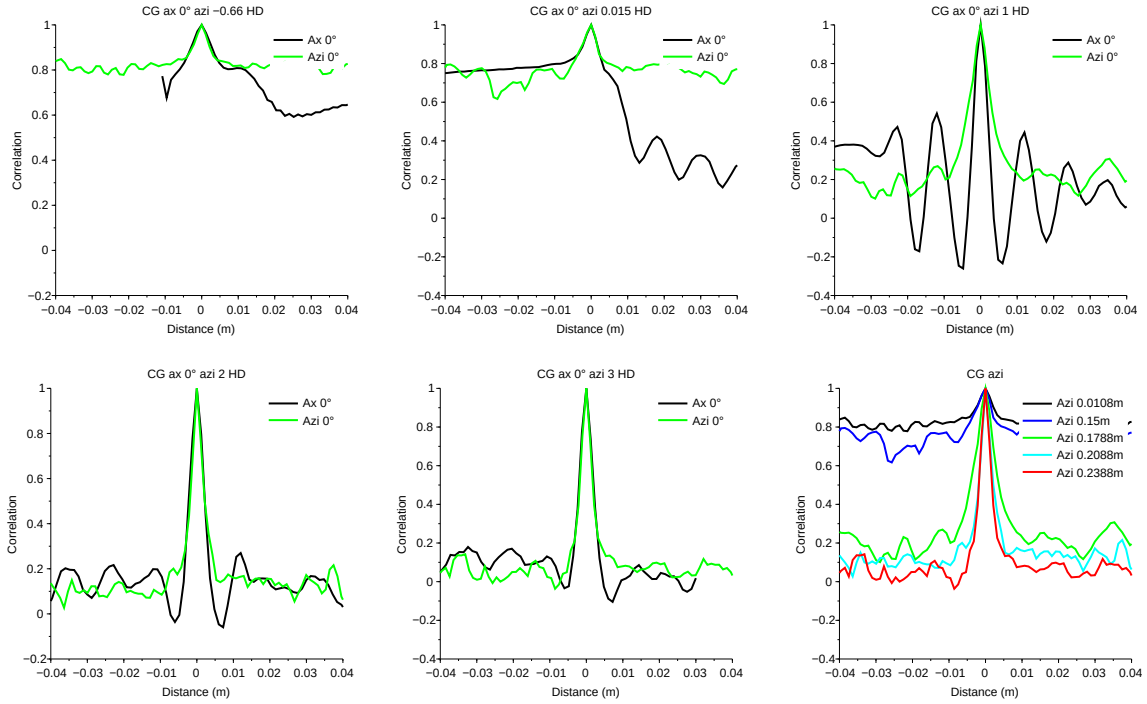

Figure B.3: Correlation for circular grid case

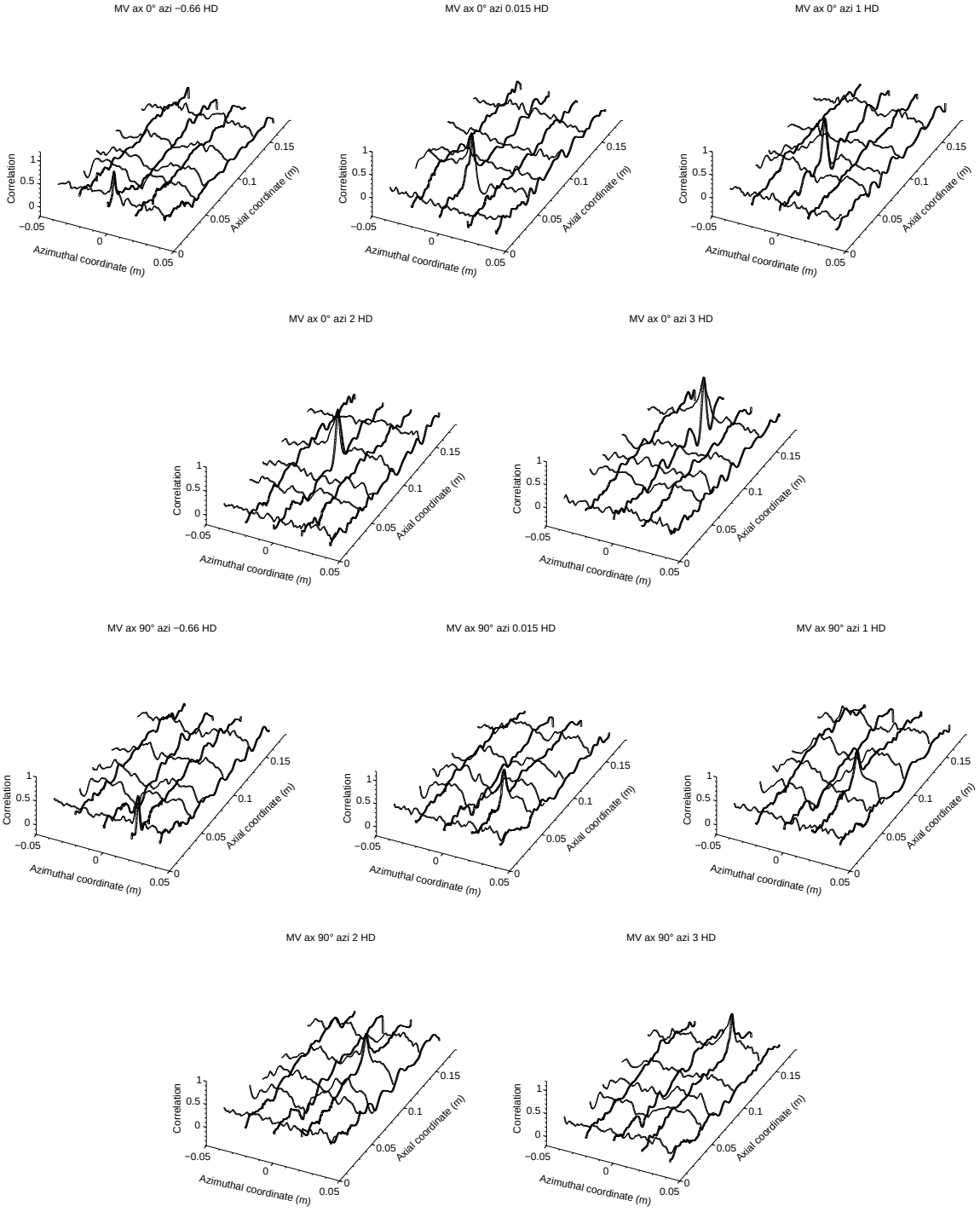

Figure B.4: Correlation for mixing vane case

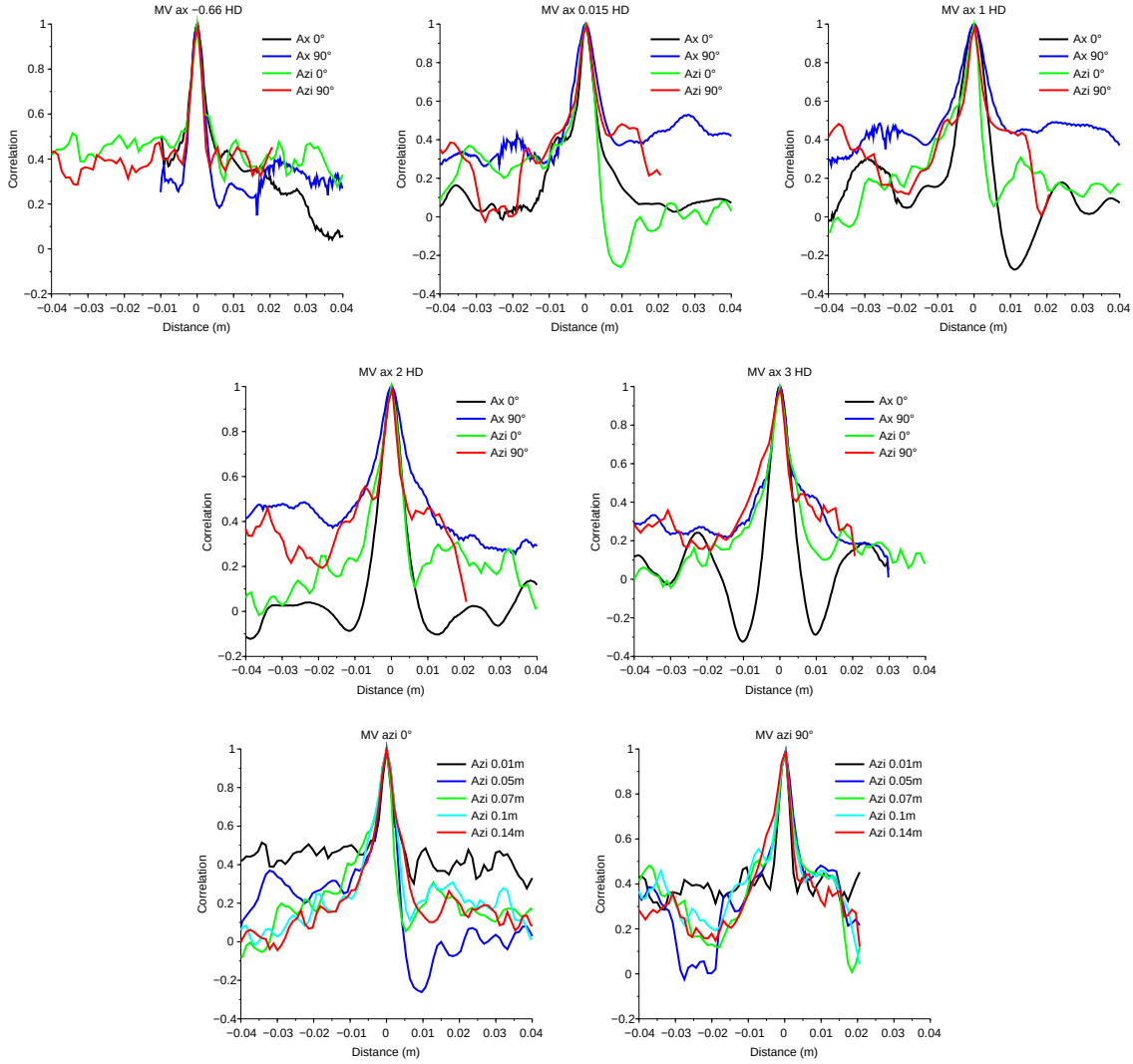

Figure B.5: Correlation for mixing vane case

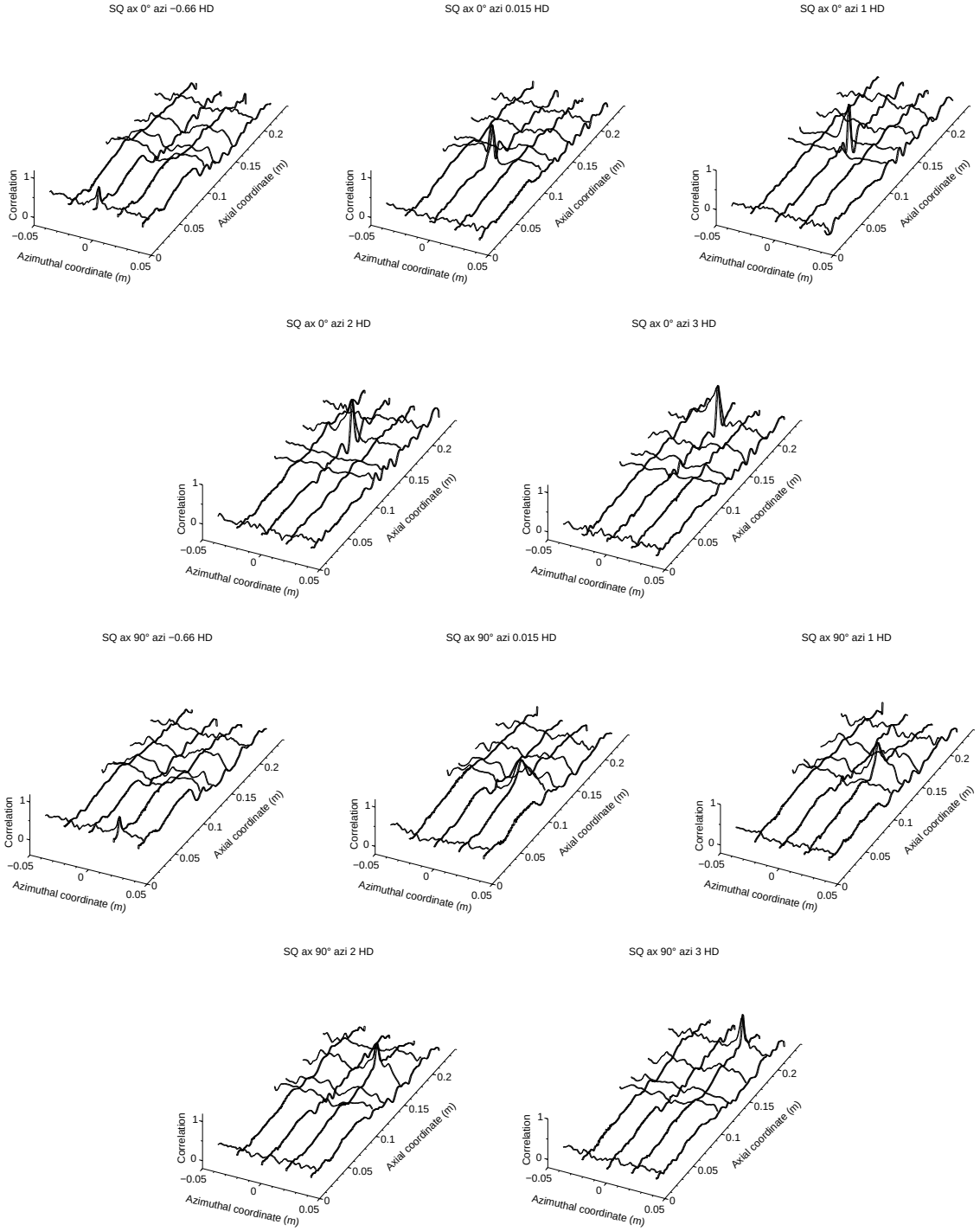

Figure B.6: Correlation for square grid with mixing vanes case

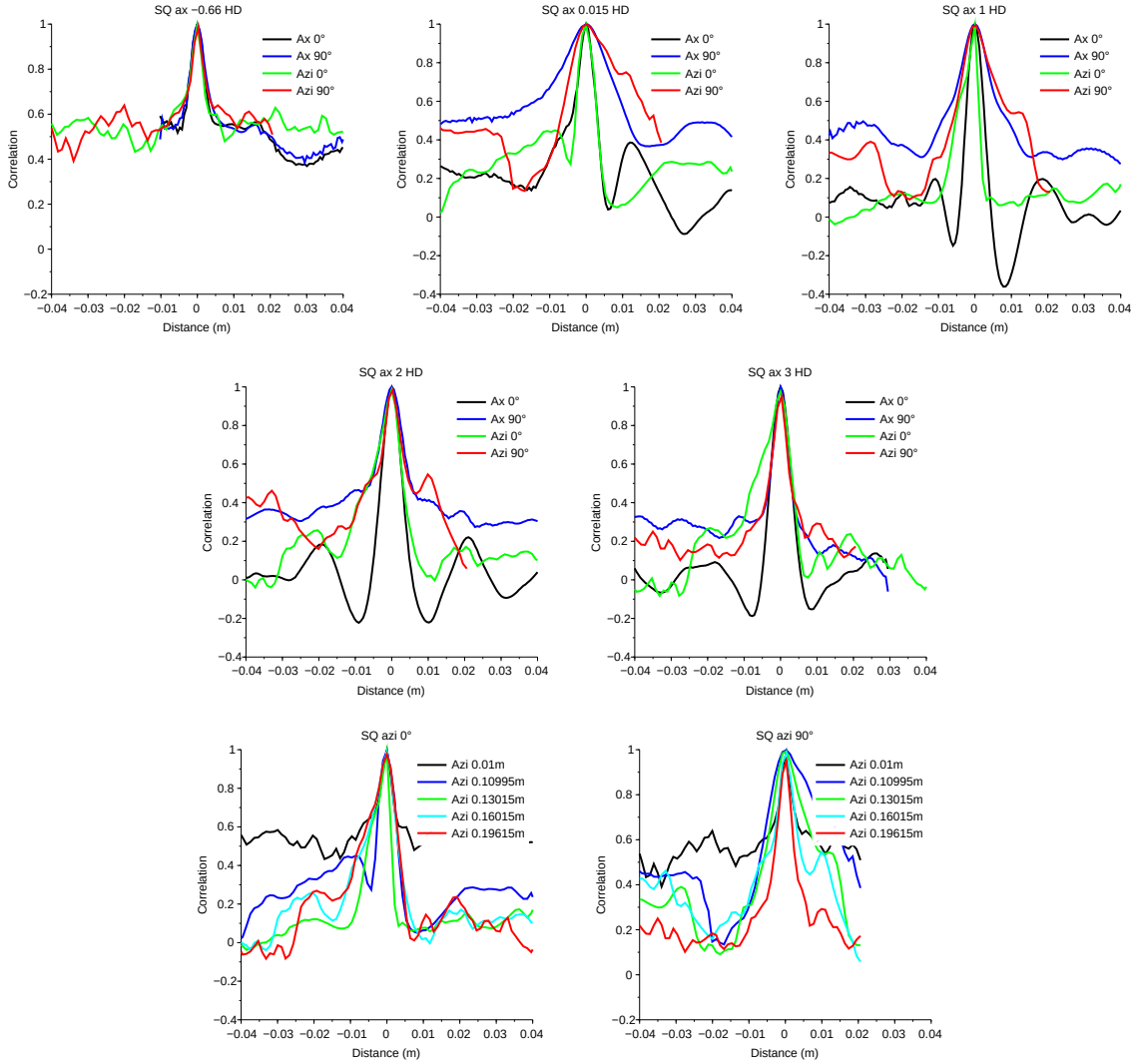

Figure B.7: Correlation for square grid with mixing vanes case

Appendix C

Coherence

The transfer functions for the five different cases (PC, PF, MV, CG and SQ) are presented here.

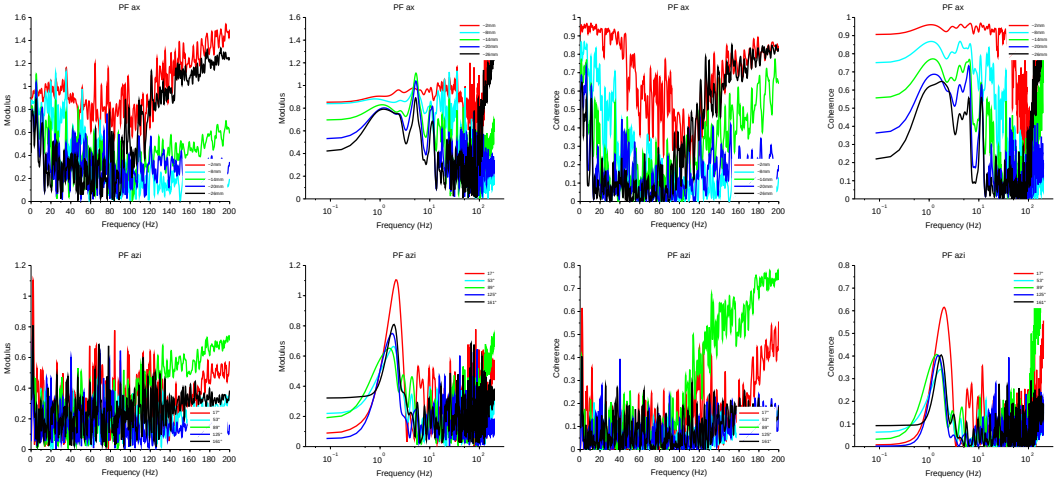

Figure C.1: Transfer function for annular pipe fine mesh case around 0° in axial direction (top) and azimuthal direction (bottom)

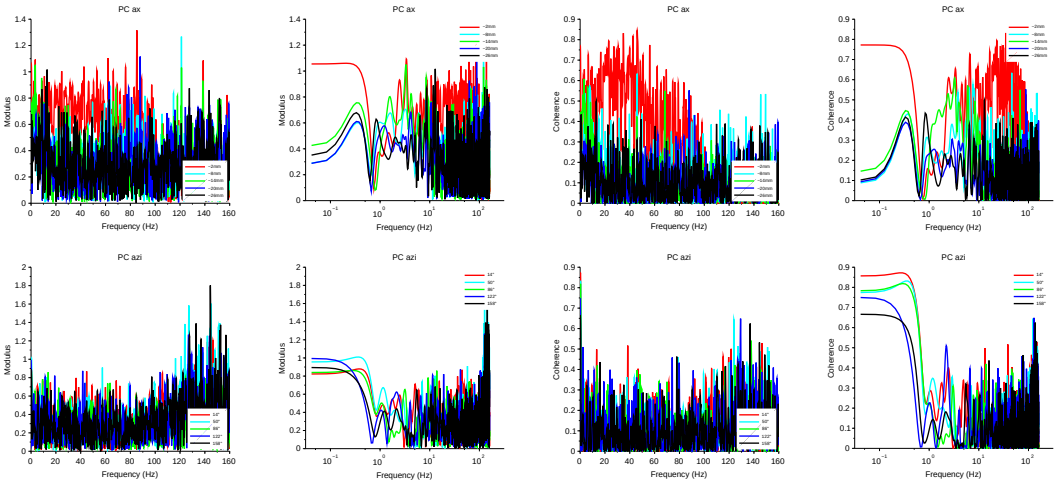

Figure C.2: Transfer function for annular pipe coarse mesh case around 0° in axial direction (top) and azimuthal direction (bottom)

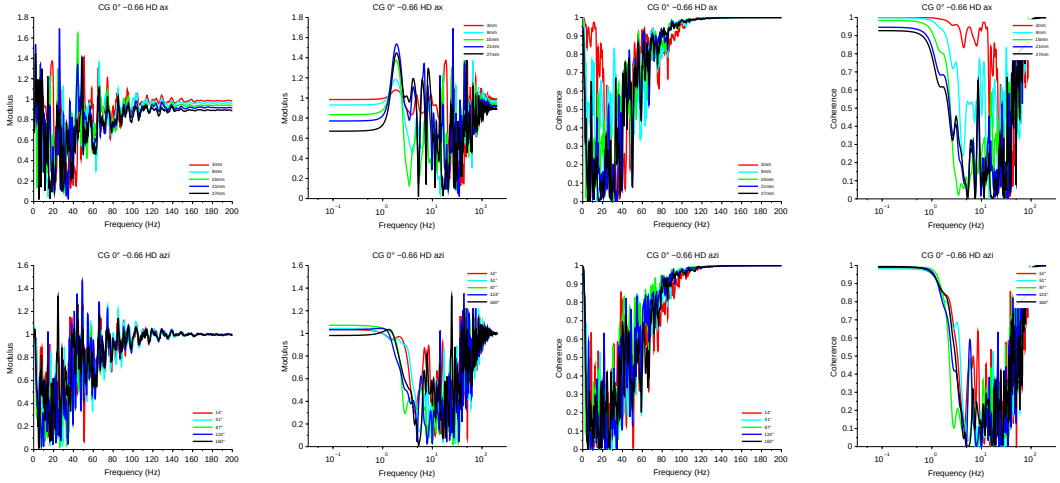

Figure C.3: Transfer function for circular grid case around 0°
-0.66 HD in axial direction (top) and azimuthal direction (bottom)

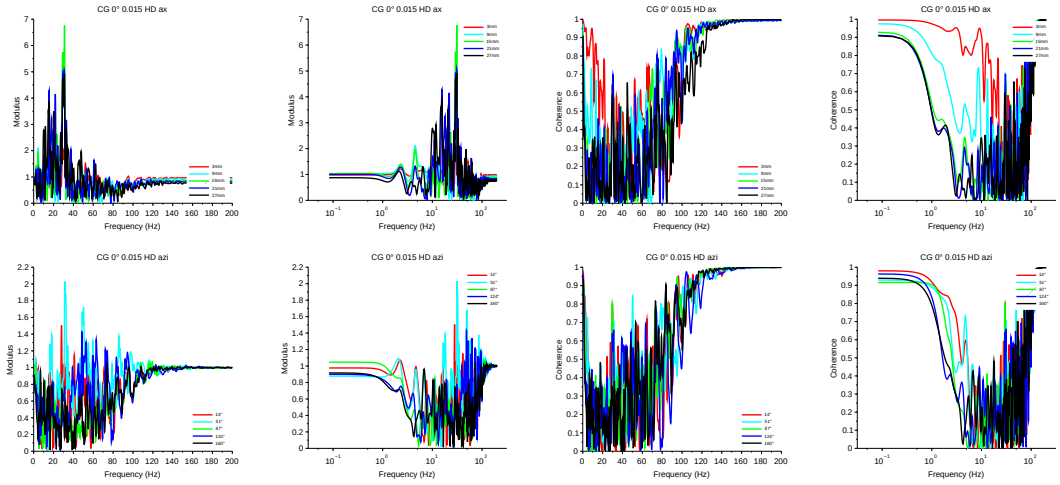

Figure C.4: Transfer function for circular grid case around 0°
0.015 HD in axial direction (top) and azimuthal direction (bottom)

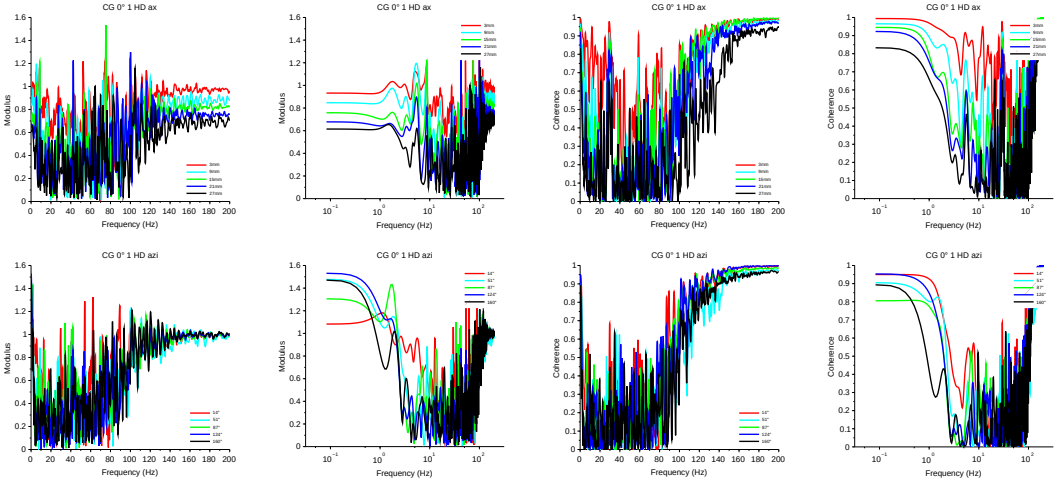

Figure C.5: Transfer function for circular grid case around 0°
1 HD in axial direction (top) and azimuthal direction (bottom)

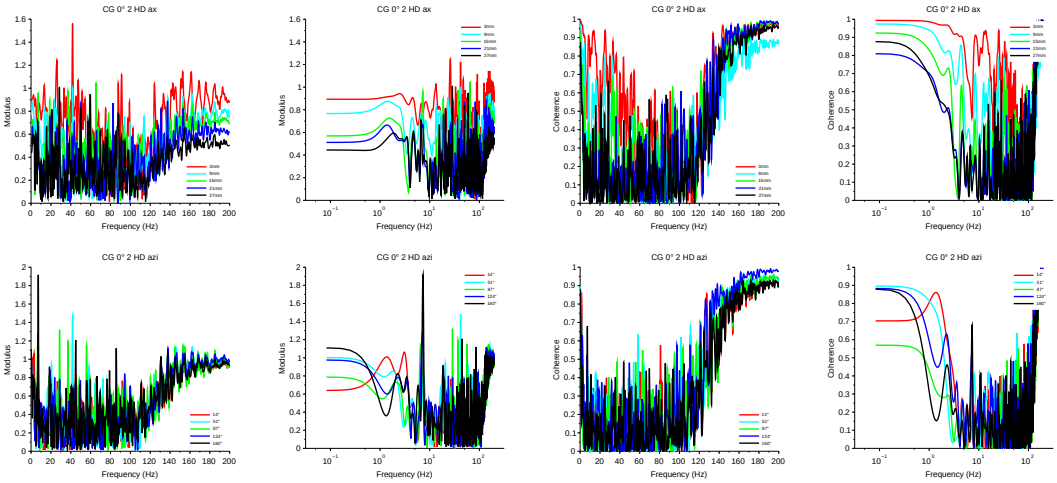

Figure C.6: Transfer function for circular grid case around 0°
2 HD in axial direction (top) and azimuthal direction (bottom)

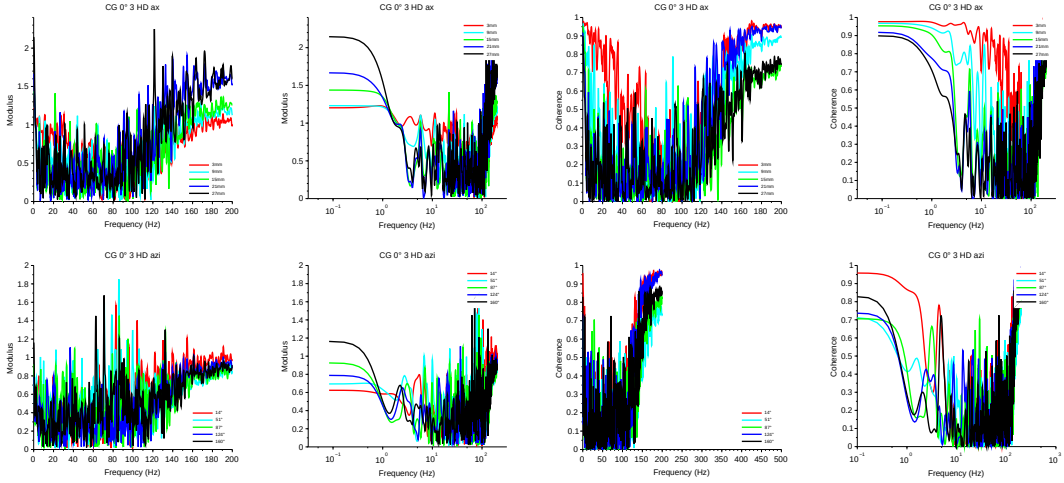

Figure C.7: Transfer function for circular grid case around 0°
3 HD in axial direction (top) and azimuthal direction (bottom)

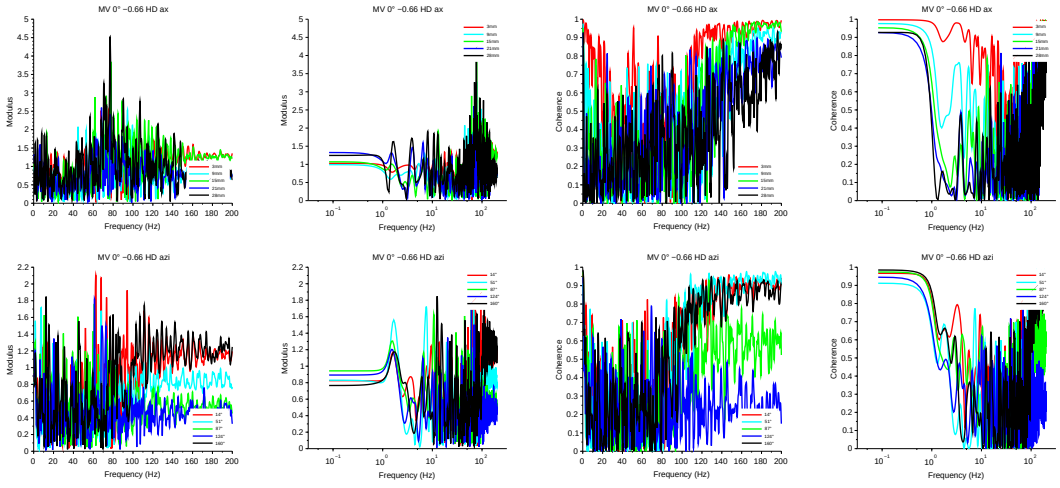

Figure C.8: Transfer function for mixing vane case around 0°
-0.66 HD in axial direction (top) and azimuthal direction (bottom)

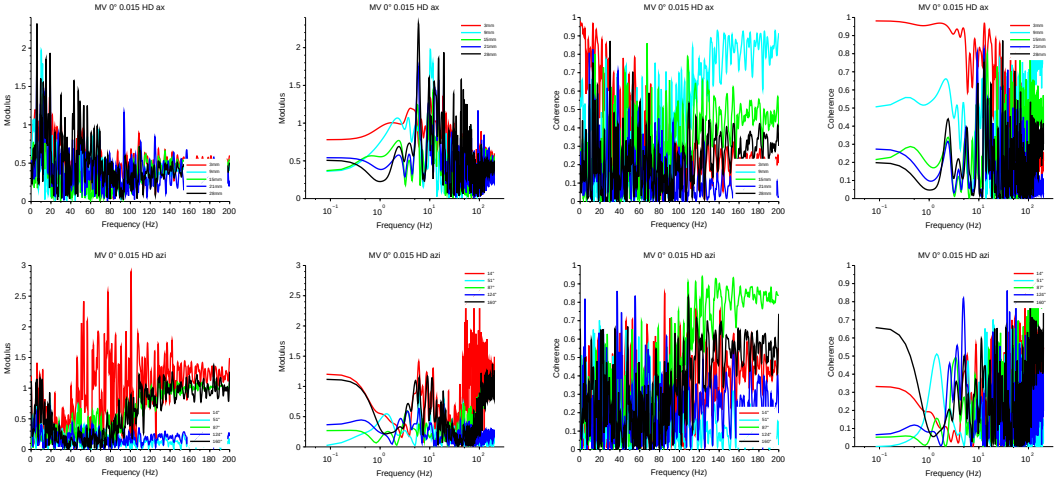

Figure C.9: Transfer function for mixing vane case around 0°
0.015 HD in axial direction (top) and azimuthal direction (bottom)

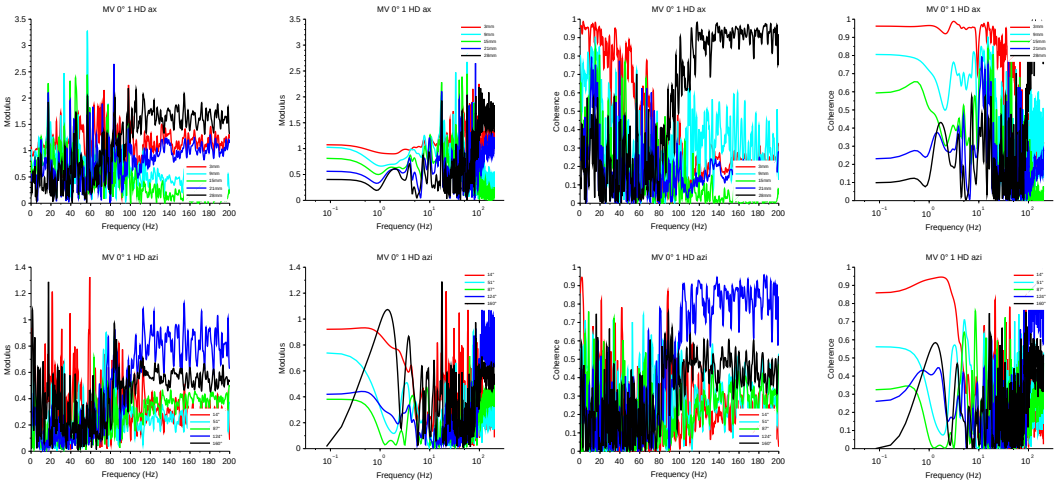

Figure C.10: Transfer function for mixing vane case around 0°
1 HD in axial direction (top) and azimuthal direction (bottom)

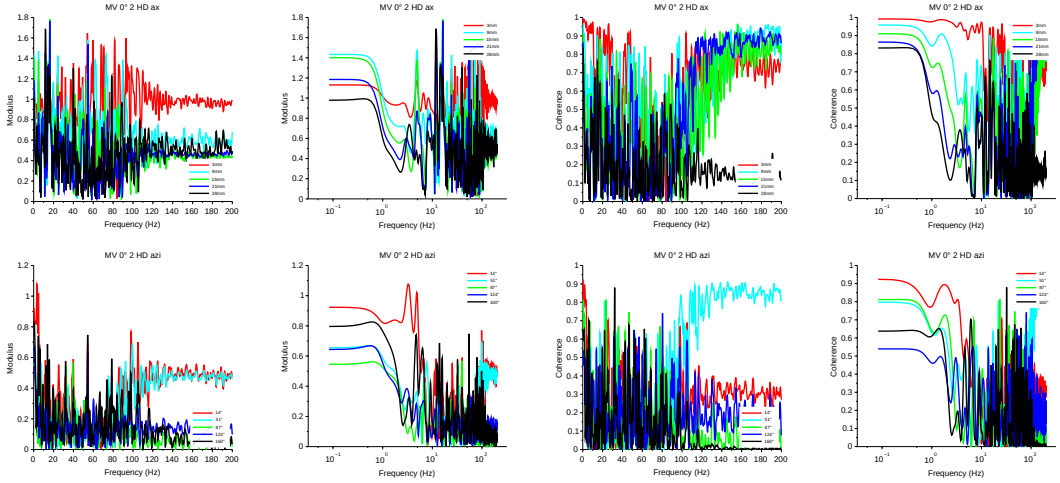

Figure C.11: Transfer function for mixing vane case around 0°
2 HD in axial direction (top) and azimuthal direction (bottom)

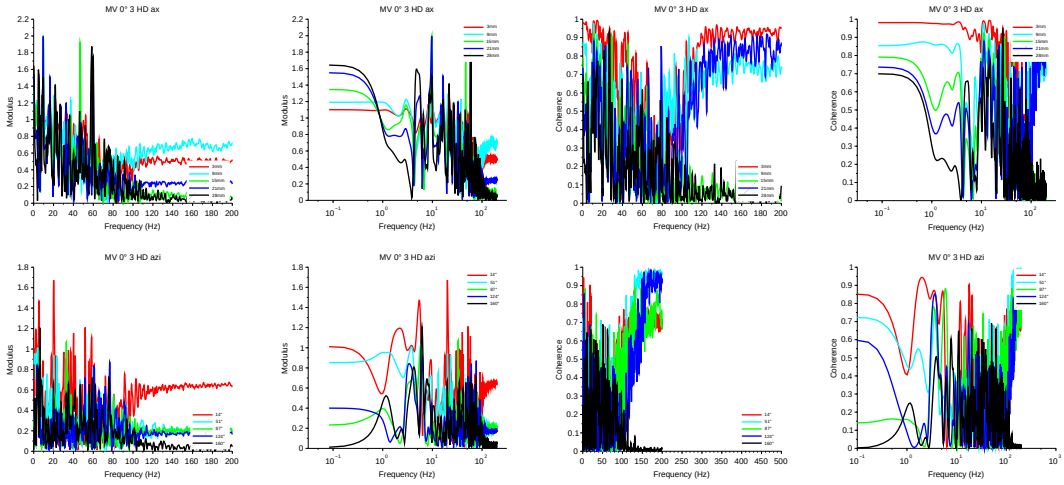

Figure C.12: Transfer function for mixing vane case around 0°
3 HD in axial direction (top) and azimuthal direction (bottom)

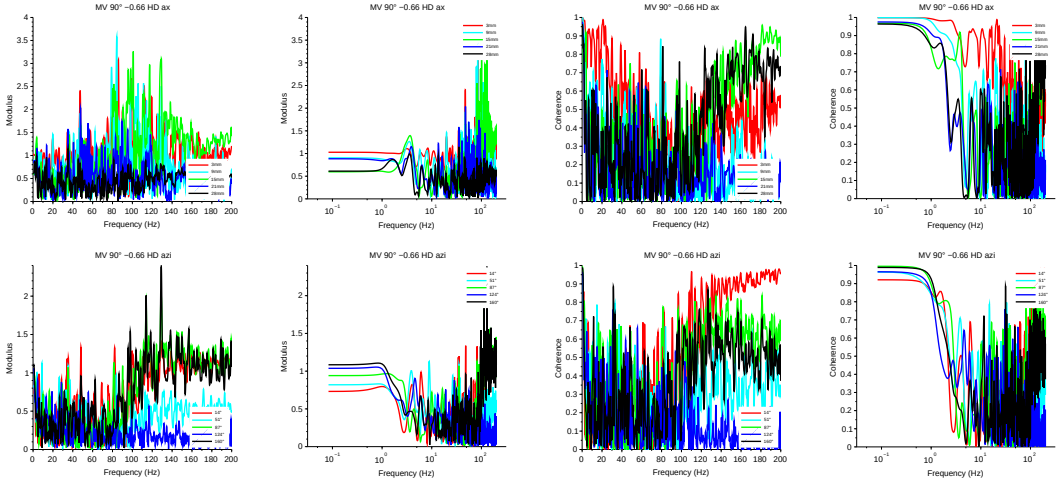

Figure C.13: Transfer function for mixing vane case around 90° -0.66 HD in axial direction (top) and azimuthal direction (bottom)

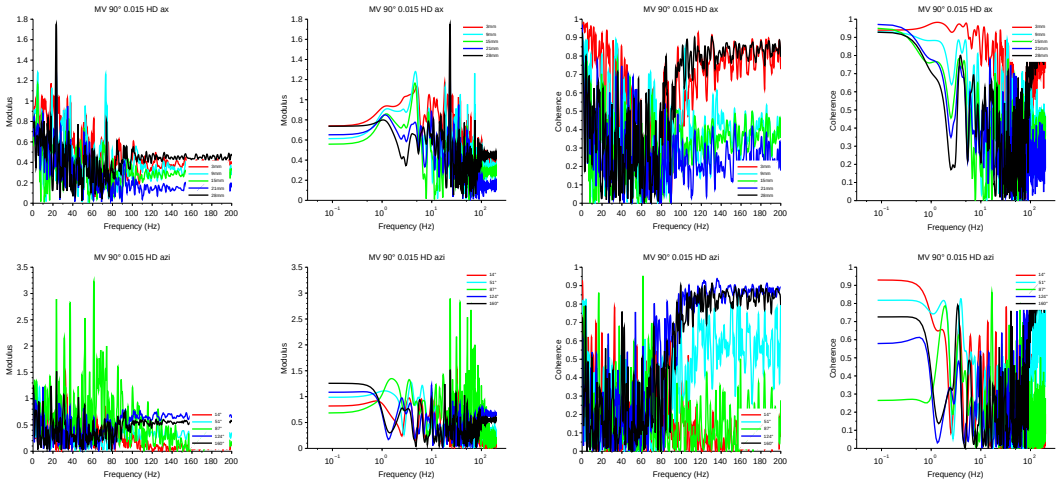

Figure C.14: Transfer function for mixing vane case around 90° 0.015 HD in axial direction (top) and azimuthal direction (bottom)

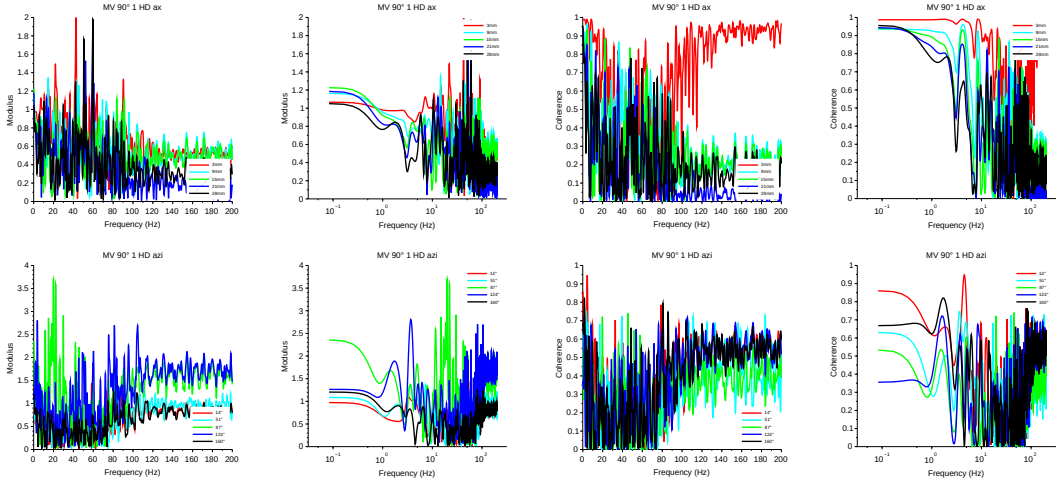

Figure C.15: Transfer function for mixing vane case around 90°
1 HD in axial direction (top) and azimuthal direction (bottom)

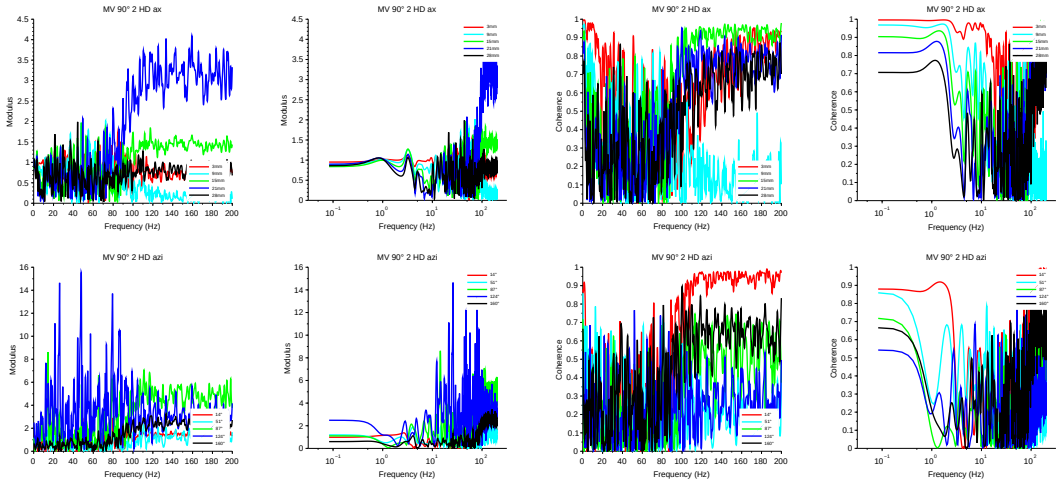

Figure C.16: Transfer function for mixing vane case around 90°
2 HD in axial direction (top) and azimuthal direction (bottom)

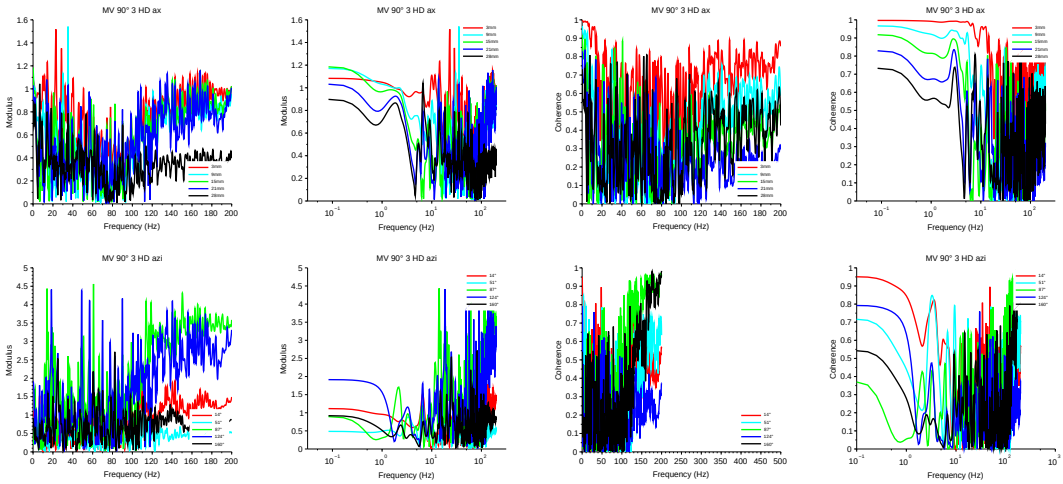

Figure C.17: Transfer function for mixing vane case around 90° 3 HD in axial direction (top) and azimuthal direction (bottom)

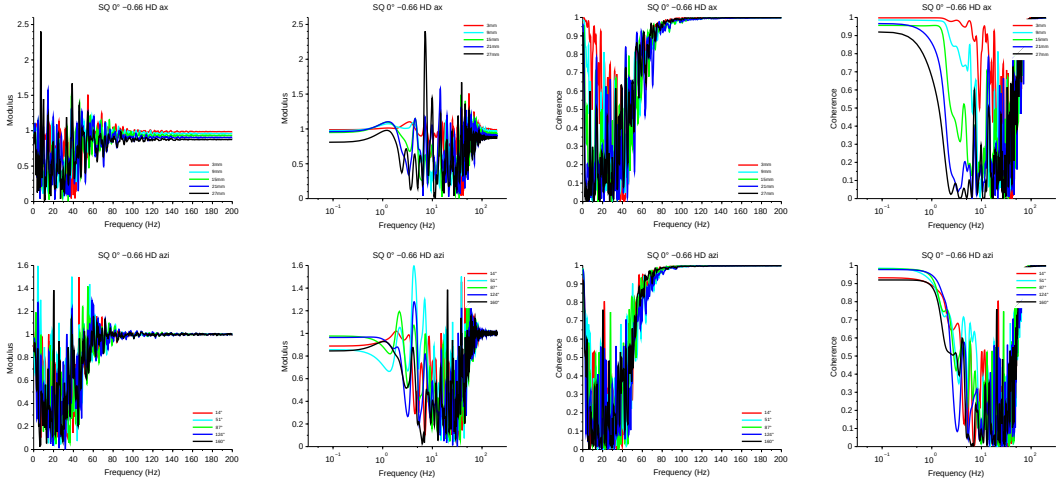

Figure C.18: Transfer function for square grid with mixing vanes case around 0° -0.66 HD in axial direction (top) and azimuthal direction (bottom)

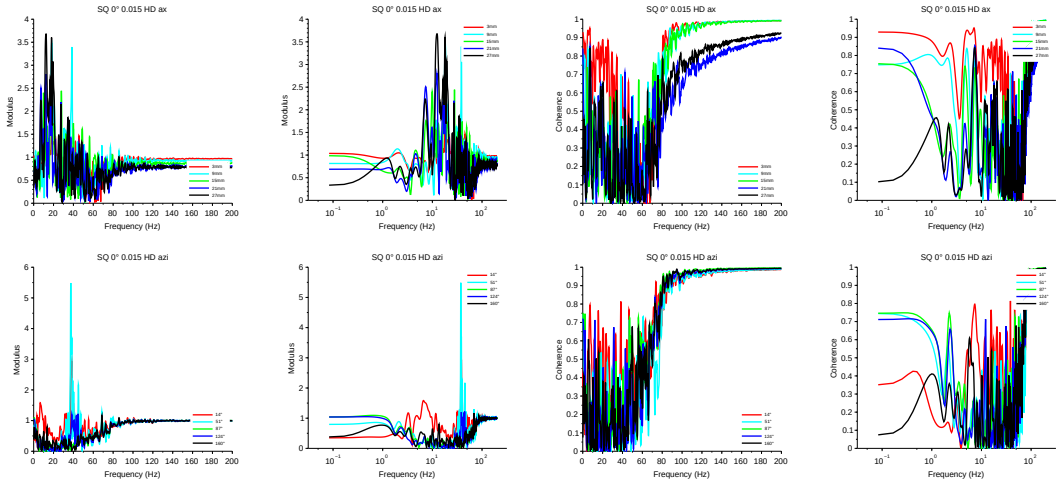

Figure C.19: Transfer function for square grid with mixing vanes case around 0° 0.015 HD in axial direction (top) and azimuthal direction (bottom)

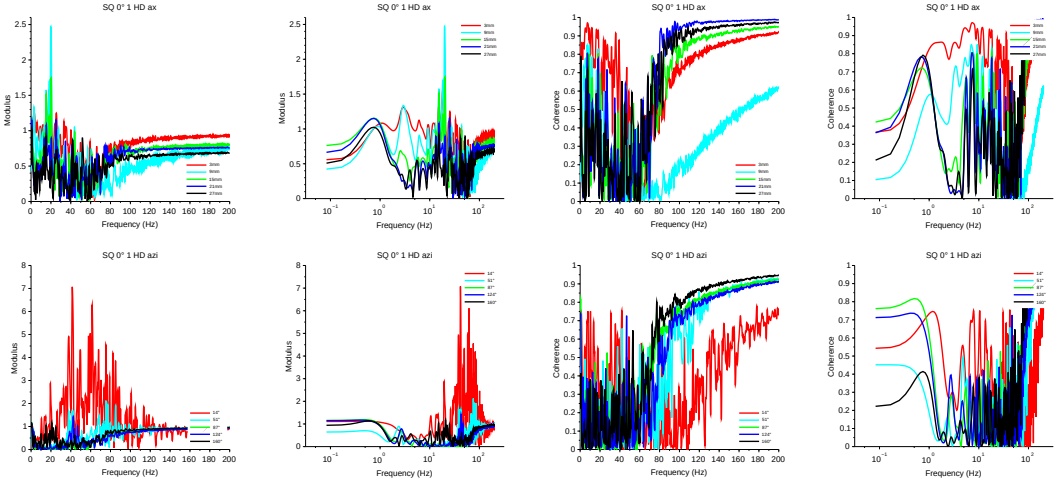

Figure C.20: Transfer function for square grid with mixing vanes case around 0° 1 HD in axial direction (top) and azimuthal direction (bottom)

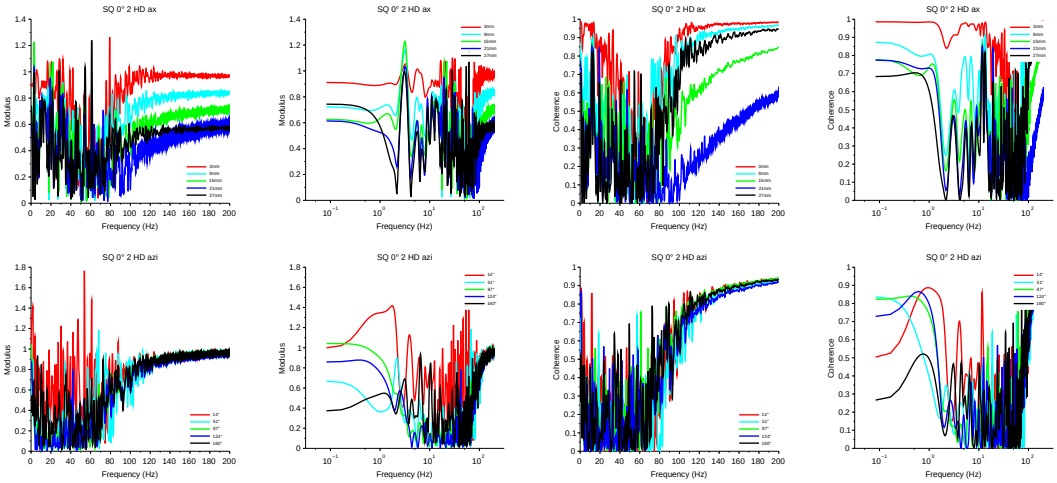

Figure C.21: Transfer function for square grid with mixing vanes case around 0° 2 HD in axial direction (top) and azimuthal direction (bottom)

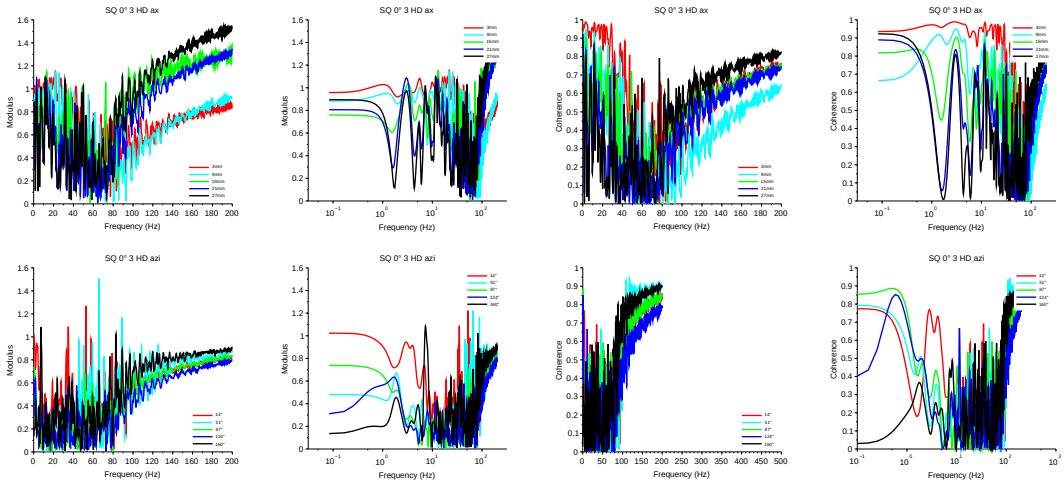

Figure C.22: Transfer function for square grid with mixing vanes case around 0° 3 HD in axial direction (top) and azimuthal direction (bottom)

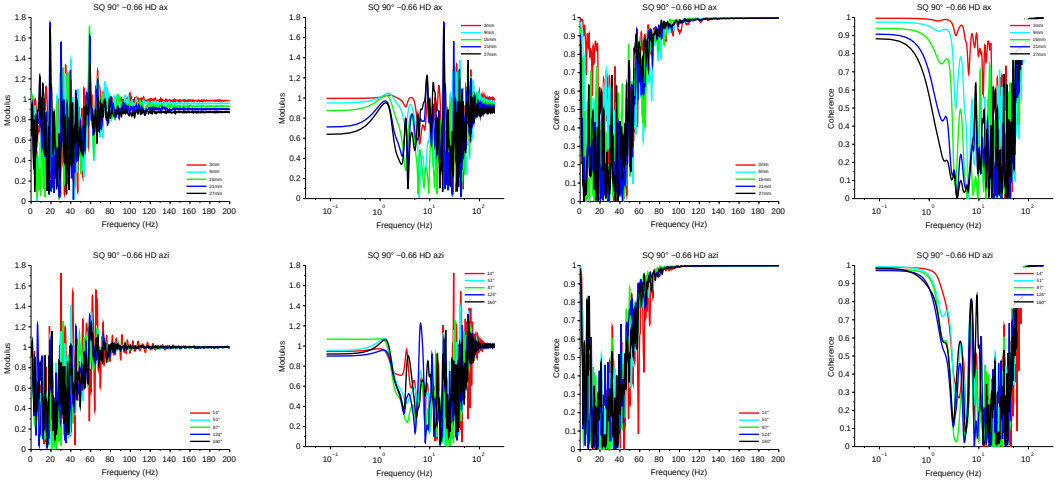

Figure C.23: Transfer function for square grid with mixing vanes case around 90° -0.66 HD in axial direction (top) and azimuthal direction (bottom)

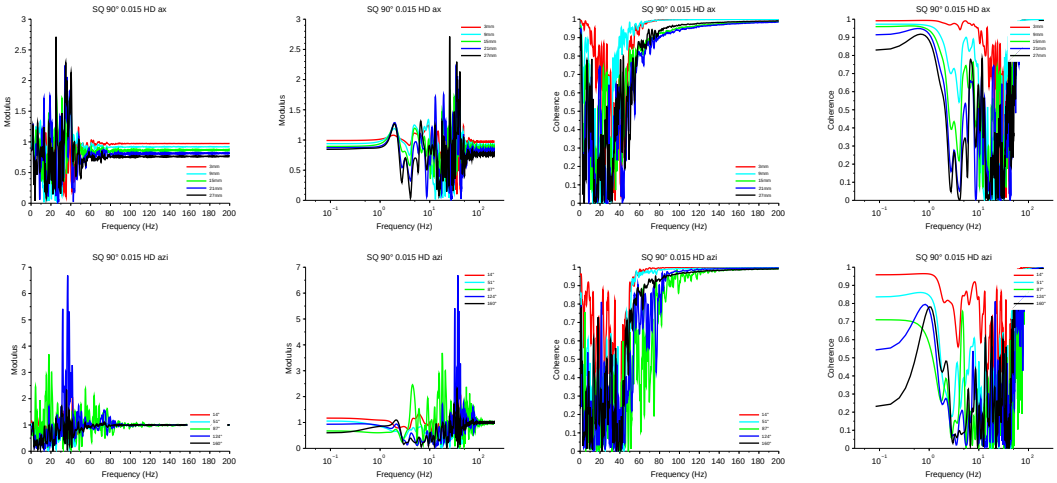

Figure C.24: Transfer function for square grid with mixing vanes case around 90° 0.015 HD in axial direction (top) and azimuthal direction (bottom)

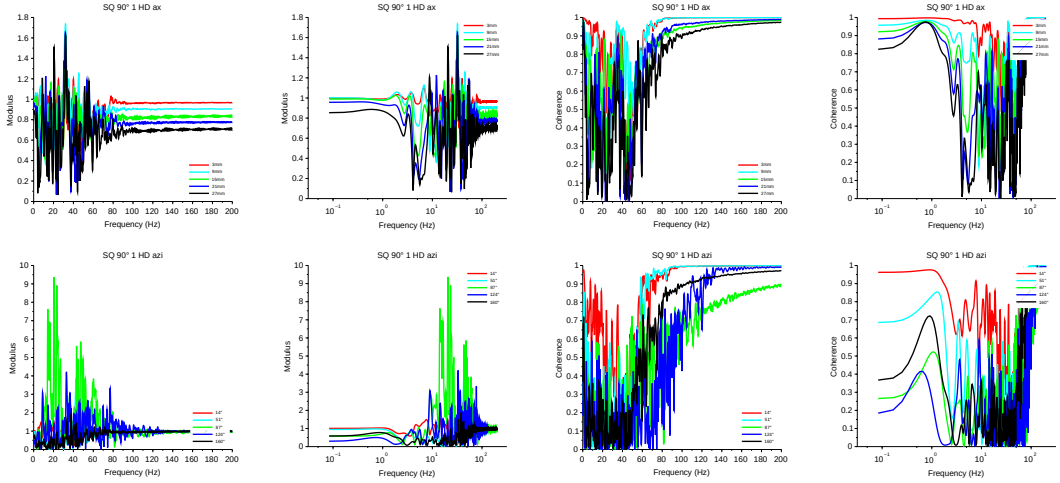

Figure C.25: Transfer function for square grid with mixing vanes case around 90° 1 HD in axial direction (top) and azimuthal direction (bottom)

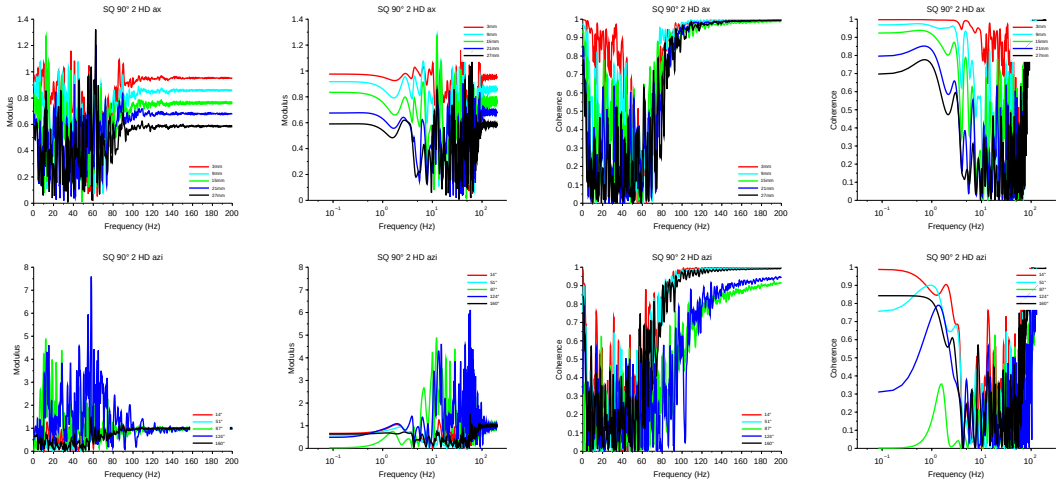

Figure C.26: Transfer function for square grid with mixing vanes case around 90° 2 HD in axial direction (top) and azimuthal direction (bottom)

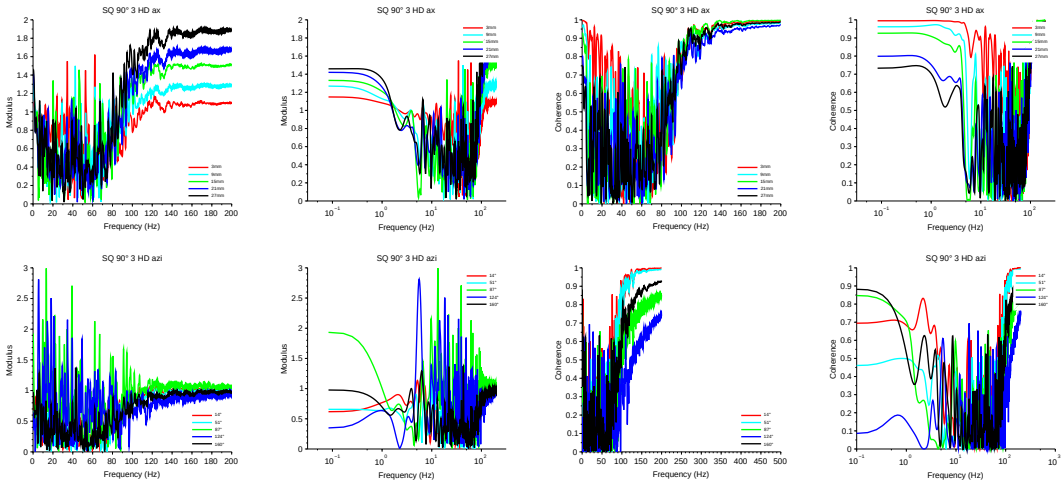

Figure C.27: Transfer function for square grid with mixing vanes case around 90° 3 HD in axial direction (top) and azimuthal direction (bottom)

Appendix D

Proper Orthogonal Decomposition

The Proper Orthogonal Modes (POM) are presented here for each of the five cases (PC, PF, MV, CG and SQ) in both axial and azimuthal directions. The frequency - POM diagrams and the wavenumber - POM diagrams are also presented.

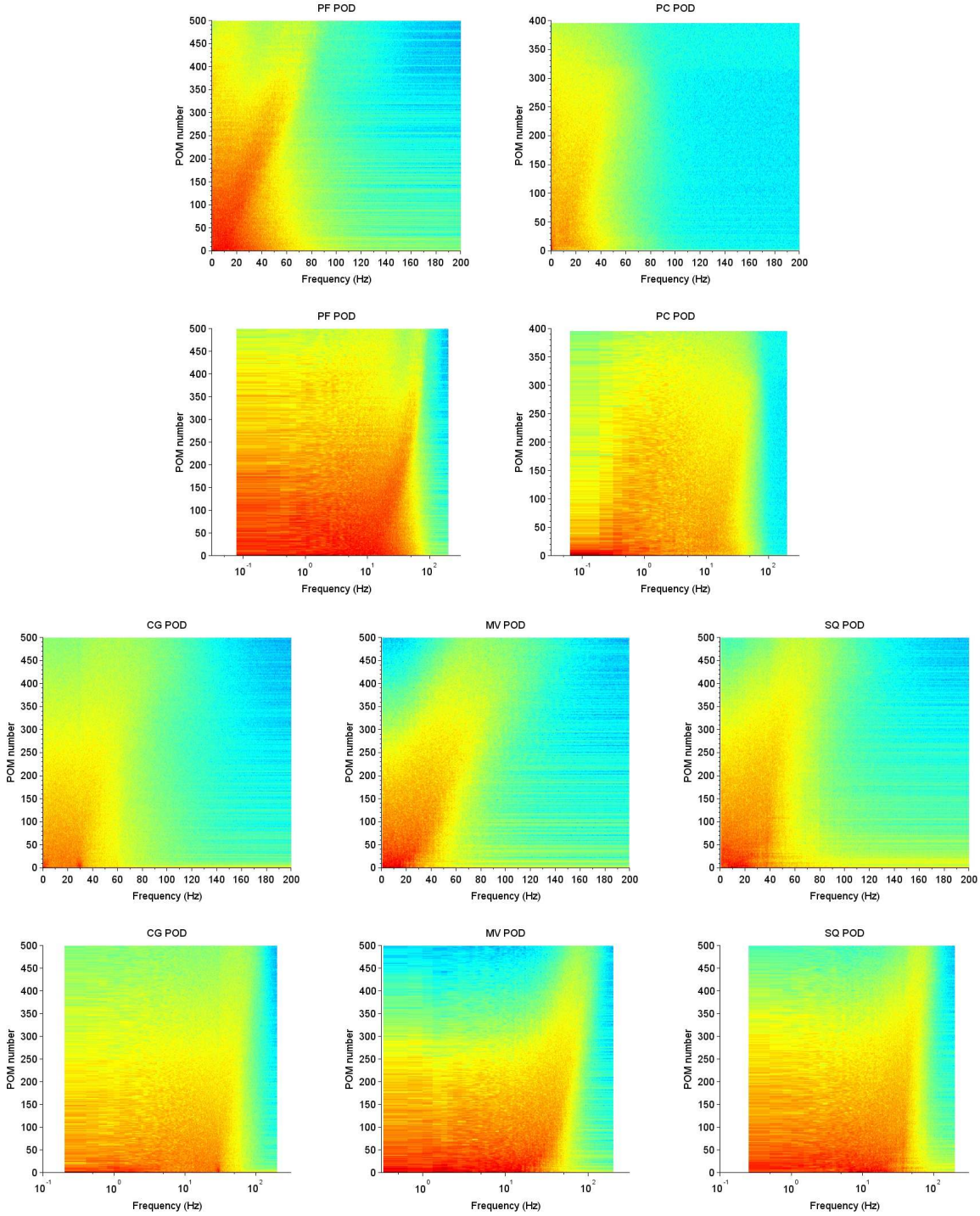

Figure D.1: Frequency POM diagrams

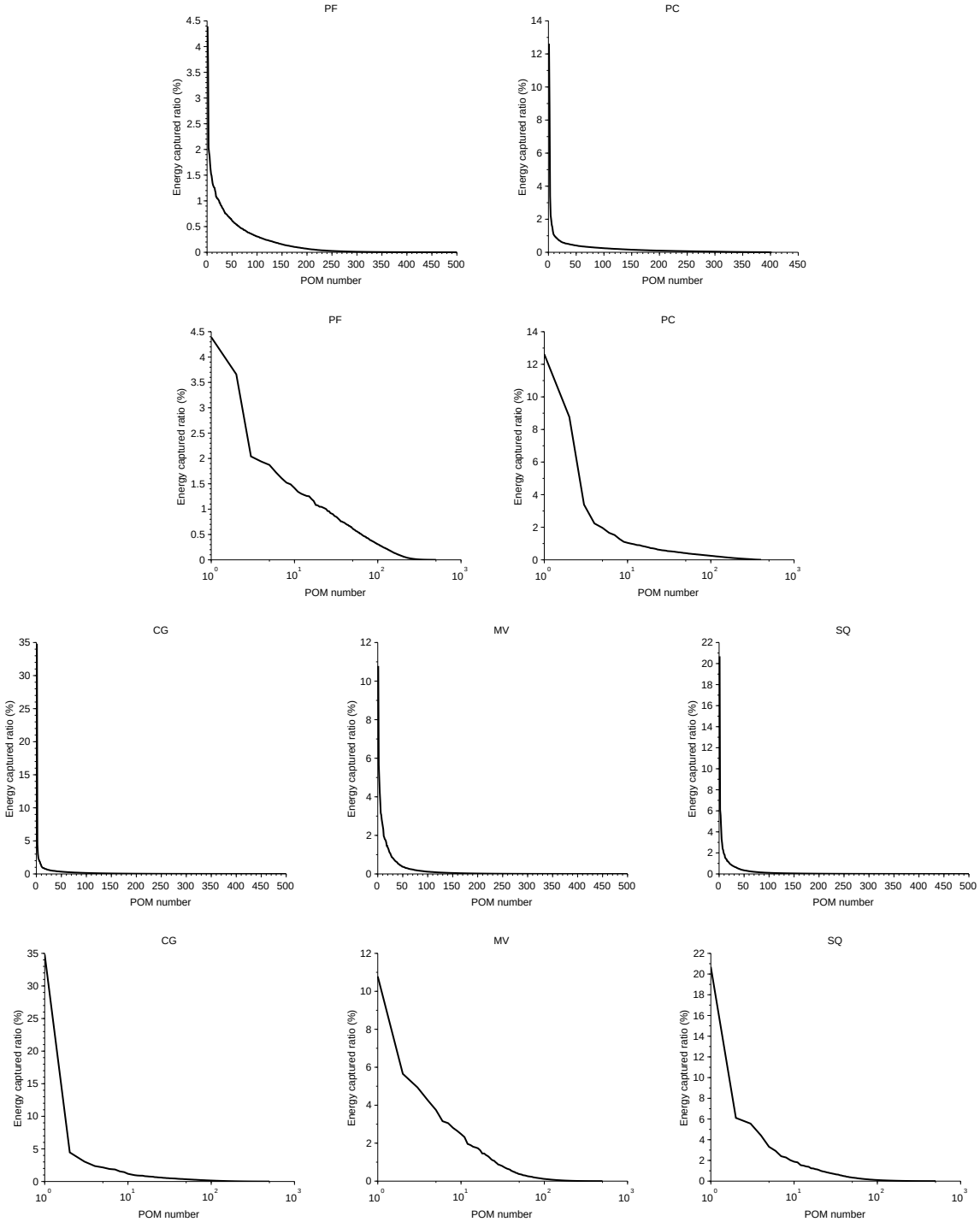

Figure D.2: Percentage of energy captured per mode

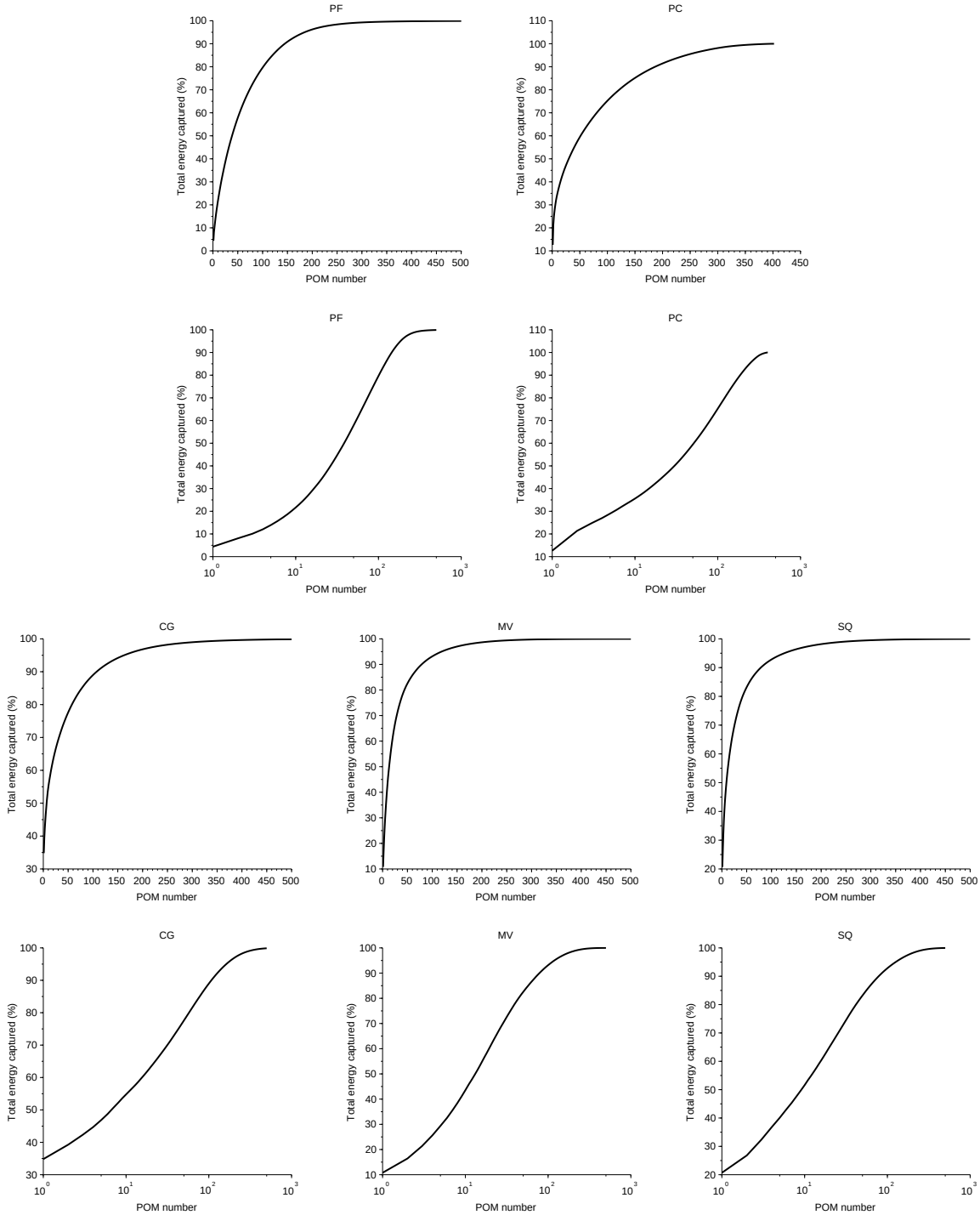

Figure D.3: Total percentage of energy captured per mode

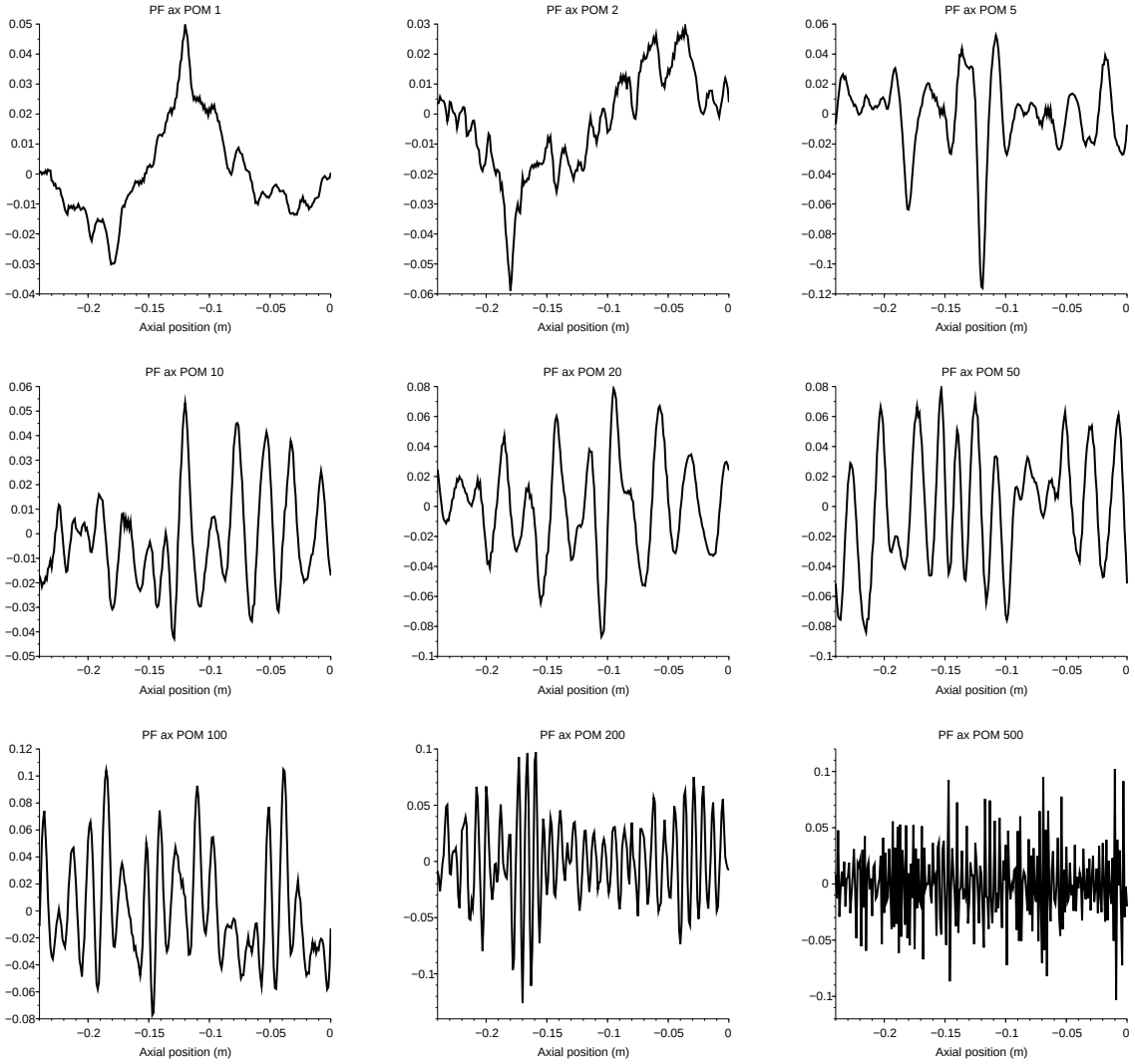

Figure D.4: POM for annular pipe fine mesh case - axial direction

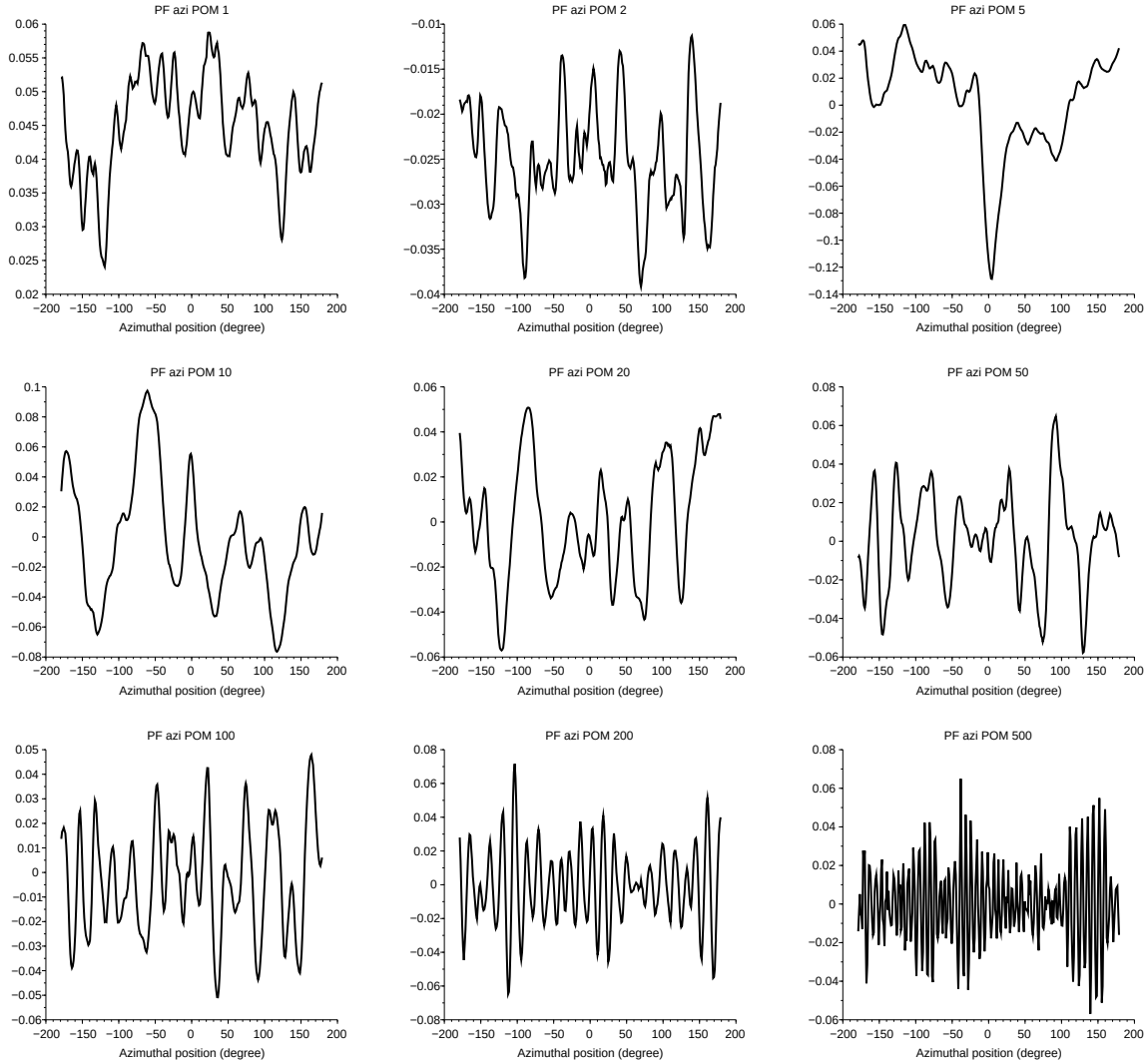

Figure D.5: POM for annular pipe fine mesh case - azimuthal direction

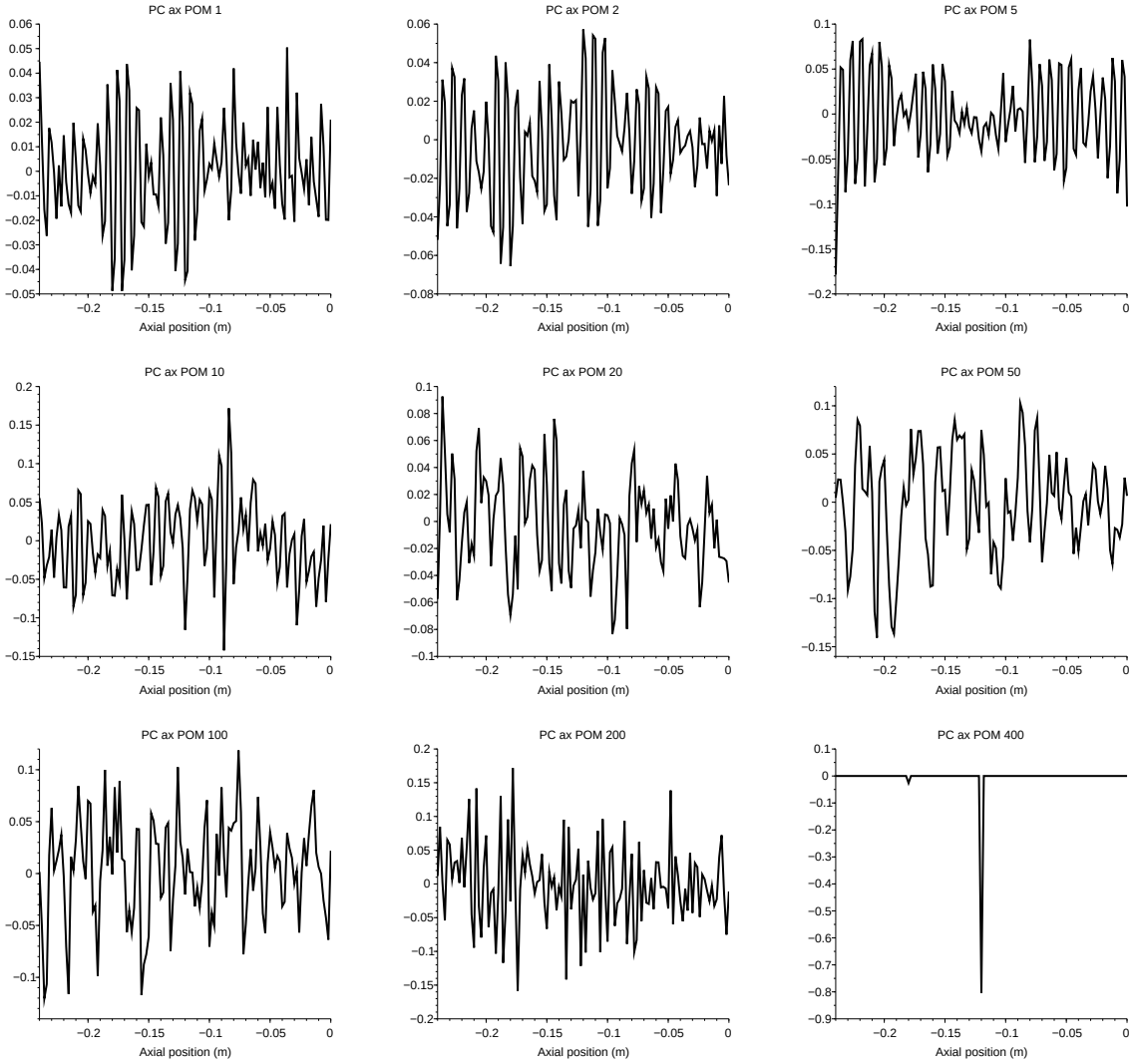

Figure D.6: POM for annular pipe coarse mesh case - axial direction

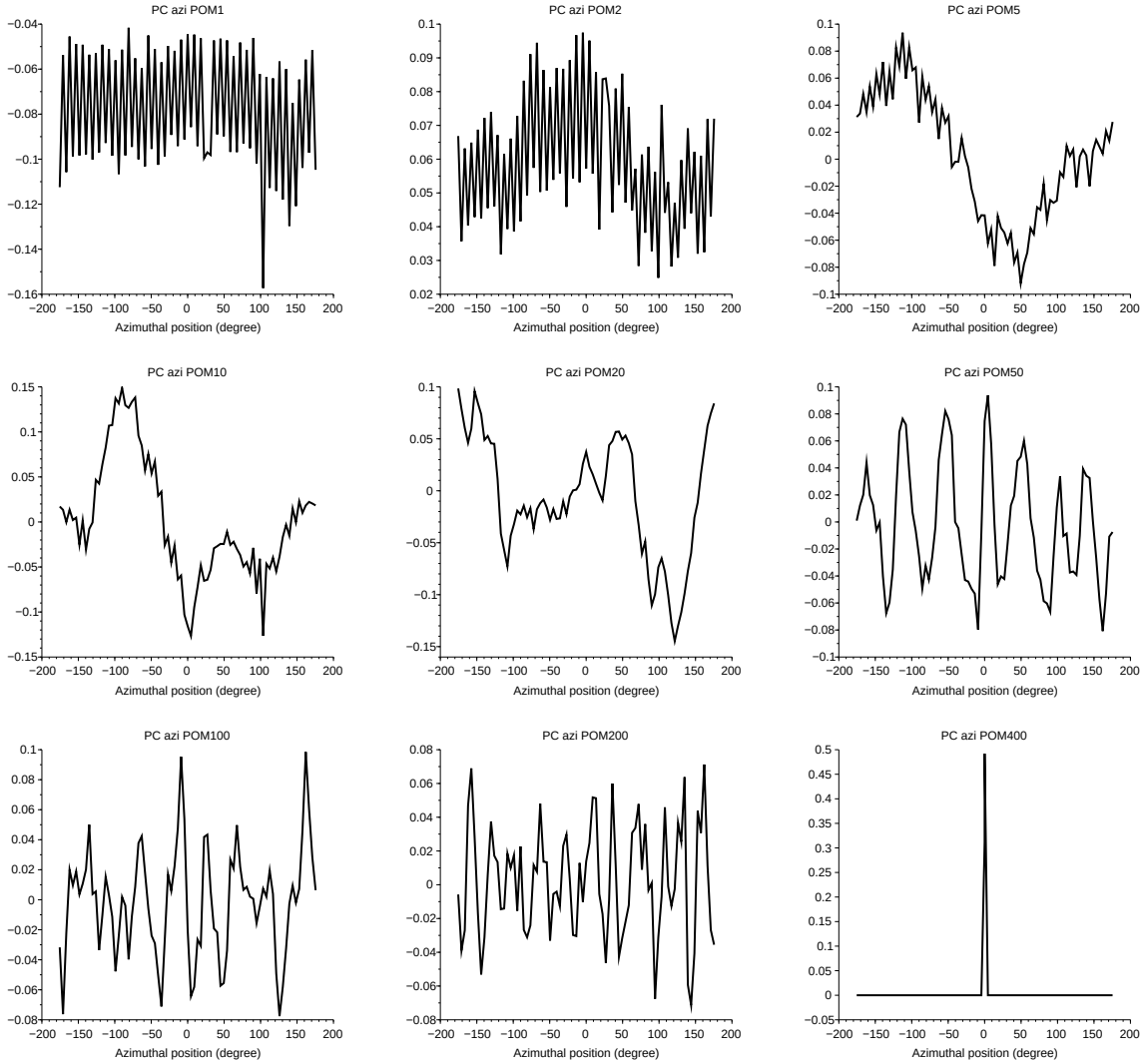

Figure D.7: POM for annular pipe coarse mesh case - azimuthal direction

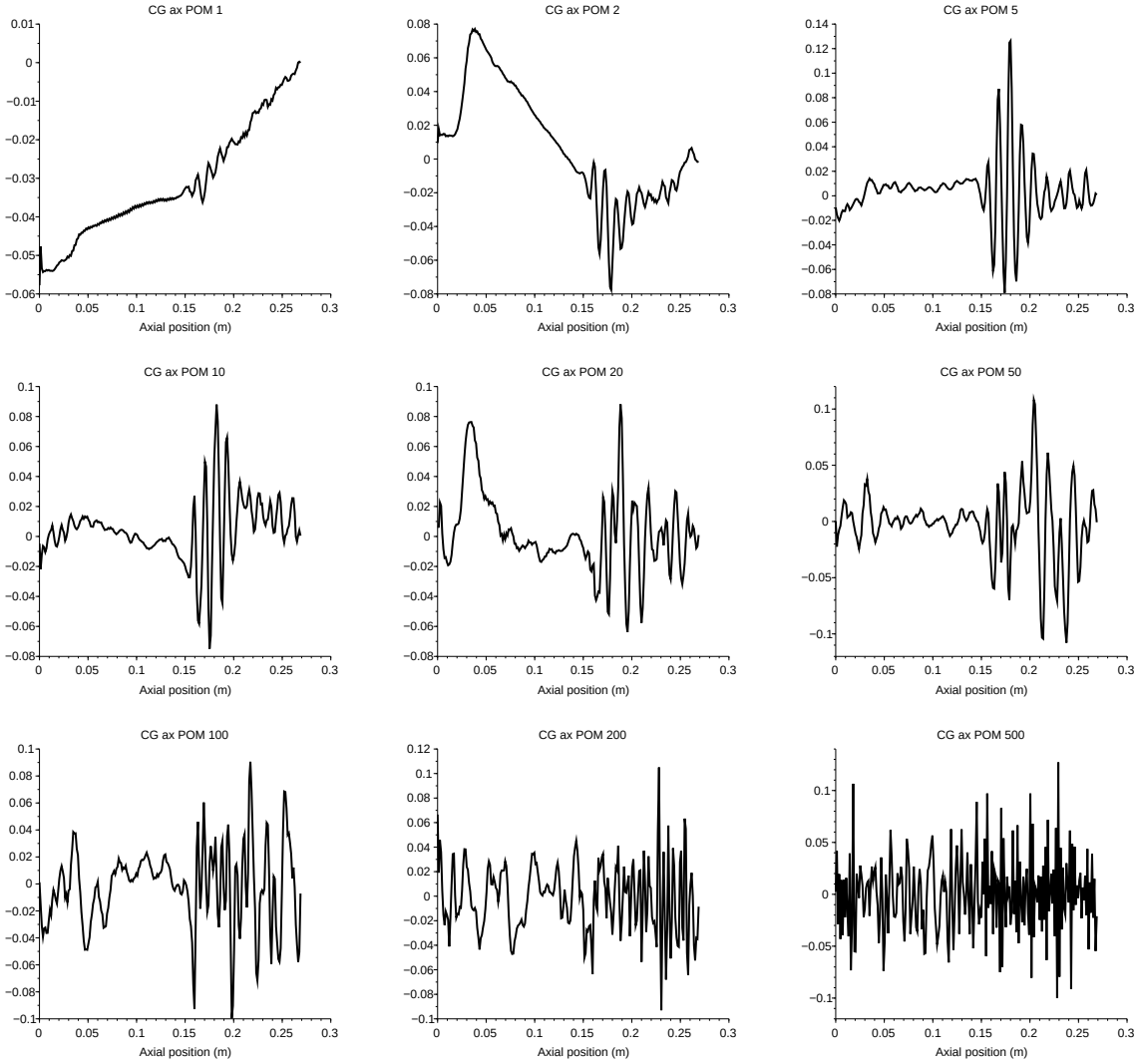

Figure D.8: POM for circular grid case - axial direction - probe at 0°

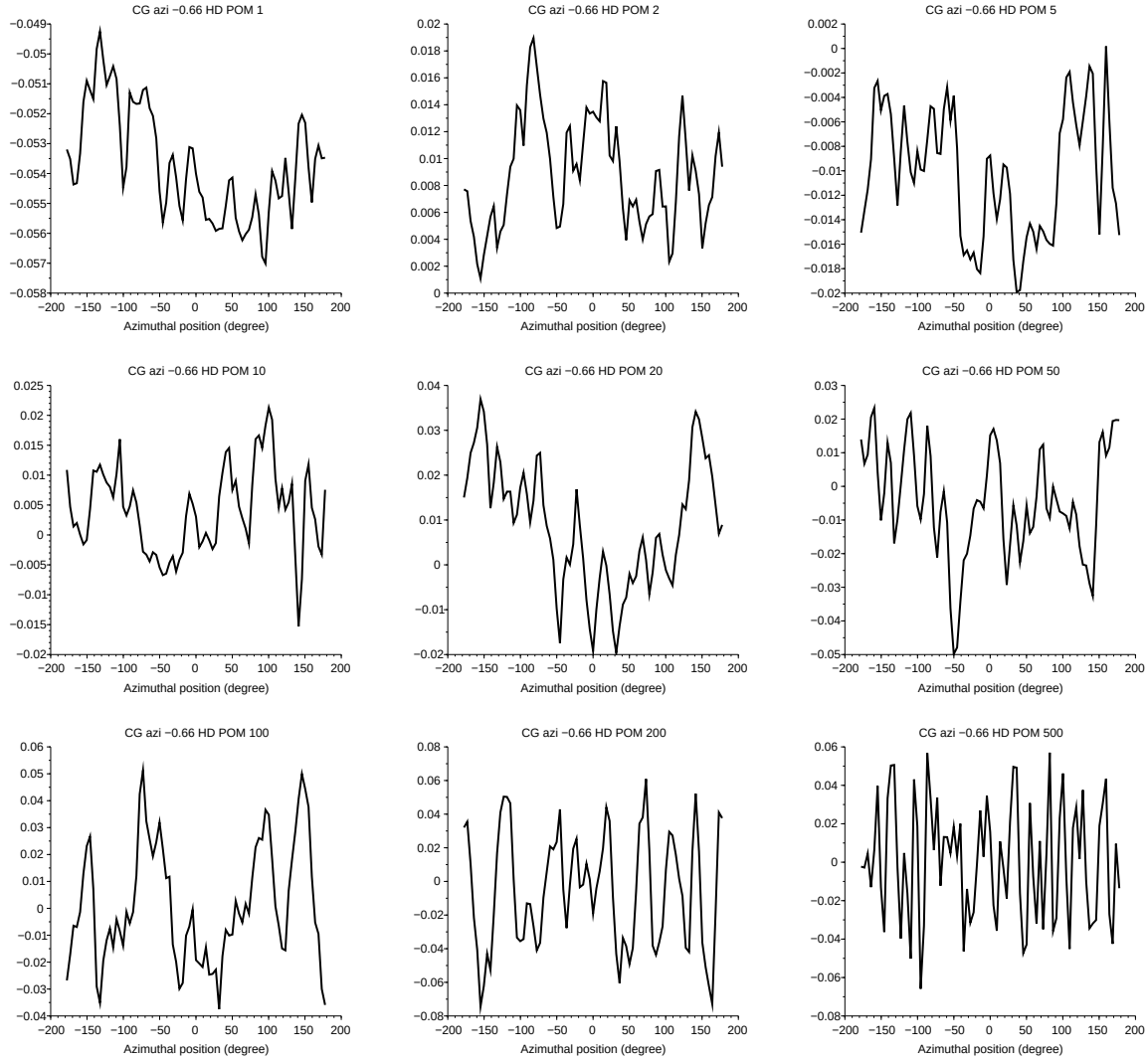

Figure D.9: POM for circular grid case - azimuthal direction - probe at -0.66 HD

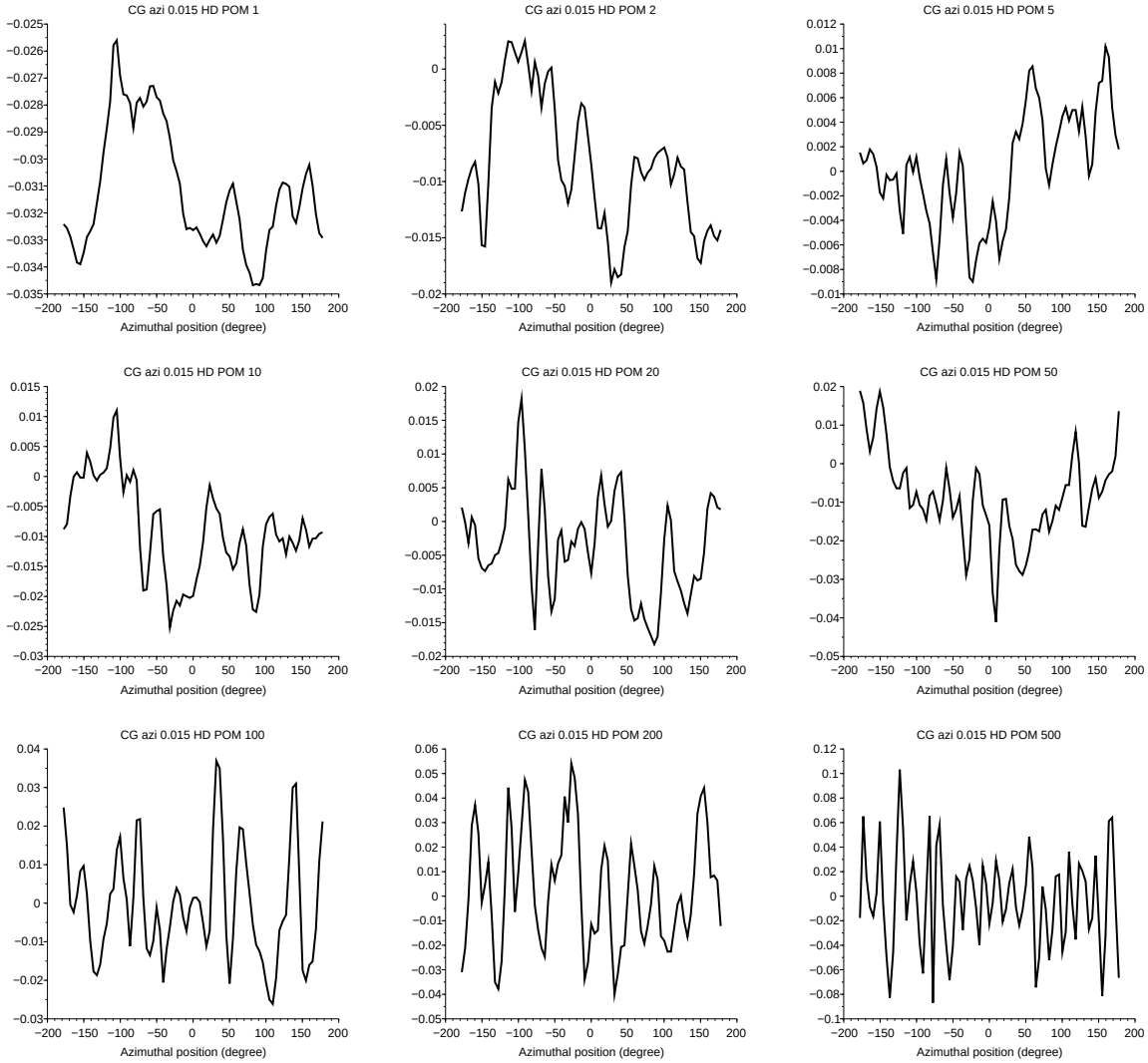

Figure D.10: POM for circular grid case - azimuthal direction - probe at 0.015 HD

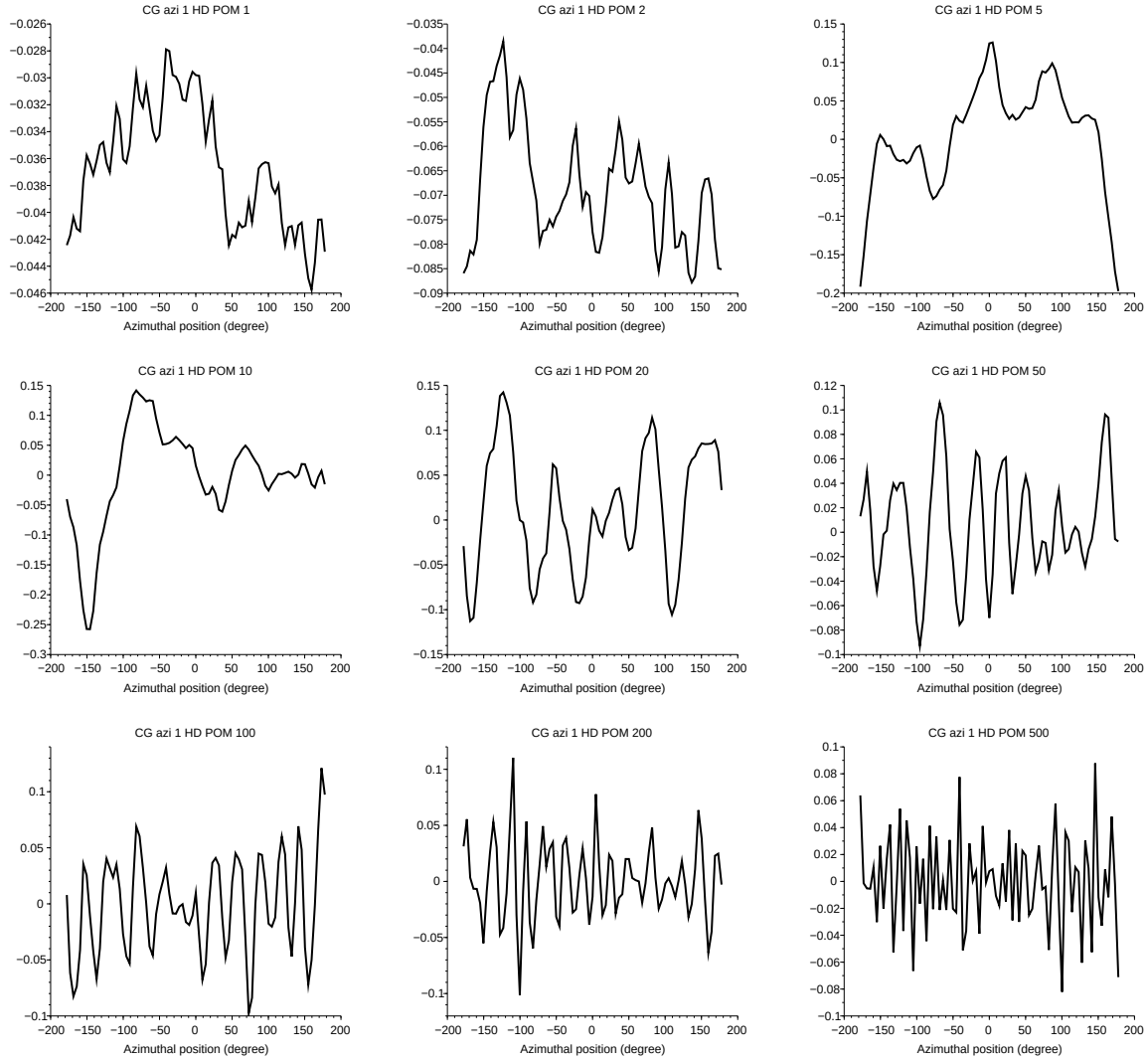

Figure D.11: POM for circular grid case - azimuthal direction - probe at 1 HD

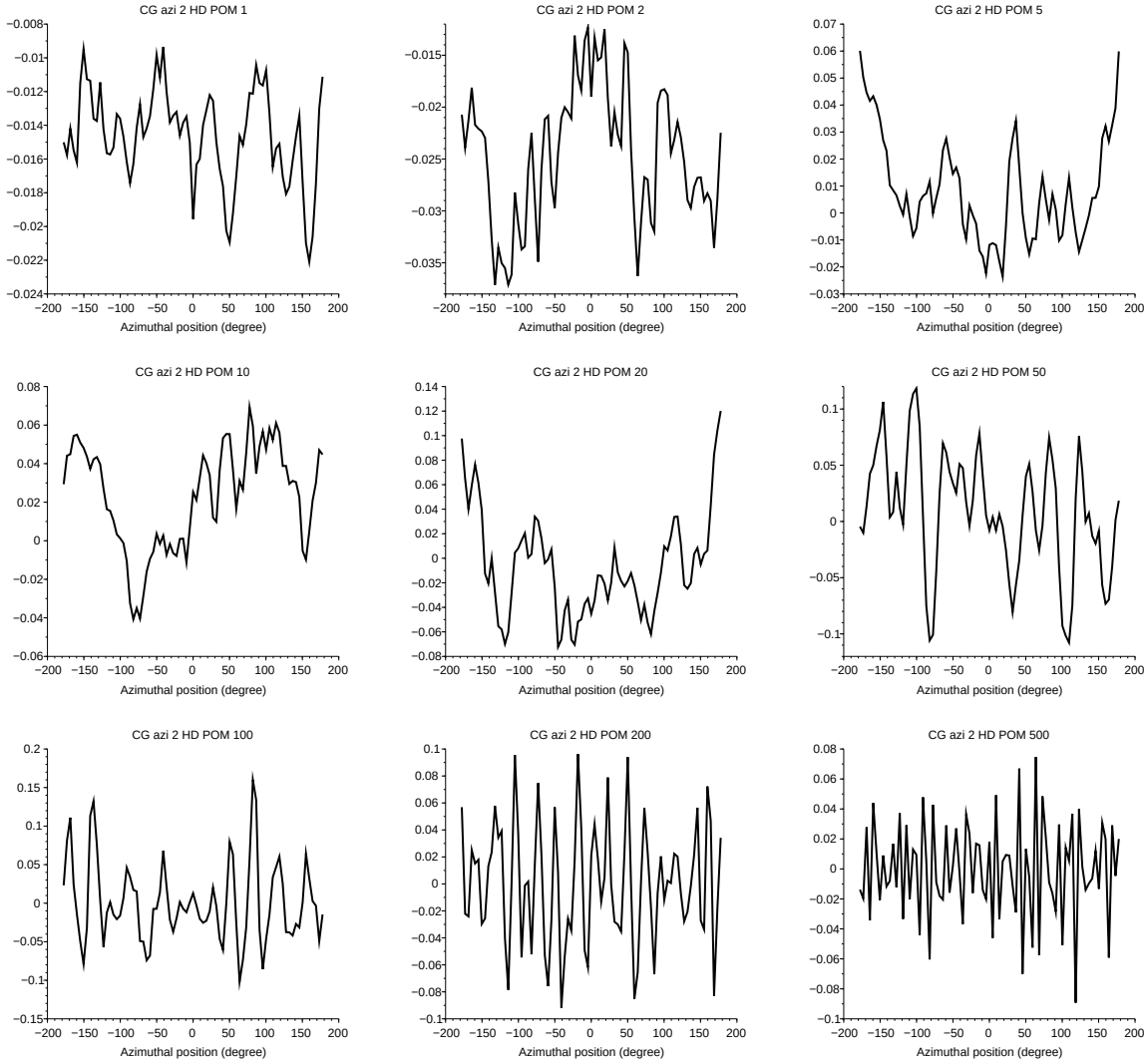

Figure D.12: POM for circular grid case - azimuthal direction - probe at 2 HD

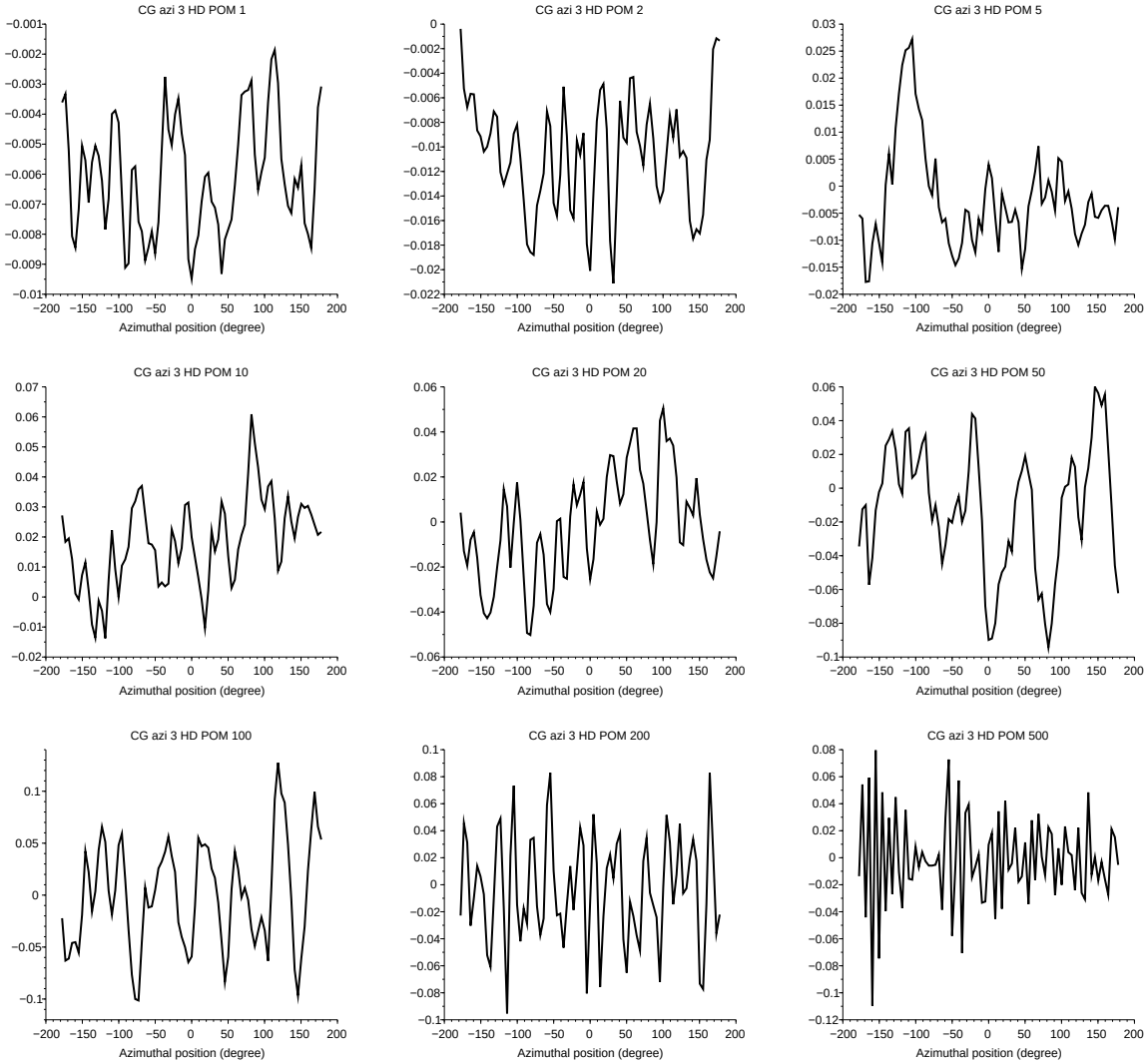

Figure D.13: POM for circular grid case - azimuthal direction - probe at 3 HD

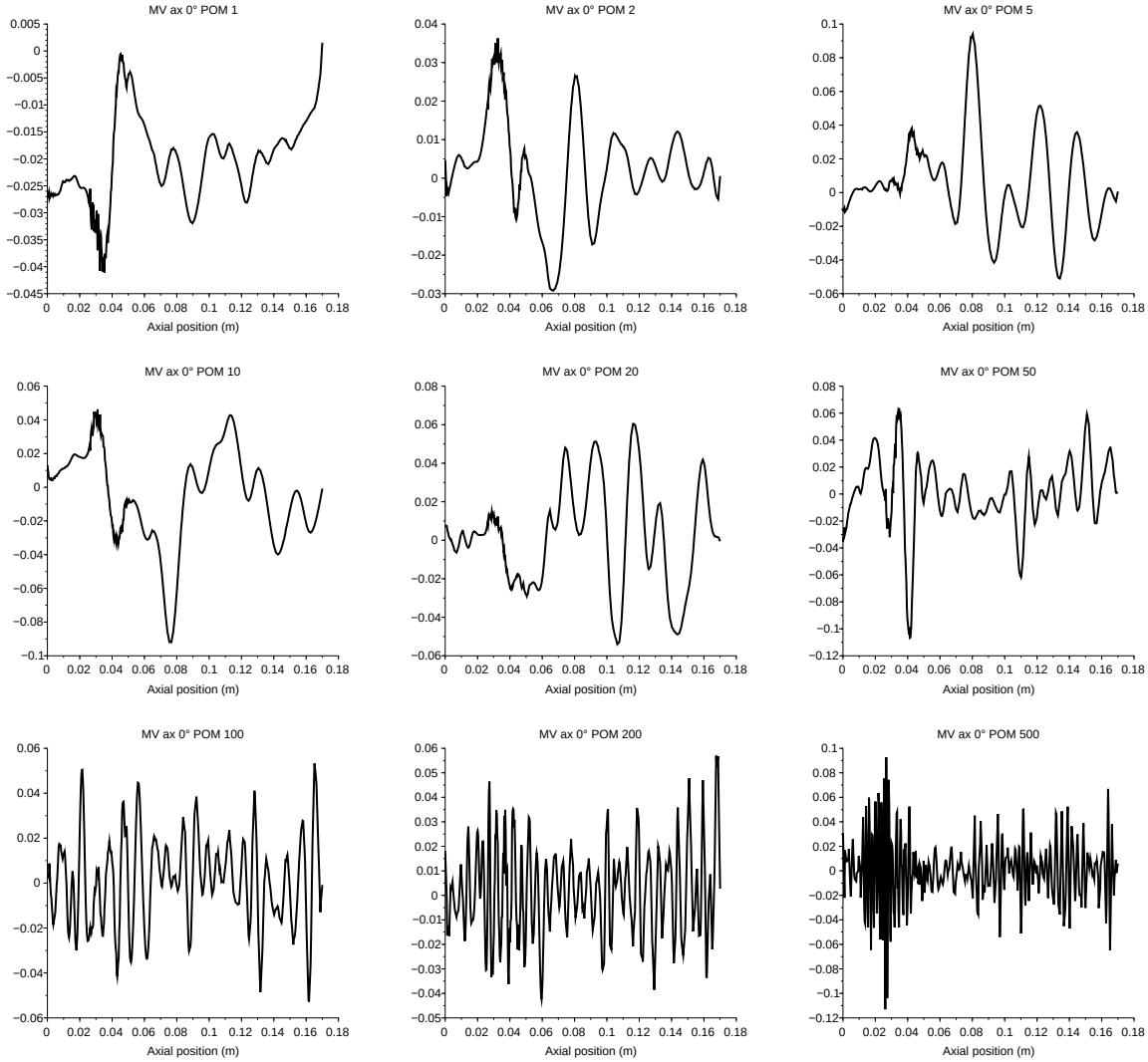

Figure D.14: POM for mixing vane case - axial direction - probe at 0°

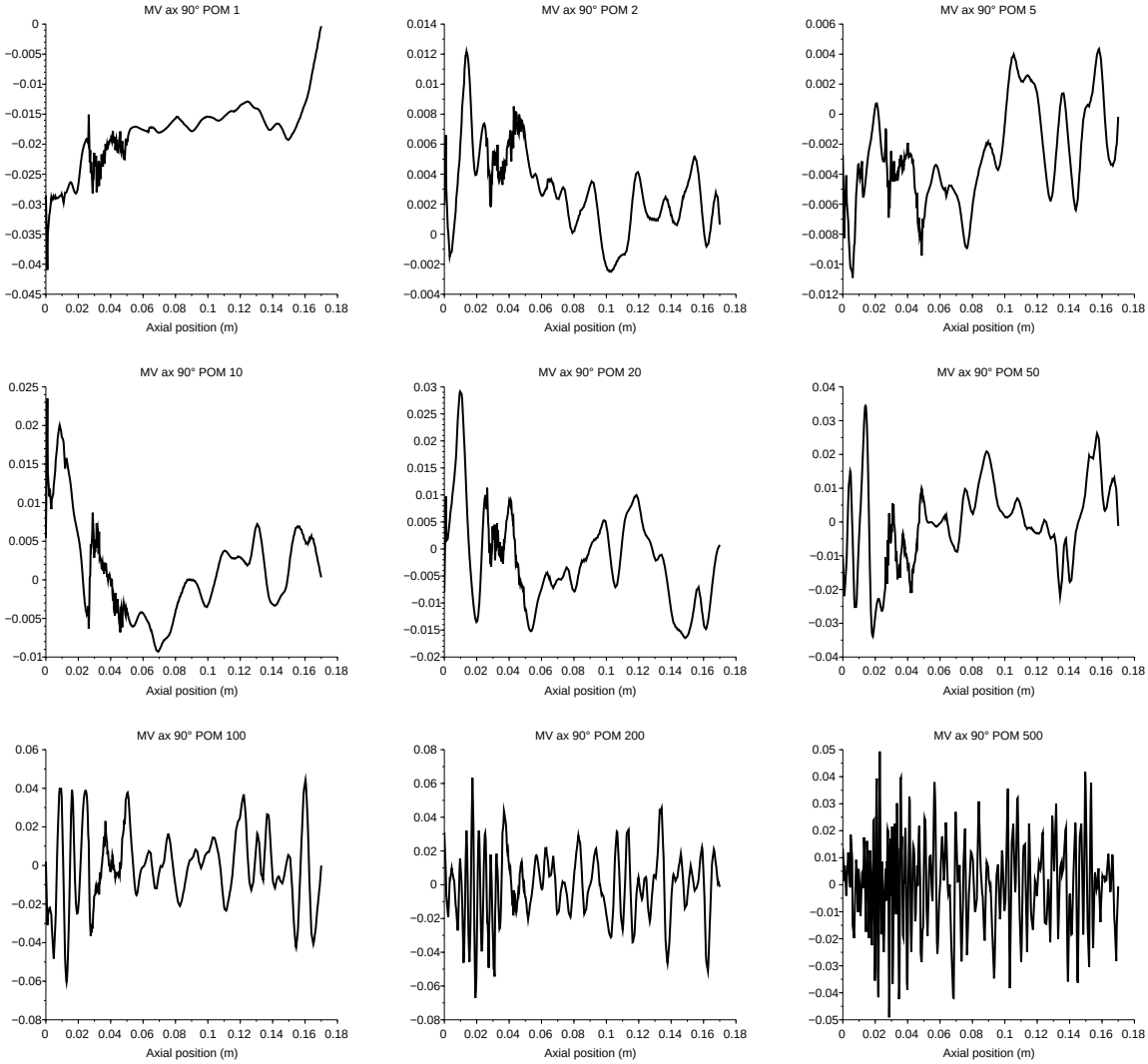

Figure D.15: POM for mixing vane case - axial direction - probe at 90°

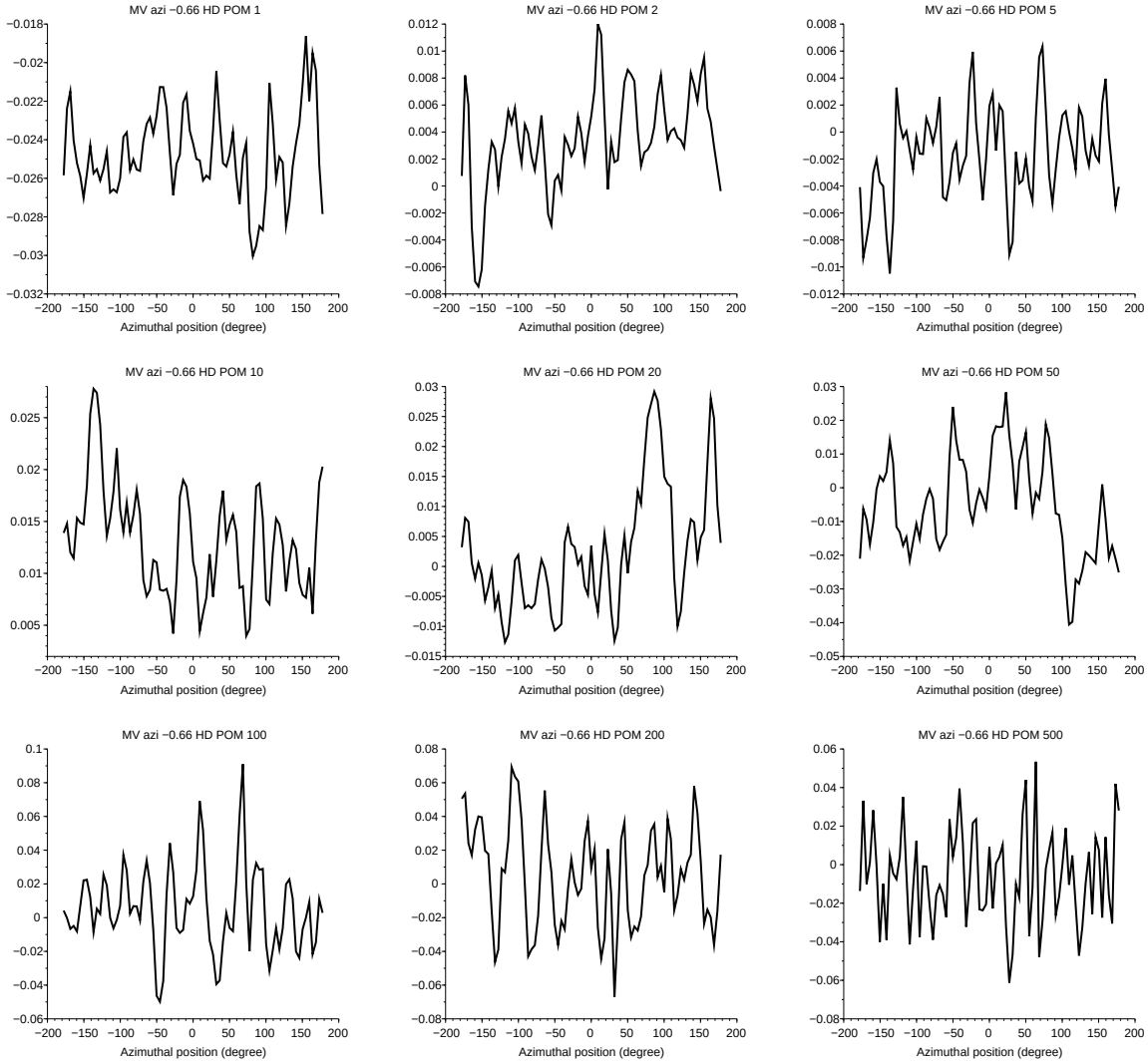

Figure D.16: POM for mixing vane case - azimuthal direction - probe at -0.66 HD

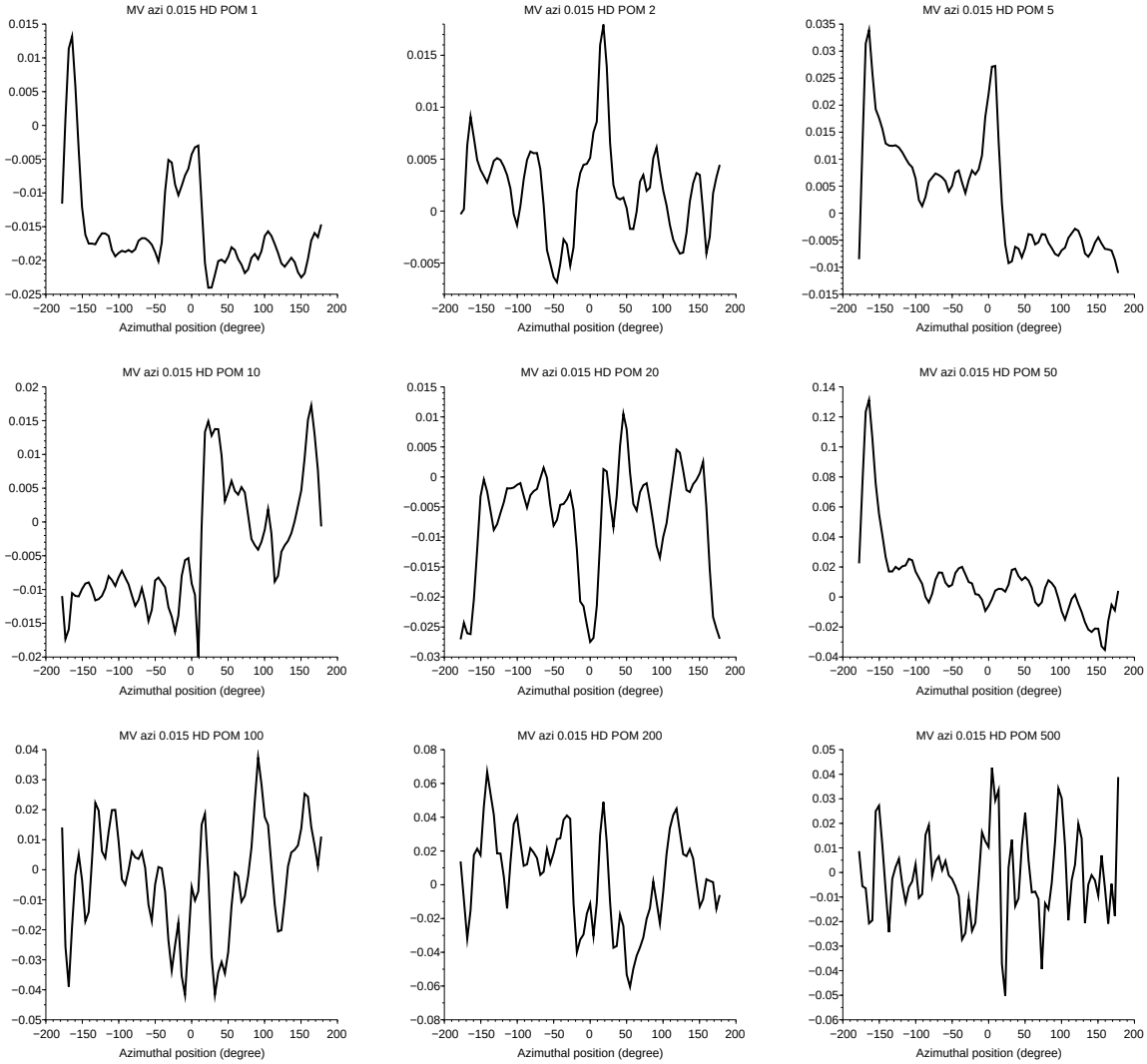

Figure D.17: POM for mixing vane case - azimuthal direction - probe at 0.015 HD

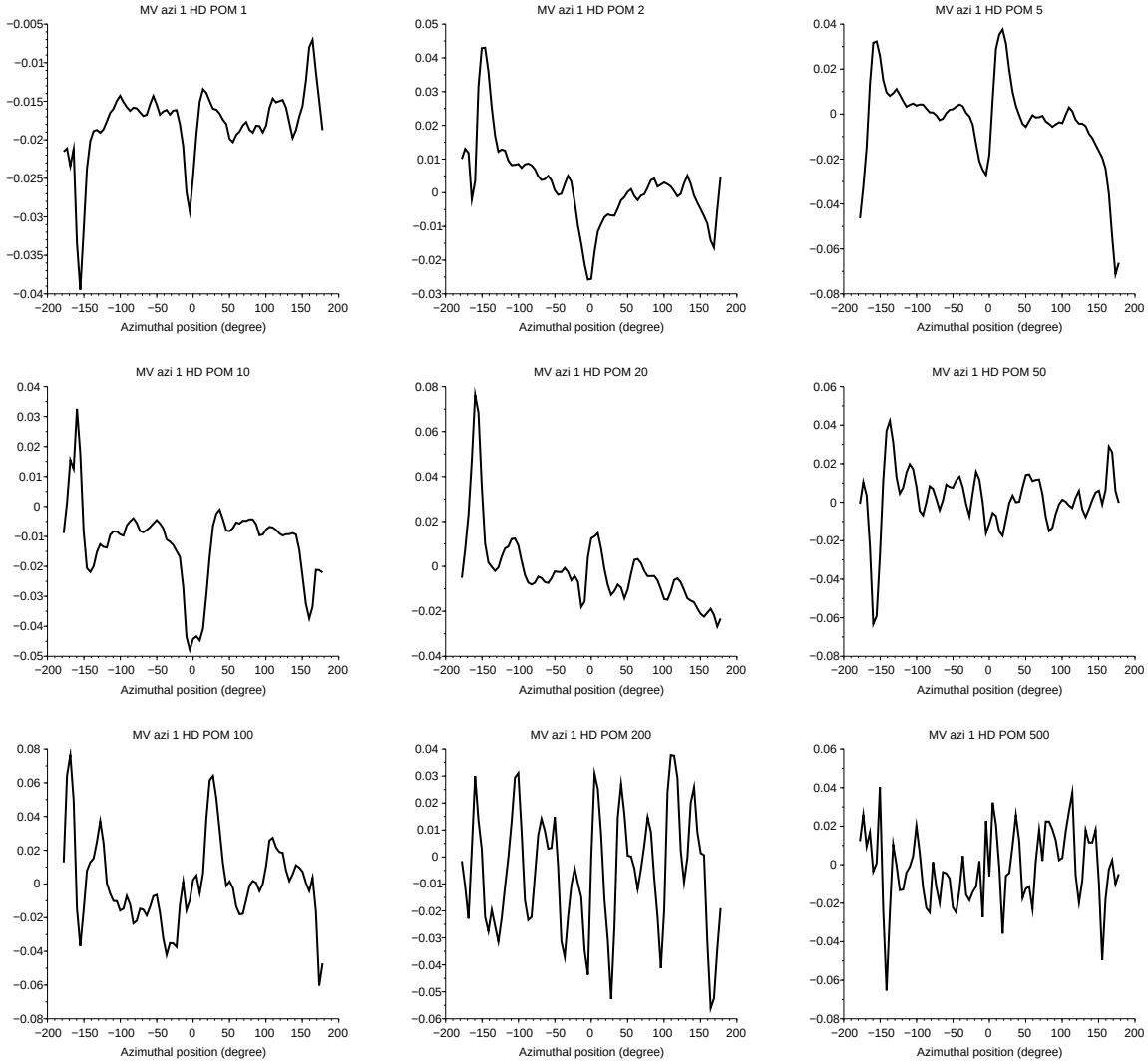

Figure D.18: POM for mixing vane case - azimuthal direction - probe at 1 HD

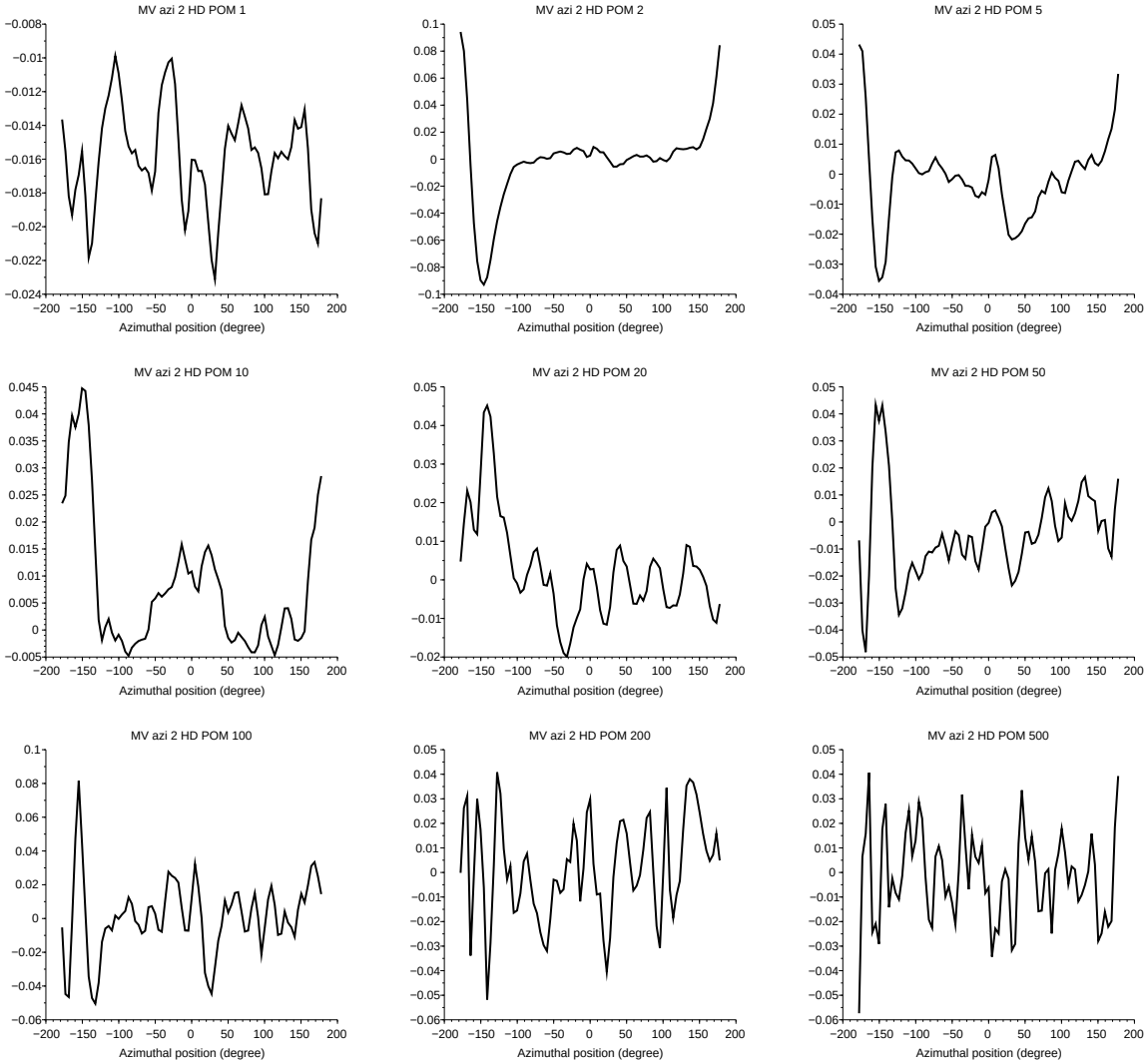

Figure D.19: POM for mixing vane case - azimuthal direction - probe at 2 HD

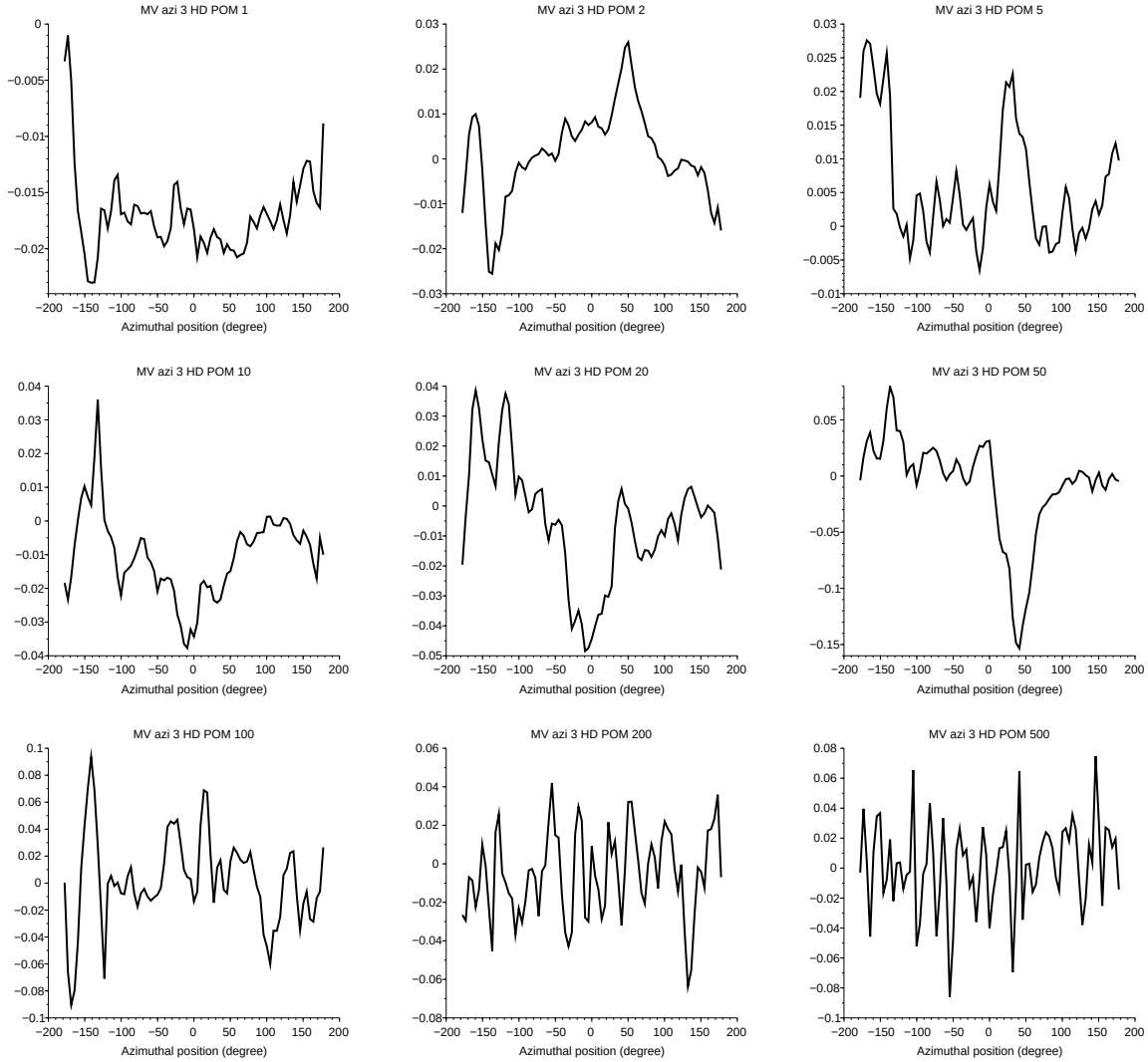

Figure D.20: POM for mixing vane case - azimuthal direction - probe at 3 HD

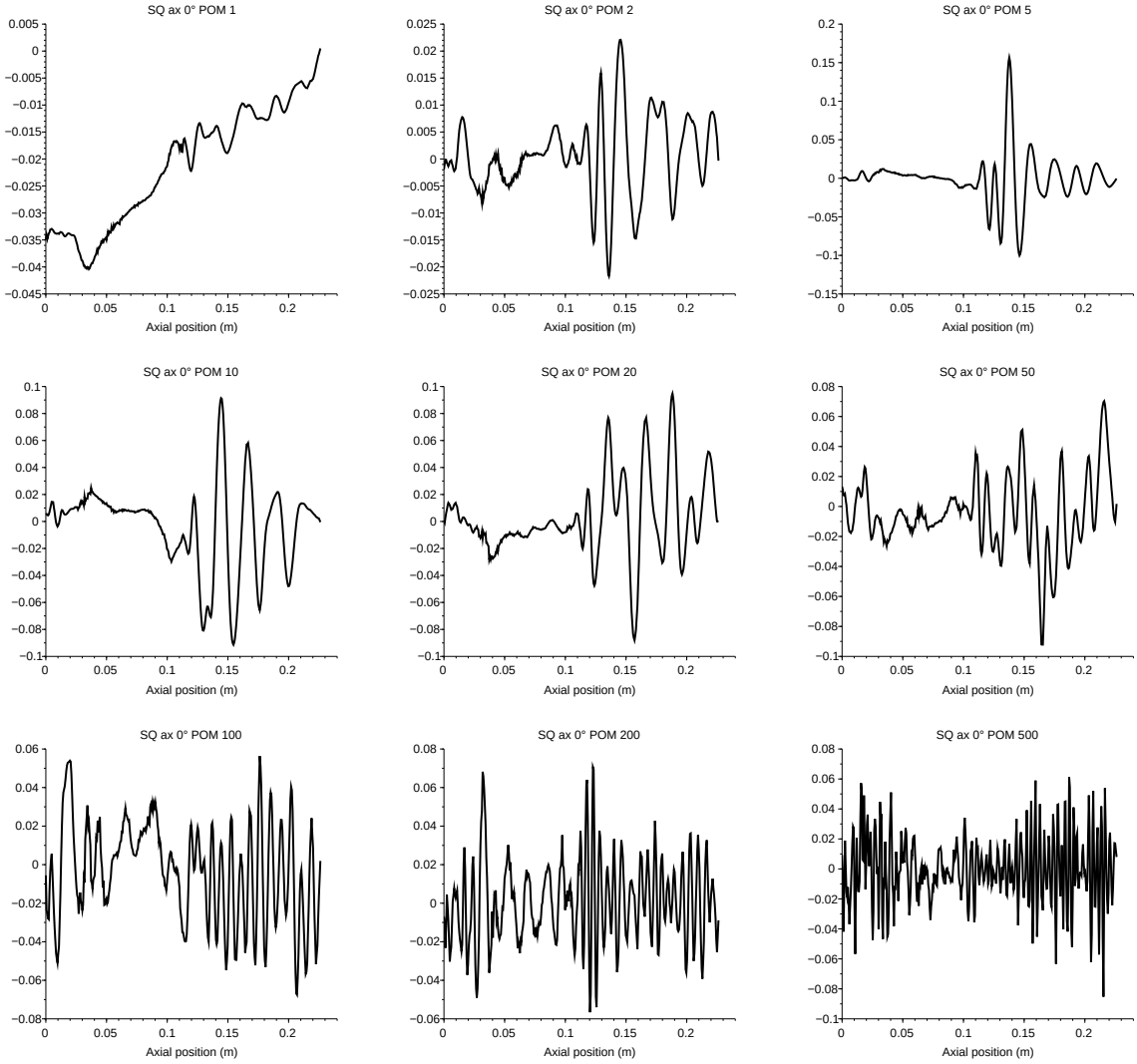

Figure D.21: POM for square grid with mixing vanes case - axial direction - probe at 0°

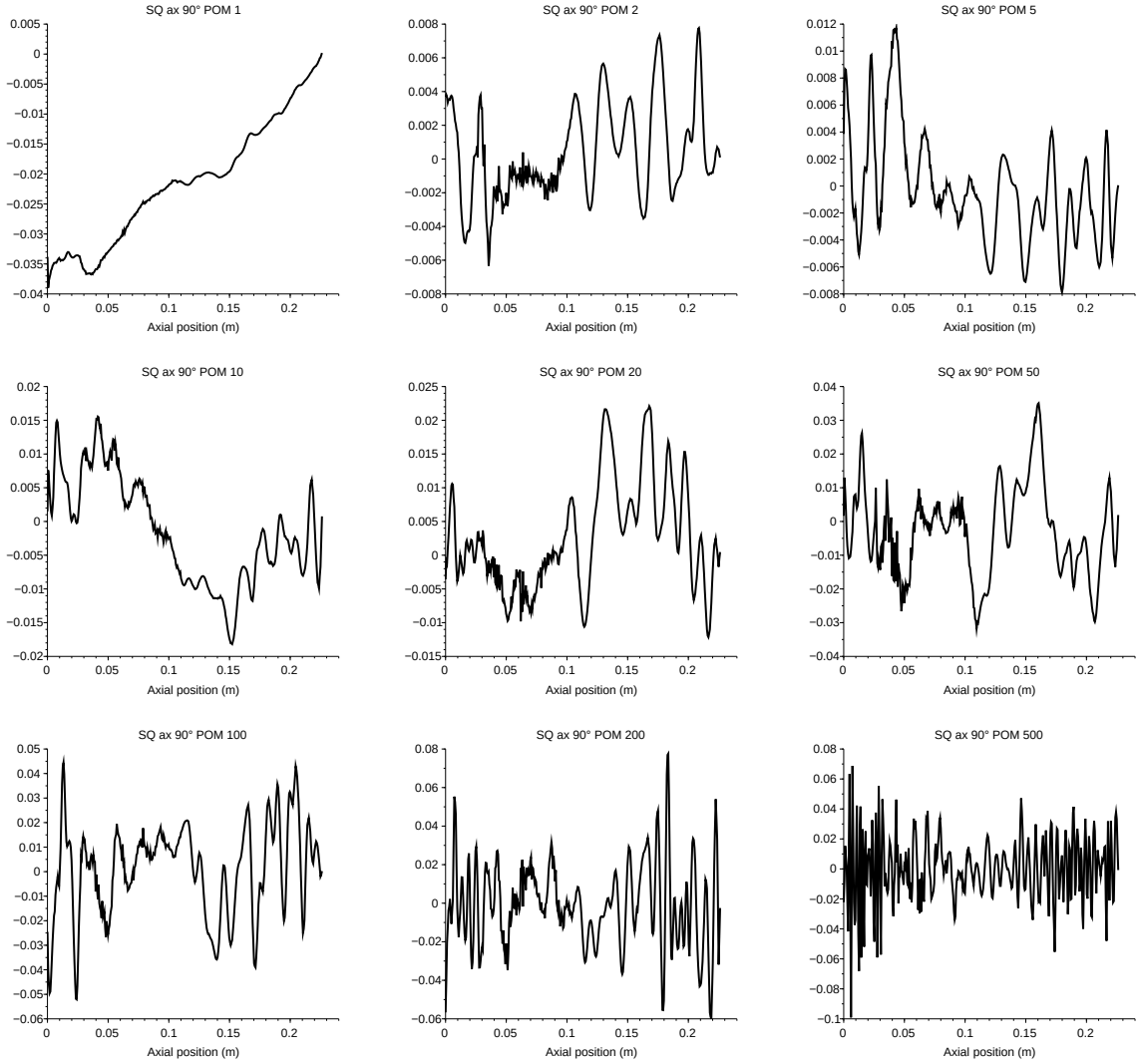

Figure D.22: POM for square grid with mixing vanes case - axial direction - probe at 90°

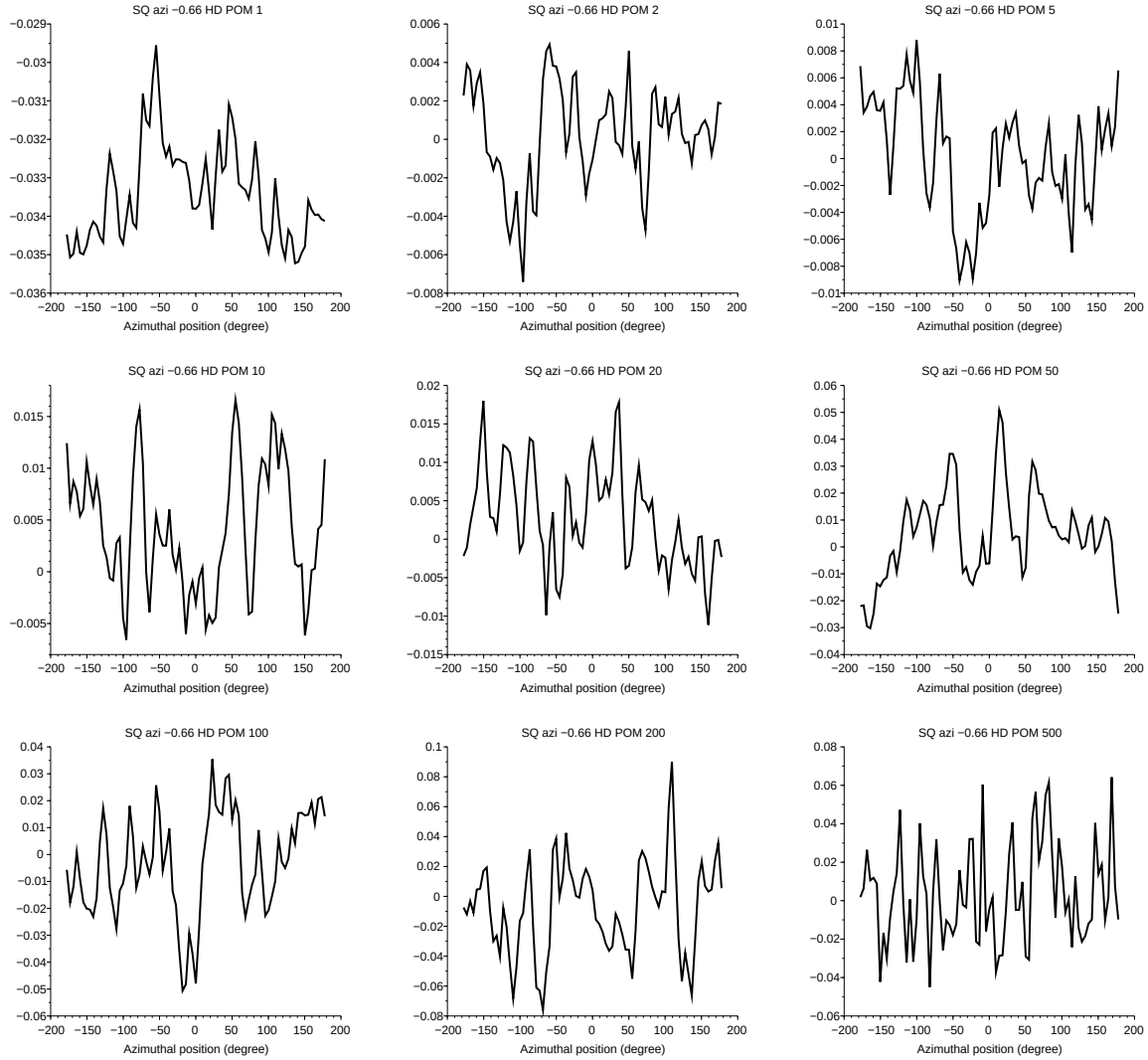

Figure D.23: POM for square grid with mixing vanes case - azimuthal direction - probe at -0.66 HD

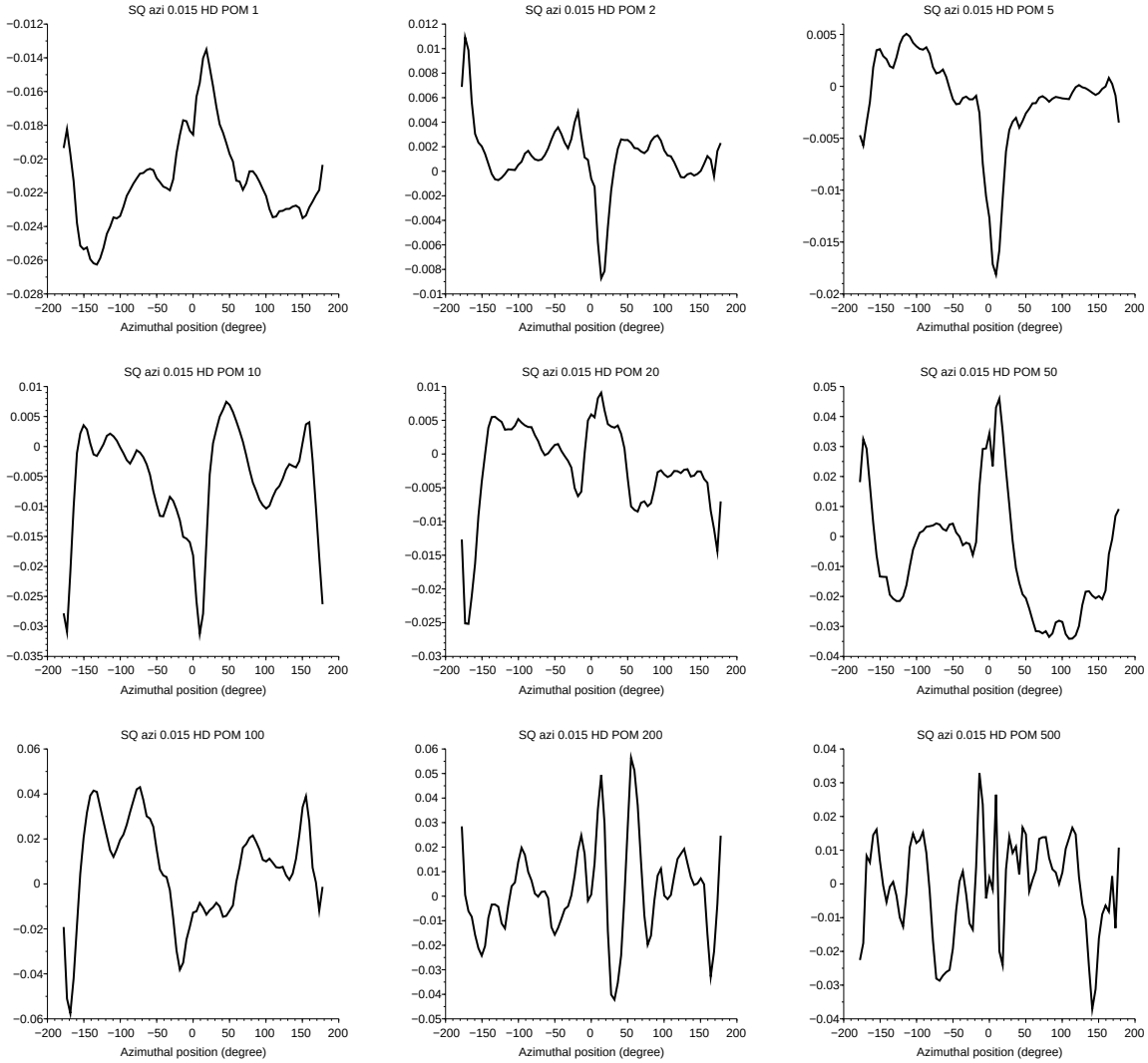

Figure D.24: POM for square grid with mixing vanes case - azimuthal direction - probe at 0.015 HD

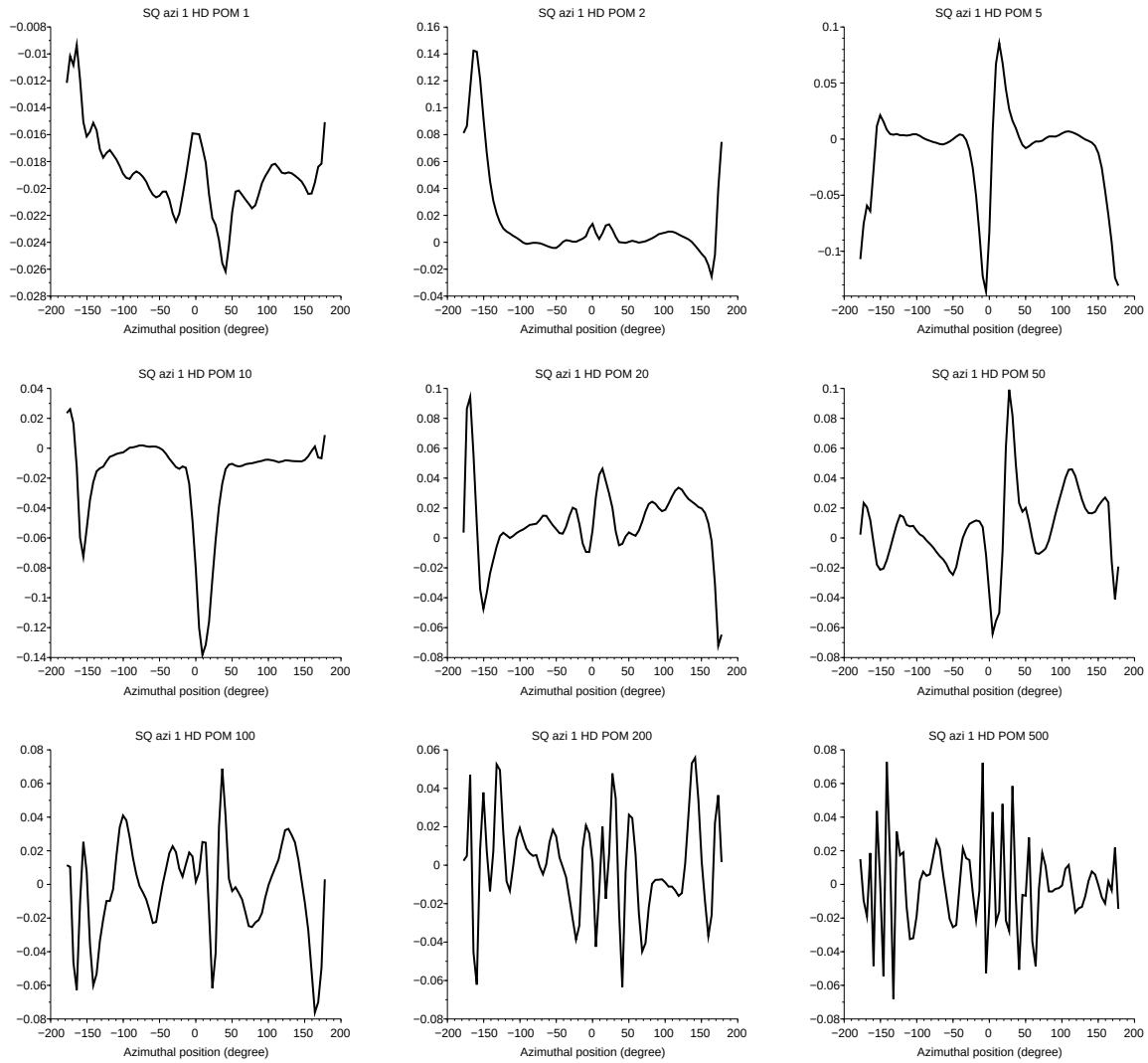

Figure D.25: POM for square grid with mixing vanes case - azimuthal direction - probe at 1 HD

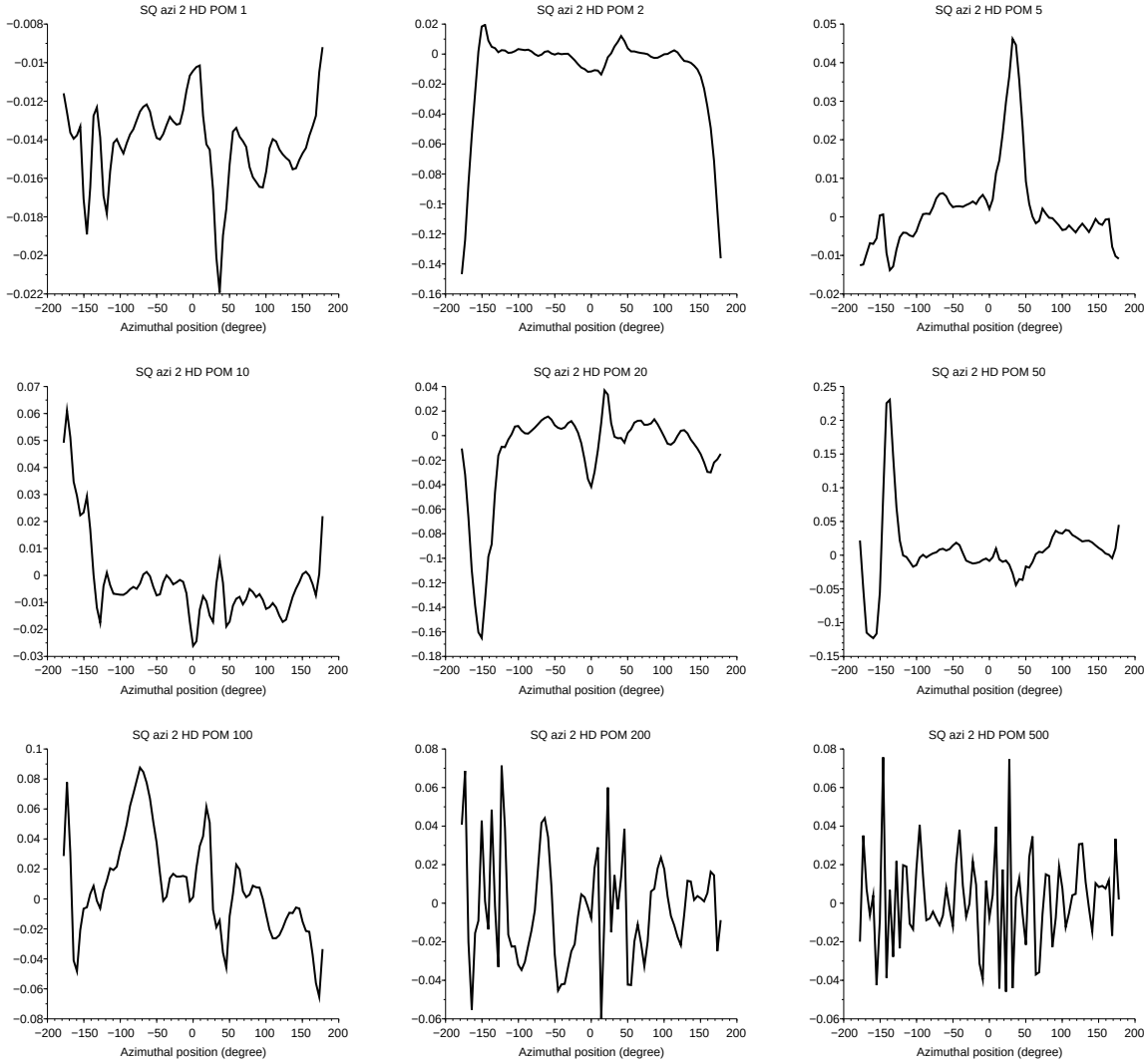

Figure D.26: POM for square grid with mixing vanes case - azimuthal direction - probe at 2 HD

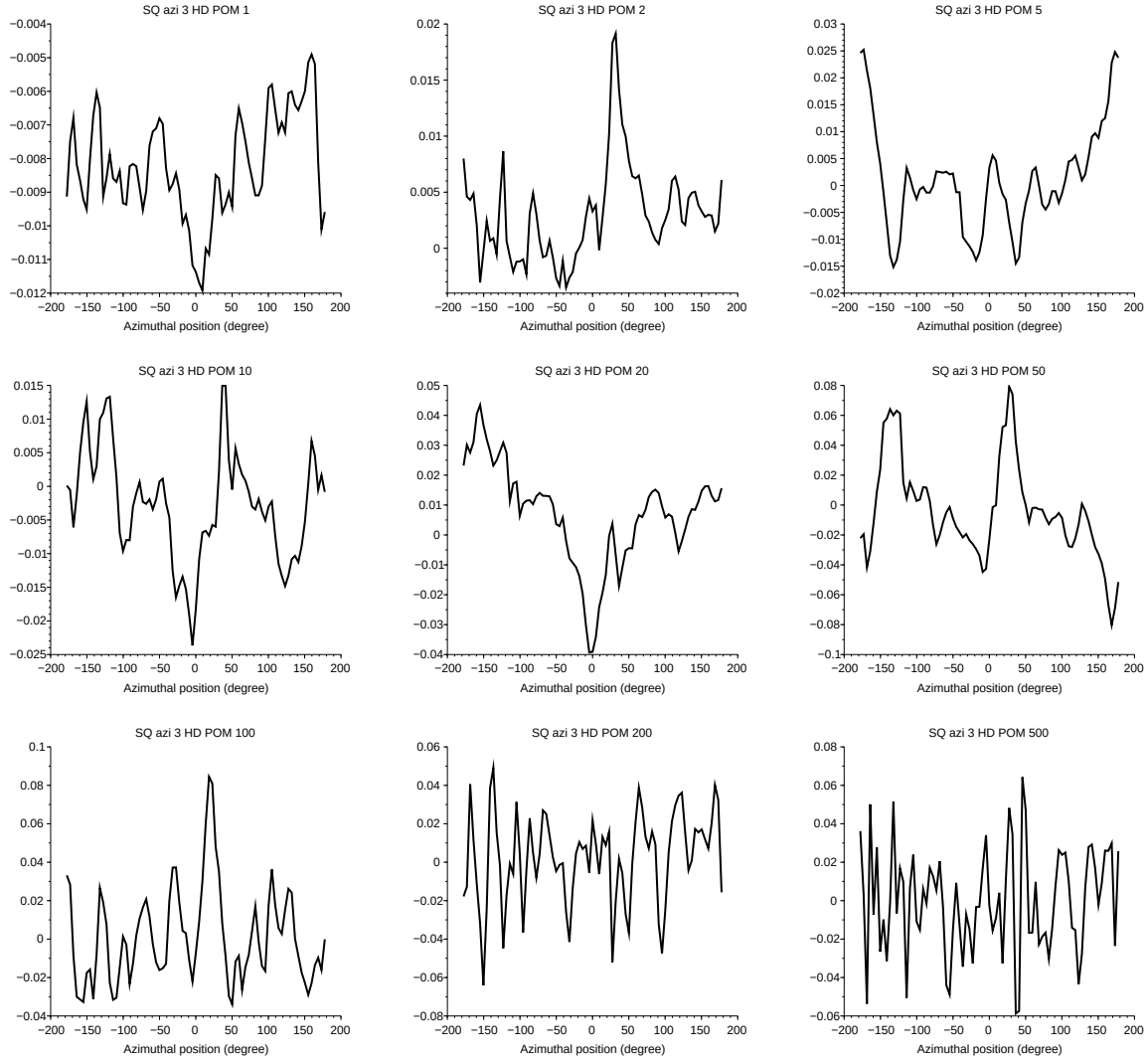

Figure D.27: POM for square grid with mixing vanes case - azimuthal direction - probe at 3 HD

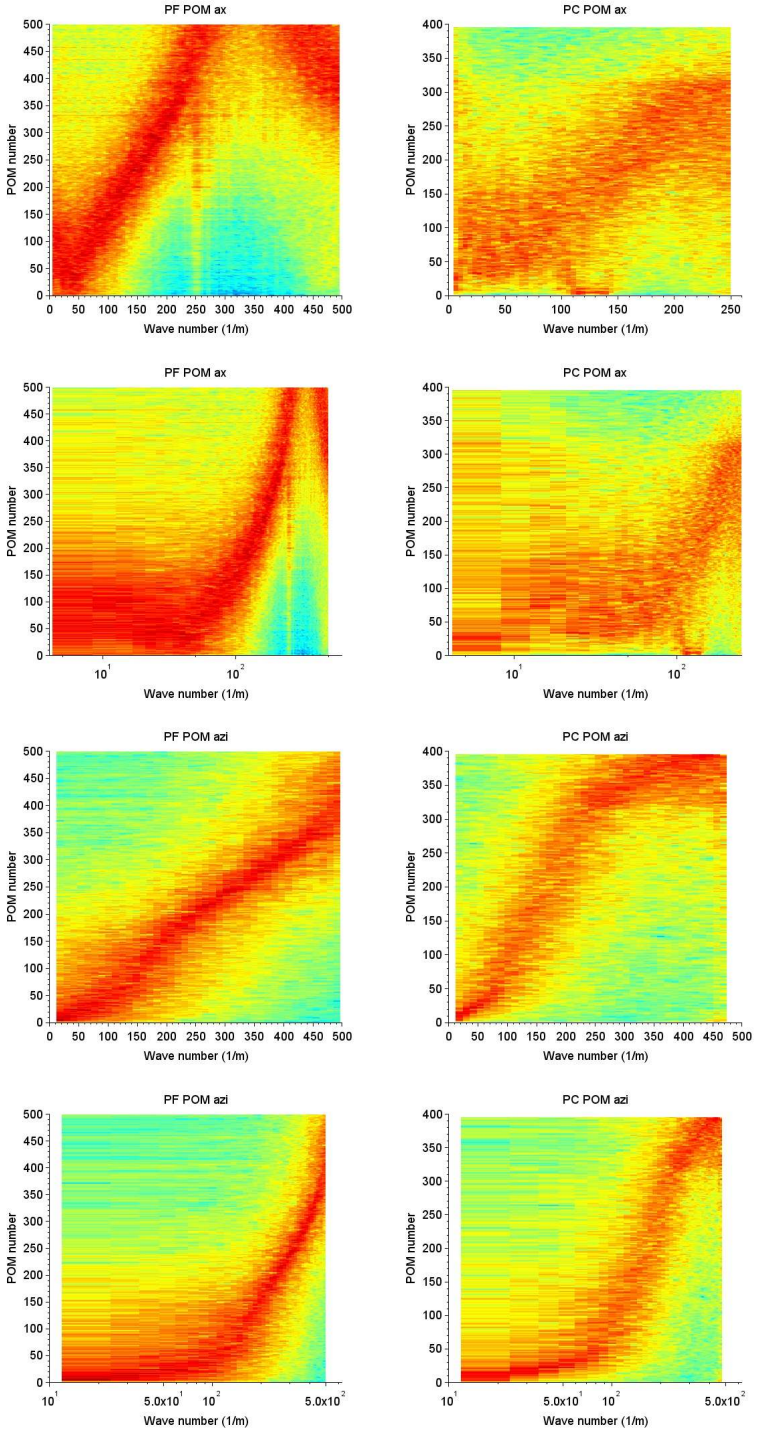

Figure D.28: Wave number POM diagram for annular pipe fine mesh (left) coarse mesh (right) - in axial direction (top) and azimuthal direction (bottom)

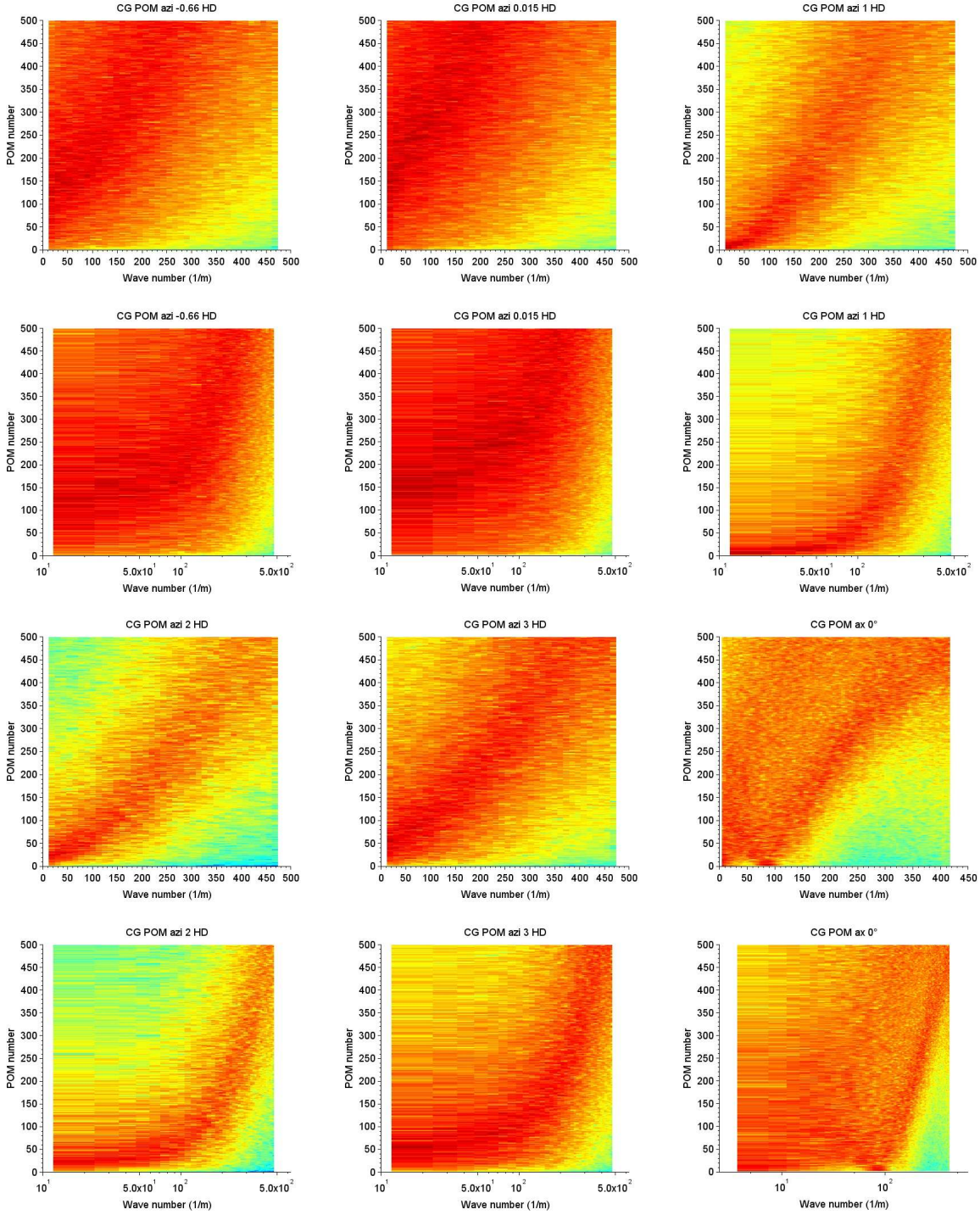

Figure D.29: Wave number POM diagram for circular grid case - in azimuthal direction - probes at -0.66 HD, 0.015 HD, 1 HD, 2 HD, 3 HD and in axial direction - probe at 0°

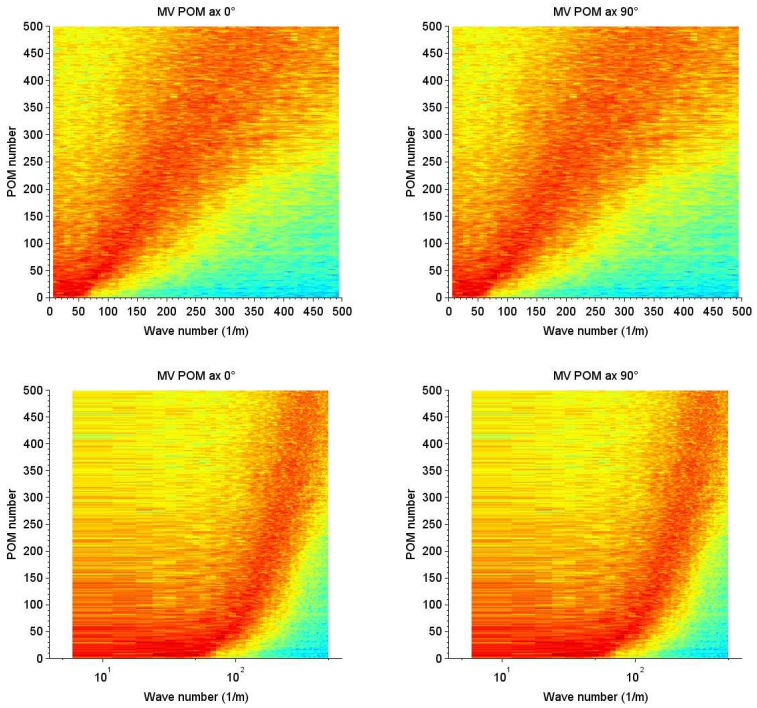

Figure D.30: Wave number POM diagram for mixing vane case - in axial direction - probes at 0° (left) and 90° (right)

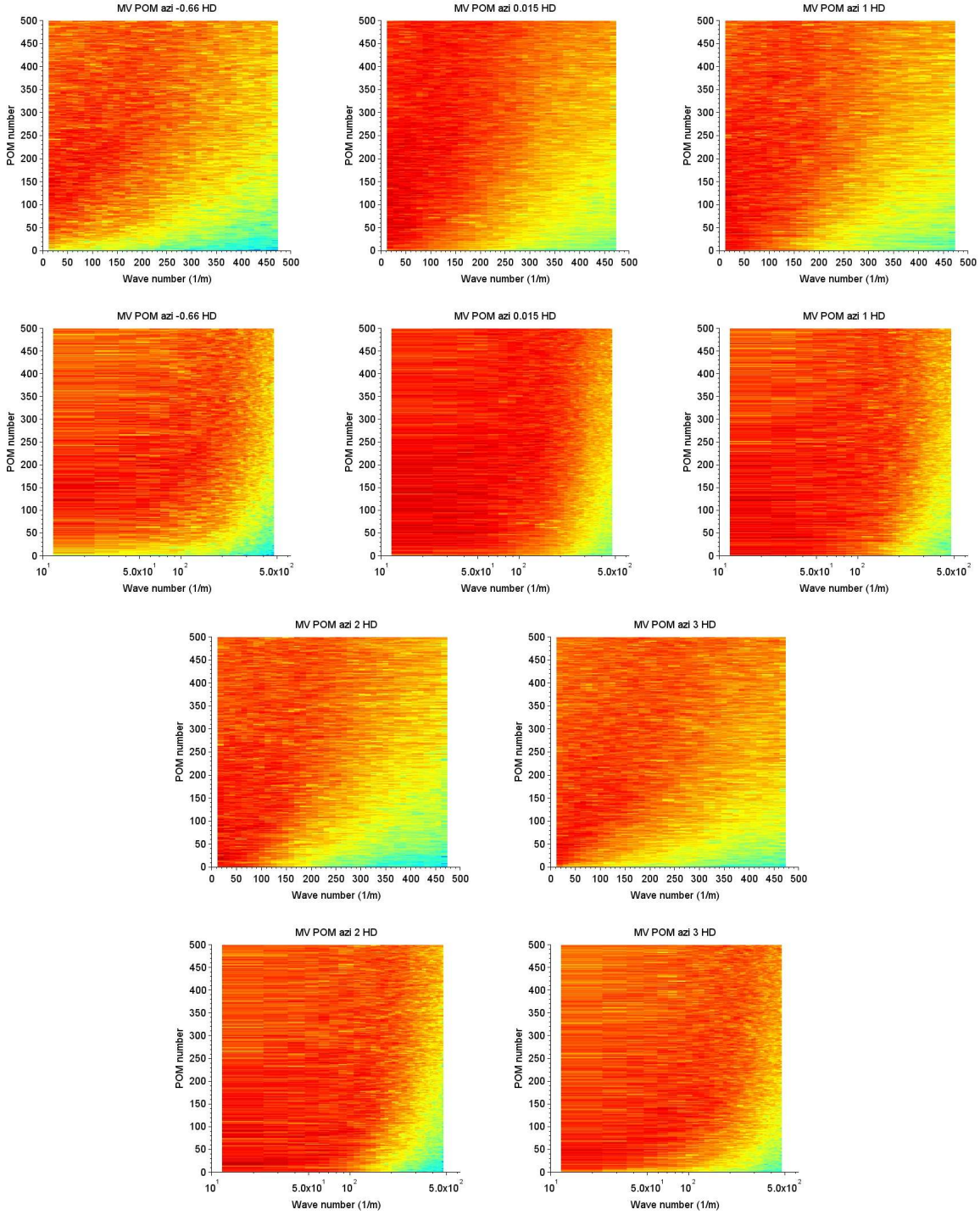

Figure D.31: Wave number POM diagram for mixing vane case - in azimuthal direction - probes at -0.66 HD, 0.015 HD, 1 HD, 2 HD and 3 HD

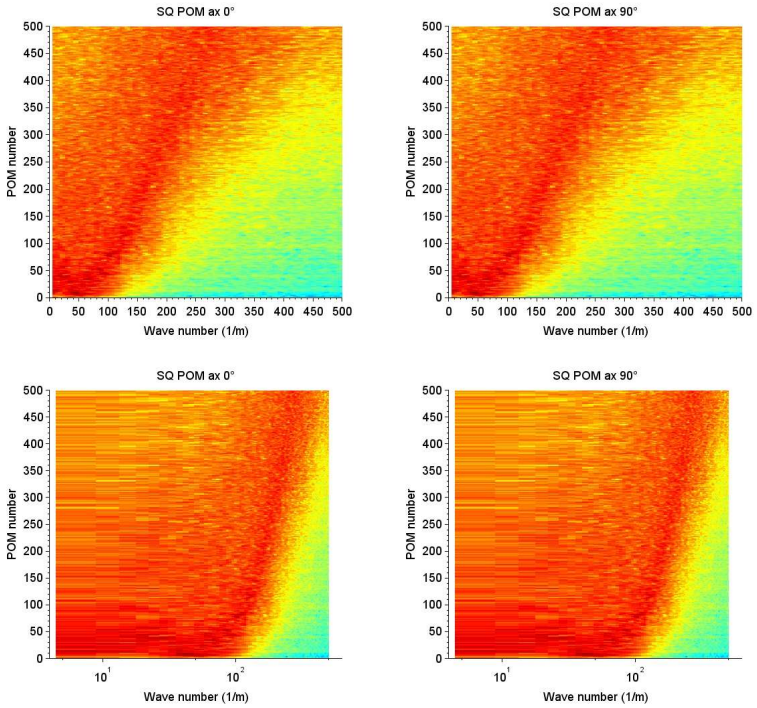

Figure D.32: Wave number POM diagram for square grid with mixing vanes case - in axial direction - probes at 0° (left) and 90° (right)

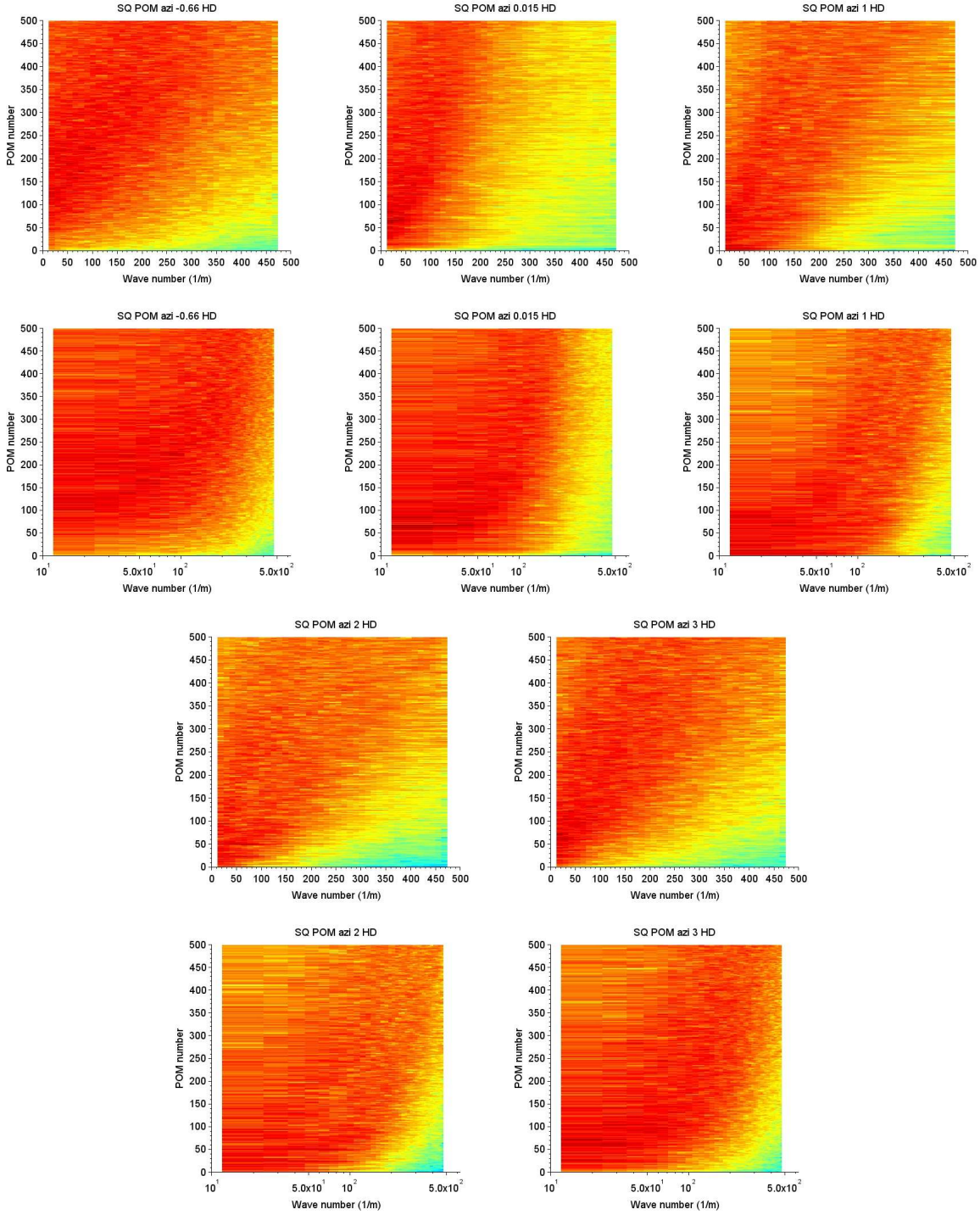

Figure D.33: Wave number POM diagram for square grid with mixing vanes case - in azimuthal direction - probes at -0.66 HD, 0.015 HD, 1 HD, 2 HD and 3 HD

Appendix E

Frequency Wavenumber Analysis

The frequency - wavenumber diagrams and time - wavenumber diagrams for the five different cases (PC, PF, MV, CG and SQ) are presented here.

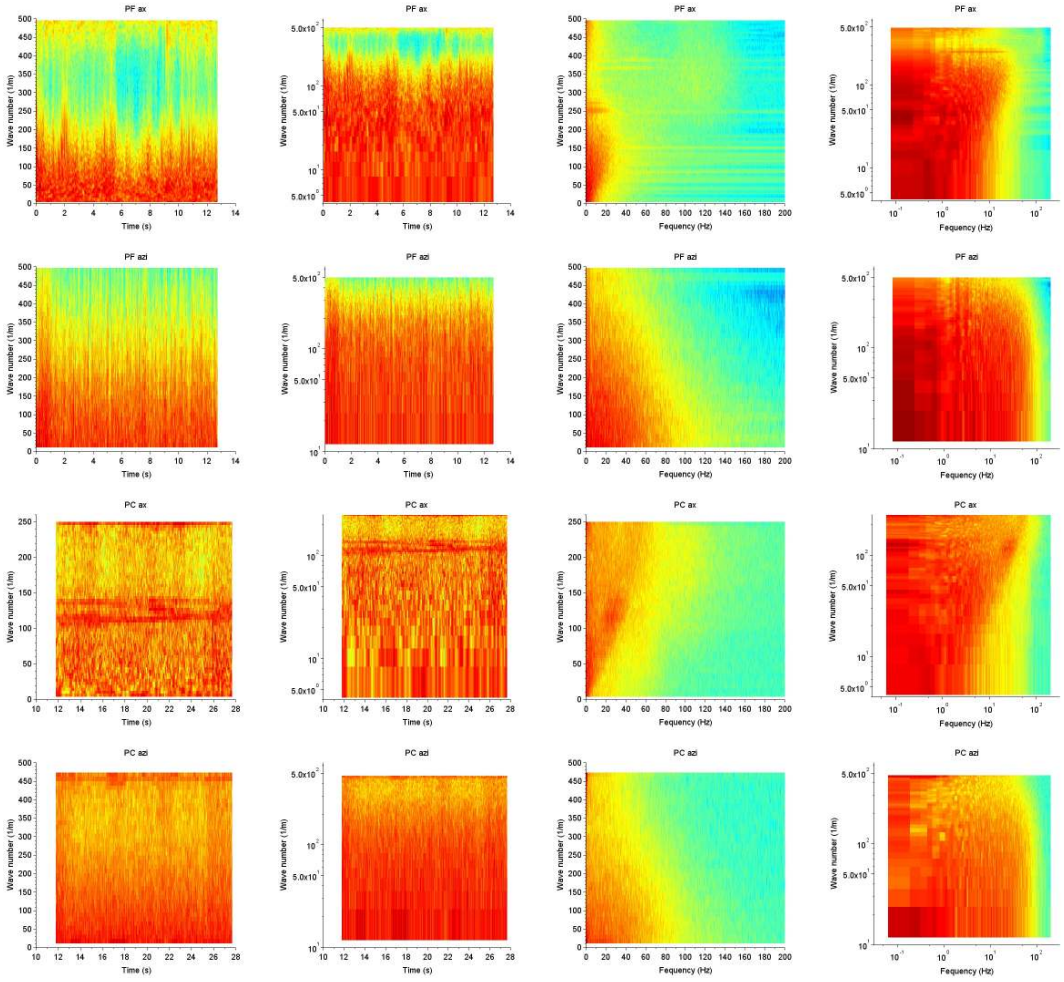

Figure E.1: Wave number time diagram for annular pipe fine and coarse mesh case - in axial direction (top) and azimuthal direction (bottom)

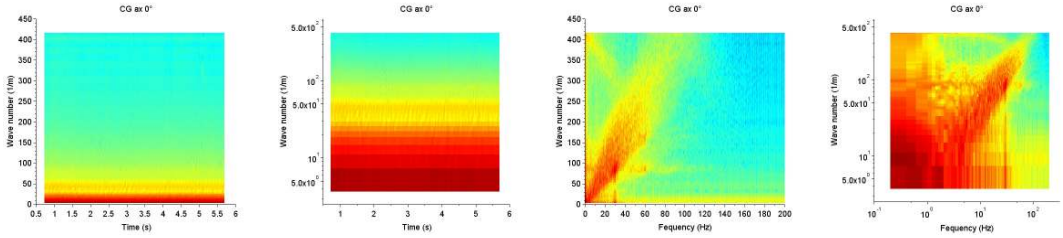

Figure E.2: Wave number time diagram for circular grid case - in axial direction - probe at 0°

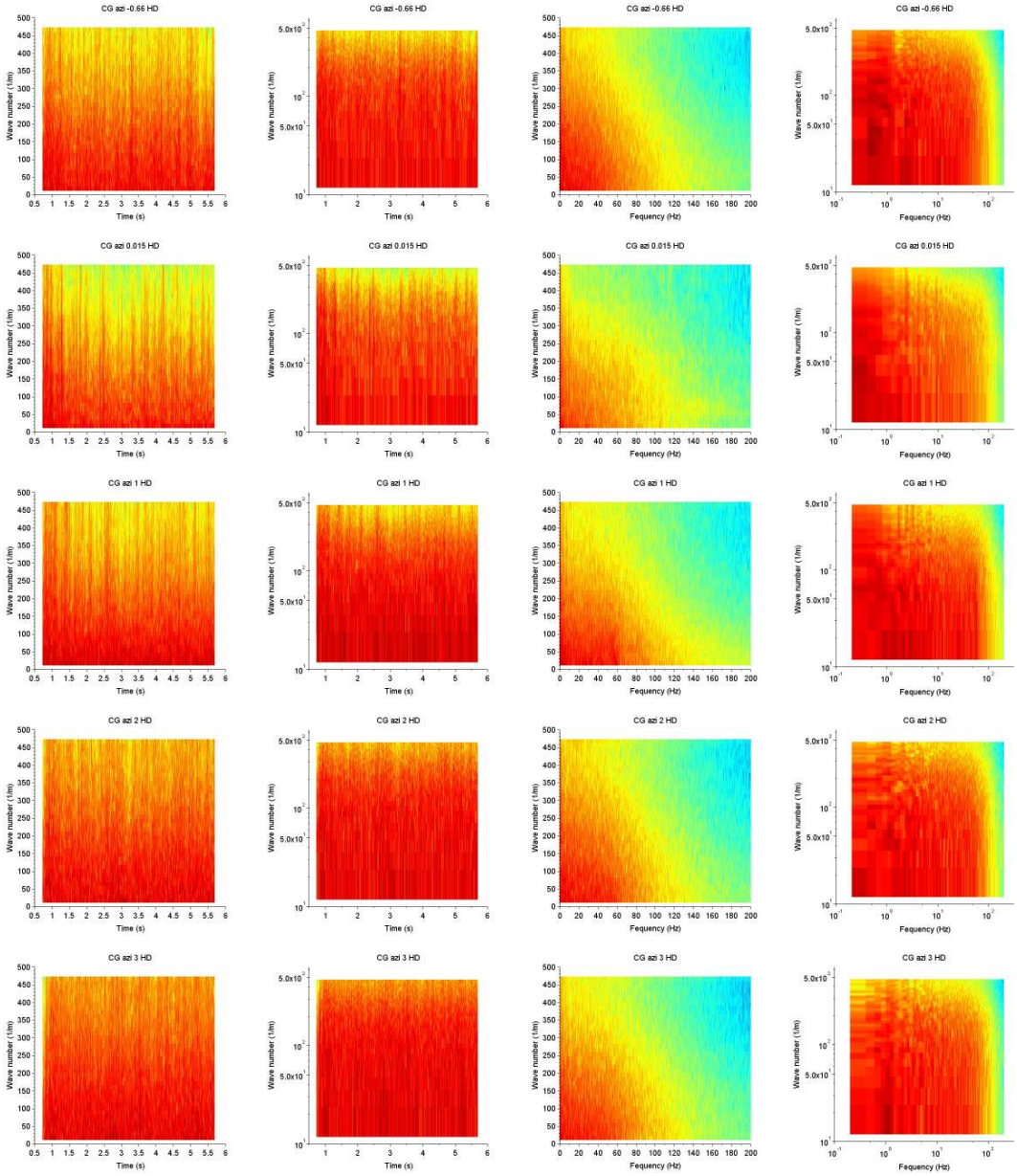

Figure E.3: Wave number time diagram for circular grid case - in azimuthal direction - probes at -0.66 HD, 0.015 HD, 1 HD, 2 HD and 3 HD

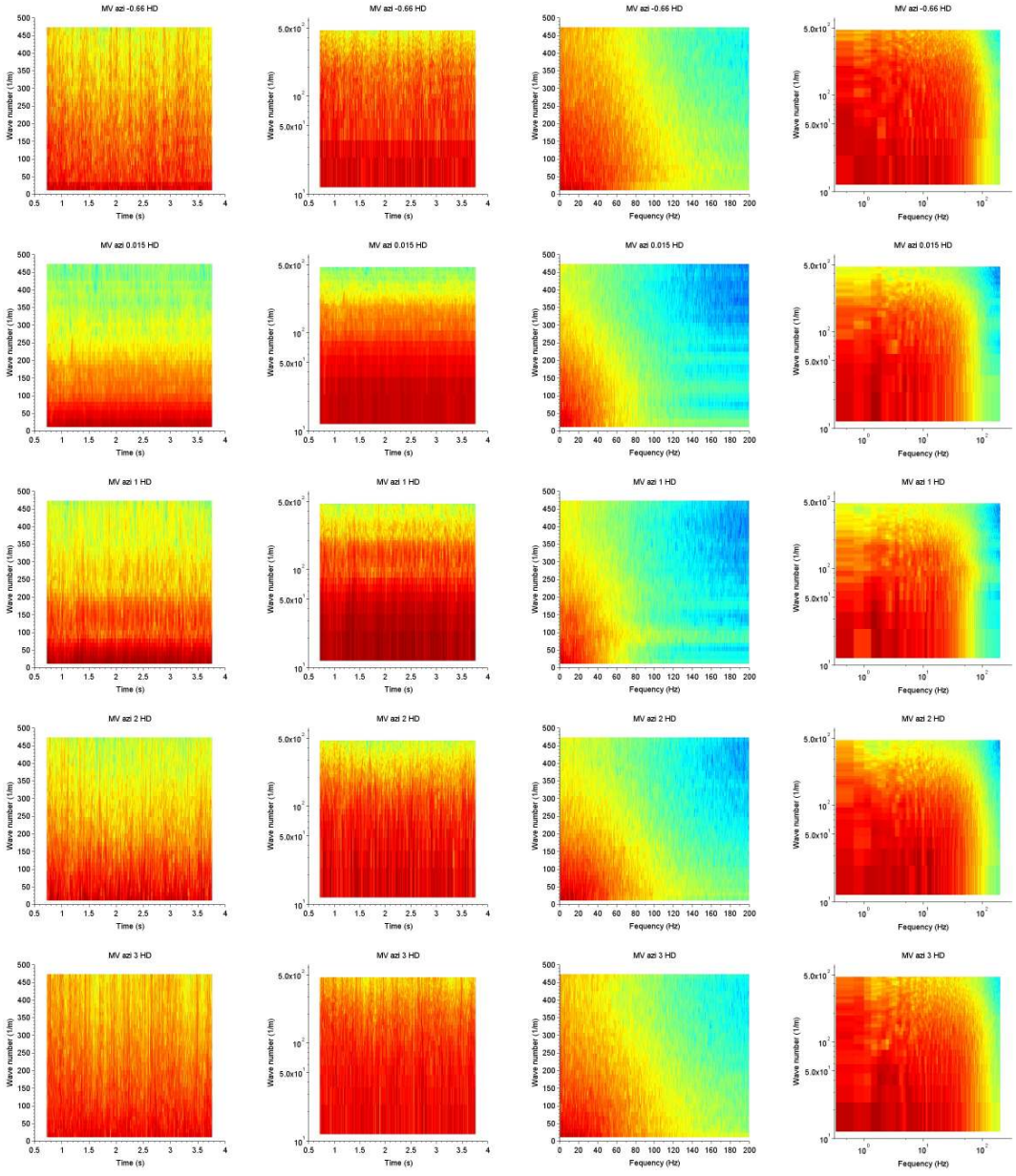

Figure E.4: Wave number time diagram for mixing vane case - in azimuthal direction - probes at -0.66 HD, 0.015 HD, 1 HD, 2 HD and 3 HD

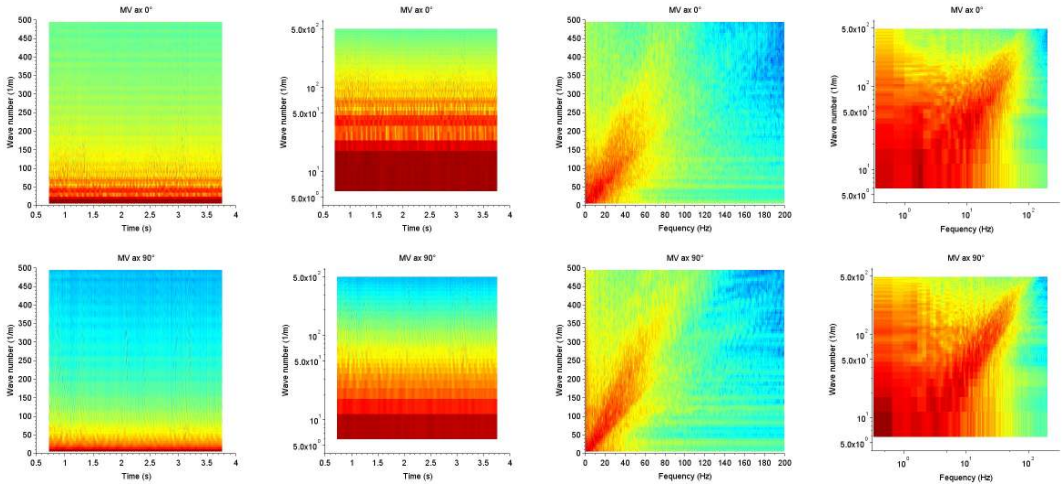

Figure E.5: Wave number time diagram for mixing vane case - in axial direction - probes at 0°(top) and 90°(bottom)

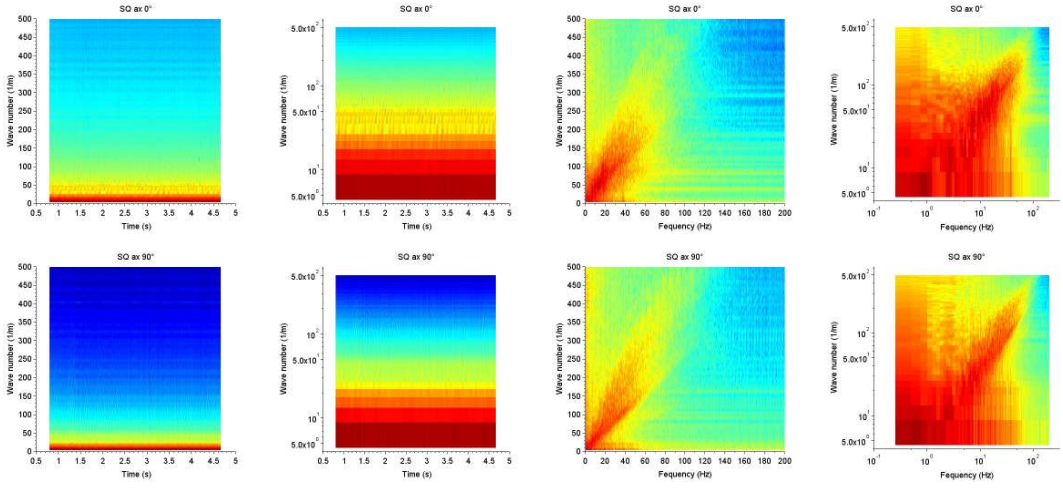

Figure E.6: Wave number time diagram for square grid with mixing vanes case - in axial direction - probes at 0°(top) and 90°(bottom)

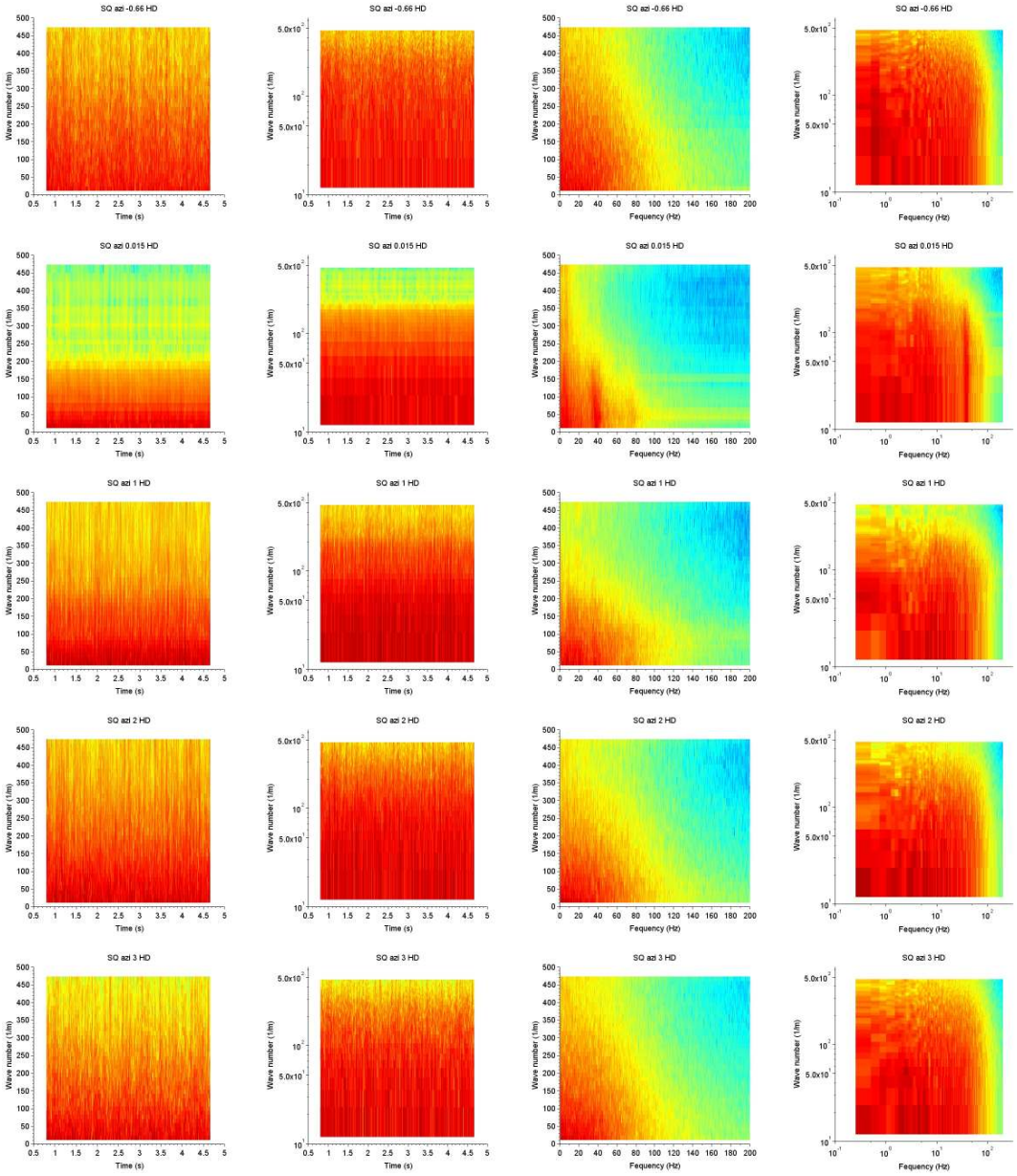

Figure E.7: Wave number time diagram for square grid with mixing vanes case - in azimuthal direction - probes at -0.66 HD, 0.015 HD, 1 HD, 2 HD and 3 HD

Appendix F

Power Spectral Density

The Power Spectral Density (PSD) curves for the five different cases (PC, PF, MV, CG and SQ) are presented here.

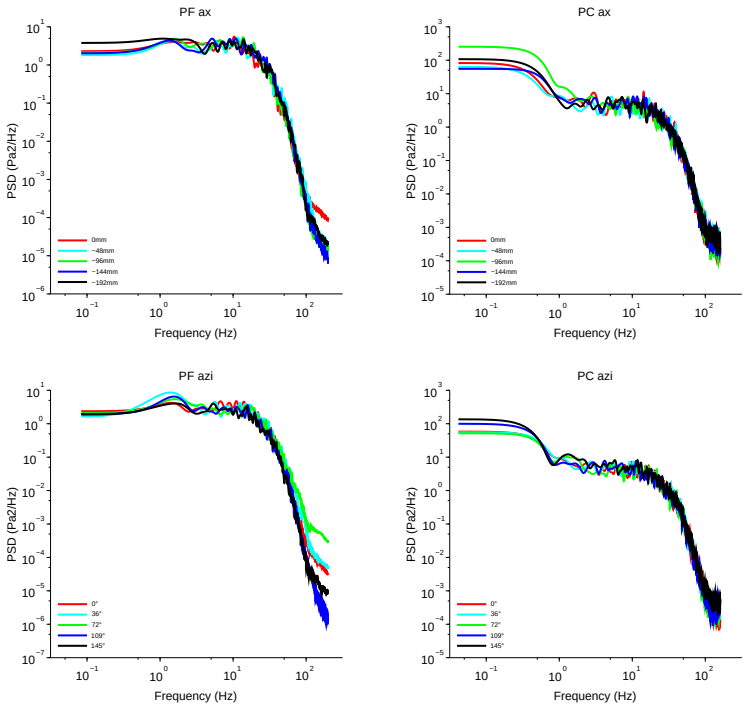

Figure F.1: PSD for annular pipe fine mesh (left) and coarse mesh (right) case - in axial direction (top) and in azimuthal direction (bottom)

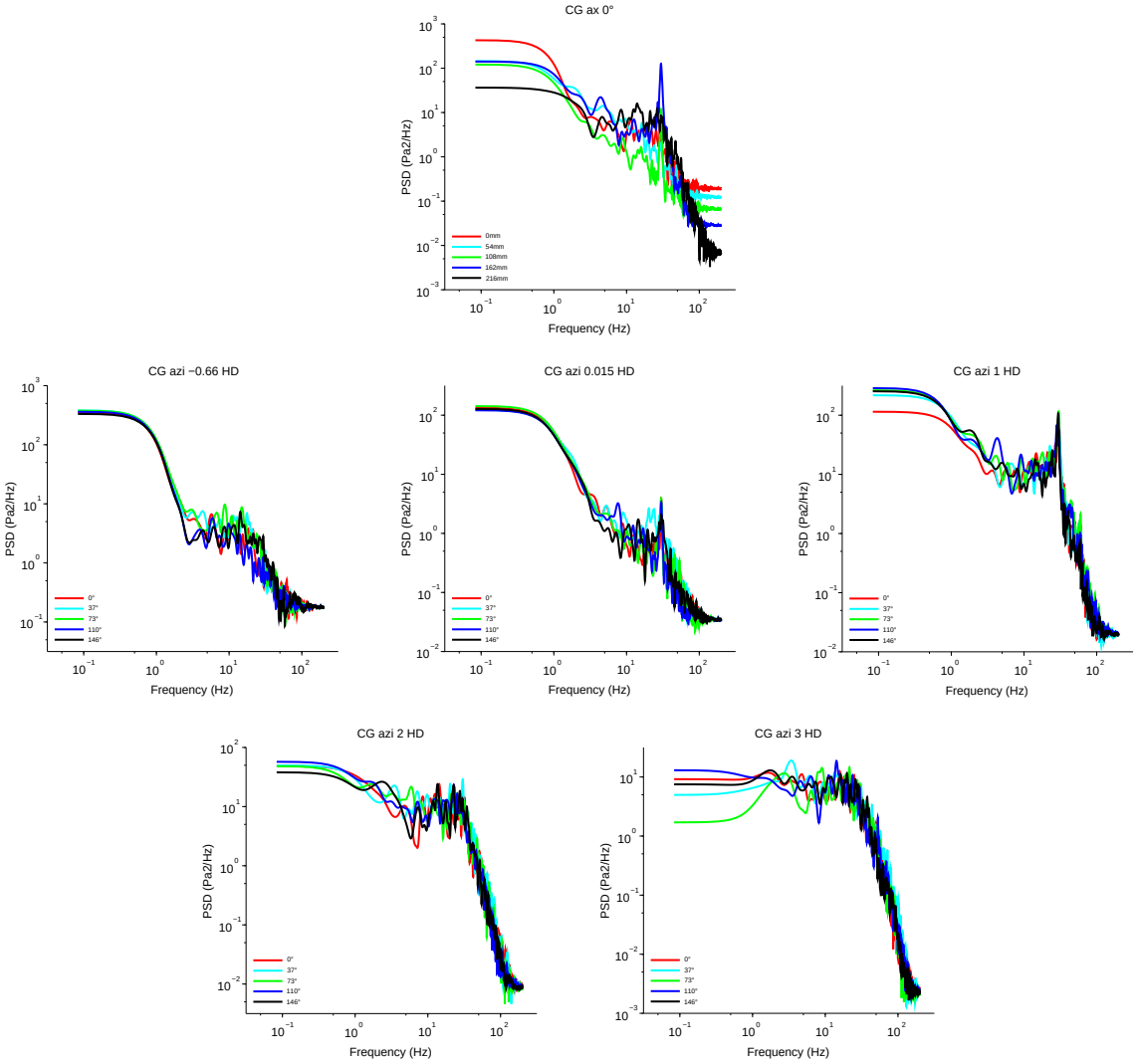

Figure F.2: PSD for circular grid case -
in axial direction - probes at 0° -
in azimuthal direction - probes at -0.66 HD, 0.015 HD, 1 HD, 2 HD and 3 HD

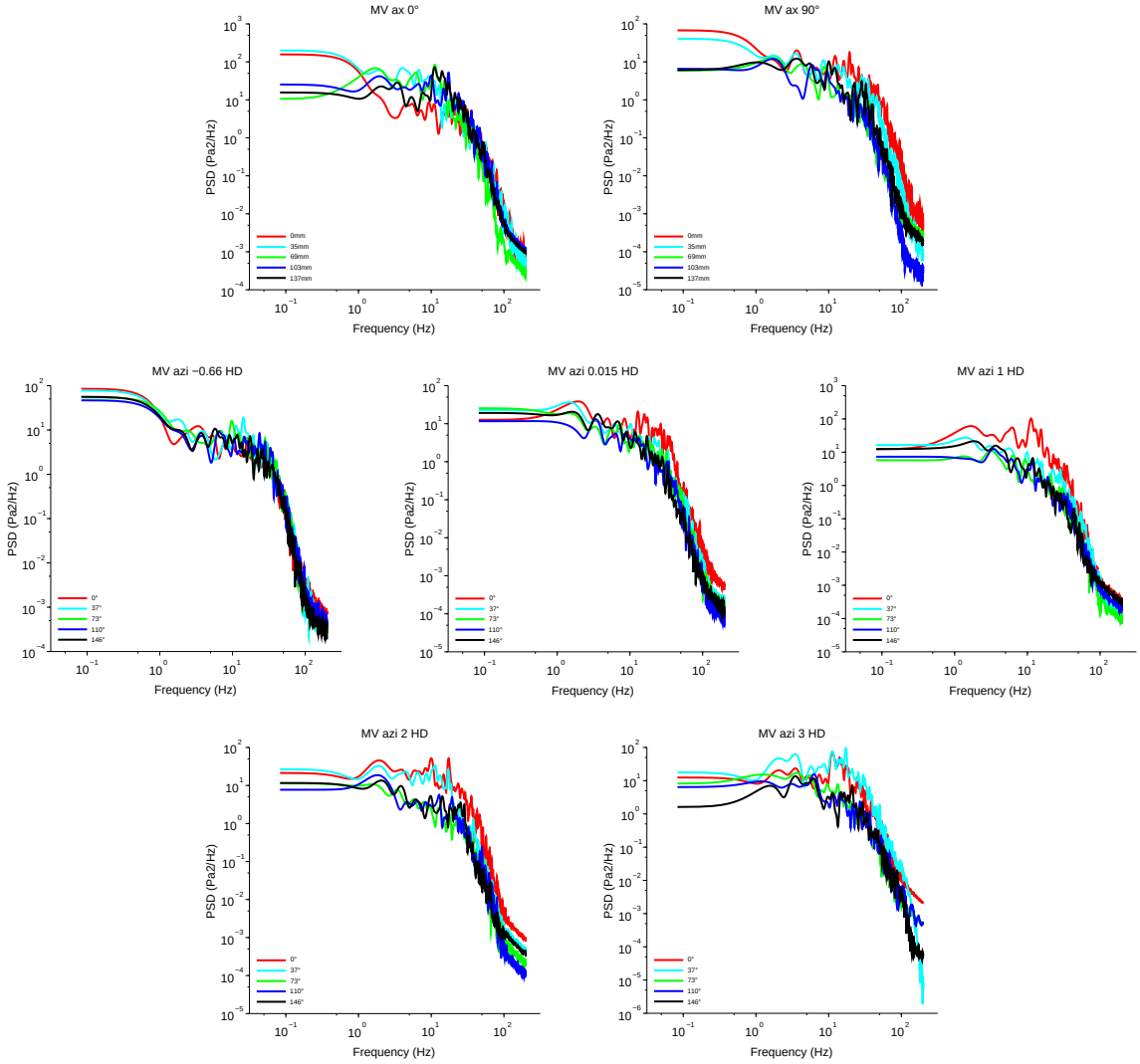

Figure F.3: PSD for mixing vane case -
in axial direction - probes at 0° and 90° -
in azimuthal direction - probes at -0.66 HD, 0.015 HD, 1 HD, 2 HD and 3 HD

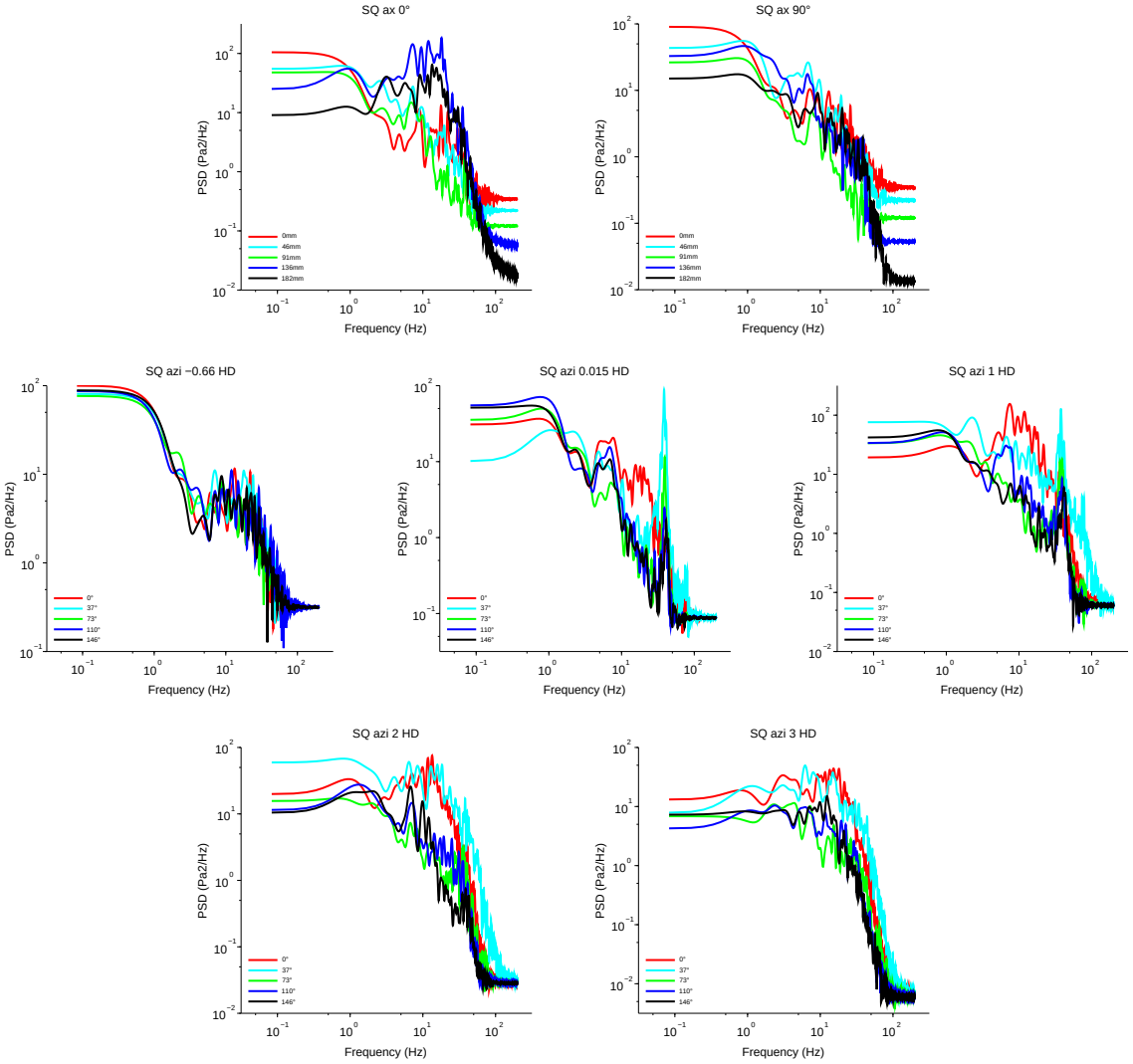

Figure F.4: PSD for square grid with mixing vanes case -
in axial direction - probes at 0° and 90° -
in azimuthal direction - probes at -0.66 HD, 0.015 HD, 1 HD, 2 HD and 3 HD

Appendix G

Comparison with CALIFS Experiment

Comparison of simulation results with CALIFS experiment is presented here for the five different cases (PC, PF, MV, CG and SQ).

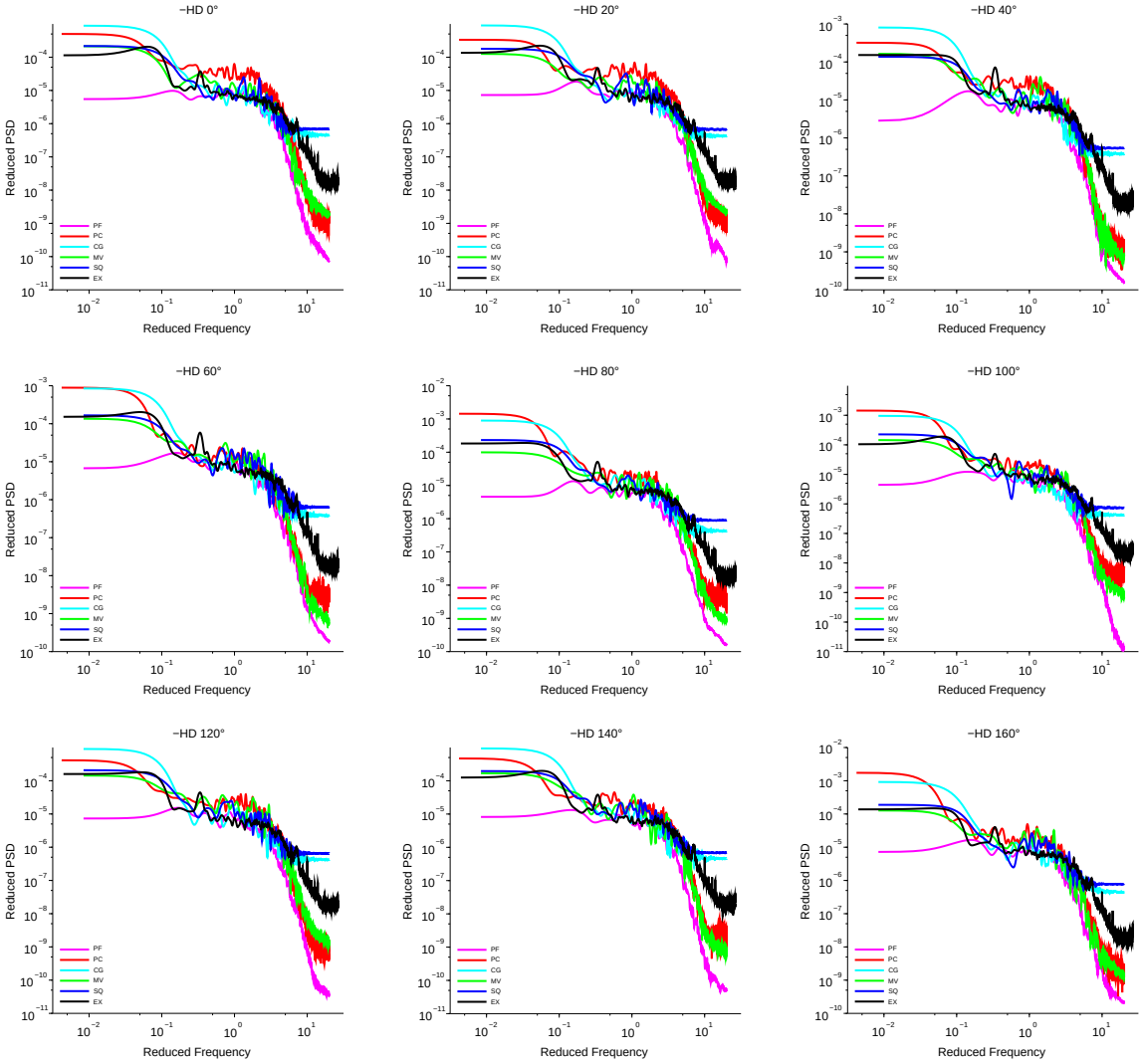

Figure G.1: Comparison of the 5 simulation cases with CALIFS experiment (EX) - upstream of the spacer grid and/or mixing vanes

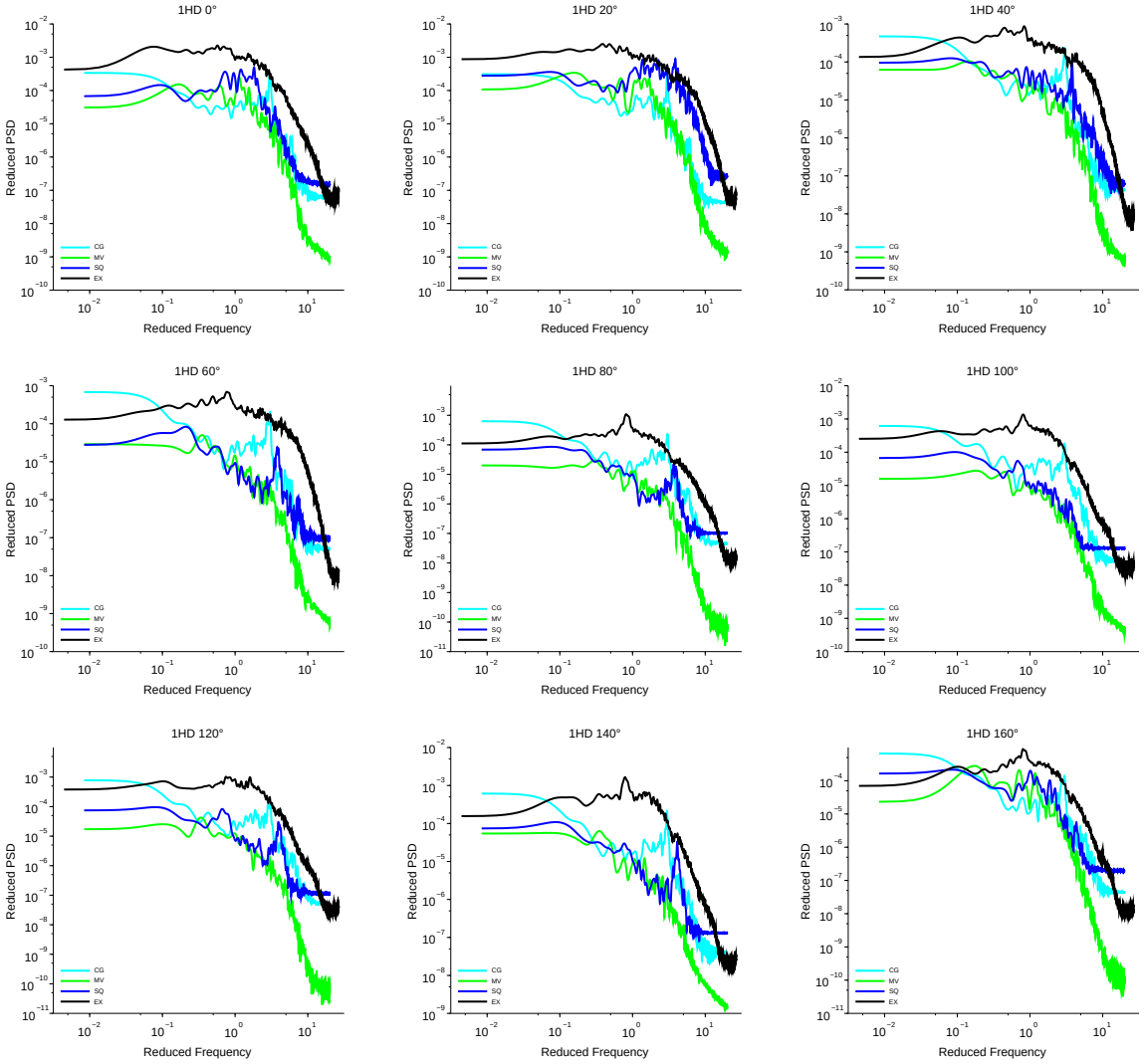

Figure G.2: Comparison of the 5 simulation cases with CALIFS experiment (EX) - 1 HD downstream of the spacer grid and/or mixing vanes

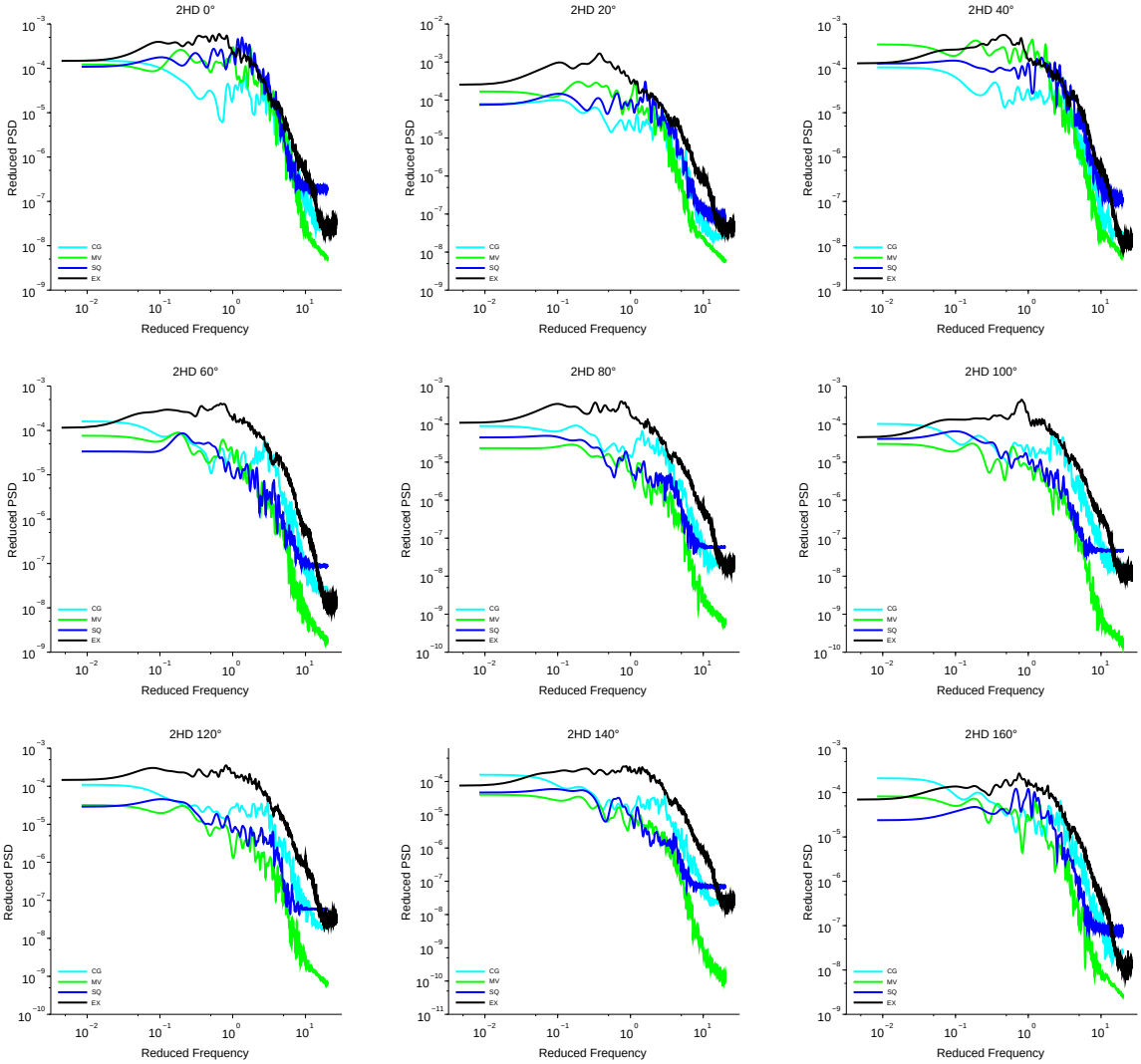

Figure G.3: Comparison of the 5 simulation cases with CALIFS experiment (EX) - 2 HD downstream of the spacer grid and/or mixing vanes

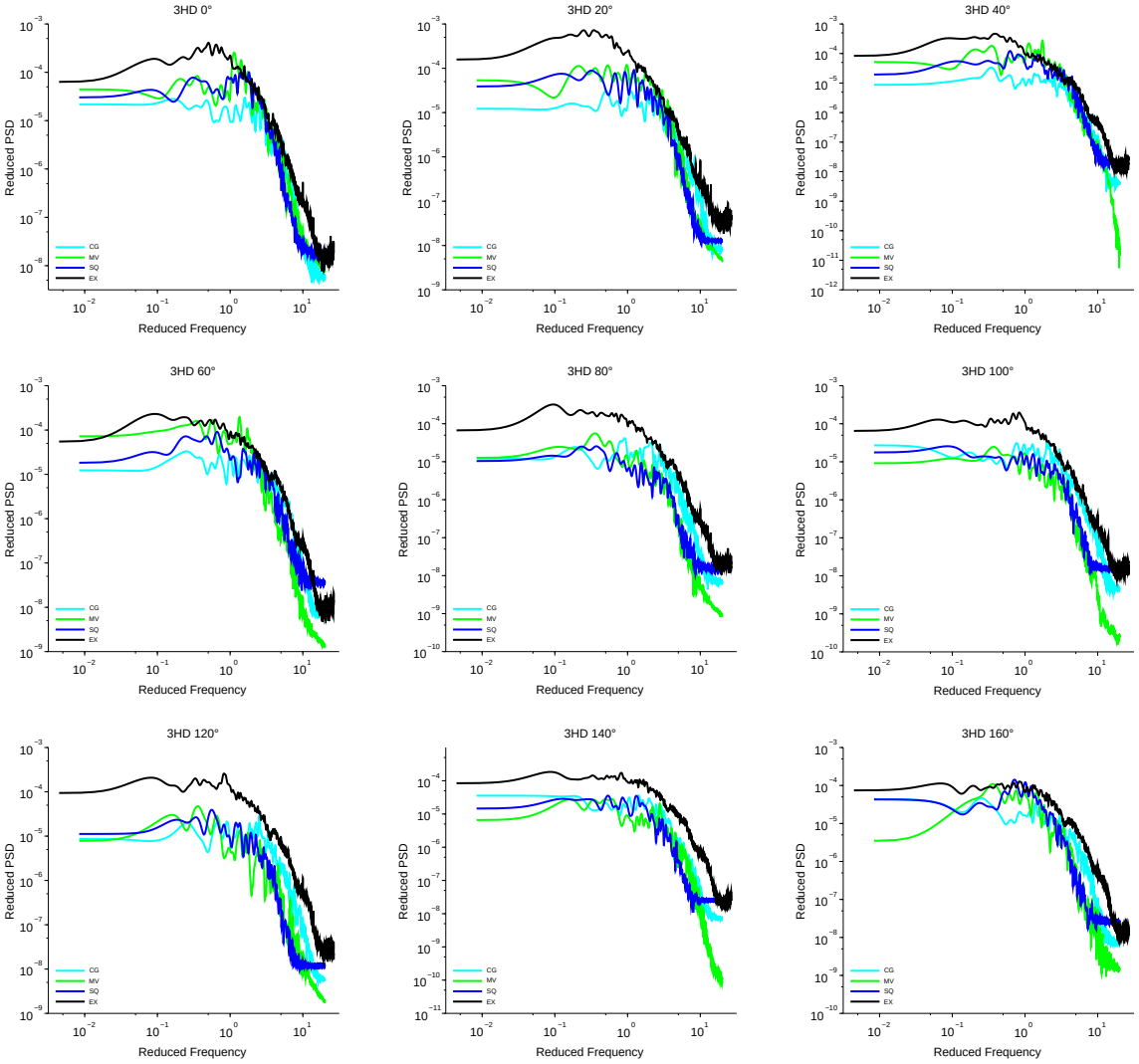

Figure G.4: Comparison of the 5 simulation cases with CALIFS experiment (EX) - 3 HD downstream of the spacer grid and/or mixing vanes

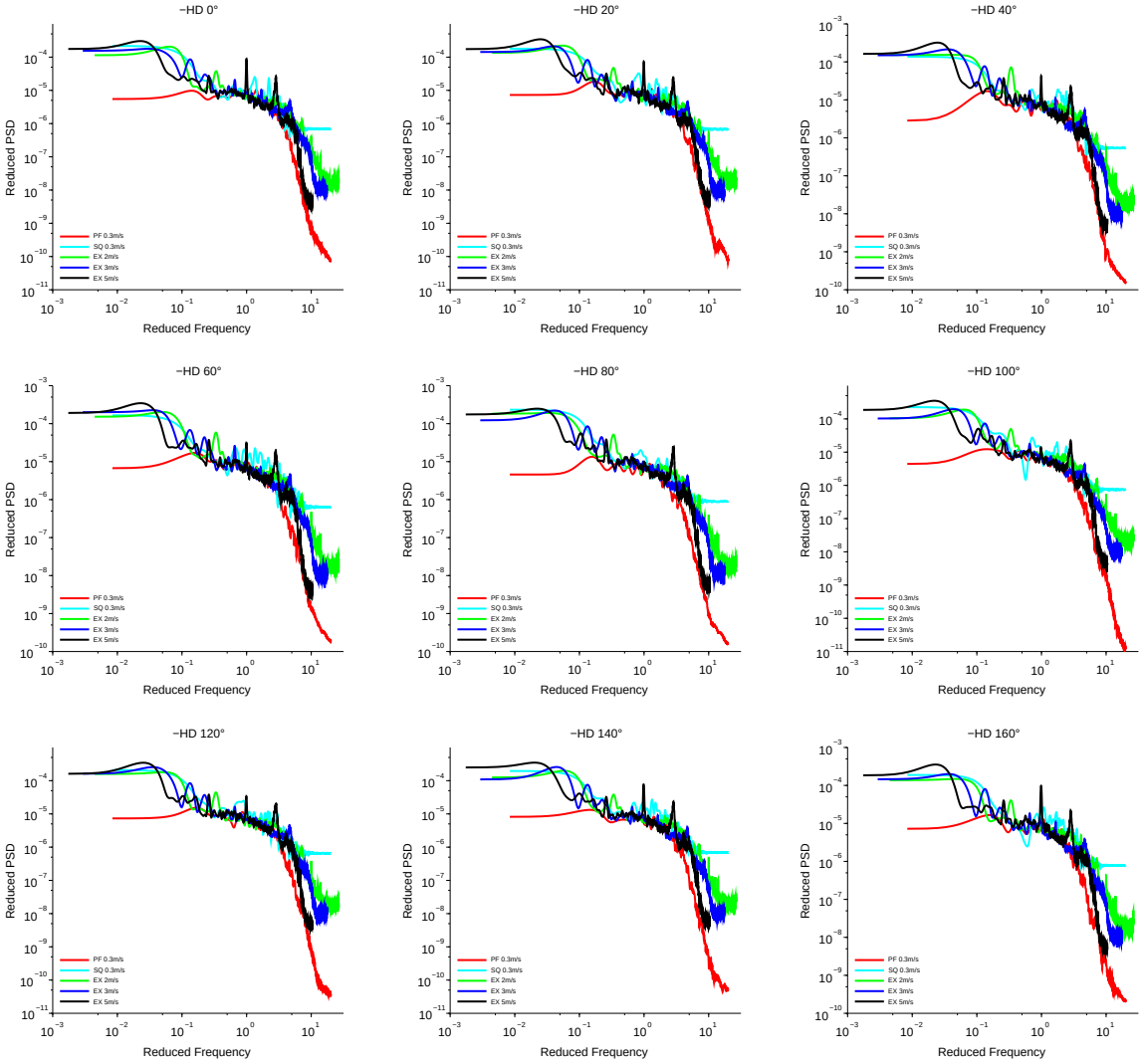

Figure G.5: Comparison of annular pipe fine mesh case (PF) and square grid with mixing vanes case (SQ) to 3 different velocities of CALIFS experiment (EX) - upstream of the spacer grid and/or mixing vanes

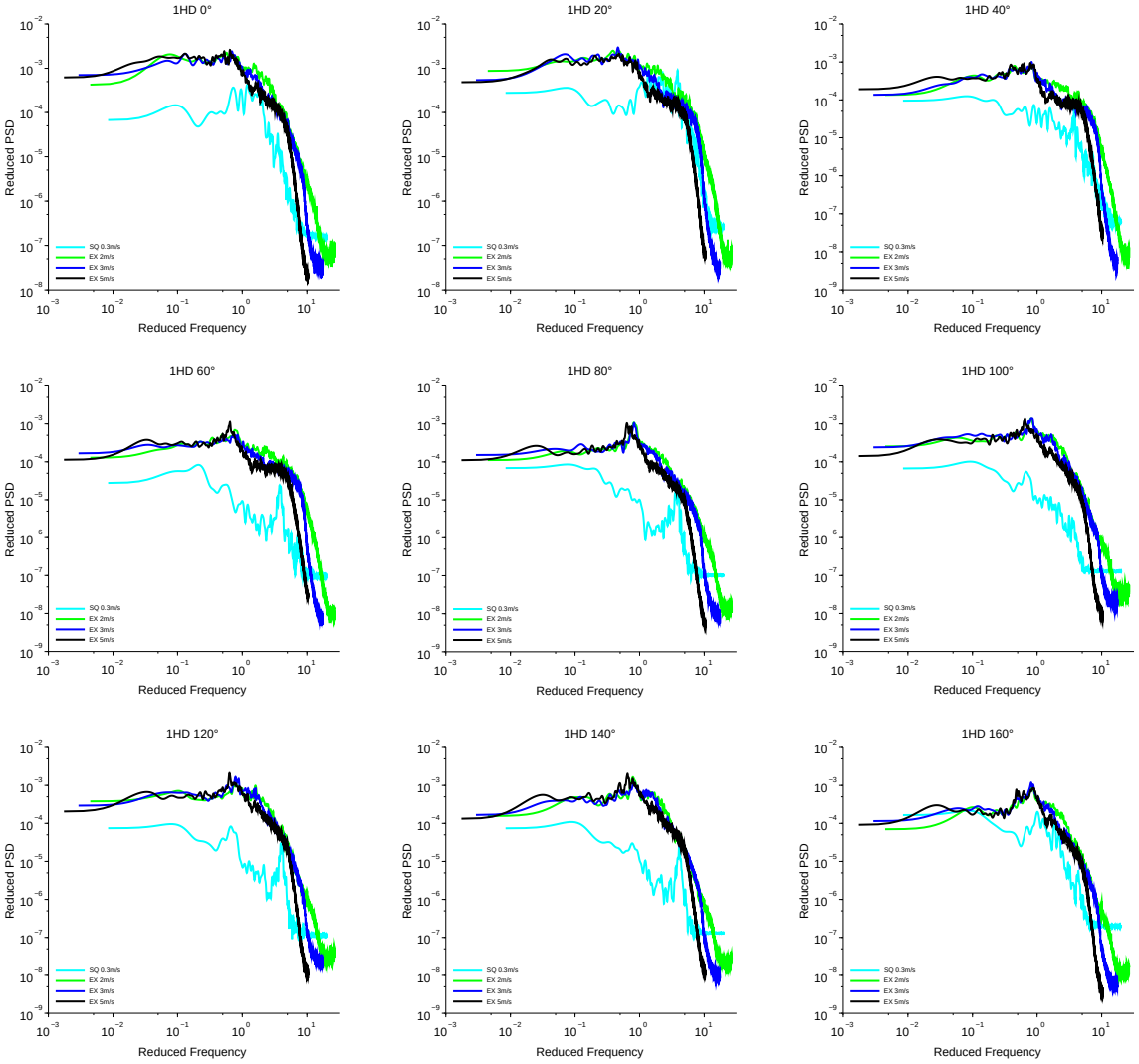

Figure G.6: Comparison of square grid with mixing vanes case (SQ) to 3 different velocities of CALIFS experiment (EX) -
1 HD downstream of the spacer grid and/or mixing vanes

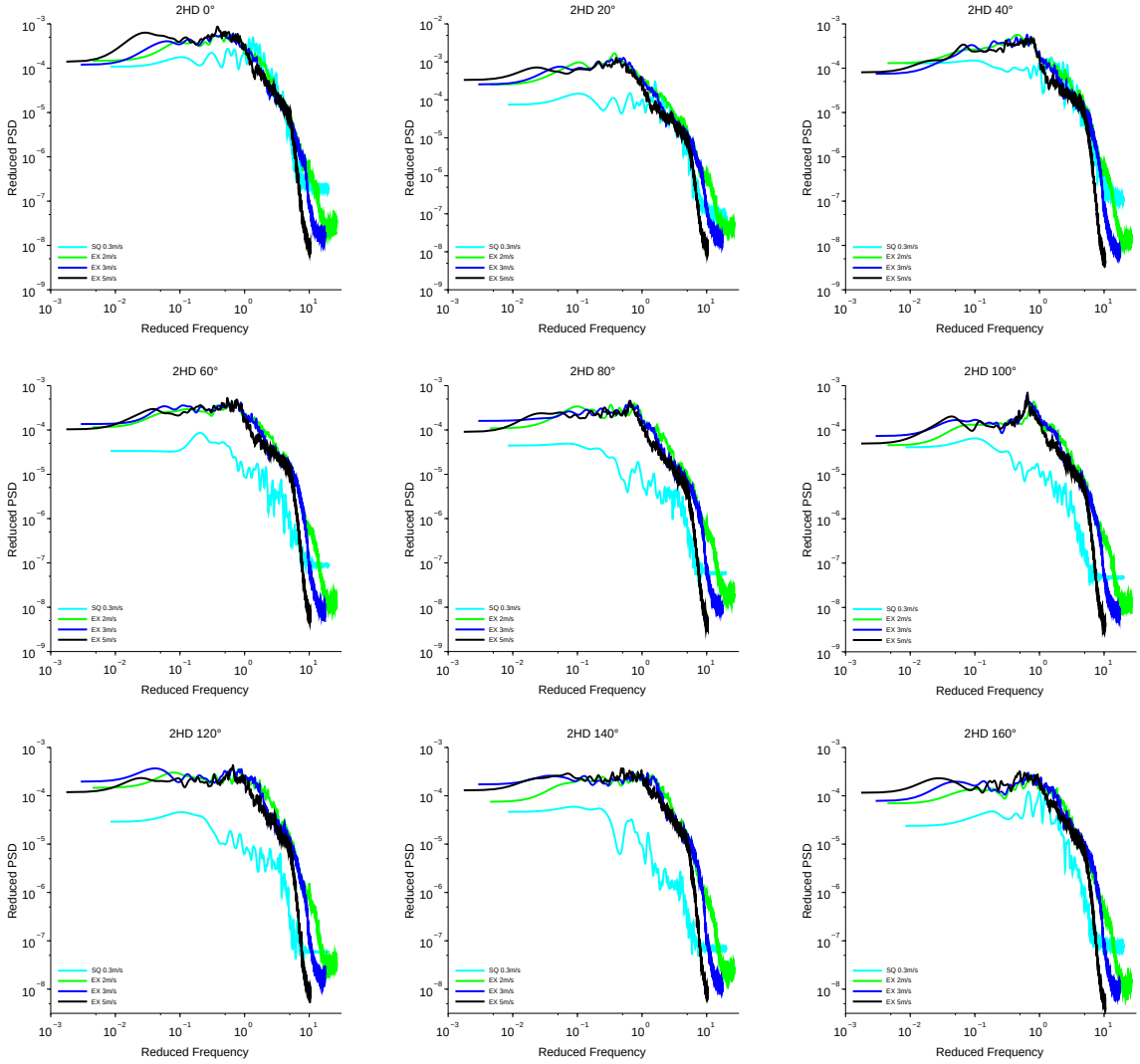

Figure G.7: Comparison of square grid with mixing vanes case (SQ) to 3 different velocities of CALIFS experiment (EX) -
2 HD downstream of the spacer grid and/or mixing vanes

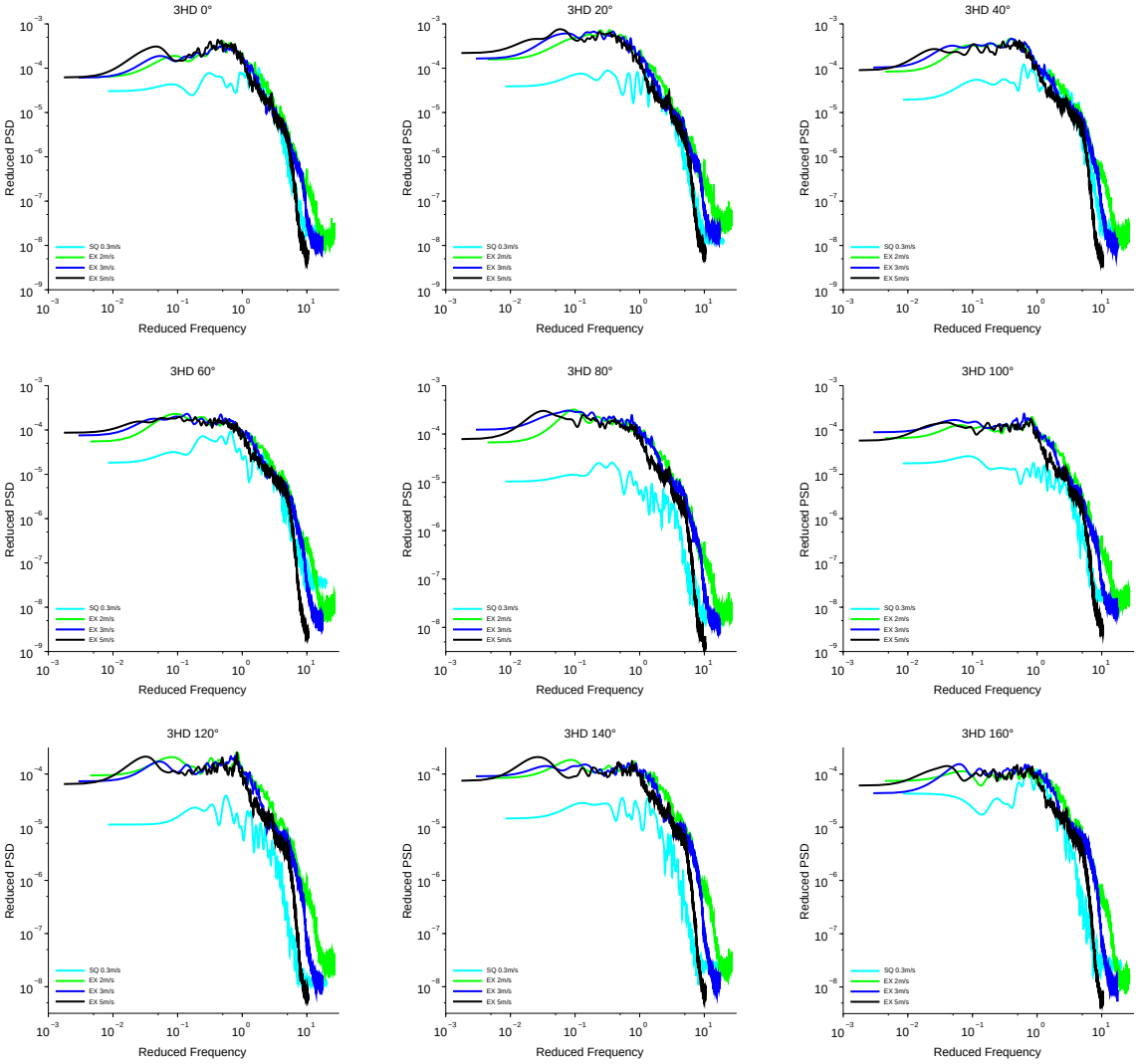

Figure G.8: Comparison of square grid with mixing vanes case (SQ) to 3 different velocities of CALIFS experiment (EX) -
3 HD downstream of the spacer grid and/or mixing vanes

Appendix H

Summary of the Thesis in French

H.1 Chapitre 1: Introduction Générale

Les crayons combustibles dans le coeur d'un réacteur à eau pressurisée (REP) sont soumis à des hautes vitesses axiales de fluide de l'ordre de 5 m/s pour assurer le transfert de la chaleur dans le coeur. Cette haute vitesse de refroidissement induit des vibrations dans les crayons combustibles connues comme ≪flow-induced vibrations (FIV)≫. Dans une telle situation, l'écoulement est turbulent avec un nombre de Reynolds $Re_D \approx 500000$. Ces vibrations induites par l'écoulement peuvent provoquer une usure par frottement des crayons combustibles par friction au niveau des contacts entre la cellule de grille et les crayons des assemblages combustibles. Aux Etats-Unis, 80 % des défaillances dans les REP, où des milliers de crayons combustibles irradiés chauds sont refroidis par l'eau à haute vitesse, sont causés par la ≪grid-to-rod-fretting wear (GTRF)≫: un problème de vibrations induites par l'écoulement qui cause l'usure et la défaillance des crayons [ADTSC Science Highlights, 2013]. Par exemple, dans le coeur d'un 17 × 17 REP, il y a environ 55000 crayons combustibles. Les points de contact entre la cellule de grille et les crayons des assemblages combustibles, i.e., les ressorts et les bossettes, (Fig. H.1) provoquent l'usure, ce qui peut causer une fuite du combustible nucléaire. La défaillance de plus de quelques crayons dans un assemblage combustible cause l'arrêt de la centrale nucléaire et augmente les coûts de maintenance. La durée typique d'un cycle du combustible s'étend de 18 à 24 mois, et en augmentant la durée de vie du combustible du réacteur, on améliore de manière significative la viabilité économique de l'électricité produite à partir de l'énergie nucléaire.

Dans les REP, la GTRF est un problème de FIV résultant de l'usure et du défaut des crayons dans les assemblages combustibles. Il n'a pas été encore possible de caractériser complètement le problème

Figure H.1: Assemblage combustible d'un REP [ADTSC Science Highlights, 2013]

d'interaction fluide-structure (FSI) induit par l'écoulement. Étant donné la nature incompressible du fluide de refroidissement, le grand nombre de Reynolds, et le caractère flexible des crayons combustibles et des cellule de grille, le problème FSI à l'échelle du coeur du réacteur est très difficile. Les assemblages combustibles en REP sont des faisceaux de barres verticales où l'eau s'écoule du bas vers le haut. Les cellules de grille sont placées le long des faisceaux à des distances axiales régulières. Les ailettes du mélange sont montées sur la partie supérieure des grilles pour générer des structures d'écoulements tourbillonnaires. Les ailettes de mélange sont responsables de l'augmentation de la turbulence et du transfert de chaleur dans les faisceaux de barres. Les structures de turbulence sont très fortes immédiatement en aval des ailettes de mélange et décroissent à mesure que l'écoulement se déplace en aval des ailettes. Les forces hydrodynamiques qui s'appliquent sur les crayons de combustible sont considérées comme responsables de la vibration du crayon et de l'usure GTRF, une des raisons d'endommagement du combustible nucléaire. Pour comprendre les causes profondes de l'usure par frottement (≪fretting wear≫), il faut étudier l'écoulement turbulent du liquide de refroidissement dans le coeur de réacteur. On ne peut pas faire disparaître cet écoulement turbulent, ni supprimer les structures comme les cellules de grille qui améliorent la turbulence et le transfert de chaleur dans le coeur [King et al., 2002]. Comme mentionné par Pettigrew [1993], Rubiolo [2006], Rubiolo and Young [2009], les dommages produits via ≪ fretting wear ≫ dans les réacteurs nucléaires peuvent être analysés à travers de multiples phénomènes qui ont lieu lors du fonctionnement du réacteur comme: les forces hydrodynamiques sur les crayons combustibles, la modification des propriétés mécaniques du crayon combustible, ou bien encore l'effet de l'irradiation par les neutrons...

Les forces fluides induites par la grille ne sont pas bien connus, bien que certains modèles empiriques existent. L'objectif de cette thèse est d'effectuer des simulations numériques afin d'analyser les forces hydrodynamiques s'exerçant sur les crayons combustibles. Comme la méthode RANS permet seulement de simuler les quantités moyennes, la simulation des grandes échelles (SGE) est nécessaire

pour étudier les quantités fluctuantes. Cependant, une simulation CFD transitoire pour un assemblage combustible complet nécessiterait une grande ressource de calcul ce qui n'est pas réalisable. Par conséquent, la caractérisation est souvent fait en utilisant des configurations géométriques simplifiées et petites [Chang et al., 2008, Caraghiaur et al., 2009, Conner et al., 2010, Christon et al., 2011, Elmahdi et al., 2011, Bieder, 2012, Delafontaine and Ricciardi, 2012, Frank et al., 2012, Bakosi et al., 2013, Nourgaliev et al., 2013, Smith et al., 2013]. Dans ce rapport de thèse, on se propose de rechercher un élément géométrique simple qui reproduit aux mieux le comportement d'une cellule de grille d'un REP. L'idée étant qu'un élément géométrique simple donne des résultats de calcul plus rapide.

Le modélisation SGE a été utilisée pour simuler un écoulement turbulent incompressible pour quatre géométries 3D:

- une conduite annulaire,
- une conduite annulaire avec deux ailettes de mélange symétriquement opposées (MV),
- une conduite annulaire avec une grille circulaire (CG), et
- une conduite annulaire avec une combinaison de grille carrée et deux ailettes de mélange symétriquement opposées (SQ).

Des simulations numériques ont été effectuées avec un nombre de Reynolds de 8900, au lieu du nombre de Reynolds estimé en réacteur de 500000. Avec ce nombre de Reynolds, il a été possible d'obtenir des solutions stables pour différentes géométries avec des temps de calcul raisonnables. Par la suite, des études comparatives entre les différentes configurations ont pu être effectuées sans grande dépense en ressource machine; en effet, une simulation à nombre de Reynolds élevé nécessite un maillage très fin et un temps de calcul plus long. De telles études permette de vérifier s'il est possible d'utiliser des modèles simplifiés. Les géométries 3D ont été construites d'après les configurations expérimentales CALIFS au CEA Cadarache en prenant en compte diverses simplifications. Les résultats de simulations ont été comparés aux résultats expérimentaux. Le nombre de Reynolds de 8900 a été choisi spécifiquement à cause des nombreuses données de simulations et d'expériences qui sont disponbles [Nouri et al., 1993, Nouri and Whitelaw, 1994, Azouz and Shirazi, 1998, Chung et al., 2002, Kaneda et al., 2003, Liu and Lu, 2004, Chung and Sung, 2005, Ould-Rouiss et al., 2009, Hadžiabdić et al., 2013].

Le chapitre suivant présente une étude bibliographique sur le sujet. Dans le chapitre 3, des simulations sur un conduit annulaire sont discutées. Des simulations SGE ont été effectuées sur 5 maillages différentes possédant un niveau de raffinement de plus en plus élevé. Une étude de sensibilité de maillage sur ces mailles est présenté. Dans le chapitre 4, trois obstacles géométriques sont introduits dans

le conduite (notée comme MV, CG et SQ) et leurs effets sur le champ d'écoulement sont étudiées. Tous ces trois cas ont une section en aval de la longueur de 4 fois le diamètre hydraulique (HD), ce qui permet une bonne comparaison entre les différentes géométries. Le chapitre 5 présente une caractérisation détaillée du champ de pression pariétale pour les cinq cas (les trois cas précédant et deux cas pour la conduite annulaire). Une comparaison est faite avec l'expérience CALIFS réalisée au CEA Cadarache. Les forces de fluide obtenues à partir de ces simulations peuvent être utilisées comme données d'entrée dans les codes de mécanique des structures pour étudier la réponse d'un crayon soumis à l'écoulement axial.

Toutes les simulations présentées dans cette thèse ont été effectuées en utilisant le code CFD ≪TrioCFD (anciennement Trio_U)≫ sur les clusters Curie et Airain. Quelques simulations d'essais courts ont également été réalisées sur le cluster Mezel au CEA Cadarache.

H.2 Chapitre 2: Étude Bibliographique

Ce chapitre discute les composants d'un coeur du REP et les phénomènes rencontrés. Les méthodes fondamentales de mécaniques de fluides - notamment la méthode simulation des grandes échelles (SGE) - ont été présentées. Le logiciel de calcul utilisé pour ce travail TrioCFD est ensuite décrit. Les expériences CALIFS du CEA Cadarache ont été utilisées pour valider les différentes simulations. En plus, ce chapitre présente un bibliographie détaillée sur les fluctuations de pression pariétale à la paroi.

H.3 Chapitre 3: Conduite Annulaire

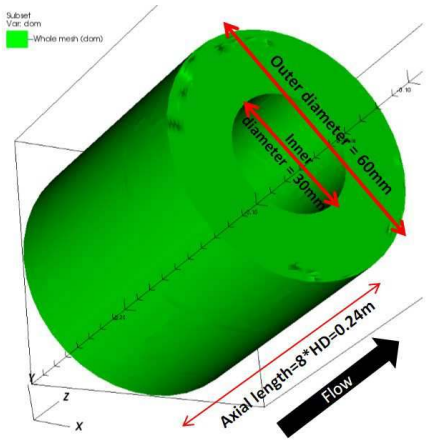

Figure H.2: Schéma d'une conduite annulaire

Les simulations des grandes échelles (SGE) ont été réalisées dans une conduite annulaire (Fig. H.2) d'un rapport de rayon de 0.5 pour cinq résolutions de maillages (Table H.1 et Figs. H.3a au H.3e) avec un nombre de Reynolds 8900. Tout les maillages étaient structurés et tétraédriques. Deux maillages grossiers et trois maillages fins ont été étudiés. L'objectif de ce chapitre était triple: tout d'abord, avoir une idée de la résolution de maillage acceptable pour effectuer des calculs dans une conduite annulaire; d'autre part, de renforcer la confiance dans le code TrioCFD; et, troisièmement, de générer les conditions d'entrée pour les géométries complexes abordées dans le chapitre suivant. En raison du maillage régulier, il n'a pas été possible de générer des turbulences en utilisant le profil uniforme comme conditions initiales ou les profils perturbés (sinusoïdal, parabolique, bruit aléatoire etc.). Ainsi, un écoulement turbulent pleinement développé à partir d'une simulation de maillage grossier a été utilisé comme condition initiale. Une étude de sensibilité a été réalisée entre les cinq maillages et on a trouvé que le profil de vitesse moyenne présente une forte dépendance de la résolution azimutale par rapport

Cas	N° de noeud de maille (N_r, N_θ, N_z)	Δ_r^+	Δ_θ^+	Δ_z^+	N° d'éléments (en millions)	Temps CPU (en heures)
C1 (Coarse)	(25,80,120)	7.7	9.2	15.3	1.3	4140
C2 (Coarse)	(25,160,120)	8.8	5.3	17.6	2.7	9315
F1 (Fine)	(73,160,480)	1.3	5.1	2.4	33	74980
F2 (Fine)	(73,320,240)	1.3	2.7	4.9	33	111780
UF (Ultra-fine)	(73,640,120)	1.3	1.3	9.6	33	74980

Table H.1: Résolution des mailles

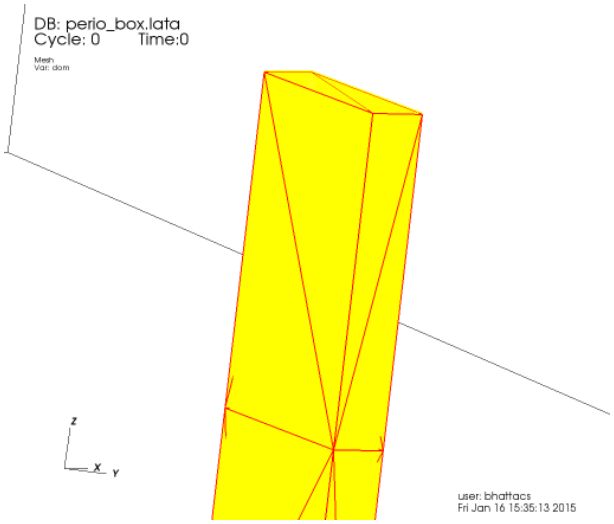

(a) C1 cas

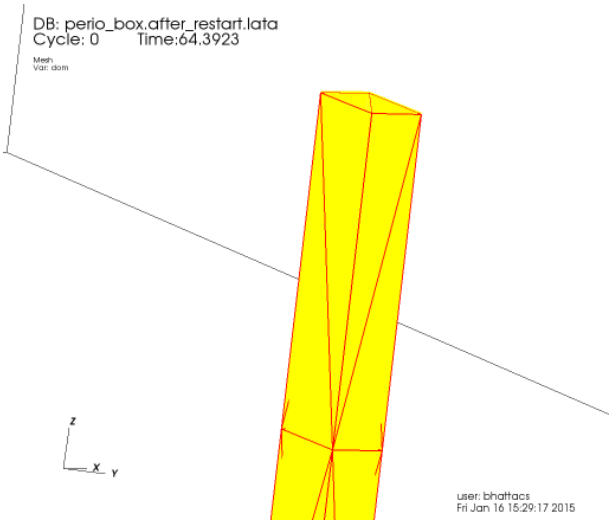

(b) C2 cas

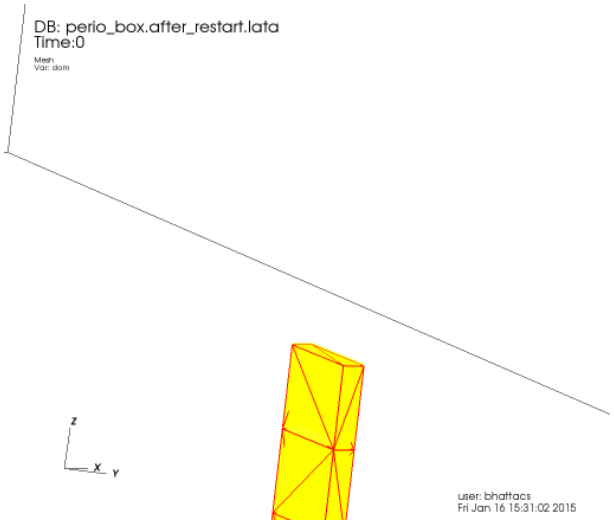

(c) F1 cas

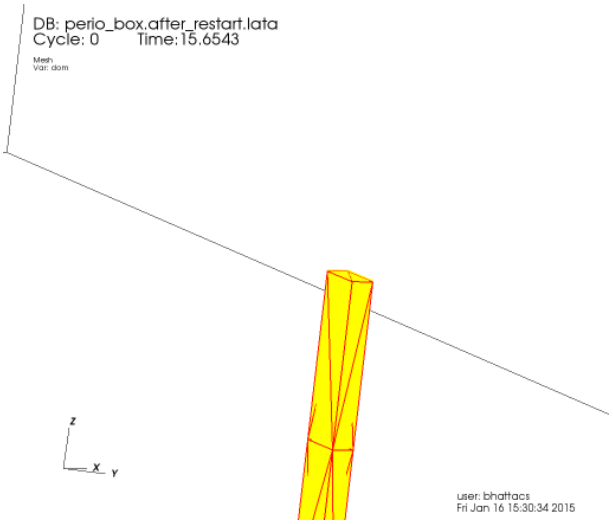

(d) F2 cas

(e) UF cas

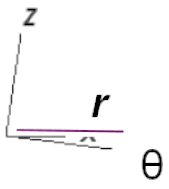

(f) Axes

Figure H.3: Comparaison de la taille relative de maille pour 5 cas

à la résolution axiale. Une comparaison des vitesses moyennes pour les maillages fins et grossiers est présentée dans les Figs. H.4 et H.5 respectivement. Pour ces cinq maillages, on peut conclure qu'une résolution de l'ordre de 1 dans la direction radiale, 3 dans la azimuthale et 10 dans la direction axiale dans les unités adimensionnelles (y^+) est acceptable pour reproduire le résultat DNS et les résultats expérimentaux trouvés dans la littérature. L'analyse de sensibilité présentée ici a été publiée par Bhattacharjee et al. [2015a]. La simulation a été répétée avec le même maillage pour un nombre de Reynolds élevé de 26600 et on a trouvé que les profils de vitesse moyenne normalisés se chevauchent. Par conséquent, le nombre de Reynolds ne semble pas avoir un fort impact.

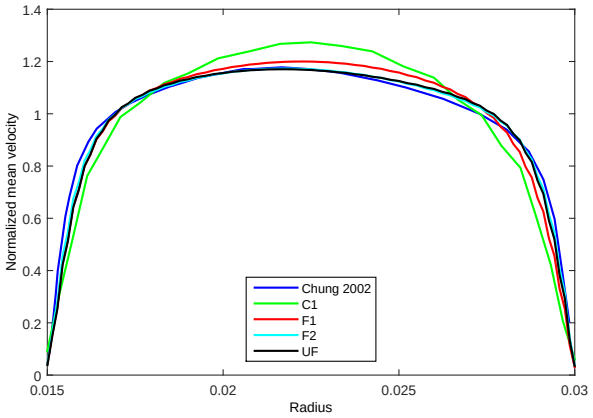

Figure H.4: Comparaison de la vitesse axiale moyenne entre les maillages fines

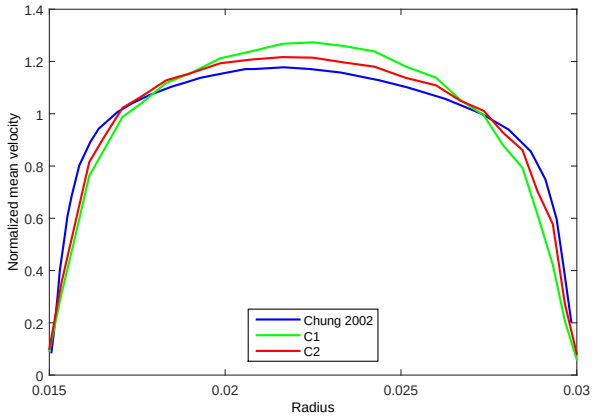

Figure H.5: Comparaison de la vitesse axiale moyenne entre les maillages grossières

H.4 Chapitre 4: Champ Hydrodynamique

Figure H.6: Schématique de la conduite avec des ailettes de mélange (MV)

Figure H.7: Schématique de la conduite avec la grille circulaire (CG)

Figure H.8: Schématique de la conduite avec la grille carrée et des ailettes de mélange (SQ)

Dans ce chapitre, trois obstacles géométriques ont été introduits à l'intérieur de la conduite annulaire, i.e., les deux ailettes de mélange (MV), une grille circulaire (CG) et une grille carrée avec des ailettes de mélange (SQ) (Figs. H.6, H.7 et H.8 respectivement). Un maillage hybride a été généré dans les cas de MV et de SQ: le maillage est non-structuré autour des obstacles et structuré dans le reste du domaine. Un maillage structuré a été utilisé dans le cas de CG en raison de sa symétrie.

En regardant les spectres de vitesse à des hauteurs différentes, un pic se trouve à 38 Hz pour une sonde placée loin des ailettes. Aucun pic n'a été observé pour une sonde placée près des ailettes. Une

comparaison de la vitesse axiale moyenne et RMS à 1 HD et 2 HD en aval des obstacles pour tout les cas est représenté sur les Figs. H.9a à H.12b. Par comparaison des sondes près et loin des MV, il est clair que les ailettes de mélange présentent les fluctuations plus importantes. Sur les Figs. H.9b et H.10b, on observe que la présence de la grille carrée près de la paroi externe diminue la vitesse dans cette région et augmente la vitesse dans la région proche de la paroi interne. A partir de ces sondes, il semble que le cas de la SQ est une combinaison des cas MT et CG. Des sondes près des MV (Figs.H.11a et H.12a), on observe que les fluctuations sont plus fortes à 1 HD en aval par rapport à 2 HD. Les analyses présentées dans ce chapitre pour le cas des ailettes de mélange (MV) ont été publiées par Bhattacharjee et al. [2015b].

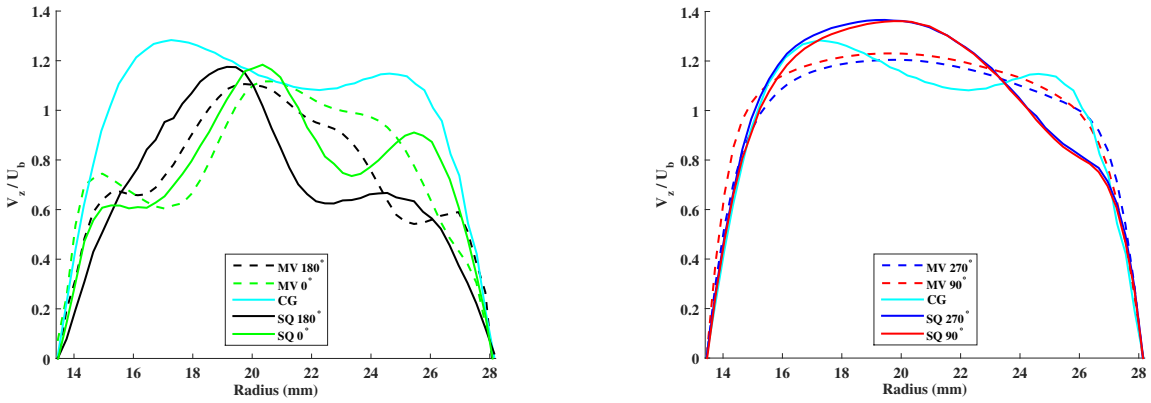

(a) Sondes près de MV

(b) Sondes loin de MV

Figure H.9: Comparaison de la vitesse moyenne axiale pour les 3 cas à 1 HD

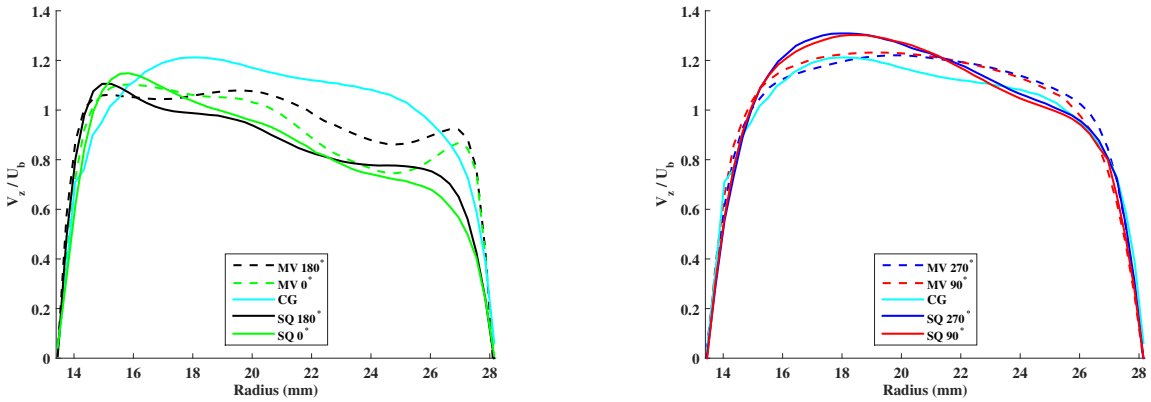

(a) Sondes près de MV

(b) Sondes loin de MV

Figure H.10: Comparaison de la vitesse moyenne axiale pour les 3 cas à 2 HD

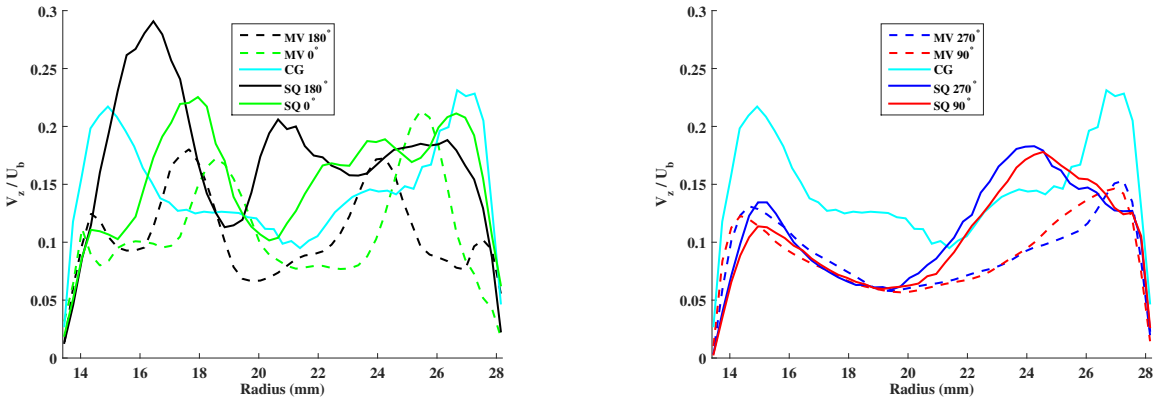

(a) Sondes près de MV

(b) Sondes loin de MV

Figure H.11: Comparaison de la RMS vitesse axiale pour les 3 cas à 1 HD

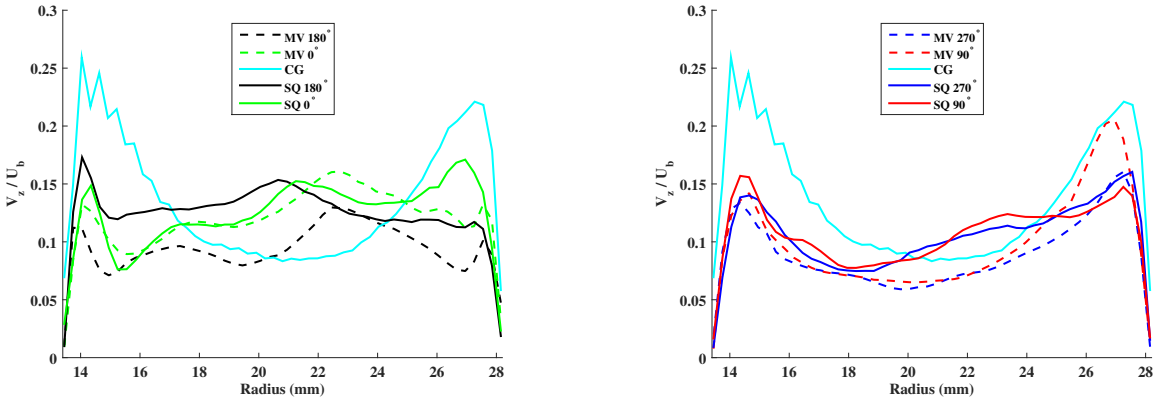

(a) Sondes près de MV

(b) Sondes loin de MV

Figure H.12: Comparaison de la RMS vitesse axiale pour les 3 cas à 2 HD

H.5 Chapitre 5: Champ Pression Pariétale

Dans ce chapitre, le champ de pression à la paroi a été analysé pour diverses simulations et comparé avec des expériences et des modèles. Dans tous les cas, les forces hydrodynamiques latérales présentent une forte fluctuation immédiatement en aval des ailettes ou grille. Les longueurs de corrélation ont été calculées pour chaque cas. La comparaison de la longueur de corrélation pour une conduit annulaire avec la littérature a montré un bon accord, la longueur diminue avec l'augmentation du nombre de Reynolds. Le maillage grossier pour la conduite annulaire ne suffit pas pour l'étude de champ de pression pariétale. Elle montrer une mauvaise prédiction du champ de pression pariétale.

Il a également été observé que la grille et les ailettes de mélange ont des effets combinés; la grille accélére l'écoulement et amplifie les fluctuations induites par les ailettes.

Malgré la simplification apportée à la géométrie en négligéant les ressorts et les bossettes, les résultats de la simulation étaient comparables aux résultats expérimentaux (Fig. H.13). Cependant, certains écarts existent et peuvent être attribués à l'absence des ressorts et des bossettes. D'autres simulations peuvent être réalisées avec des ressorts et des bossettes simplifiées pour voir leurs effets sur la pression pariétale.

Les simulations doivent être effectuées pour un nombre de Reynolds plus élevé pour voir si les pics de fréquence observés dans les simulations sont dus au phénomène de ≪vortex shedding≫. Les comparaisons préliminaires avec certains modèles semi-empiriques développés pour une plaque plane avec couche limite turbulente ont été faites. Il est intéressant de noter que le cas avec grille carrée était plus proche du modèle que celui avec conduite annulaire. Cela peut être attribué à la présence des obstacles géométriques qui modifient la structure de l'écoulement, ce qui modifie ainsi le champ de pression pariétale. Toutefois, pour obtenir des conclusions définitives, des modèles plus appropriés doivent être développées.

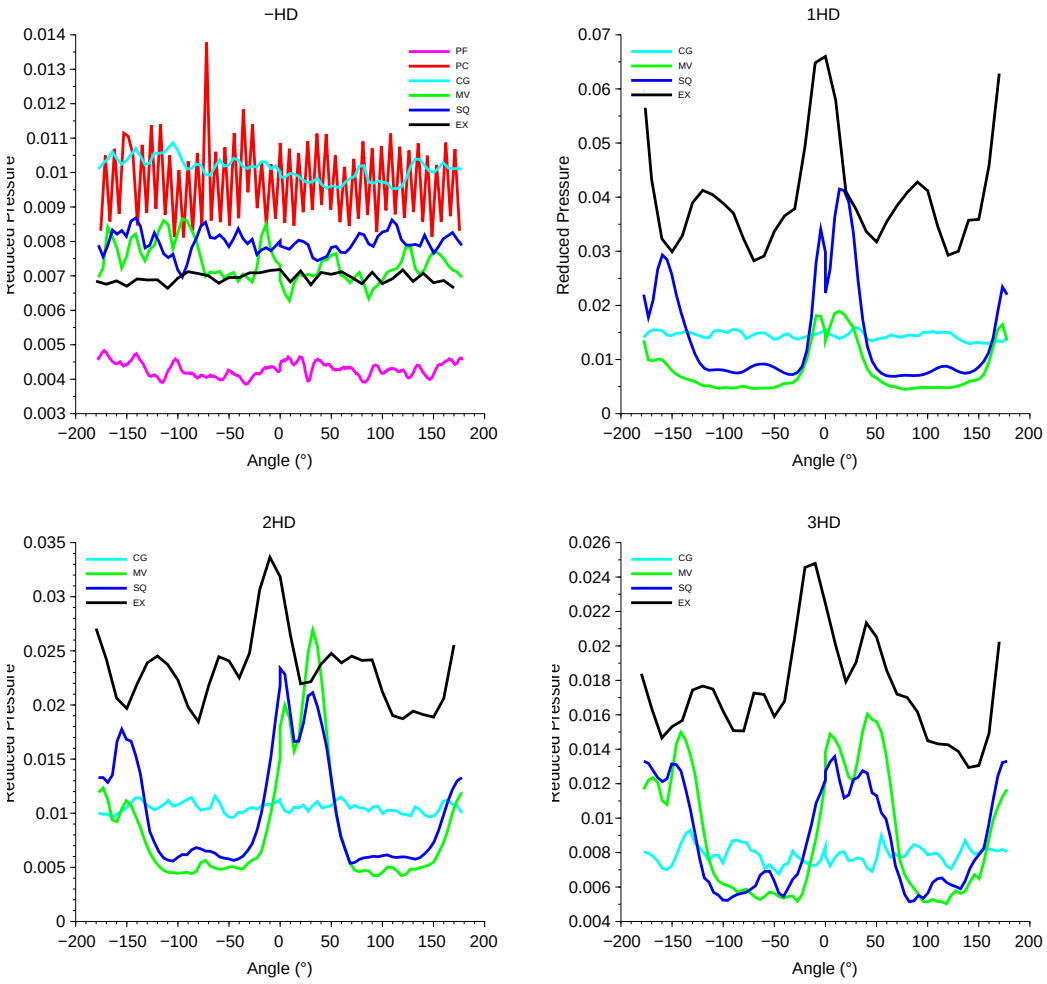

Figure H.13: RMS de pression réduite, en amont et en aval de la grille et/ou des ailettes (CG, MV, SQ). EX représente les données expérimentales CALIFS à $Re_D = 58500$

H.6 Chapitre 6: Conclusion Générale

A cause de la structure très complexe d'un assemblage combustible de REP, certaines simplifications ont été faites dans le modèle avant l'exécution des calculs transitoires. Tout d'abord, les calculs SGE ont été effectués sur une conduite annulaire avec un rapport de rayon de 0.5 à mailles tétraédriques et structurées en utilisant le code CFD TrioCFD et l'outil open-source CAD Gmsh. Cinq résolutions différentes de maillages ont été choisies avec un ordre de raffinement croissant. Une forte dépendance de la résolution azimutale du maillage a été observée par rapport de la résolution axiale. En considérant cinq maillages, un compromit acceptable entre la précision et les ressources de calcul nécessaires, une résolution de l'ordre de 1 en radiale, 3 en azimutale et 10 en le direction axiale dans les unités adimensionnels (y^+) est acceptable pour simuler cette conduite annulaire. Les vitesses axiales moyennes normalisées ont le même profil pour les deux nombres de Reynolds 8900 et 26600. Ces simulations nous ont permis de développer des conditions aux limites d'entrée appropriées pour les futures géométries complexes et aussi améliorer notre confiance dans le code TrioCFD.

Ensuite, trois singularités géométriques ont été introduites à l'intérieur de la conduite annulaire: deux ailettes de mélange placées symétriquement (MV), une grille circulaire (CG) et une grille carrée avec des ailettes de mélange (SQ). Une stratégie hybride de maillage a été adoptée pour les cas avec des ailettes de mélange: maillage non structuré autour des ailettes et maillage structuré dans les régions en amont et en aval du obstacles. La résolution axiale était moins bonne lorsque l'on s'éloignait de la région non-structurée. La grille circulaire, bien que fictive, a été construit en prenant en compte le ratio des diamètres hydrauliques des zones d'écoulement interne et externe. En raison de sa symétrie inhérente, le maillage tétraédrique et structuré peut être généré pour le cas de la grille circulaire. L'idée de maintenir un maillage structuré permet d'améliorer la vitesse de la simulation mais également de réduire les erreurs numériques qui peuvent survenir en raison de l'interpolation par le code à partir du noeud de calcul à l'emplacement de la sonde. Dans les trois cas, la résolution de maillage en direction ≪wall normal≫ est environ 3 unités de paroi. En raison du manque de ressources de calcul, le SGE paroi-résolu ($y^+ \approx 1$) ne pouvait pas être effectuée. Par conséquent, la loi de paroi de Reichardt a été utilisée pour modéliser le comportement près des parois. La comparaison des caractéristiques d'écoulement à 1 HD et 2 HD en aval d'obstacles pour les cas MV et SQ montrent une vitesse de pointe plus élevée pour le cas SQ. Cela est provoqué par l'accélération de l'écoulement dans la région centrale du canal hydraulique dans la cas SQ. La présence de la grille à proximité de la paroi externe

diminue la vitesse dans cette région. Cet effet diminue à mesure que nous allons plus loin en aval. En comparant les profils de vitesse pour les sondes près de MV et loin de MV, il est clair que les ailettes de mélange introduisent les fluctuations maximales. Les ailettes de mélange créent une déviation dans l'écoulement, créant une structure de ≪swirl≫ qui évolue dans la direction axiale. En plus, il semble que le cas de la SQ est un effet de sommation des cas MV et CG. Les fluctuations RMS de la vitesse sont plus forts à 1 HD par rapport à 2 HD.

Ensuite, le champ de pression pariétale sur la paroi interne de la conduite a été analysé pour les différentes simulations et comparé avec des expériences. En regardant les corrélations spatiales axiales et azimutales, on observe que la résolution du maillage grossier ne suffit pas à caractériser le champ de pression pariétale pour la conduite annulaire. De manière similaire aux observations faites sur les profils de vitesse, il semble que le cas SQ montre un effet sommation entre les cas MV et CG pour le champ de pression. Bien que la présente simulation possède un Reynolds de 8900 environ six fois inférieur à celle de l'expérience CALIFS (≈ 58500), les simulations illustrent des résultats comparables. Les différences observées peuvent être attribuées à l'absence des ressorts et bossettes sur la surface de grille carrée qui accélére l'écoulement. Dans l'ensemble, les ailettes de mélange et la grille circulaire semblent avoir un effet cumulatif équivalent à la grille carré.

Des comparaisons préliminaires avec les modèles semi-empiriques pour une couche limite turbulente sur une plaque plane ont été réalisées. Il a été constaté que le cas avec la grille carrée était plus proche du modèle que dans le cas avec la conduite annulaire. Cela peut être attribué à la présence des obstacles géométriques qui modifient la structure d'écoulement ainsi que le champ de pression pariétale. Cependant, les modèles appropriés devraient être développés pour obtenir des conclusions définitives.

Dans le futur, il serait intéressant d'effectuer de nouvelles simulations avec plus de complexités géométriques, i.e., en incluant la configuration ≪ressorts et bossettes simplifiés≫ sur la surface de la grille. Bieder [2013] a effectué une simulation SGE en utilisant TrioCFD sur un ≪ 5×5 rod bundle ≫ sans prendre en compte les ressorts et les bossettes, certains écarts ont été signalés entre la simulation et les résultats expérimentaux. Dans cette thèse, l'effet du nombre de Reynolds a été présenté pour le cas de la conduite annulaire. Ainsi, les simulations doivent être effectuées sur le MV, CG et les cas SQ pour plusieurs nombres de Reynolds pour voir l'effet de la hausse du nombre de Reynolds sur les caractéristiques hydrauliques et les fluctuations de pression pariétale. Même si en regardant les résultats de l'expérience CALIFS, il ne semble pas avoir un effet significatif. Les expériences peuvent

être réalisées avec des structures simplifiées pour valider ces simulations et pour avoir une idée sur la façon dont chaque structure affecte l'écoulement. Dans l'expérience CALIFS, en raison du seuil de débit de la pompe, les mesures ne pouvaient pas être effectués pour un nombre de Reynolds inférieur à 58500 (vitesse = 2 m/s). Il serait intéressant d'examiner les résultats expérimentaux à des nombres de Reynolds inférieurs. Les simulations doivent être effectuées sur des maillages avec la résolution $y^+ \approx 1$ de manière à examiner l'effet de la résolution du maillage. Enfin, l'effet de l'utilisation de la fonction de Reichardt sur le champ de pression de la paroi doit être étudié soit en raffinant le maillage près de la paroi, soit en simulant un nombre de Reynolds inférieur pour le même maillage. De cette manière, l'utilisation des fonctions de parois pourraient être évités.

Les spectres de la pression sur la paroi obtenus grâce à ces simulations CFD peuvent êtres utilisés comme données d'entrées dans les codes de mécanique des structures pour étudier la réponse d'un crayon à un écoulement axiale. Cela pourrait fournir une estimation de $\ll$ fretting wear $\gg$ sur ces crayons. Quelques développements dans ce sujet sont cités: Meng and Ludema [1995], Kim [1999], Rubiolo [2006], Rubiolo and Young [2008, 2009].

Abstract

Flow-induced vibrations in a pressurized water reactor (PWR) core can cause fretting wear in the fuel rods. Due to friction, wear occurs at the contact locations between the spacer grid and the fuel rod. This could compromise the first safety barrier of the nuclear reactor by damaging the fuel rod cladding. In order to ensure the integrity of the cladding, it is necessary to know the random fluctuating forces acting on the rods. However, the spectra for these fluid forces are not well known.

The goal of this PhD thesis was to use simple geometrical elements to check the reproducibility of realistic pressurized water reactor spacer grids. As a first step, large eddy simulations were performed on a concentric annular pipe for different mesh refinements using the CFD code TrioCFD (previously Trio_U) developed by CEA. A mesh sensitivity study was performed to obtain an acceptable mesh for reproducing standard literature results. This information on mesh resolution was used when carrying out simulations using various geometric obstacles inside the pipe, namely, mixing vanes, circular spacer grid and a combination of square spacer grid with mixing vanes. The last of the three configurations is the closest to a realistic PWR fuel assembly. Structured mesh was generated for the annular pipe case and circular grid case. An innovative hybrid mesh was used for the two remaining cases of the mixing vanes and the square grid: keeping unstructured mesh around the obstacles and structured mesh in the rest of the domain. The inner wall of the domain was representative of the fuel rod cladding. Both hydraulic and wall pressure characteristics were analyzed for each case. The results for the square grid case were found to be an approximate combination of the mixing vane case and circular grid case. Simulation results were compared with experiments performed at CEA Cadarache. Some preliminary comparisons were also made with classical semi-empirical models.

***Keywords**: large eddy simulation, LES, wall pressure fluctuations, spacer grid, mixing vanes, CFD, Trio_U, TrioCFD.*

Résumé

Les vibrations induites par l'écoulement dans le coeur du réacteur à eau pressurisée (REP) peuvent provoquer une usure par frottement des crayons combustibles par friction au niveau des contacts entre la cellule de grille et les crayons des assemblages combustibles. Cela peut entraîner des dommages irréversibles de la gaine du crayon combustible et compromettre la première barrière de sûreté du réacteur. Assurer l'intégrité de la gaine est une préoccupation majeure dans la sûreté du réacteur. Par conséquent, il est nécessaire d'améliorer les connaissances sur les forces fluides agissant sur les crayons. Cependant, les spectres d'excitation de ces forces fluides ne sont pas bien connus.

Le but de cette thèse est d'utiliser des éléments géométriques simples pour reproduire des cellules de grilles d'un REP. Tout d'abord, des simulations des grandes échelles ont été effectuées sur une conduite annulaire concentrique avec différents maillages en utilisant le code TrioCFD (précédammant Trio_U) développé par le CEA. Une étude de sensibilité de maillage a été réalisée afin de proposer un maillage reproduisant correctement les résultats dans la littérature. Ces informations de résolution de maillage ont été utilisées lors de la réalisation des simulations en utilisant divers obstacles géometriques intérieurs à la conduite, *i.e.*, des ailettes de mélange, une grille circulaire et une combinaison de grille carrée et d'ailettes de mélange. La dernière des trois configurations est la plus proche d'un REP. Un maillage structuré a été généré dans le cas de la conduite annulaire et dans le cas de la grille circulaire. Un maillage hybride a été utilisé dans le cas des ailettes de mélange et dans le cas de cellule de grille carrée: le maillage est non-structuré autour des obstacles et structuré dans le reste du domaine. La paroi interne du domaine représente la gaine du crayon combustible. Les caractéristiques hydrauliques ainsi que la pression pariétale ont été analysées dans chaque cas. Il apparaît que la grille carrée est une combinaison approximative du cas des ailettes de mélange et du cas de la grille circulaire. Les résultats des simulations ont été comparés avec des mesures réalisées au CEA Cadarache. De plus, des comparaisons préliminaires ont été effectués avec certains modèles semi-empiriques classiques.

***Mots-clés**: simulation des grandes échelles, fluctuations de pression pariétale, cellule de grille, ailettes de mélange, CFD, Trio_U, TrioCFD.*